Supernova Neutrinos: Production, Oscillations and Detection

A. Mirizzi([1])([2]), I. Tamborra([3]), H.-Th. Janka([4]), N. Saviano([5]), K. Scholberg([6]), R. Bollig([4])([7]), L. Hüdepohl([8]), and S. Chakraborty([9])

([1]) *Dipartimento Interateneo di Fisica "Michelangelo Merlin," Via Amendola 173, 70126 Bari, Italy.*

([2]) *Istituto Nazionale di Fisica Nucleare - Sezione di Bari, Via Amendola 173, 70126 Bari, Italy.*

([3]) *GRAPPA Institute, University of Amsterdam, Science Park 904, 1098 XH Amsterdam, The Netherlands.*

([4]) *Max-Planck-Institut für Astrophysik, Karl-Schwarzschild-Str. 1, 85748 Garching, Germany.*

([5]) *Institute for Particle Physics Phenomenology, Department of Physics, Durham University, Durham DH1 3LE, United Kingdom.*

([6]) *Department of Physics, Duke University, Durham, NC, 27708, USA.*

([7]) *Physik Department, Technische Universität München, James-Franck-Str. 1, 85748 Garching, Germany.*

([8]) *Max Planck Computing and Data Facility (MPCDF), Gießenbachstr. 2,85748 Garching, Germany.*

([9]) *Max-Planck-Institut für Physik (Werner-Heisenberg-Institut), Föhringer Ring 6, 80805 München, Germany.*

Summary. — Neutrinos play a crucial role in the collapse and explosion of massive stars, governing the infall dynamics of the stellar core, triggering and fueling the explosion and driving the cooling and deleptonization of the newly formed neutron star. Due to their role neutrinos carry information from the heart of the explosion and, due to their weakly interacting nature, offer the only direct probe of the dynamics and thermodynamics at the center of a supernova. In this paper, we review the present status of modelling the neutrino physics and signal formation in collapsing and exploding stars. We assess the capability of current and planned large underground neutrino detectors to yield faithful information of the time and flavor dependent neutrino signal from a future Galactic supernova. We show how the observable neutrino burst would provide a benchmark for fundamental supernova physics with unprecedented richness of detail. Exploiting the treasure of the measured neutrino events requires a careful discrimination of source-generated properties from signal features that originate on the way to the detector. As for the latter, we discuss self-induced flavor conversions associated with neutrino-neutrino interactions that occur in the deepest stellar regions; matter effects that modify the pattern of flavor conversions in the dynamical stellar envelope; neutrino-oscillation signatures that result from structural features associated with the shock-wave propagation as well as turbulent mass motions in post-shock layers. Finally, we highlight our current understanding of the formation of the diffuse supernova neutrino background and we analyse the perspectives for a detection of this relic signal that integrates the contributions from all past core-collapse supernovae in the Universe.

PACS 14.60.Pq, 14.60.Lm, 97.60.Bw – .

1. – Introduction

Core-collapse supernovae are among the most powerful sources of neutrinos in our Universe. During a supernova explosion, 99% of the emitted energy ($\sim 10^{53}$ erg) is released by neutrinos and antineutrinos of all flavors, with energy of several MeV, which play the role of "astrophysical messengers," escaping almost unimpeded from the supernova core. The supernova neutrino flux has been extensively studied as a probe of both fundamental neutrino properties and core-collapse physics. Therefore, supernova neutrinos represent a truly interdisciplinary research field at the interface between particle physics, nuclear physics and astrophysics.

While Galactic supernovae are rare, existing or proposed large neutrino detectors will allow collection of a high-statistics neutrino signal from the next Galactic explosion. The supernova neutrino detection will be crucial to test the explosion mechanism and thus to compare current supernova models with direct empirical information from the supernova core. Originating from deep inside the core, neutrinos are affected by flavor conversions in the dense supernova matter on their way through the stellar mantle and envelope. Therefore, the neutrino fluxes reaching the detectors will carry intriguing signatures of oscillation effects in the deepest supernova regions, depending on the unknown neutrino mass hierarchy. In this sense, the dense supernova interior represents a unique laboratory to probe neutrino flavor mixing under high-density conditions.

Matter effects in a supernova can be truly dramatic as neutrinos propagate through a dense turbulent environment. Furthermore in the deepest supernova regions, the neutrino

density is so high that it dominates the flavor evolution, producing a fascinating *collective* behavior associated with ν-ν interactions. In the recent past, our description of self-induced neutrino oscillations has seen substantial progress. The seminal studies started almost a decade ago [1-6] stimulated a still-ongoing torrent of analytical and numerical works to clarify several aspects of this unusual flavor dynamics (see [7] for a review).

It is thus evident that the physics potential of a supernova neutrino detection is enormous. Stellar collapse neutrinos were observed for the first (and so far only) time in 1987. Within a decade since the advent of large underground neutrino detectors, Nature was kind enough to provide a neutrino burst associated with the collapse of Sanduleak -69^0 202 in the Large Magellanic Cloud, 51 kpc away. Two kiloton-scale water Cherenkov detectors, one in Japan, Kamiokande-II [8], and one in the United States, the Irvine-Michigan-Brookhaven (IMB) experiment [9], observed about 20 events within 13 seconds, with timing consistent with the optical observation of the SN 1987A explosion. The positron spectra produced by inverse beta decays of supernova $\bar{\nu}_e$ in the two detectors are represented in Fig. 1. Two smaller scintillator detectors, Baksan [11] and the Mont Blanc Liquid Scintillation Detector (LSD) [12] also reported several events ([1]).

The detection of SN 1987A neutrinos has long been taken as a confirmation of the salient features of our physical comprehension of the core-collapse supernova phenomenon and of the associated neutrino emission. This observation allowed us to put strong constraints on exotic neutrino properties (e.g., decays, neutrino charge) that would have altered the supernova neutrino emission. Most importantly, the total energy of $\bar{\nu}_e$ and the inferred cooling time scale of a few seconds of the proto-neutron star put severe limits on non-standard cooling mechanisms associated with new particles emitted from the supernova core, notably right-handed neutrinos and axions (see [13] for a review). At the same time, with the poor statistics of the SN 1987A events, determining both supernova and neutrino parameters is impossible, although some hints could be obtained, e.g., the signal of SN 1987A was analysed in the light of neutrino oscillations [14, 15].

The Galactic supernova rate can be estimated with different techniques (see, e.g., Table X in [16]). Typically one expects 1-3 core-collapse supernovae per century. However, except for SN 1987A in the Large Magellanic Cloud, no stellar collapse has been observed over more than 30 years of neutrino experiments. This absence of a signal allowed different neutrino experiments to place non-trivial upper bounds to the rate of collapses and failed supernovae [17-19], which confirm that a Galactic supernova explosion is a rare event.

However, there are ~ 10 supernova explosions per second in the visible Universe. The cumulative emission of neutrinos from all the past core-collapse supernovae produces a cosmic background of (anti)neutrinos, the so-called Diffuse Supernova Neutrino Background (DSNB), whose existence was predicted already before the observation of SN 1987A [20]. Although weak, the DSNB is a "guaranteed" signal that can also probe physics different from a Galactic explosion, including processes which occur on cosmological scales in time or space. The DSNB covers a wide range of physics, including the cosmic star formation rate, the stellar dynamics and fundamental neutrino properties. Forecasts of the DSNB can be obtained using the neutrino spectra predicted by supernova simulations or the ones reconstructed from SN 1987A data [21], as shown in Fig. 2. The stringent observational upper limit on the DSNB flux, obtained by Super-

([1]) The reported LSD burst is more controversially associated with the supernova, because the events were recorded some hours earlier than the others.

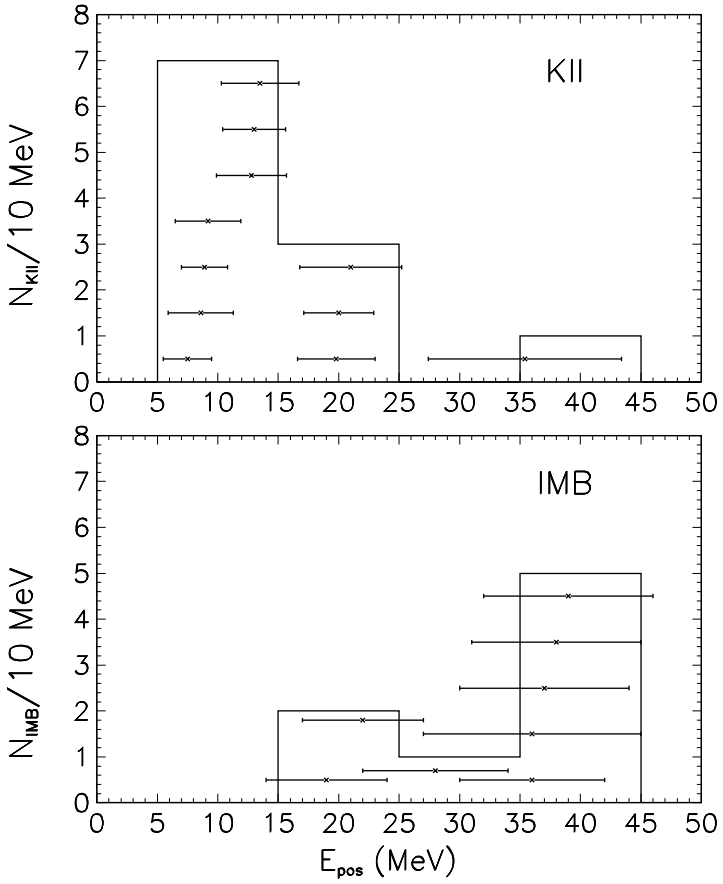

Fig. 1. – Positron spectra detected at Kamiokande-II (upper panel) and IMB (lower panel) in connection with SN 1987A. (Reprinted figure from [10]; copyright (2005) by the American Physical Society.)

Kamiokande [22,23], is only a factor of ~ 2 higher than typical theoretical estimates [24]. This suggests an imminent detection of the DSNB in current and planned detectors.

Nearly three decades after SN 1987A, we are eager for the next supernova neutrino signal. Meanwhile our understanding of supernova neutrinos has grown significantly. Remarkably, our modeling of the supernova neutrino emission and of flavor conversions in the stellar matter has experienced several breakthroughs. On the other side there is vivid experimental activity in low-energy neutrino astronomy, whose main goal is the detection of Galactic and diffuse supernova neutrino signals. Given the recent advances both on the theoretical and experimental fronts, in this review we aim to present state-of-the-art supernova neutrino physics and astrophysics. Our plan is as follows.

In Section **2** we review the neutrino-emission phases of core-collapse supernovae, the characteristic signal properties expected during these phases, and our current understanding of the delayed neutrino-driven mechanism based on multi-dimensional modeling of stellar collapse and explosion. Besides reporting new and unexpected neutrino-emission

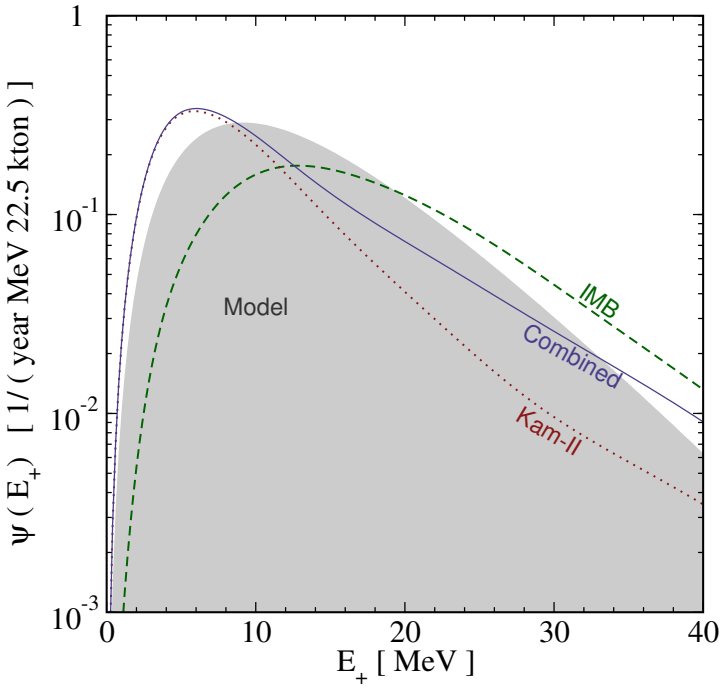

Fig. 2. – The DSNB detection spectra based on the neutrino spectra inferred from either the Kamiokande-II or IMB data sets alone or their combination, compared to a model (shaded shape) with canonical neutrino emission parameters. (Reprinted figure with permission from [21]; copyright (2007) by the American Physical Society.)

features associated with the nonradial hydrodynamic flows during the accretion phase, we also present long-timescale proto-neutron star cooling calculations with state-of-the-art treatment of neutrino transport, in which —for the first time— convective transport effects were taken into account by a mixing-length description for spherically symmetric simulations. In Section **3** we discuss the detectability of (extra)galactic supernova neutrinos in current and planned detectors. We describe the physics potential of the different detection techniques proposed to measure the neutrino burst and present the most relevant applications of a supernova detection to neutrino astronomy and astrophysics. Section **4** is devoted to the characterization of supernova neutrino flavor conversions. Self-induced effects associated with the neutrino-neutrino interactions in the deepest supernova regions and matter effects in the dynamical supernova environment are discussed. Finally, observable signatures of flavor conversions imprinted on the neutrino burst are presented. In Section **5** we focus on the DSNB. We discuss our current knowledge of the cosmic supernova rate and present estimates of the expected DSNB signal in large underground neutrino detectors by taking into account the effects of flavor conversions as well as delicate background issues, and including core-collapse and invisible supernova progenitors. Finally, conclusions and future perspectives are discussed in Section **6**.

We remark that in the current review we assume a standard three-neutrino oscillation framework. We neglect exotic neutrino properties such as a neutrino magnetic moment, neutrino decays or extra sterile neutrino states that would have a potential impact on the

supernova neutrino signal [13]. Also, aspects of neutrino-induced and neutrino-affected nucleosynthesis will only be mentioned in passing. This field is linked to a large diversity of questions that reach far beyond the scope of the topic of our review and which are addressed in Ref. [25].

2. – Neutrino Signals from Stellar Collapse and Supernova Explosions

Authors: H.-Th. Janka, R. Bollig, L. Hüdepohl

In a sequence of hydrostatic nuclear burning stages massive stars build up degenerate iron or oxygen-neon-magnesium cores, whose gravitational collapse terminates the stellar life. These events are the strongest cosmic sources of MeV neutrinos, comparable to neutron-star mergers, but roughly 1000 times more frequent. An intense burst of order 10^{58} neutrinos is released on a time scale of several seconds when a neutron star (NS) or black hole (BH) is born, possibly accompanied by a supernova (SN) explosion that expels several solar masses of stellar debris with velocities up to some ten percent of the speed of light.

Neutrinos are the main agents for the transport of energy and lepton number during the infall of the stellar core and the formation of its compact relic. Therefore they play a decisive role during all stages of such an event. Electron neutrinos (ν_e) are produced by electron captures on nuclei and on free protons and thus accelerate the initial implosion. Their continuous release drives the evolution from the lepton-rich post-collapse configuration to the final deleptonized NS, while neutrinos and antineutrinos of all flavors carry away the gravitational binding energy of the assembling remnant. Neutrino-energy deposition behind the stalled bounce shock can revive the shock and can thus initiate the SN explosion. The interaction of electron neutrinos and antineutrinos with the neutrino-heated outflow sets the neutron-to-proton ratio and hence determines the nucleosynthesis in the innermost SN ejecta. The intense neutrino radiation that escapes from the central regions can trigger nuclear spallations, whose free nucleons can seed interesting chemical element formation even in the outer stellar shells. Matter and neutrino-induced flavor oscillations inside the exploding star can affect these processes, and vacuum oscillations as well as the matter effects in the Earth contribute in shaping the neutrino signal that is detectable in experimental facilities on earth.

In this Section we summarize the present status of the numerical modeling of stellar core collapse and explosion and of the associated neutrino emission by spherically symmetric and multi-dimensional simulations. The effects of neutrino flavor oscillations, which are usually ignored in the source modeling and only computed in a post-processing treatment, will be discussed in Section **4**.

2˙1. *Neutrinos from supernovae and SN 1987A in retrospect.* – The Nobel prize awarded detection of neutrinos from SN 1987A on February 23, 1987, sets a landmark for the beginning of extragalactic neutrino astronomy. It is the first direct empirical proof of the formation of a hot NS in the gravitational collapse of the core of a massive, evolved star. The overall properties of the measured neutrinos [8, 9, 11], i.e., their individual particle energies, signal duration, and total signal energy, were compatible with theoretical predictions of the neutrino emission from the birth of NSs [26]. Although the limited statistics of only two dozen registered events did not allow for high significance, numerous relevant constraints on particle properties and fundamental physics could be derived on the basis of this neutrino observation in the months and years after SN 1987A [13].

The lack of signal statistics also appears as the most likely explanation of some puzzling features of the neutrino detection, in particular the gap of roughly 7 s between ∼2 s and ∼9 s in the Kamiokande-II data, and the clear excess of events pointing away from the source. Moreover, the Kamiokande and IMB measurements are only marginally consis-

tent with each other. A joint analysis of both experiments also yields a best-fit value for the spectral temperature of the detected electron antineutrinos ($\bar{\nu}_e$) that is considerably lower than expected for the time-integrated neutrino emission on grounds of the most detailed models existing at the time of SN 1987A. This tension is even enhanced given the neutrino mixing parameters indicated by the current phenomenology (cf. Sec. **4**) and the high mean energies that had been predicted for the radiated heavy-lepton neutrinos ($\nu_x = \nu_\mu$, $\bar{\nu}_\mu$, ν_τ, $\bar{\nu}_\tau$) by those early models [14].

Meanwhile, however, this conflict has disappeared because state-of-the-art simulations of the Kelvin-Helmholtz cooling of nascent NSs yield significantly softer heavy-lepton neutrinos and a smaller difference of their spectrum compared to that of electron antineutrinos [27-30]. These trends are along the lines of model adjustments that had been identified in Ref. [14] as a necessary implication of the SN 1987A neutrino data if solar neutrino experiments would bear out a large mixing angle between $\bar{\nu}_e$ and a heavy-lepton neutrino. The improvements in modern treatments of neutrino transport in SNe are connected to the introduction of nucleon-nucleon bremsstrahlung as the most important pair-production process [31, 32], whose relevance for neutrino-spectra formation in NS cooling models had first been pointed out in Ref. [33]. The similarity of $\bar{\nu}_e$ and ν_x spectra is further enhanced by the inclusion of energy transfers in neutrino-nucleon scatterings [27, 34]. A detailed reanalysis of the SN 1987A neutrino detections on the basis of signal predictions by modern hydrodynamical models of SN 1987A, also applying our current knowledge of SN neutrino oscillations, still needs to be performed. This would remove some of the uncertainties in the two-phase parametrizations used in Refs. [35-37] and would allow for a closer assessment of the remaining discrepancies between model predictions and SN 1987A neutrino measurements.

One of the biggest unsolved riddles in connection to SN 1987A is a cluster of 5 neutrinos of 7–11 MeV registered within 7 s by the LSD scintillator experiment in the Mont Blanc Laboratory roughly 4.5 hours before the Kamiokande II, IMB and Baksan events occurred [12]. The fact that none of these other experiments reported any significant detection at the time of the Mont Blanc measurement might be understood by the relatively low energies of these neutrinos and the higher detection thresholds of the experiments, whereas the small active mass of only 90 tons of the LSD detector has been used as an argument why this facility did not see any neutrinos when the other three experiments captured their events. However, the detection of five low-energy neutrinos by the small LSD mass requires a total energy in the neutrino burst that is several times higher than the typical energy release from NS formation [38]. No truly convincing scenario has been proposed as an explanation so far. In Refs. [39, 40] a two-stage collapse scenario was suggested in which the fragmentation of the collapsing stellar core leads to the formation of a binary NS whose inspiral is driven by gravitational radiation and whose final merger causes the second neutrino burst. While core fragmentation seems possible in the presence of extreme rotation [41], the long delay to the second burst can hardly be attributed to gravitational-wave emission, because the collapse fragments are embedded in the dense, infalling gas of the SN progenitor and must be expected to dissipate the energy of their orbital motion by hydrodynamic effects (pressure waves and shocks) much faster.

Another long-standing question concerns the possible formation of a BH in SN 1987A. Considering the fact that recent observations set the lower limit of the maximum mass of nonrotating, cold NSs to more than $2\,M_\odot$ [42, 43], BH formation from the collapse of an 18–20 $M_\odot$ progenitor of SN 1987A [44] appears very unlikely from the theory perspective. Neither the stellar iron core of such a star nor the fallback mass expected for an

explosion energy of more than 10^{51} erg, which was deduced from SN 1987A observations, are sufficiently large to push the NS beyond the BH threshold after the emission of the detected neutrino burst. From the observational perspective there is also no real problem with the lack of clear evidence for a pulsar so far. The current luminosity of the ejecta cloud of this SN ($\sim 10^{36}\,\mathrm{erg\,s^{-1}}$; [45, 46]) is not compatible with the spin-down power of a bright pulsar like Crab ($\sim 4.5\times10^{38}\,\mathrm{erg\,s^{-1}}$). However, the ejecta emission is strongly affected by the shock interaction with the circumstellar medium, and the corresponding brightening is well able to cover the radiation of a thermally cooling NS like the compact object in Cassiopeia A with a present bolometric luminosity of about $7 \times 10^{33}\,\mathrm{erg\,s^{-1}}$ [47] and an initial luminosity of at most $\sim 10^{35}\,\mathrm{erg\,s^{-1}}$ (e.g., [48, 49]). Interestingly, very recent spectral and morphological analysis of the remnant of SN 1987A with ALMA and ATCA data seems to indicate the possible presence of a diffuse synchrotron source in the unshocked ejecta at a westward offset from the SN position. If caused by the energy release of a pulsar wind nebula it would set an upper limit to the pulsar spin-down power of $\sim 10^{35}\,\mathrm{erg\,s^{-1}}$ [50]. The pulsed emission of such a spinning NS would so far have remained undetected because of its relative faintness and the obscuration of the scattering and absorbing stellar debris around the SN site.

While the neutrinos from SN 1987A were able to yield basic confirmation of the theory of NS formation, their event statistics was too poor to allow for useful insights into the dynamics of the beginning explosion and thus into the still debated explosion mechanism of core-collapse SNe. A next Galactic SN, however, is likely to provide a high-statistics neutrino signal, depending on the availability of running experimental facilities. It will therefore carry valuable information about the properties of the neutrinos themselves (e.g., [51]), and it will, in particular, help us unravelling one of the most nagging problems of stellar astrophysics, namely why and how massive stars achieve to reverse their catastrophic collapse to the gigantic blast of the SN. But even if a massive star in our Milky Way ends its life without a brilliant explosion, which is a possibility that could happen in a fair fraction of up to several 10% of all stellar core collapses [52-55], the formation of a BH will be accompanied by a luminous outburst of neutrinos. In this case neutrinos (and possibly gravitational waves) might be the only messengers of the "silent" stellar death. The magnitude of the neutrino luminosity will be a measure of the rate of mass infall from the collapsing stellar core to the accreting NS, and large-amplitude luminosity variations will reflect the dynamics of the (unsuccessful) SN shock, caused by shock expansion or contraction episodes, which modulate the NS accretion rate. The final termination of the neutrino emission will mark the collapse of the transiently stable NS to a BH and thus might set constraints to the uncertain equation of state (EoS) at supernuclear densities.

A high-statistics measurement of neutrinos from a future Galactic SN will therefore be of paramount importance not only for astrophysics and neutrino physics but for nuclear physics, too. Also the measurement of the diffuse supernova neutrino background (DSNB) as an integral signal of stellar core collapses in the past will bear a high potential for interesting astrophysics. It will be able to set limits on the total rate of stellar core-collapse events in the local Universe. If the rate of BH formation cases accounts for a considerable fraction of these events, they might leave characteristic fingerprints in the DSNB spectrum because of pronounced differences between the neutrino luminosities and spectra radiated by NS and BH formation. Improved predictions of the properties of the DSNB are an important task for future studies to be performed when more detailed stellar collapse and SN models with sophisticated neutrino transport have become available for large sets of progenitors.

2˙2. *Numerical methods for supernova modeling in this work.* – All simulations by the Garching group reported in this article, spherically symmetric (1D) as well as multi-dimensional, were performed with the PROMETHEUS-VERTEX SN code [56]. It utilizes a two-moment scheme for the transport of neutrinos and antineutrinos of all three flavors, which employs a Boltzmann closure for the variable Eddington factor and accounts for the full energy and velocity (to order (v/c)) dependence of the transport in the comoving frame of the fluid. For multi-dimensional problems a "ray-by-ray-plus" approximation is applied [56, 57]. Gravity is generalized beyond the Newtonian description by an effective relativistic potential [56], adopting "Case A" of Ref. [58], and relativistic reshifting is taken into account in the neutrino transport. The code includes the whole set of neutrino opacities as detailed in Ref. [56] with the improvements of Ref. [57]; see also the summaries in Refs. [59, 60]. Recent upgrades of the code include([2]):

(i) The possibility to treat all individual types of muon and tau neutrinos and antineutrinos as separate species instead of clustering them together into one representative heavy-lepton neutrino [61];

(ii) the implementation of self-energy shifts of unbound neutrons and protons in their charged-current β-reactions with neutrinos;

(iii) an optional treatment of quasi-stationary convection in 1D simulations by a mixing-length description (see Sect. **2˙**4.1).

These upgrades will be mentioned when they are applied in the models described in this section.

Although PROMETHEUS-VERTEX makes use of an approximate description of the effects of general relativistic gravity (the hydrodynamics solver is Newtonian), it permits simulations up to the onset of BH formation. Tests did not only show good compatibility with fully relativistic calculations during the whole cooling evolution of nascent NSs [62]. Also for proto-neutron stars that approach gravitational instability by continuous accretion, test calculations in comparison to cases in the literature [63] revealed an almost perfect match of the time scale to reach the collapse of the NS and very good agreement with respect to the neutrino-emission properties (with minor differences for ν_e and $\bar{\nu}_e$ and maximal differences of 10–20% for ν_x; [64]).

2˙3. *Multi-dimensional phenomena in supernova cores and explosion mechanism.* –

2˙3.1. *The neutrino-driven mechanism.* When nuclear-matter densities are reached at the center of a gravitationally imploding stellar core, a NS begins to assemble from the infalling matter. The stiffening of the EoS due to repulsive forces between the nucleons leads to an abrupt bounce that sends a strong hydrodynamical shock wave into the supersonically collapsing outer material of the stellar core. Only milliseconds after core bounce, however, the newly formed SN shock is weakened by iron photo-disintegration and a prompt burst of electron neutrinos, which drain energy from the postshock material and reduce the pressure behind the shock. Therefore the shock stagnates and becomes an accretion shock with mass infall instead of expansion characterizing the flow in the downstream region. Increasingly more sophisticated numerical models have consolidated

([2]) The implementations of points (ii) and (iii) in the simulation code in an early, preliminary version were assisted by Bernhard Müller.

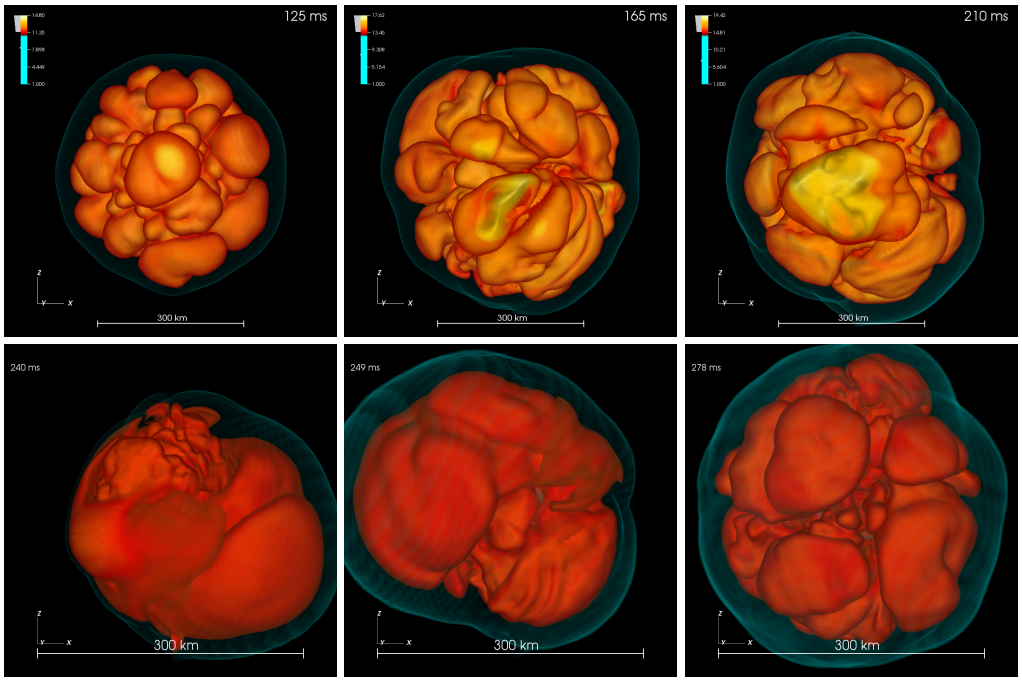

Fig. 3. – *Top:* Three post-bounce snapshots (125, 165, 210 ms p.b.) of a 3D simulation of an 11.2 $M_\odot$ star, whose postshock accretion flow is characterized by convection. (Image from Ref. [98]; copyright (2014) by the American Astronomical Society.) *Bottom:* Three images (240, 249, 278 ms p.b.) from a 27 $M_\odot$ 3D simulation, in which episodes of strong activity by the standing accretion shock instability (SASI) alternate with convection-dominated periods. (Image from Ref. [66]; copyright (2013) by the American Astronomical Society.) Surfaces of constant entropy are displayed in yellow and red; the SN shock is visible as a bluish, semi-transparent envelope. SASI sloshing or spiral motions show up by large-amplitude unipolar or dipolar deformations, whose orientation flips between the hemispheres on time scales of milliseconds.

this nowadays generally accepted failure of the prompt bounce-shock mechanism (see [59] for a review). On a much longer time scale of tens to hundreds of milliseconds after core bounce, however, neutrinos leaving the nascent NS deposit energy in the gain layer between the so-called gain radius and the shock, mainly through charged-current reactions with free nucleons:

$$\nu_e + n \longrightarrow p + e^- \,, \tag{1}$$

$$\bar{\nu}_e + p \longrightarrow n + e^+ \,. \tag{2}$$

As time goes on, the conditions for this neutrino heating become continually more favorable because the neutrinos are radiated with increasingly harder spectra as the neutrinospheric temperature rises in the contracting and compressionally heated NS.

If the energy transfer by neutrinos is strong enough, it can raise the postshock pressure to trigger the reacceleration of the SN blast wave and to thus initiate a successful explosion [65]. At later times after bounce, not only the rising spectral temperatures of the radiated neutrinos improve the conditions for this shock revival. Also the rate

at which matter of the collapsing stellar core falls into the shock gradually declines and with it the ram pressure of the infalling material. This also favors the rejuvenation of the stalled shock when the mass accretion rate drops below the critical value at which the thermal pressure created by neutrino heating can overcome the ram pressure of matter ahead of the shock. The explosion therefore sets in with a considerable time delay after the initial shock formation at the moment of core bounce.

For a period of 30 years, Wilson's "delayed neutrino-driven mechanism" has survived as the standard paradigm for explaining how massive stars achieve to explode, despite the fact that numerical modeling repeatedly experienced setbacks in its efforts to demonstrate the viability of the mechanism and despite the nagging lack of an ultimately convincing theoretical or observational confirmation, both of which still nourish scepticism and criticism. However, in the absence of rapid rotation and very strong magnetic fields, whose relevance for ordinary SNe is disfavored by current stellar evolution models [67], neutrinos are the most efficient way to extract energy from the rich reservoir of the hot, newly formed NS and to transfer parts of this energy to the overlying stellar shells in order to reverse their infall to an explosion. In fact, neutrinos carry away the huge gravitational binding energy of the compact remnant, several 10^{53} erg, and less than one percent of this energy is well sufficient to account for the observed power of a typical SN.

The basic functioning of the neutrino-driven explosion mechanism can be understood as a global runaway instability of the postshock accretion layer caused by the neutrino-energy deposition. According to the "critical luminosity condition" [68] the explosion is launched when the neutrino luminosity exceeds a critical threshold value that depends on the mass-accretion rate of the stalled shock. This concept is now widely accepted and basically consistent with many parametric numerical models (e.g., [69-73]) and analytic studies (e.g., [74, 75]), although many details are still disputed, e.g. which parameters define the critical condition most accurately and can be used as most reliable indicator of the threshold for runaway (e.g., [72, 75, 76]).

2˙3.2. *Importance of non-radial hydrodynamic instabilities.* Hydrodynamic simulations with an increasingly more sophisticated description of the crucial neutrino physics and transport, however, have shown that a state-of-the-art treatment of the microphysics (in particular of the neutrino interactions and EoS) does not allow for explosions in spherical symmetry (i.e., in one dimension; 1D). An exception to this are the lowest-mass progenitors of SNe, i.e., ∼9–10 $M_\odot$ stars with oxygen-neon-magnesium cores [30,77,78] or small iron cores [79], which are surrounded by extremely dilute overlying shells with very low gravitational binding energy. But even in these cases the neutrino-heated postshock layer is convectively unstable and high-entropy, neutrino-heated plasma becomes buoyant and rises in Rayleigh-Taylor plumes (see Fig. 3, upper row). These multi-dimensional flows assist neutrinos in triggering the explosion earlier, accelerate the expansion of the SN shock, enhance the explosion energy, create asymmetries in the explosion ejecta, and modify the conditions for element formation in the neutrino-processed gas as well as in the layers of explosive nucleosynthesis [79, 80].

For progenitor stars that are more massive than about 10 $M_\odot$, the support by multi-dimensional hydrodynamic instabilities is indispensable to reach the critical condition for a neutrino-driven explosion. There is a variety of effects by which non-radial flows in the postshock layer can aid the onset of the SN explosion [69, 81, 82]. Non-radial convective flows stretch the residence time of matter in the heating layer and thus enhance the energy transfer by neutrinos (e.g., [28, 70, 83]). The buoyant rise of neutrino-heated matter also reduces the energy loss by the re-emission of neutrinos (mostly through the

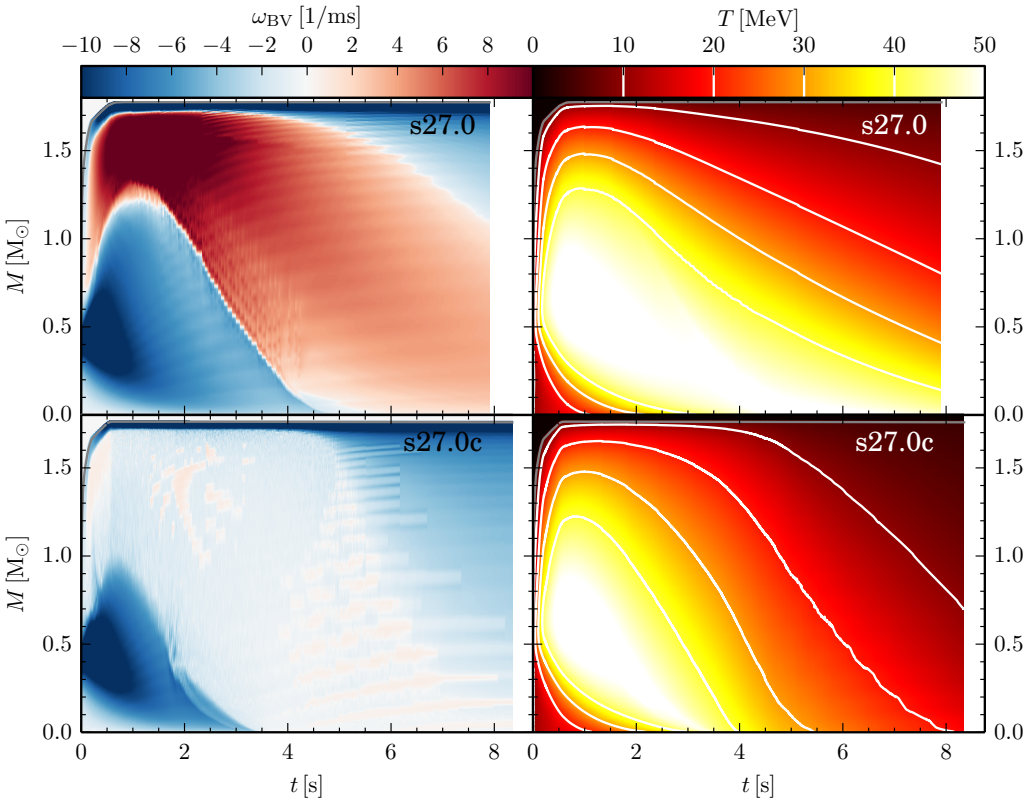

Fig. 4. – Evolution of the convective region in the newly formed NS of a collapsing and exploding 27 $M_\odot$ star [64] using the EoS of Lattimer & Swesty [86] with a nuclear incompressibility modulus of $K = 220$ MeV. The NS has a baryonic (final gravitational) mass of 1.776 (1.592) $M_\odot$. Time is normalized to bounce. The *upper panels* show a 1D simulation without convection, the *lower panels* with a mixing-length treatment of convection. The *left column* displays the evolution of the Brunt-Väisälä frequency, positive values of which indicate instability for Ledoux convection. In the model that includes convective energy and lepton-number transport, the convectively unstable regions (red in the upper left plot) become convectively neutral (whitish in the lower left plot). The *right panels* display the temperature evolution. The cooling (and deleptonization) of the nascent NS is considerably faster when convective fluxes accelerate the neutrino loss.

inverse reactions of Eqs. (1,2)). Moreover, the expanding plumes push the shock to larger radii and thus increase the mass and the volume of the neutrino-heated layer. With the larger optical depth of the gain layer the efficiency of neutrino heating grows even more, creating ideal conditions for a runaway. Some authors have attributed the combination of these explosion-assisting effects, which are associated with the non-radial mass motions in the postshock layer, to the generation of turbulent pressure behind the shock [84, 85]. The corresponding turbulent energy scales with the neutrino-energy deposition rate [32, 76], and the turbulent pressure in addition to the gas pressure has been shown to effectively reduce the critical neutrino luminosity for shock revival [76]. Although this conceptual picture seems to be able to capture some basic features found in multi-dimensional explosion models, the actual, highly time-dependent gas dynamics in collapsing stellar cores is probably too complex to be compatible in all phases and in all

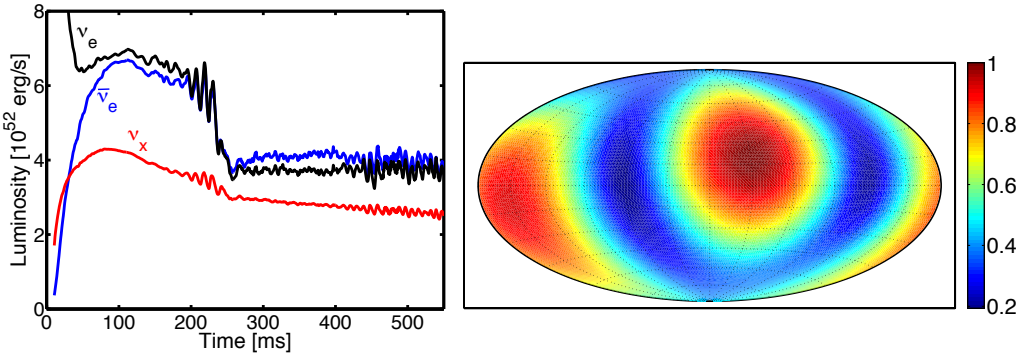

Fig. 5. – *Left:* Post-bounce luminosities of ν_e, $\bar{\nu}_e$, and ν_x as measured by a distant observer for a 3D collapse simulation of a 27 $M_\odot$ star. The observer position is close to the plane of a spiral SASI shock-oscillation mode between ∼120 ms and ∼250 ms. For the displayed luminosities the neutrino emission was integrated over the hemisphere facing the observer with limb-darkening effects taken into account as described in the appendix of Ref. [87], from where the figure was taken. (Image copyright (2014) by the American Physical Society.) The SASI modulations of the mass-accretion of the NS imprint large-amplitude, near-sinusoidal variations on the neutrino emission. There is a second phase of SASI activity starting at ∼400 ms, whose orientation is inclined to the direction of the observer. Therefore the plot does not reflect the full amplitude of these later modulations. *Right:* Relative amplitude of the $\bar{\nu}_e$ signal variations on a "sky-plot" of all observer directions during the first SASI phase (120–250 ms p.b.) in the 27 $M_\odot$ model. (Image from Ref. [88]; copyright (2013) by the American Physical Society.)

aspects with the properties of fully developed turbulent flows at steady-state conditions.

Theoretical models therefore led to the conclusion that the neutrino-driven SN mechanism is a generically multi-dimensional phenomenon. This important insight is in line with observations of SN 1987A and of other relatively nearby and well studied SNe, and it is further supported by the morphological properties seen in young SN remnants. All of these events show large-scale asymmetries, non-spherical deformation, and extended radial mixing of the chemical elements ejected during the explosion, none of which could be understood if the onion-shell stratification of the pre-collapse star was preserved during the SN blast.

The existence of convectively unstable regions in the SN core was recognized soon after the first detailed hydrodynamic simulations had revealed the evolution and structure of the newly formed NS and its surrounding layers. Besides the negative entropy gradient that is built up by neutrino heating behind the stalled shock, and which is unstable to convective overturn [89] setting in typically 80–100 ms after bounce, the decelerating and weakening bounce shock also leaves a negative entropy profile behind, which can decay in an early post-bounce phase of prompt convection lasting some ten milliseconds [90-93]. Moreover, in the hot and still lepton-rich proto-neutron star the combination of a negative entropy gradient and an unstable lepton-number gradient drives Ledoux convection in a thick shell interior to the neutrinosphere [90,94]. Over a period of seconds this convective activity penetrates deeper and deeper towards the center and accelerates the cooling and deleptonization of the nascent NS (Fig. 4; [26, 95-97]).

In addition to being stirred by convective mass motions, the accretion shock and the whole postshock accretion flow are unstable to global, non-radial deformation modes, which do not allow the accretion shock to remain spherical and at a stationary radius.

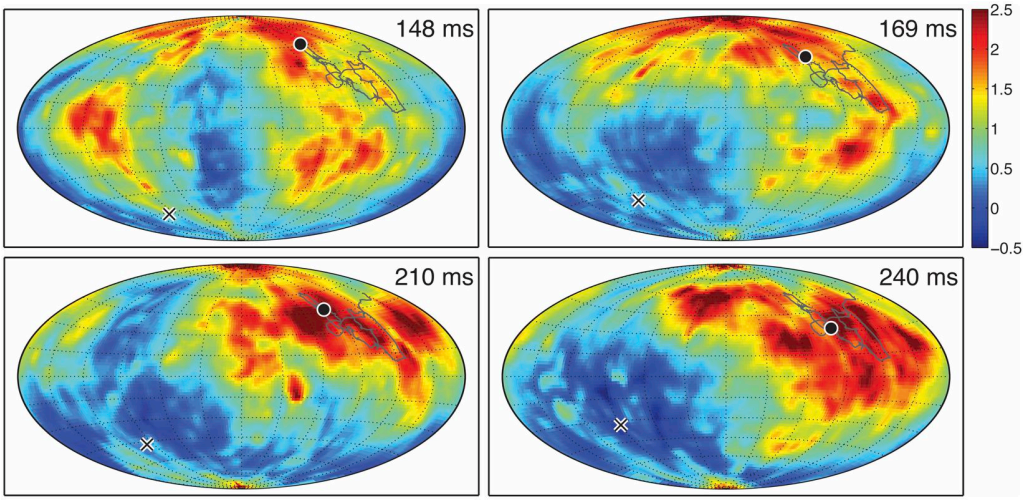

Fig. 6. – Time evolution of the lepton-number (ν_e minus $\bar{\nu}_e$) flux density normalized by the average value over all directions in a 3D core-collapse simulation of an 11.2 $M_\odot$ progenitor. The panels show "all-sky" images for the indicated post-bounce times. One can see the emergence of a clear dipole pattern with strong excess of the ν_e emission in one hemisphere and a reduced ν_e emission or even excess flux of $\bar{\nu}_e$ in the opposite hemisphere. This phenomenon has been found in all 3D simulations of the Garching group and was termed LESA for lepton-emission self-sustained asymmetry. The black dot marks the maximum of the dipole, the cross the anti-direction. The gray line indicates the path described by a slow drift of the dipole direction. (Image from Ref. [98]; copyright (2014) by the American Astronomical Society.)

The possibility of such a non-convective instability in the SN core was first discussed in Ref. [99] and was termed "standing accretion shock instability" (SASI). It leads to the oscillatory growth of an initially small seed perturbation with the largest growth rates being found for the spherical harmonics modes of lowest order, i.e., the dipolar and quadrupolar modes [100-102]. This instability leads to large-amplitude shock sloshing and spiral motions [103] (see Fig. 3, bottom row). The underlying growth mechanism for this instability is a so-called advective-acoustic cycle in the accretion flow between stagnant shock and proto-neutron star [104-106] and can also be studied in an inexpensive water experiment that shares basic features with the accretion flow in a SN core ([107]; for a nice review with focus on this instability and a more complete collection of relevant references, see Ref. [108]).

Both instabilities, postshock convection and the SASI, can provide crucial support to the onset of neutrino-driven explosions. A growing number of groups with energy-dependent neutrino-transport schemes of different levels of sophistication (and quite a variety of differences in other important numerical and physical aspects of the hydrodynamical modeling) have meanwhile obtained successful neutrino-driven explosions of progenitors above $\sim$10 $M_\odot$ in self-consistent, first-principle simulations in two dimensions (2D), i.e., in simulations that were artifically constrained to axisymmetry (e.g., [28, 60, 83, 109-115]). This suggests the basic viability of the neutrino-driven mechanism, although there is still no unanimous agreement [116]. Simulations in 2D, however, are problematic because of the artifically imposed axial symmetry, which attributes a toroidal geometry to all structures, and because of the inverse direction of the turbulent energy

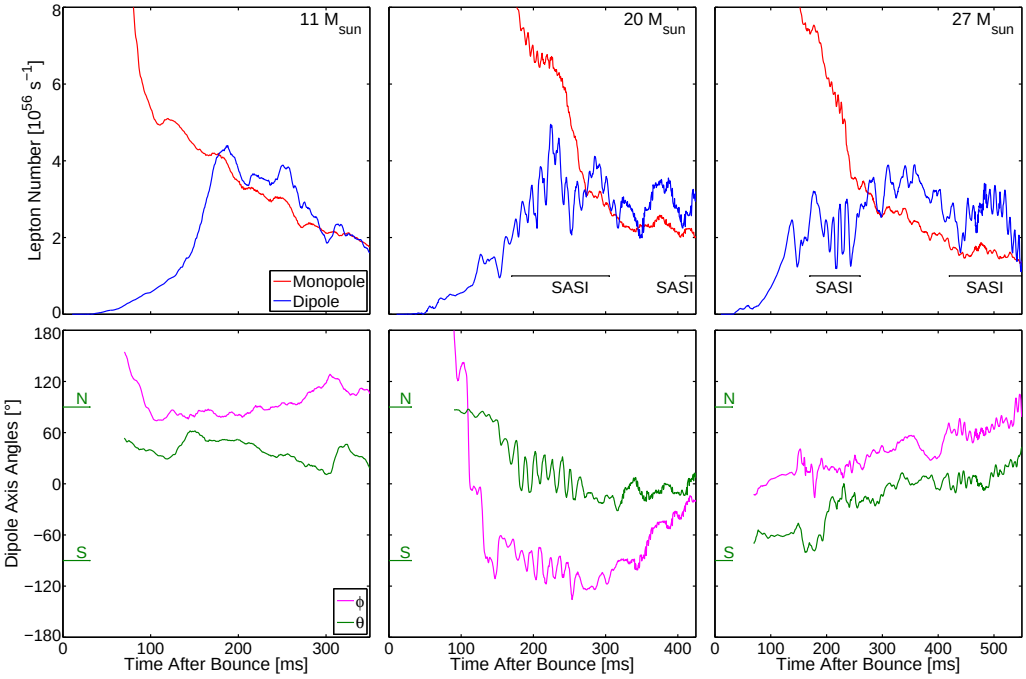

Fig. 7. – Post-bounce evolution of the lepton-number emission in 3D core-collapse simulations of 11.2 $M_\odot$ (*left*), 20 $M_\odot$ (*middle*) and 27 $M_\odot$ (*right*) progenitors. The upper panels show the monopole, i.e., the total lepton-number flux (red curve), and the dipole component (blue curve). The bottom panels display the polar angles θ and ϕ defining the dipole direction (i.e., the direction of the maximum excess of the ν_e emission relative to the $\bar{\nu}_e$ emission) in the polar coordinate grid of the star (north and south pole directions are indicated by "N" and "S", respectively). The monopole and dipole amplitudes $A_{\rm mon}$ and $A_{\rm dip}$ are normalized such that the lepton-number flux is given by $A_{\rm mon} + A_{\rm dip} \cos\vartheta$ in coordinates aligned with the dipole direction, if the flux distribution contains only monopole and dipole terms. (Image from Ref. [98]; copyright (2014) by the American Astronomical Society.)

cascade (from small to large scales) compared to the realistic three-dimensional (3D) situation. It is therefore indispensable to confirm the functioning of the mechanism by 3D simulations, which have recently become possible because of the increasing power of modern supercomputers.

2˙3.3. *Status of explosion modeling in 3D.* The first self-consistent 3D simulations of stellar core collapse and explosion were performed with a relatively schematic neutrino treatment by grey diffusion [117, 118]. More recently, first-principle 3D simulations with energy-dependent neutrino transport (however applying transport schemes with largely differing degrees of sophistication) have also obtained successful explosions, although the revival of the stalled shock happens somewhat later than in the corresponding 2D models [119-122]. The longer delay of the onset of the explosion may be problematic because later explosions tend to be weaker and might be incompatible with observed SN energies. However, the detailed effects in 3D and the differences between 2D and 3D models are still a matter of intense research, and the current models do not yet provide final answers, in particular concerning the role of the SASI in 3D (cf. [123]) and concerning the energetics

of the explosions (cf. [124]). Moreover, more studies are needed to investigate the question of numerical convergence in describing the potentially turbulent postshock flow (e.g., [125-127]) and to explore the influence of so far poorly understood perturbations and non-sphericities in the convective silicon and oxygen burning layers of the pre-collapse star (e.g., [76, 128, 129]).

Also the details of the microphysics in the newly formed NS remain a matter of concern. Interestingly, in Ref. [121] it was found that a modest reduction of the neutrino-nucleon neutral-current scattering opacity by just 10–20%, e.g. due to possible effects of strange-quark spins in the axial-vector structure factor of the scattering cross section, is sufficient to convert a 3D simulation of a $27\,M_\odot$ by the Garching group from failure to a successful explosion. This result clearly demonstrates the proximity of current state-of-the-art 3D simulations of stellar core collapse to explosions, and it emphasizes the sensitivity of the outcome of these simulations to the detailed input in the neutrino-opacity sector. A similar sensitivity exists with respect to the NS EoS, because it has been known for a while already that "softer" EoSs are favorable for the possibility of neutrino-driven explosions [83, 110, 113]. Both effects, reduced neutral-current neutrino-nucleon scattering rates as well as a soft EoS, lead to a faster contraction of the newly formed, hot NS in the first $\sim$0.5 s after bounce([3]). In the case of a reduced neutrino-scattering opacity the faster contraction is a consequence of the enhanced emission of heavy-lepton neutrinos. A faster NS contraction causes more rapid compressional heating of the neutrinospheric layer and thus allows for higher accretion luminosities and a steeper rise of the average energies of the radiated neutrinos with time. Both higher luminosities and higher mean energies enhance the neutrino heating behind the shock and are therefore supportive for neutrino-driven explosions.

Non-radial hydrodynamic instabilities in the SN core are not only of crucial importance for the neutrino-driven mechanism; they also impose asymmetries on the beginning explosion and therefore set the conditions for NS acceleration through the "gravitational tug-boat mechanism", which can yield NS kick velocities in agreement with those observed for young pulsars (e.g., [130, 131]). Moreover, they seed the observable ejecta asymmetries that develop by the interaction of the primary non-sphericities with secondary mixing instabilities that grow during the first day of the SN blast (e.g., [132]). The violent hydrodynamic flows associated with convective overturn and the SASI in the postshock layer also produce characteristic imprints on the neutrino signal emitted during the shock-stagnation phase after bounce. While convection leads to small-amplitude, high-frequency ($\gtrsim 100$ Hz) fluctuations of the neutrino luminosities and mean energies, SASI sloshing and spiral motions create quasi-periodic variations of much bigger amplitudes (up to 10–20 percent in the neutrino luminosities, cf. the left panel of Fig. 5, and 1–2 MeV in the mean neutrino energies; [87,88]) and with typical frequences of $\lesssim 100$ Hz, because the large-scale shock expansion and contraction phases associated with the SASI modulate the mass-accretion flow towards the nascent NS massively. During episodes of enhanced accretion the emission of neutrinos is boosted by additional accretion lumi-

([3]) Note that here a "softer" EoS is defined by the faster contraction of the newly formed NS during the early post-bounce accretion phase and *not* by a lower maximum mass of a cold, non-rotating NS, which is often considered as the criterion for discriminating soft from stiff EoSs. It is important to realize that neither the radius nor the maximum mass of a cold NS are of direct relevance for the properties of the hot, accreting remnant immediately after core bounce and therefore for the conditions that influence the onset of the SN explosion during this phase.

nosity, and the neutrinos escape with higher mean energies because of the compressional heating of the accretion layer.

Measurements of neutrinos from a future Galactic SN with Cherenkov telescopes will well be able to detect these signal modulations [87, 88, 133, 134] (see Sect. **3**˙3.3 for more information). The observation of SASI modulations for SN neutrinos would provide a very important confirmation of our present, purely theoretical picture of the shock dynamics in the SN core. The presence of one or more SASI episodes is more probable in cases of more massive progenitor stars (maybe with masses beyond $\sim$15 $M_\odot$), where the shock expansion comes to a longer halt and even shock contraction can occur before the onset of runaway. However, the possibility to see the corresponding neutrino signal modulations will depend on the viewing angle relative to the main direction or the plane of the SASI sloshing or spiral motions. Observers with positions close to the SASI sloshing axis or near the main plane of the SASI spiral mode will receive bigger modulation amplitudes (Fig. 5, right panel; see also Sect. **3**˙3.3) and will have the better chance to diagnose them in the detection.

2˙3.4. *LESA: A dipolar neutrino-emission asymmetry as new phenomenon.* Another interesting and novel phenomenon was recently discovered in the neutrino emission of the first 3D stellar core-collapse models with state-of-the-art multi-group three-flavor neutrino transport. Instead of persistently picturing the high-order multipole pattern of buoyant plumes and sinking downdrafts in the convection zones in the interior of the proto-neutron star and in the neutrino-heated postshock layer, the neutrino emission develops a strong dipolar asymmetry on a time scale of about 100–150 ms after bounce (Fig. 6; [98]). The observable hemispheric luminosity difference of electron neutrinos, ν_e, and electron anti-neutrinos, $\bar{\nu}_e$, individually can reach up to $\sim$20% and even higher for the lepton-number (ν_e minus $\bar{\nu}_e$) luminosity (Fig. 6), whereas it is only of order 1–2% for the sum of ν_e and $\bar{\nu}_e$ and for heavy-lepton neutrinos, ν_x. This astonishing and completely unexpected phenomenon was found in all 3D SN simulations conducted by the Garching group so far, i.e., in a convection-dominated 11.2 $M_\odot$ model as well as in SASI-dominated 20 and 27 $M_\odot$ cases (see Fig. 7) and also in a more recently published model of a 9.6 $M_\odot$ progenitor, in which the explosion starts on a short post-bounce time scale of only $\sim$130 ms [79]. The development of a strong lepton-emission dipole therefore seems to be a generic instability of the neutrino transport in the convectively stirred proto-neutron star. The exact growth conditions of this instability are not yet understood, but the main contribution to the emission dipole builds up in the convective layer well inside of the neutrinosphere, while the outer accretion develops a dipolar asymmetry, too, and enhances the hemispheric difference of the lepton-number emission. In fact, the accretion asymmetry might trigger the growth of the dipole and seems to stabilize its existence over periods of at least hundreds of milliseconds. The phenomenon was therefore named "lepton-emission self-sustained asymmetry" or LESA (see Ref. [98] for a detailed discussion).

After its steep growth phase until roughly 200 ms post bounce, the amplitude of the LESA lepton-number emission dipole can become even larger than the corresponding monopole (Fig. 7). The dipole direction is amazingly stable if one compares its slow drifting with the much shorter life time of convective cells in the inner and outer convection regions, which collapse and are regenerated on a time scale of typically $\sim$10 ms only. SASI and LESA are two different phenomena, which can be well distinguished also with respect to their effects on the neutrino emission [87]. SASI modulates the ν_e and $\bar{\nu}_e$ emission coherently, whereas LESA amplitudes of the ν_e and $\bar{\nu}_e$ fluxes have opposite

signs. The LESA dipole direction and SASI mass motions can have arbitrary orientations relative to each other, for example the LESA dipole and normal vector of the plane of SASI spiral mode are roughly parallel during the first SASI episode in the $20\,M_\odot$ model and nearly perpendicular in the $27\,M_\odot$ case. The LESA amplitude and dipole orientation can reflect the SASI-imposed modulations of the neutrino emission (see Fig. 7), but the presence of the LESA is not overruled by the SASI, and the LESA dipole direction is also remarkably stable during the phases of violent SASI sloshing and spiralling activity.

The LESA phenomenon is a new type of instability, which occurs as a combined effect of multi-dimensional hydrodynamics and neutrino transport. Presently, however, it cannot be rigorously excluded that this stunning phenomenon is a numerical artifact, e.g. connected to the "ray-by-ray-plus" approximation used for the neutrino transport in the multi-dimensional simulations [116]. It is also possible that the growth of the LESA dipole is fostered by some special (but not necessarily realistic) aspects of the employed microphysics, in particular of the neutrino opacities. Nevertheless, even in these cases a lepton-number emission dipole would still be an interesting result of the 3D simulations.

If happening in nature, LESA would have far-reaching observable consequences for SNe. It would not only imply that the detectable signal of electron antineutrinos is a function of the viewing direction during the LESA-active phase of the SN evolution. Depending on the duration of the asymmetry, a neutrino-emission dipole (as sum over all neutrino species) with an amplitude of about one percent could also lead to a NS kick of tens of kilometers per second. Such velocities, however, are far too low to account for the typical space velocities observed for young pulsars, and they are subdominant compared to the velocities that can be achieved by the "gravitational tug-boat mechanism" associated with asymmetries of the mass ejection in SN explosions ([130, 131] and references therein). Also the nucleosynthesis conditions in the innermost, neutrino-processed ejecta, whose neutron-to-proton ratio is set by the reactions of Eqs. (1) and (2), will depend on the direction, with proton excess being present on the side of the stronger ν_e emission and neutron excess in the opposite hemisphere. 3D models that track the explosion considerably beyond the onset of shock revival are needed to study the exact implications of these possibilities for a varity of progenitors.

2˙4. *Neutrino signals from proto-neutron star cooling.* – Full 3D modeling of SN explosions has only just begun and many aspects of the neutrino-driven mechanism are still heavily debated and not generally agreed on (see Sect. **2˙3**). In particular, it is presently still uncertain which progenitor stars explode, when exactly the explosions set in, which energies they develop, and which stars collapse to give birth to BHs. Parametric explosion simulations are therefore useful to explore the landscape of possibilities and to predict progenitor dependent variations of the neutrino signal as input to the investigation of neutrino oscillations in SNe (Sect. **4**), to calculations of the DSNB (Sect. **5**), and to studies of neutrino detection in connection with future Galactic SNe (Sect. **3**).

Spherically symmetric, i.e. one-dimensional (1D), simulations are a very efficient way to achieve this goal, in particular if the long-time cooling evolution of the newly formed NS over seconds to tens of seconds shall be followed, too. However, 1D simulations do not explode in a self-acting way (except for the lightest progenitor stars of core-collapse SNe, cf. Sect. **2˙3**) and therefore the explosions have to be triggered artificially. Moreover, 1D models lack in the generically multi-dimensional effects in the neutrino emission associated with convection, the SASI and the LESA during the accretion phase that precedes the runaway acceleration of the shock. Also the transition from the accretion phase to the Kelvin-Helmholtz cooling phase of the remnant cannot be reliably represented by 1D

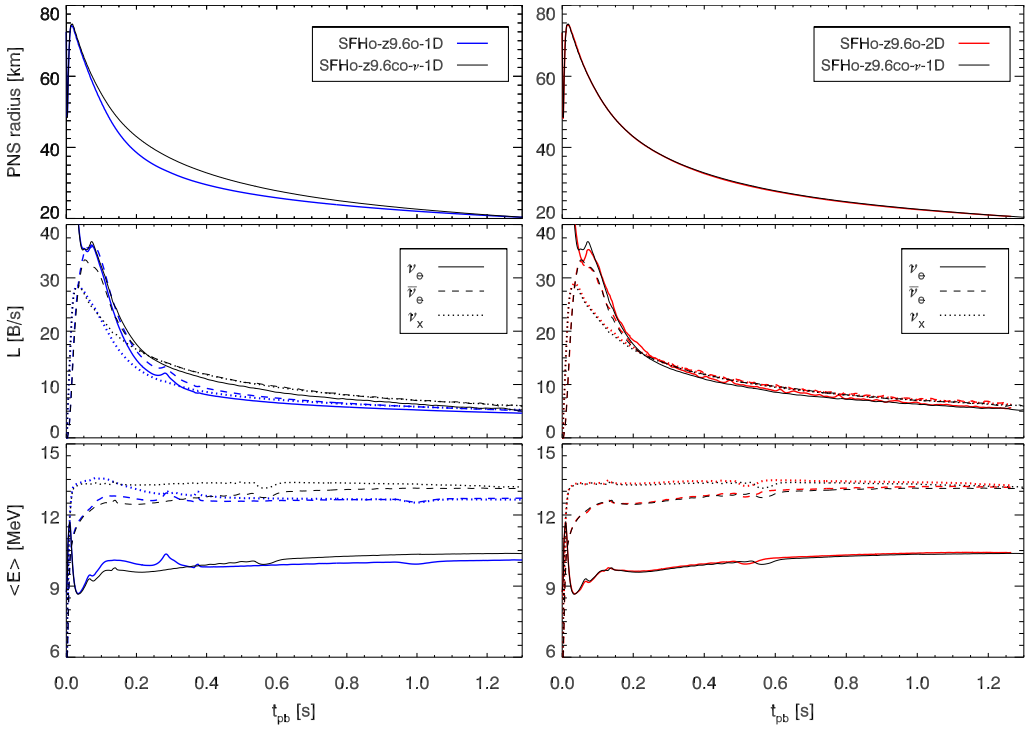

Fig. 8. – Post-bounce evolution of the NS radius (defined by a density of $10^{11}\,\mathrm{g\,cm^{-3}}$; *top panels*), luminosities of ν_e, $\bar{\nu}_e$, and (a single representative of) ν_x (given in units of $\mathrm{B\,s^{-1}} = 10^{51}\,\mathrm{erg\,s^{-1}}$; *middle panels*) and corresponding mean energies (defined as the ratio of energy flux to number flux; *bottom panels*) in the laboratory frame for the proto-neutron star formed during the SN explosion of a $9.6\,M_\odot$ progenitor star. The baryonic (final gravitational) mass of the compact remnant is $\sim$1.363 (1.252) $M_\odot$. The *left panels* show a comparison of 1D models with mixing-length treatment of NS convection (SFHo-z9.6co-ν-1D; thin black lines) and without (SFHo-z9.6o-1D; thick blue lines). The *right panels* demonstrate the excellent agreement between the 1D model with convection and a corresponding 2D simulation, in which the convection is treated hydrodynamically. Both models explode self-consistently at nearly the same time in the 1D and 2D cases, which offers ideal conditions for a clean and accurate comparison.

models, because such models are unable to describe the simultaneous presence of shock expansion and accretion that continues even after the revival of the stalled SN shock. This post-runaway accretion phase might last for hundreds of milliseconds [83, 124] and will not only exhibit an enhanced level of ν_e and $\bar{\nu}_e$ emission due to the persistent accretion contribution to the neutrino luminosity; it may also show short, spike-like eruptions caused by bursts of ν_e and $\bar{\nu}_e$ production when particularly massive accretion downflows hit the proto-neutron star surface and dissipate their kinetic energy in shock-heated plasma [112].

2˙4.1. *Mixing-length treatment of proto-neutron star convection.* After accretion has ended, the proto-neutron star is left behind as a quasi-spherical object (if rotation does not play an important role). However, as discussed already in Sect. **2˙**3, a convective layer eats itself deeper and deeper into the NS and accelerates the transport of energy and

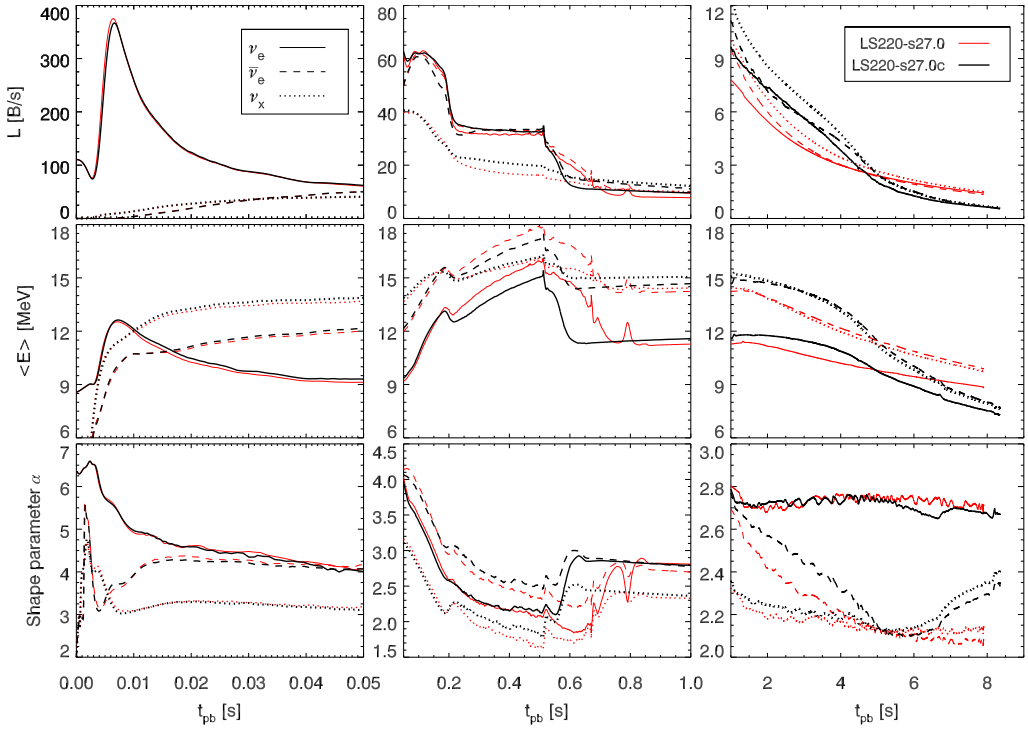

Fig. 9. – Neutrino-signal evolution for the ∼1.776 (∼1.592) $M_\odot$ baryonic (final gravitational) mass NS formed in the explosion of a 27 $M_\odot$ progenitor. The red lines correspond to a 1D simulation without convection, the black lines to a 1D model with a mixing-length treatment of proto-neutron star convection (indicated by the letter "c" in the model name). The *left column* shows the phase of the ν_e-burst at shock-breakout, the *middle column* displays the accretion phase, the *right column* the Kelvin-Helmholtz cooling phase of the proto-neutron star. The *top panels* display the neutrino luminosities for ν_e, $\bar{\nu}_e$ and a single species of ν_x (given in units of $\mathrm{B\,s^{-1}} = 10^{51}\,\mathrm{erg\,s^{-1}}$), the *middle panels* show the radiated mean energies (ratios of energy fluxes to number fluxes), and the *bottom panels* the shape parameters α of the neutrino spectra, all given as functions of time after bounce and as measured by an observer in the laboratory frame. Note that the explosions of the displayed 1D models were artificially triggered at ∼0.5 s p.b. (in contrast to the explosions of the low-mass progenitor of Fig. 8, which developed self-consistently). The initiation of the explosion was done slightly differently in both models, which explains the differences that are visible between ∼0.5 s and ∼0.8 s during the transition from the accretion to the cooling phase.

lepton number compared to neutrino diffusion on its own. In contrast to the highly time-dependent and aspherical mass flows associated with convective overturn and the SASI in the neutrino-heating layer, the quasi-stationary convection inside of the proto-neutron star offers the possibility to describe the effects of convective energy and lepton-number transport in 1D simulations by a mixing-length approximation (e.g., [135]), because the time scale of hydrostatic equilibration is much smaller than the time scale of convective transport, which again is much smaller than the time scale of evolutionary changes of

the NS. For the convective lepton-number and energy fluxes one can thus write [64]:

$$F_{\rm conv}^{\rm lep} = \rho v_{\rm c} \lambda_{\rm c} \frac{{\rm d}Y_{\rm lep}}{{\rm d}r} \,, \tag{3}$$

$$F_{\rm conv}^{\rm erg} = \rho v_{\rm c} \lambda_{\rm c} \left(\frac{{\rm d}\varepsilon}{{\rm d}r} + P \frac{{\rm d}(\rho^{-1})}{{\rm d}r} \right) \,, \tag{4}$$

where r is the radius, ρ the baryonic-mass density, P the pressure and ε the specific internal energy. In the neutrino-trapping regime at densities above the neutrinospheres, these thermodynamic quantities include the contributions from neutrinos. Correspondingly, $Y_{\rm lep}$ is the total electron-lepton number including electron neutrinos and antineutrinos. The mixing length is coupled to the pressure scale height, $\lambda_{\rm c} = \zeta P |{\rm d}P/{\rm d}r|^{-1}$, where ζ is a dimensionless free parameter of order unity. The convective velocity is determined as $v_{\rm c} = \sqrt{2g\Delta\rho\,\rho^{-1}\lambda_{\rm c}}$ with $g > 0$ being the local gravitational acceleration, and $\Delta\rho = \lambda_{\rm c} C_{\rm Ledoux}$ is the density contrast between surrounding medium and convective fluid elements after travelling a distance $\lambda_{\rm c}$ when $C_{\rm Ledoux}$ is the Ledoux-convection criterion given by

$$\begin{aligned} C_{\rm Ledoux} = \frac{\rho}{g}\,\omega_{\rm BV}^2 &= \left(\frac{\partial\rho}{\partial s}\right)_{P,Y_{\rm lep}} \frac{{\rm d}s}{{\rm d}r} + \left(\frac{\partial\rho}{\partial Y_{\rm lep}}\right)_{P,s} \frac{{\rm d}Y_{\rm lep}}{{\rm d}r} \\ &= \frac{{\rm d}\rho}{{\rm d}r} - \frac{1}{c_{\rm s}^2}\frac{{\rm d}P}{{\rm d}r} \\ &= -\frac{\rho}{\Gamma_\rho}\left(\Gamma_s \frac{{\rm d}\ln s}{{\rm d}r} + \Gamma_{Y_{\rm lep}} \frac{{\rm d}\ln Y_{\rm lep}}{{\rm d}r}\right) . \end{aligned} \tag{5}$$

Here, s is the entropy per baryon, $c_{\rm s} = \sqrt{(\partial P/\partial\rho)_{s,Y_{\rm lep}}}$ is the adiabatic sound speed, and the thermodynamic Γ-indices are given by the derivatives

$$\Gamma_\rho = \left(\frac{\partial \ln P}{\partial \ln \rho}\right)_{s,Y_{\rm lep}} , \qquad \Gamma_s = \left(\frac{\partial \ln P}{\partial \ln s}\right)_{\rho,Y_{\rm lep}} , \qquad \Gamma_{Y_{\rm lep}} = \left(\frac{\partial \ln P}{\partial \ln Y_{\rm lep}}\right)_{\rho,s} . \tag{6}$$

Instability to Ledoux convection requires $C_{\rm Ledoux} > 0$, in which case the Brunt-Väisälä frequency $\omega_{\rm BV}$ is real and $\omega_{\rm BV} = {\rm sign}(C_{\rm Ledoux})\sqrt{g\rho^{-1}|C_{\rm Ledoux}|} > 0$ denotes the growth rate of convective perturbations in the linear regime. In the numerical simulations a value of $\zeta = 1$ is used, but tests showed no noticeable changes for values between 1 and 10.

Figure 8 testifies the good agreement that can be achieved between 1D simulations utilizing this mixing-length treatment of convection and corresponding 2D calculations. Results of a proto-neutron star formed in the collapse of a $9.6\,M_\odot$ progenitor are displayed. The compact remnant assembles a baryonic mass of about $1.363\,M_\odot$, corresponding to a final gravitational mass of $\sim$$1.252\,M_\odot$ for the nuclear EoS used in the simulation. Proto-neutron star convection sets in typically 30–50 ms after bounce, which is the time when differences between convective and non-convective models become visible first. The NS radius shows the usual increase associated with interior convection, and the radiated neutrino luminosities and mean energies reveal the well known time and neutrino-species dependent relative changes compared to the 1D, non-convective case (for a detailed discussion of the pre-explosion effects, see Ref. [28]; for post-explosion differences, see Refs. [26, 96, 97]). The neutrino luminosities during the displayed phase of the

first 1.3 s after bounce are enhanced by convective energy and lepton-number transport by up to about 20%, and the mean neutrino energies are initially reduced and at later times increased by up to nearly 2 MeV with the largest effects for heavy-lepton neutrinos. The 2D model and the 1D simulation with convection exhibit basically identical time evolutions of the NS radius and neutrino parameters (right panels of Fig. 8).

2˙4.2. *Neutrino-emission phases and characteristics.* The effects of post-bounce accretion on the nascent NS are not very prominent in the neutrino signal emitted from SNe of low-mass progenitors like the $9.6\,M_\odot$ star of Fig. 8. In these events the shock moves outward essentially in a continuous expansion and the explosion sets in early after bounce. In the $9.6\,M_\odot$ star this happens already at $\sim$130 ms in the convective models and at roughly 300 ms p.b. in the non-convective case [79]. The accretion phase is therefore very short in such a low-mass progenitor, and the mass delivered on the accreting NS during this time interval is relatively small.

The influence of longer and stronger accretion and of convection in the proto-neutron star interior on the neutrino emission of a more massive compact remnant can be seen in Fig. 9. The NS there is born in the collapse of a $27\,M_\odot$ progenitor and has a baryonic mass of $1.776\,M_\odot$ and a final gravitational mass of $\sim$$1.592\,M_\odot$. Note that in contrast to the $9.6\,M_\odot$ model the explosion of the $27\,M_\odot$ star cannot be obtained self-consistently in 1D but requires artificial initiation. This was done at 0.5 s after bounce in both of the models shown in Fig. 9 by applying slightly different methods. This is the reason for the differences in the neutrino emission between 0.5 s and $\sim$0.8 s after bounce. The features seen during this time and the differences between both models should not be interpreted by physics.

Figure 9 displays the neutrino signal properties for the three main phases of neutrino production after core bounce, which are

(a) the high-luminosity ν_e burst at shock breakout from the neutrino-trapping regime,

(b) the subsequent accretion phase of the stalled shock until the beginning of the explosion,

(c) the long-time Kelvin-Helmholtz cooling of the newly formed NS on its way to a final, deleptonized and cold compact remnant.

The neutronization burst radiates away the electron neutrinos that are abundantly produced by rapid electron captures on protons when the hot postshock matter becomes transparent to neutrinos. It exhibits universal properties concerning its width (several milliseconds) and height (around $4 \times 10^{53}\,\mathrm{erg\,s^{-1}} = 400\,\mathrm{bethe\,s^{-1}} = 400\,\mathrm{B\,s^{-1}}$), which depend only weakly on the progenitor star and uncertain nuclear physics in the SN core ([136]; cf. Fig. 39 in Sec. **4**). Also the faster rise of the ν_x luminosities compared to the slower increase of the $\bar{\nu}_e$ emission in the first 10–20 ms after bounce is a generic feature of state-of-the-art neutrino transport simulations. It can be understood by the high electron and ν_e degeneracy in the postshock material right after shock breakout, which suppresses the rapid production of $\bar{\nu}_e$. These neutrino-emission features, which are predicted to be independent of the progenitor star, offer interesting possibilities for neutrino diagnostics and neutrino astronomy (see Sec. **4**). Differences of the neutrino emission from different collapsing stars grow as time after core bounce progresses. This is a consequence of the gradual infall of the stellar shells that surround the initially collapsing inner core and whose density profiles vary greatly between progenitors of different masses.

In contrast to the $9.6\,M_\odot$ model of Fig. 8, the $27\,M_\odot$ star shows evidence for prompt post-bounce convection, which causes small differences in the neutrino luminosities and energies even during the first ∼50 ms after bounce. Towards the end of this phase the convective activity interior to the neutrinosphere begins to develop. Since the explosion in 1D simulations of such a massive star has to be triggered artificially, the duration of the accretion phase is uncertain (in fact, it is prescribed by the modeler), and the transition from the accretion to the cooling phase is not reliable. Moreover, neither the accretion phase nor the transition to the cooling phase can exhibit special features of the neutrino emission associated with multi-dimensional flows in the accretion region between the stalled shock and the NS (e.g., convective overturn, SASI, or sporadic, post-explosion accretion episodes), which were discussed in Sect. **2**˙3 and at the beginning of this section. Nevertheless, the neutrino signal of 1D models still reflects some generic properties of the accretion phase. These include the following aspects:

- The luminosities of heavy-lepton neutrinos can rather well be expressed in terms of a Stefan-Boltzmann relation,

$$L_{\nu_x} = 4\pi\phi\sigma_\nu T_\nu^4 R_\nu^2\,, \tag{7}$$

  where $\sigma_\nu = 4.751\times10^{35}\,\mathrm{erg\,MeV^{-4}cm^{-2}s^{-1}}$. The luminosity, L_{ν_x}, effective spectral temperature, T_ν (measured in MeV), and neutrinospheric radius, R_ν, are measured at infinity, and the radiated neutrino spectrum is assumed to be represented by a Maxwell-Boltzmann distribution, in which case $\langle E_\nu\rangle = 3T_\nu$. The "greyness factor" ϕ is determined by numerical simulations to range between ∼0.4 and ∼0.8 [29,112].

- The luminosities of ν_e and $\bar\nu_e$ are enhanced by an accretion component that strongly depends on the progenitor star through the mass-accretion rate of the infalling stellar core and the mass and radius of the assembling proto-neutron star (see Fig. 39). The sum of ν_e and $\bar\nu_e$ luminosities can be expressed as

$$L_{\nu_e} + L_{\bar\nu_e} = 2\beta_1 L_{\nu_x} + \beta_2\,\frac{GM_{\rm ns}\dot M}{R_{\rm ns}}\,. \tag{8}$$

  The first term on the r.h.s. represents the "core component" of the luminosity carried by neutrinos diffusing out from the high-density inner region of the proto-neutron star. This component can be assumed to be similar to the heavy-lepton neutrino luminosity, because the core radiates neutrinos in roughly equal numbers from a reservoir in thermal equilibrium, which is confirmed by the close similarity of the luminosities of all neutrino species found after the end of accretion. The second term on the r.h.s. of Eq. (8) stands for the accretion component of neutrinos lost from the hot, inflated accretion mantle around the neutrinosphere. It can be approximately represented by the product of mass accretion rate, $\dot M$, and Newtonian surface gravitational potential of the NS, $\Phi = GM_{\rm ns}/R_{\rm ns}$, with neutron-star mass $M_{\rm ns}$ and radius $R_{\rm ns}$. By a least-squares fit to a large set of 1D results for the post-bounce accretion phase of different progenitor stars, the values $\beta_1 \approx 1.25$ and $\beta_2 \approx 0.5$ were deduced in Ref. [64]. These values apply later than about 150 ms p.b., when the postshock accretion layer has settled into a quasi-steady state, and they depend only weakly on the nuclear EoS. In Ref. [112] the authors used a form similar to Eq. (8) with $\beta_1 = 1$; they found $\beta_2 \approx 0.5$–1 for the pre-explosion phase of the 2D models they investigated.

- During the accretion phase the mean energies of all neutrino species show an overall trend of increase, which is typically steeper for ν_e and $\bar{\nu}_e$ than for ν_x. Interestingly, for progenitors more massive than $\sim$10 $M_\odot$, which possess extended accretion phases, this leads to a violation of the canonical hierarchy of the mean neutrino energies (defined as ratios of energy to number fluxes), i.e., one observes a moment when the usual order $\langle E_{\nu_e}\rangle < \langle E_{\bar{\nu}_e}\rangle < \langle E_{\nu_x}\rangle$ changes to $\langle E_{\nu_e}\rangle < \langle E_{\nu_x}\rangle < \langle E_{\bar{\nu}_e}\rangle$ (see Ref. [137]). The reason for this behavior is a local temperature maximum somewhat inside of the neutrinospheres of ν_e and $\bar{\nu}_e$, which forms because of the compressional heating of the growing accretion layer, whose cooling becomes ineffective when the radius of the proto-neutron star shrinks and the density profile becomes steeper [64,112]. The hierarchy inversion is enhanced and shifted to a considerably earlier time when energy transfer in neutrino-nucleon scattering is taken into account. Non-isoenergetic neutrino-nucleon scattering reduces the mean energies of ν_x in a "high-energy filter" layer between the ν_x number sphere and the ν_x scattering sphere [27,34]. The corresponding energy transfer to the stellar medium also raises the luminosities and mean energies of ν_e and $\bar{\nu}_e$. Different from the mean energies, $\langle E_\nu\rangle$, the rms energies, $\sqrt{\langle E_\nu^2\rangle}$, always obey the canonical hierarchy.

- The secular rise of the mean energies of the radiated ν_e and $\bar{\nu}_e$ during the accretion phase is rather well captured by the proportionality $\langle E_\nu\rangle \propto M_{\rm ns}(t)$ between the mean energies and the growing mass of the proto-neutron star. The proportionality constant depends on the neutrino type but is only slightly progenitor-dependent [112].

During the accretion phase, convection inside of the massive NS of Fig. 9 causes differences compared to the non-convective case similar to those already mentioned for the low-mass remnant of a 9.6 $M_\odot$ star above. It is stressed again that the transition from accretion to proto-neutron star cooling exhibits features that differ between the two models shown in Fig. 9, because in both cases the artificial initiation of the explosion was handled slightly differently. During the Kelvin-Helmholtz cooling the influence of convection leads to growing effects and prominent differences in the long-time evolution of the neutrino emission properties. Convection enhances the luminosities over the first few seconds and thus reduces the late-time luminosities (Fig. 9, right upper panel), because the NS cooling and deleptonization are accelerated by convective transport effects; see also Fig. 4 for the faster evolution of the temperature profile in the convective model. Correspondingly, the mean neutrino energies are increased by up to $\sim$1.5 MeV in the first seconds, followed by a faster decline because of the cooler NS at late times (Fig. 9, right middle panel).

2˙4.3. *Spectral properties of the neutrino emission.* The spectrum of radiated neutrinos is usually somewhat different from a thermal spectrum. Since neutrino-matter interactions are strongly energy dependent, neutrinos of different energies decouple from the background medium at different radii with different temperatures of the stellar plasma. Nevertheless, the emitted neutrino spectrum can still be fitted by a Fermi-Dirac distribution, $f(E) \propto E^2[1+\exp{(E/T-\eta)}]^{-1}$, with fit temperature T and effective degeneracy parameter η [138]. A mathematically more convenient representation was introduced in Ref. [27], who proposed the following dimensionless form for the energy distribution at

a large distance from the radiating source:

$$f_\alpha(E) = \left(\frac{E}{\langle E\rangle}\right)^\alpha e^{-(\alpha+1)E/\langle E\rangle}\,, \tag{9}$$

where

$$\langle E\rangle = \frac{\int_0^\infty \mathrm{d}E\, E f(E)}{\int_0^\infty \mathrm{d}E\, f(E)} \tag{10}$$

is the average energy([4]). The parameter α represents the amount of spectral pinching and can be computed from the two lowest energy moments of the spectrum, $\langle E\rangle$ and $\langle E^2\rangle$, by

$$\frac{\langle E^2\rangle}{\langle E\rangle^2} = \frac{2+\alpha}{1+\alpha}\,. \tag{11}$$

Higher energy moments $\langle E^\ell\rangle$ for $\ell > 1$ are defined analogue to Eq. (10) with E^ℓ under the integral in the numerator instead of E. Besides its analytic simplicity, this functional form has the advantage to also allow for the representation of a wider range of values for the spectral (anti)pinching than a Fermi-Dirac fit. A Fermi-Dirac spectrum with vanishing degeneracy parameter ($\eta = 0$) corresponds to $\alpha \approx 2.3$, a Maxwell-Boltzmann spectrum to $\alpha = 2$, and $\alpha \gtrsim 2.3$ yields pinched spectra whereas $\alpha \lesssim 2.3$ gives antipinched ones. Comparing to high-resolution transport results, the authors of Ref. [139] showed that these "α-fits" also reproduce the high-energy tails of the radiated neutrino spectra very well.

In Fig. 9 the shape parameters α as functions of time are given in the bottom panels. The evolution is similar in the convective and non-convective models, with moderate quantitative differences in some phases. The modest effects of convection are not astonishing, because the convective layer is located well inside of the neutrinospheres and the neutrinospheric layer itself is convectively stable. The region where the radiated spectrum is shaped is therefore dominated by neutrino radiative transport and not by convective transport. In particular neutrinos of higher energies, around and beyond the spectral peak, which have the strongest influence on the higher energy moments $\langle E^\ell\rangle$ with $\ell \geq 2$, are still diffusively coupled to the stellar medium outside of the convective layer. Therefore a major change of the shape and time evolution of the emitted spectra due to convection cannot be expected.

Figure 9 shows that the ν_e spectrum during the shock breakout burst has a considerable pinching (α up to nearly 7), but the pinching decreases with time. The opposite trend occurs for $\bar{\nu}_e$ during the early post-bounce evolution ($t_{\mathrm{pb}} \gtrsim 3\,\mathrm{ms}$), while heavy-lepton neutrinos have spectra closest to the Maxwell-Boltzmann form. As the growing and contracting accretion mantle of the proto-neutron star heats up during the accretion phase, the pinching of the spectra of all types of neutrinos decreases. During the subsequent cooling phase, ν_e and ν_x exhibit fairly stable shape parameters ($\alpha \approx 2.7$ for ν_e and $\alpha \approx 2.2$ for ν_x), whereas the spectra of $\bar{\nu}_e$ become more similar to those of ν_x as time goes

([4]) With α being determined, a normalization factor A relates the spectrum to the neutrino luminosity: $L = 4\pi r^2 A \int_0^\infty \mathrm{d}E E f(E) = 4\pi r^2 A \langle E\rangle \int_0^\infty \mathrm{d}E f(E)$.

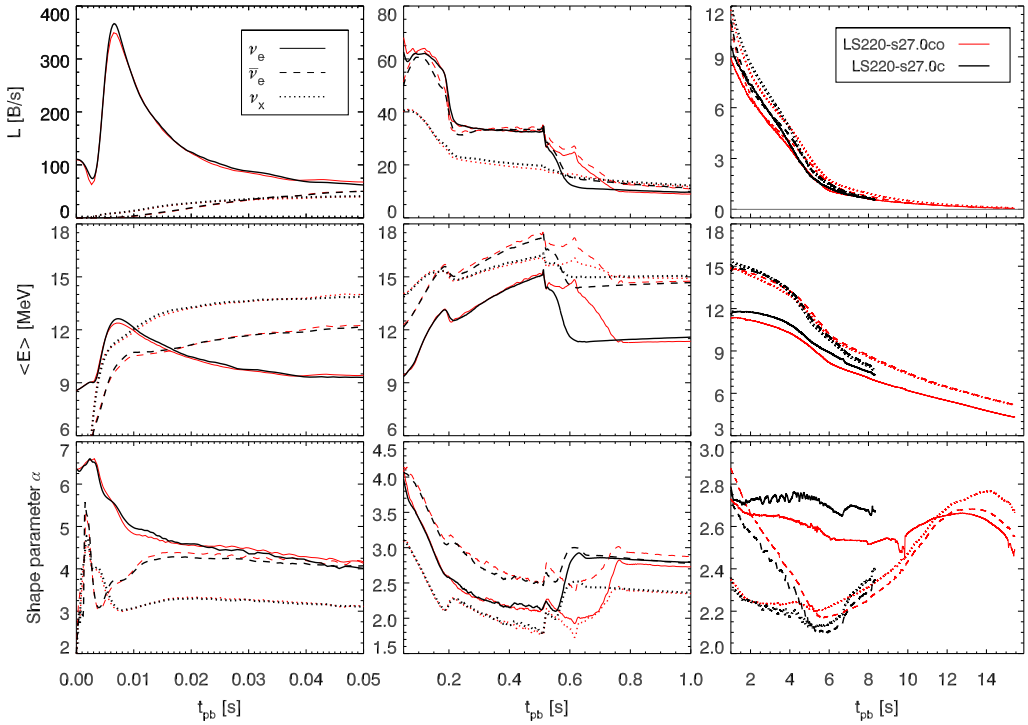

Fig. 10. – Similar to Fig. 9 but for 1D collapse and explosion simulations of the 27 $M_\odot$ star that include nucleon self-energy shifts in the charged-current neutrino-nucleon interactions in one case (model LS220-s27.0co) while ignoring these self-energy potentials in the other case (model LS220-s27.0c). Both models were performed with a mixing-length treatment of convection. Note that similar to the models shown in Fig. 9, also here the explosions of the two cases were triggered slightly differently, for which reason the simulations exhibit artificial differences in the time interval from ∼0.5 s to ∼0.8 s p.b. without any deeper physical meaning and without any significant perturbing consequences for the subsequent evolution. The effects of nucleon self-energy shifts during the ν_e-burst and accretion phases are small as pointed out before [140]. During the proto-neutron star cooling evolution, there are visible differences of up to about 10% in the neutrino luminosities. The main, persistent effect of the nucleon mean-field potentials is a reduction of the average energy of the emitted ν_e by up to ∼0.7 MeV. At very late times ($t_{\rm pb} \gtrsim 6$ s) the relative enhancement of the luminosity of ν_x for the case with nucleon self-energies increases and the mean energies of $\bar{\nu}_e$ and ν_x become ∼1 MeV higher than in the other model.

on. In the convective model, different from the non-convective one, the pinching of the $\bar{\nu}_e$ and ν_x spectra increases again at late times. This reflects the much faster progression of cooling in the convective model (cf. Fig. 4), where the late evolution towards more pinching of the $\bar{\nu}_e$ and ν_x spectra occurs earlier than in the non-convective case.

2˙4.4. *Nucleon self-energy shifts in β-reactions.* Besides convection in newly formed NSs, the EoS of hot NS matter and the mean-field potentials of the nucleons play an important role for the neutrino emission and cooling evolution of the compact remnant. The importance of the EoS-dependent nucleon self-energies has been pointed out in the recent past [140-144] after the corresponding physics had been ignored in earlier studies of proto-neutron star cooling [29, 30, 145] and of proto-neutron star accretion to

BH formation [63]. Considering neutrons and protons as gases of nonrelativistic quasi-particles that move in a single-particle mean-field potential, U, one can write their energy-momentum relation $E_i(\mathbf{p_i})$ in generalization of the non-interacting case as

$$E_i(\mathbf{p}_i) = \frac{\mathbf{p}_i^2}{2m_i^*} + m_i c^2 + U_i \quad \text{for} \quad i = n, p\,, \tag{12}$$

with m_i and m_i^* being the particle rest masses and the (Landau) effective masses, respectively. Both the masses m_i^* and the potentials U_i depend on density, temperature, and the neutron-to-proton ratio (or the electron-to-nucleon ratio Y_e). The electron and positron energies of the reactions of Eqs. (1) and (2) are therefore related with the energies of their corresponding ν_e and $\bar{\nu}_e$ by

$$E_{\nu_e} = E_{e^-} + \frac{\mathbf{p}_p^2}{2m_p^*} - \frac{\mathbf{p}_n^2}{2m_n^*} - (m_n - m_p)c^2 - (U_n - U_p)\,, \tag{13}$$

$$E_{\bar{\nu}_e} = E_{e^+} + \frac{\mathbf{p}_n^2}{2m_n^*} - \frac{\mathbf{p}_p^2}{2m_p^*} + (m_n - m_p)c^2 + (U_n - U_p)\,. \tag{14}$$

The potential difference $\Delta U = U_n - U_p$ is directly related to the nuclear symmetry energy [144]:

$$\Delta U \cong 4(1 - 2Y_e)E_{\rm sym}^{\rm int,0}(\rho)\,, \tag{15}$$

where $E_{\rm sym}^{\rm int,0}$ is the interaction part of the symmetry energy at zero temperature, and the r.h.s. ignores terms of higher than linear order in Y_e. Since ΔU is positive at the very neutron-rich conditions in forming NSs, the contribution from the mean-field potentials reduces the energy of ν_e and increases the energy of $\bar{\nu}_e$ created in the β-reactions. Moreover, the mean-free path for ν_e absorption on neutrons is decreased because the extra energy associated with the potential difference ΔU diminishes the importance of Pauli phase-space blocking in the final state of the electron, whereas the mean-free path for $\bar{\nu}_e$ is increased at low energies and decreased at high energies.

As a consequence of these changes, the authors of Ref. [140] reported a strong impact of the nucleon self-energy shifts on the luminosities and spectra of all neutrinos, but with an important difference between pre-explosion and post-explosion phases. While they found the nucleon mean-field potentials in the charged-current reactions to have a negligible influence during the accretion phase prior to explosion, they obtained reduced luminosities for all neutrino species and a considerable decrease of the mean energy of the emitted ν_e during the Kelvin-Helmholtz cooling of the proto-neutron star. They also observed values for the electron fraction in the neutrino-driven wind (see Sect. **2**˙4.5) that were significantly lower (down to $Y_{e,\rm wind} \sim 0.45$) than in the simulation without nucleon mean-field potentials. Using a more accurate determination of $Y_{e,\rm wind}$, Ref. [25] obtained less neutron-rich ejecta with $Y_{e,\rm wind} \sim 0.48$ despite having replaced the TM1 EoS [146] of the previous work by a DD2 EoS table provided by M. Hempel [143], which predicts higher values of ΔU between the neutrinospheric layer and the nuclear saturation density, from where most of the neutrino emission originates.

Using the STOS TM1 EoS [146] and the LS220 EoS [86], Ref. [64] confirmed the basic trends of the results of Ref. [140]. Similar absolute shifts were obtained for both investigated EoSs, although the symmetry energy of the STOS EoS is larger. Ref. [64]

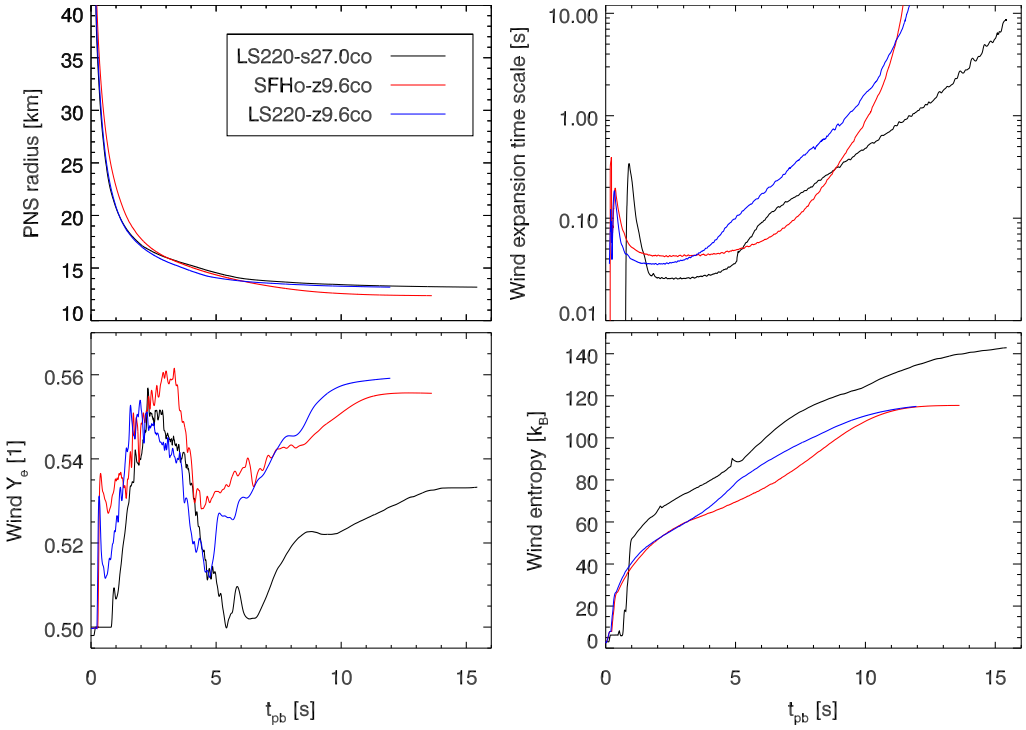

Fig. 11. – Evolution of the proto-neutron star radius (*upper left*) and of characteristic parameters of the neutrino-driven wind: expansion time scale from 5×10^9 K to 2×10^9 K (*upper right*), asymptotic electron fraction, $Y_{e,\mathrm{wind}}$ (*bottom left*), and asymptotic entropy (*bottom right*); the last two quantities were evaluated at a radius of 1000 km. The two 1D simulations for the $9.6\,M_\odot$ progenitor (LS220-z9.6co and SFHo-z9.6co) were performed with different hadronic EoSs and produced explosions self-consistently, whereas the explosion of the $27.0\,M_\odot$ star in 1D was triggered artificially at 0.5 s after bounce. All simulations were performed with a mixing-length treatment of proto-neutron star convection and including nucleon self-energy shifts in the charged-current neutrino-nucleon reactions. All wind ejecta are proton-rich.

also found that nucleon self-energy potentials lead to reduced luminosities for all neutrino species with the biggest effects for ν_e. While the average energy of the emitted ν_e is lowered by roughly 0.75 MeV compared to the case without self-energy shifts, the effect is about one third of that for ν_x and even smaller for $\bar{\nu}_e$, in contrast to the slight rise seen in Ref. [140](5). More important, however, is the fact that mixing-length convection shrinks the differences between the results with and without nucleon self-energies to about half of the values obtained without convection. Because convection speeds up the transport of electron-lepton number out of the NS, it enhances the ν_e emission and partly compensates the effects of the mean-field potentials in the neutrino opacities, at

(5) Our simulations differ from those of Ref. [140] in many aspects of the neutrino opacities. In particular, our models take into account weak magnetism and recoil effects in neutrino-nucleon interactions, while these relevant corrections were ignored in the calculations discussed in Ref. [140] (Meng-Ru Wu; private communication).

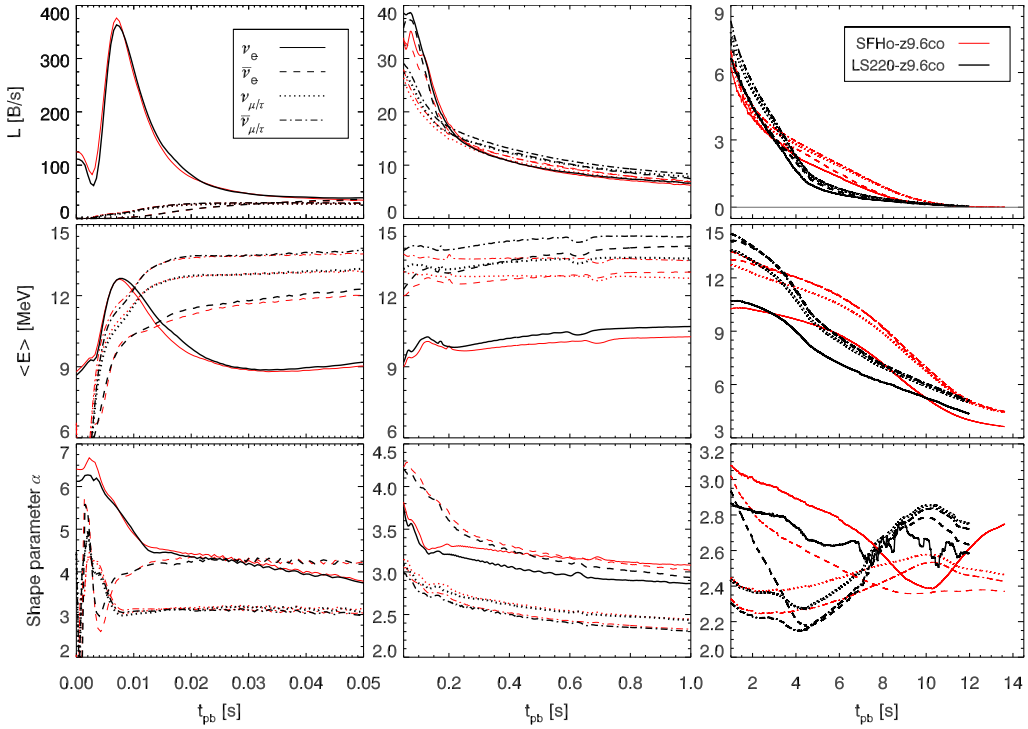

Fig. 12. – Similar to Fig. 9 but for two 1D collapse and explosion simulations of a 9.6 $M_\odot$ star with two different nuclear EoSs. Model LS220-z9.6co uses the EoS of Ref. [86] with a nuclear incompressibility modulus of $K = 220\,\mathrm{MeV}$, whereas model SFHo-z9.6co employs the SFHo hadronic SN EoS of Ref. [147]. The cooling evolution of the proto-neutron star is clearly different for both EoSs. Both models were performed with a mixing-length treatment of convection and in both cases the explosions developed self-consistently within 170–200 ms after bounce. Note that different from Figs. 8–10, the neutrino emission properties are shown here for ν_e, $\bar{\nu}_e$, one species of ν_μ or ν_τ, and one species of $\bar{\nu}_\mu$ or $\bar{\nu}_\tau$, because the neutral-current scattering cross sections of neutrinos and antineutrinos differ in the sign of the weak-magnetism corrections [148]. The slightly lower nucleon-scattering opacity of $\bar{\nu}_{\mu,\tau}$ leads to slightly higher luminosities and up to ∼1 MeV higher mean energies. In all other simulations discussed in this Section, the four heavy-lepton neutrinos were treated equally by one representative species ν_x, whose emission properties turned out to agree well with the average of those of $\nu_{\mu,\tau}$ and $\bar{\nu}_{\mu,\tau}$ [61].

least as long as the deleptonization of the proto-neutron star is proceeding. Figure 10 displays two simulations for our 27 $M_\odot$ progenitor for comparison. As pointed out before in Ref. [140], the nucleon self-energy shifts are not relevant during the shock-breakout and accretion phases. However, even during the proto-neutron star cooling the differences are small until very late times, $t_{\mathrm{pb}} \gtrsim 6\,\mathrm{s}$. The main consequences are a persistent reduction of the mean energy of the radiated ν_e by at most ∼0.7 MeV and no late-time convergence of all mean energies as observed in the case without nucleon self-energies. Also the spectral pinching of the ν_e is moderately lowered when the mean-field potentials are taken into account.

2˙4.5. *Neutrino-driven outflows from proto-neutron stars.* Neutrinos leaving the hot proto-neutron star deposit energy just outside of the neutrinosphere and thus launch a

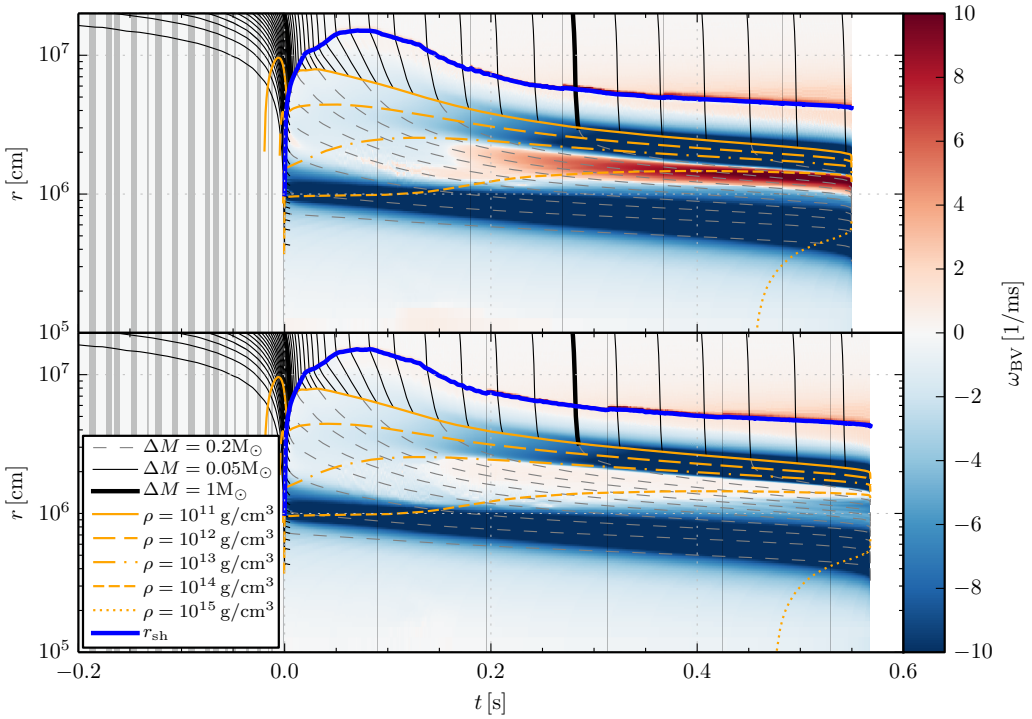

Fig. 13. – Mass-shell plots for the evolution of a collapsing progenitor star with a birth mass of $40\,M_\odot$ (model s40s7b2 of [149]) towards BH formation without mixing-length treatment of proto-neutron star convection (*upper panel*) and including such a treatment (*lower panel*). The simulations made use of the LS220 model of the nuclear EOS ([86] with incompressibility modulus of $K = 220\,\mathrm{MeV}$). The color coding shows the Brunt-Väisälä frequency as defined in Eq. (5). The different lines are explained in the legend of the plot. The thick blue, solid line is the stalled and retreating shock, the ingoing solid lines indicate continuous accretion of infalling matter, the thin dashed lines the contraction of the proto-neutron star. Convection slightly stretches the evolution time until the proto-neutron star becomes unstable to BH formation, because the accelerated deleptonization leads to a faster heating of the proto-neutron star interior and therefore enhanced thermal support.

baryonic mass outflow, the so-called "neutrino-driven wind" (e.g., [151, 152] and references therein). This wind is discussed as a potentially important site of heavy-element formation (for recent reviews, see Refs. [153, 154]). The neutron-to-proton ratio in the ejected matter is set by ν_e and $\bar{\nu}_e$ absorption via the processes of Eq. (2). If neutrons dominate over protons, the wind environment may provide favorable conditions for the formation of neutron-rich nuclei in the rapid-neutron capture process (r-process), depending on sufficiently high entropies and/or sufficiently short expansion time scales of the ejecta (cf., e.g., [155-157]). If the outflow material develops a proton excess, nuclei on the proton-rich side of the valley of stability might form through the neutrino-proton process [158, 159].

The neutrino-driven winds computed in our models are proton-rich during the whole proto-neutron star cooling evolution. Figure 11 displays two simulations for the $9.6\,M_\odot$ progenitor and one for the $27\,M_\odot$ star, which bracket the conditions that can be expected

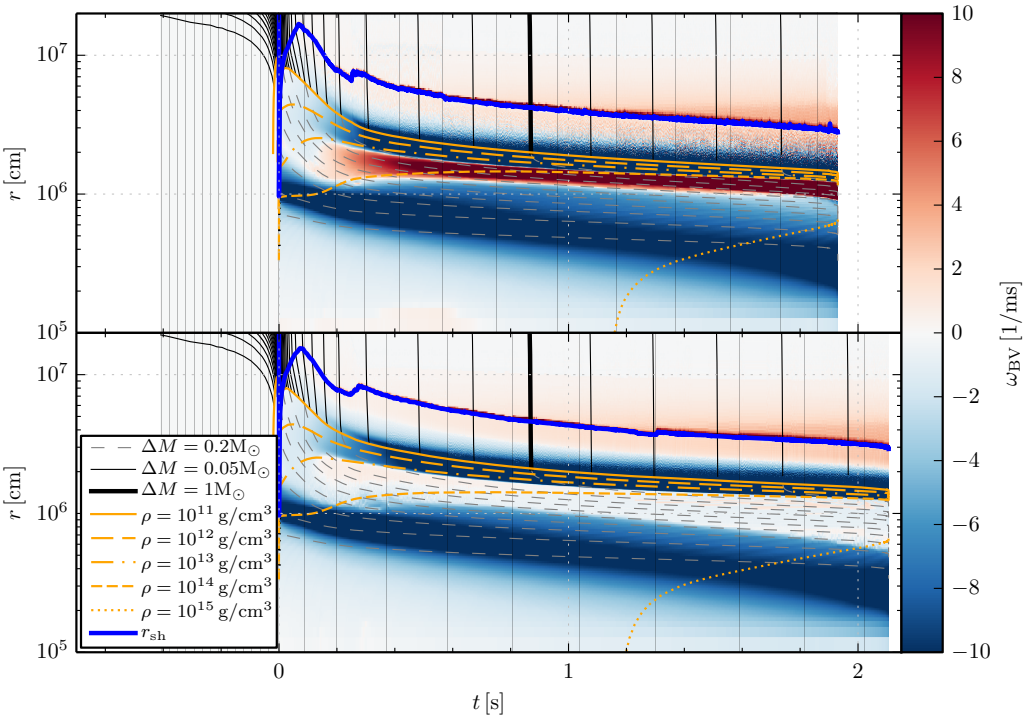

Fig. 14. – Same as Fig. 13, but for the 40 $M_\odot$ progenitor s40.0 of [150]), which has a lower mass-accretion rate and therefore needs a much longer evolution until BH formation.

for proto-neutron stars in the range of baryonic masses of 1.36–1.8 $M_\odot$ (final gravitational masses of 1.25–1.6 $M_\odot$), which are representative for the far majority of core-collapse SNe. All three displayed simulations include the mixing-length treatment of convection and the mean-field potentials of nucleons in the β-processes. The lower-mass case was computed with two different nuclear EoSs, both yielding qualitatively similar time evolutions of the wind parameters. Instead of an early wind phase of about 3 s with $Y_{e,\mathrm{wind}} < 0.5$, which was reported as a consequence of the nucleon self-energy shifts in Ref. [140], the simulations shown in Fig. 11 exhibit a prominent maximum of $Y_{e,\mathrm{wind}} > 0.5$ during the early cooling phase. This maximum is a consequence of proto-neutron star convection, which was not included in the models of Ref. [140]. Correspondingly, the maximum is also absent in simulations that we performed without the mixing-length treatment of convection or for conditions (e.g., nuclear EoSs) that yield only weak convection, in which cases $Y_{e,\mathrm{wind}}$ increases monotonically during the proto-neutron cooling [64]. Convective enhancement of the lepton-number transport inside of the nascent NS increases the ν_e number flux relative to that of $\bar{\nu}_e$ and, in particular, leads to increased pinching of the $\bar{\nu}_e$ spectrum (see Fig. 9), thus reducing $\bar{\nu}_e$ captures on protons compared to ν_e absorptions on neutrons in the outflowing wind material. This favors higher values of $Y_{e,\mathrm{wind}}$ until the main period of deleptonization is over and the proto-neutron star convection becomes weaker at around 3–4 s after bounce (cf. Fig. 4), at which time $Y_{e,\mathrm{wind}}$ declines from a local maximum. Only subsequently, after having gone through a local minimum on the proton-rich side, $Y_{e,\mathrm{wind}}$ resumes the trend found in Ref. [140] with increasing values

towards later times. The entropies in the neutrino-driven outflows rise continuously until they reach maximum values of 120–140 $k_{\rm B}$ per nucleon with the higher values for the more massive NS. Such conditions of entropy and proton excess clearly disfavor the formation of r-process elements in this environment, confirming previous results of less complete models [29, 30].

Active-active as well as active-sterile neutrino-flavor oscillations modify the neutrino emission from the proto-neutron star and can thus have an impact on the neutron-to-proton ratio in the neutrino-driven wind. This requires that the flavor-changing effects occur interior to the neutrinosphere or in the close vicinity of the nascent NS, i.e., in the region where neutrino interactions set the electron fraction of the outflowing matter. While quite a number of studies have explored the implications of matter-enhanced neutrino conversions to active (e.g., [160]) and sterile channels (e.g., [161-167]) in relevant parts of the space of possibilities for mixing parameters and scenarios, the implications of additional neutrino-background induced flavor conversions are not yet satisfactorily understood. First investigations have not been able to reveal promising conditions for r-processing in the wind ejecta [166, 167], but more studies that account for the growing insight into the complex physics of collective flavor transformations are urgently needed (see also Sec. **4**).

2˙4.6. *Equation-of-state dependence of the neutrino emission.* The neutrino signal from the proto-neutron star cooling phase of a future Galactic SN explosion has the potential to provide us with extremely valuable information about the nuclear EoS that describes the physics in the NS interior. Figure 12 shows interesting EoS dependent effects of the neutrino signal radiated by the NS forming in the collapsing and exploding 9.6 $M_\odot$ progenitor. Both displayed simulations were carried out with different models of the high-density EoS above $10^{11}\,{\rm g\,cm^{-3}}$ and both include a mixing-length treatment of NS convection as well as the nucleon self-energy effects in the β-processes. During the shock-breakout and the post-bounce accretion phase, which in this low-mass model lasts only until ∼200 ms after bounce, the differences of the neutrino luminosities and mean energies are still modest, with slightly higher values for the LS220 EoS. At later times, however, the differences become considerable and the simulation with the LS220 EoS yields 10–20% higher neutrino luminosities and mean energies until ∼3 s after bounce. This can be understood as a consequence of the more rapidly contracting proto-neutron star and the smaller NS radius over a period of ∼6 s in the case of the LS220 EoS (see left upper panel of Fig. 11). Also differences in the efficiency of convective transport in the NS interior play a role, because the region of convective instability is sensitive to the properties of the nuclear EoS, in particular to the symmetry energy of the matter composed of neutrons and protons [168]. At intermediate times during the cooling evolution, $3\,{\rm s} \lesssim t_{\rm pb} \lesssim 10\,{\rm s}$, the order of the luminosities and mean energies for the two investigated EoSs is reversed. Now the NS computed with the SFHo EoS exhibits considerably higher values of the neutrino-emission parameters, because the remnant with the LS220 EoS has cooled faster and its temperatures have become correspondingly lower. As a consequence of the accelerated cooling of the latter model, the time $t_{\nu,90}$ at which 90% of the gravitational binding energy of the cold, compact remnant have been radiated away is considerably shorter for LS220. The effect is so extreme that for our ∼1.36 $M_\odot$ (baryonic mass) NS computed with the SFHo EoS as well as for our ∼1.8 $M_\odot$ (baryonic mass) NS described by the LS220 EoS, $t_{\nu,90} \approx 6\,{\rm s}$ is roughly the same, although the total release of gravitational binding energy is $198\,{\rm B} = 1.98 \times 10^{53}\,{\rm erg}$ in the former case and $335\,{\rm B} = 3.35 \times 10^{53}\,{\rm erg}$ in the latter case.

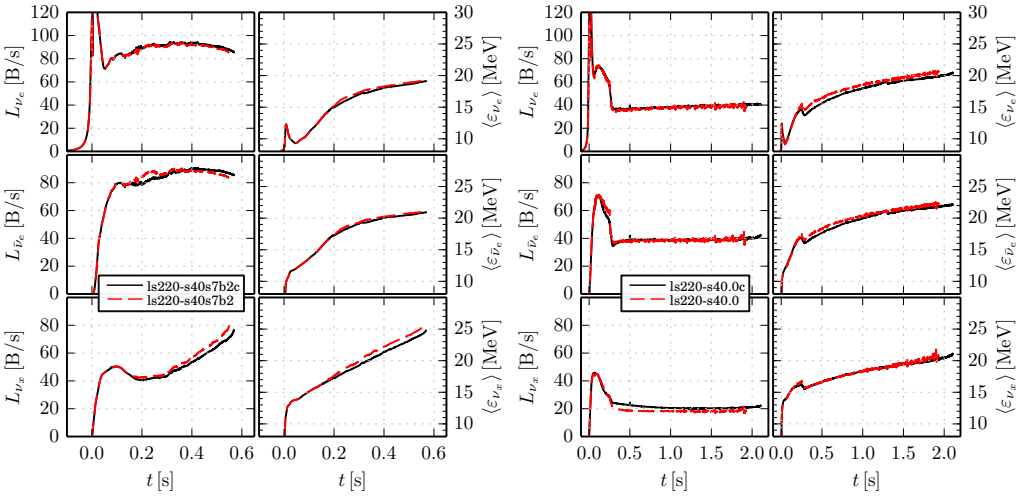

Fig. 15. – Neutrino signals (luminosities and mean energies for an observer in the laboratory frame) for ν_e (*top*), $\bar{\nu}_e$ (*middle*), and one species of ν_x (*bottom*) for the 40 $M_\odot$ BH formation simulations shown in Fig. 13 (*left panel*) and Fig. 14 (*right panel*). The results of the models including mixing-length convection in the proto-neutron star (black solid lines) exhibit only relatively small differences compared to the models without convection (red dashed lines). In the case of the s40s7b2 progenitor (*left*) convection mainly reduces the luminosities and mean energies of heavy-lepton neutrinos, whereas in the s40.0 case (*right*) it reduces the mean energies of ν_e and $\bar{\nu}_e$ by up to ∼1 MeV.

Such differences indicate the paramount importance of the high-density EoS model for reliable calculations of the neutrino-cooling signal of nascent NSs. They also suggest that highly valuable constraints of the still incompletely understood properties of matter in the interior of NSs could be deduced from the measurement of the neutrino signal from a future Galactic SN. If the distance to the SN is well determined, the energy-loss time scale and calorimetric arguments can yield useful information. But even if the SN distance is not known, the characteristic time structure of the signal [168] and the spectral evolution can provide crucial evidence. This will require most accurate predictions of the SN neutrino emission (employing consistent microphysics of the EoS and neutrino opacities) and the combined information from detections in all existing, upcoming, and planned experimental facilities. All together this will allow one to interpret the detailed features of a high-statistics measurement of the time structure and spectral evolution of the neutrino emission during all phases of stellar collapse and explosion, despite the complexities of the SN physics and of various neutrino oscillation phenomena on the way from the SN core to the detectors on earth. Because of the stochasticity of multi-dimensional hydrodynamics phenomena that assist shock revival and because of the limited sensitivity of the early-time neutrino emission to the high-density EoS, the post-explosion emission, in particular the late-time neutrino signal, will be the most reliable probe of the state of matter at nuclear and supernuclear densities in the deep interior of the NS.

2˙5. *Neutrino signals from black hole formation.* – A considerable fraction of all stellar core collapses, possibly similarly frequent as SNe, might fail to explode. In these cases

the newly formed NS continues to accrete matter from the infalling stellar core until it reaches the mass limit for BH formation and gravitational instability sets in. Modern calculations of the neutrino emission of such events, performed with energy-dependent neutrino transport schemes, were carried out, e.g., in Refs. [63, 169-173] for different EoSs of hot NS matter. However, these models did not include convection in the NS and also ignored many aspects of the neutrino interactions, e.g., did not take into account neutrino-pair conversion between different flavors [174], energy transfers in neutrino-nucleon interactions, and nucleon-correlations in the dense medium.

Here we present models of the Garching group [64] that include all of these effects. Figures 13 and 14 show mass-shell plots of two $40\,M_\odot$ progenitors (s40s7b2 of Ref. [149] and s40.0 of Ref. [150], respectively), both of which were computed with the LS220 EoS. The upper panels of the figures display results of simulations without mixing-length treatment of convection, the lower ones with convection inside of the proto-neutron stars. Figure 15 provides the time evolution of the corresponding neutrino luminosities and mean energies. The differences between convective and non-convective models are relatively small because the convective shell is buried below a hot, convectively stable accretion layer that is growing in mass and whose neutrino production dominates the properties of the radiated neutrinos. The models with active proto-neutron star convection exhibit slightly lower values of some quantities of the neutrino emission. Most remarkably, the convective models tend to collapse to BHs a bit later than their counterparts without mixing-length convection, despite the higher values of the integrated energy and lepton-number loss through neutrinos. This delay is explained by the stabilizing influence of thermal pressure, because the accelerated deleptonization associated with convective lepton-number transport leads to a faster rise and higher values of the temperature in the deep interior of the NS.

The two considered $40\,M_\odot$ stars differ significantly with respect to the duration of their evolution until BH formation. While it takes $\sim$0.57 s after bounce for model s40s7b2 to reach this moment, the gravitational instability in model s40.0 occurs as late as $\sim$2.1 s after bounce, because the mass accretion rate of the collapsing stellar core in this latter case is much lower after a composition-shell interface has passed the stalled shock at $\sim$0.3 s after bounce. Correspondingly, the neutrino luminosities in the s40.0 run are only roughly half of those in the s40s7b2 model; also the mean energies of the radiated neutrinos rise more slowly and remain lower in model s40.0 when the same times are compared. For heavy-lepton neutrinos these differences in the time-dependent behavior are most prominent. While their luminosity and mean energy grow steeply in the s40s7b2 simulation, L_{ν_x} in s40.0 is basically constant for $t_{\rm pb} \gtrsim 0.3$ s and $\langle E_{\nu_x} \rangle$ increases only with a flatter gradient (Fig. 15). These differences reflect the compression and corresponding heating of the rapidly mass-accumulating accretion layer in model s40s7b2, whereas in s40.0 neutrino cooling can well keep pace with the inflow of energy by the accretion of fresh gas, for which reason the mantle layers of the newly formed NS in the latter model remain cooler.

Failed SNe, i.e., "direct" BH formation events in which the transiently formed NS is pushed across the BH formation limit by permanent post-bounce accretion, therefore produce neutrino signals with distinct features like a continuous hardening of the emitted spectra before the emission terminates abruptly. The two discussed simulations show that the detailed properties of the neutrino radiation depend strongly on the survival time of the NS. Better predictions of the integrated neutrino emission of such events, whose contribution might imprint characteristic structures on the DSNB, will therefore require systematic calculations of failed explosions for large model sets of progenitor stars, taking

into account the growing understanding of stellar core-collapse cases that are not likely to blow up as SNe [53, 54, 175-177].

One should keep in mind, however, that spherically symmetric simulations (even if they include a mixing-length treatment of convection interior to the neutrinosphere) are unlikely to capture all effects of relevance for the neutrino emission. When the stalled shock retreats in reaction to the contraction of the NS, favorable growth conditions of the SASI are established and, correspondingly, episodes of violent SASI sloshing and spiral-mode activity are found in 3D simulations that follow the post-bounce accretion of non-exploding massive stars over hundreds of milliseconds [66,87,88,126,127]. It must be expected that large-amplitude neutrino-emission variations caused by SASI modulations of the NS accretion (cf. Sect. **2**˙3) accompany the whole evolution at least until the collapse of the NS to a BH sets in. Future 3D simulations will also have to clarify the long-time development of the LESA dipole that was found for the neutrinos radiated during the accretion phase [98]. It is presently unclear at which level these and other multi-dimensional phenomena (e.g. connected to stellar core rotation, whose effects potentially increase on the way to NS collapse) can affect the predictions of the DSNB from failed SNe (see Sect. **5**). Although most (maybe all) of the direction dependences and short-time signal modulations of the observable neutrino emission will average away in the time and direction-integrated signals that are relevant for the DSNB, the interpretation of a Galactic BH formation event will greatly benefit from a precise knowledge of the signal structure until the emission is terminated.

2˙6. *Conclusions*. – In this Section we discussed the current status of modeling the neutrino emission from stellar core collapse events. Hydrodynamical simulations with most sophisticated neutrino transport are needed to calculate detailed signal properties, which are necessary for studies of neutrino oscillations in supernovae, for investigations of neutrino-dependent and neutrino-induced nucleosynthesis, and for the exploration of detection possibilities of the DSNB and of neutrinos from a future Galactic supernova.

The neutrino emission from core-collapse supernovae is strongly affected by multi-dimensional hydrodynamic instabilities inside and around the newly formed NS. Convective overturn and the SASI (standing-accretion shock instability) in the postshock accretion layer support the initiation of the explosion and impose large-amplitude time variations and large-scale directional asymmetries on the neutrino emission during the accretion phase (Sec. **2**˙3; [87,88]). Proto-neutron star convection is active interior to the neutrinospheres during this phase as well as during the post-explosion Kelvin-Helmholtz cooling phase of the compact remnant.

Recent 3D simulations with detailed neutrino transport have led to the discovery of the growth of hemispheric differences in the strength of proto-neutron star convection on a time scale of about 150 ms after core bounce (Sec. **2**˙3). These hemispheric differences produce a large dipolar asymmetry of the lepton-number flux with relative enhancement of the ν_e emission compared to $\bar{\nu}_e$ in one hemisphere and increased $\bar{\nu}_e$ emission on the opposite side. The hemispheric differences of the lepton-number (ν_e minus $\bar{\nu}_e$) flux normalized to the average can be factors of a few, corresponding to dipole amplitudes of the individual emission of ν_e and $\bar{\nu}_e$ of 10–20%, whereas the ν_x emission dipole is only of order percent [98]. While this unexpected and stunning new phenomenon is not yet fully understood and still needs further exploration and confirmation by independent results, the first successful explosions in 3D simulations with sophisticated, energy-dependent neutrino transport have become available [79,120-122]. They provide support for the viability of the neutrino-driven mechanism for driving and powering supernova explosions.

During the Kelvin-Helmholtz cooling phase convection interior to the neutrinospheres accelerates the lepton-number and energy loss of the nascent NS. The basic effects of this quasi-stationary convective transport can be well described in spherically symmetric simulations by a mixing-length treatment, whose results we showed to compare nicely with those of direct hydrodynamic modeling of convection in 2D calculations (Sec. **2**˙4). We also presented here the first time-dependent, hydrodynamical simulations with state-of-the-art spectral neutrino transport, in which a mixing-length treatment was applied during the whole cooling evolution of proto-neutron stars. The calculations were performed with different nuclear equations of state and include the recently intensely discussed effects of nucleon self-energy shifts in the charged-current β-reactions of free nucleons.

Convection interior to the neutrinospheres facilitates the faster deleptonization of the high-density core of the NS and thus enhances the emission of ν_e relative to $\bar{\nu}_e$ during the first seconds, thus leading to more proton-rich conditions in the neutrino-driven wind. The possibility of a ν-p process [158,159] during the early phase of proto-neutron star cooling has to be reinvestigated. However, with the neutrino physics used (which excludes effects of active or sterile neutrino-flavor oscillations in the hydrodynamic modeling), neutron-rich conditions in the wind are not found at any time during the cooling evolution of compact remnants that bracket the mass range of NSs formed in the far majority of all supernova explosions; models with NS baryonic (final gravitational) masses of $\sim$1.363 (1.252) $M_\odot$ and 1.776 (1.592) $M_\odot$ were discussed. Spherically symmetric simulations of proto-neutron star formation, however, require artificial initiation of the supernova explosion. Even in stars near the low-mass end of supernova progenitors, where multi-dimensional hydrodynamic effects are not crucial for the onset of the explosion [77, 79], convective overturn stirs the postshock accretion layer. One-dimensional models therefore cannot correctly describe the transition from the accretion phase to the explosion and proto-neutron star cooling phase, because simultaneous inflows and outflows coexist in the postshock layer during this transition. Two-dimensional explosion models show the ejection of matter with moderate neutron excess in rapidly expanding plumes of buoyant plasma during the early expansion phase of the shock front in particular in low-mass oxygen-neon-magnesium and iron-core progenitors [80, 113]. These ejecta might provide the conditions for a weak r-process with production of neutron-rich nuclei up to mass numbers of $A \sim 100$–110 [80].

Continuing accretion of matter onto the nascent NS in the case of unsuccessful explosions unavoidably leads to BH formation. Recent insights suggest that these failed supernovae might be more common than previously thought (e.g., [52-55, 175-177]) and might therefore account for a significant contribution to the DSNB. Neutrino signals from such events up to the moment when the NS becomes gravitationally unstable were computed with energy-dependent neutrino transport before [63, 169-173]. Here we presented state-of-the-art 1D hydrodynamic simulations that include proto-neutron star convection by a mixing-length treatment and the full set of currently discussed neutrino interactions of relevance in the core of collapsing stars (Sec. **2**˙5). While convection inside of the neutrinospheres does not have a major impact on the calculated neutrino emission (except for slightly stretching the life time of the transiently existing NS), it must be expected that violent SASI sloshing and spiral-mode activity induces large-amplitude modulations on the neutrino luminosities and spectra radiated by the accreting NS all the way until BH formation. Three-dimensional simulations of the evolution from the onset of stellar core collapse to the gravitational instability of the NS will therefore have to be performed also for obtaining reliable predictions of the neutrino (and gravitational-wave) signals from failed supernovae in order to get prepared for the —not unlikely— case of

a future Galactic event.

Neutrino data and structural profiles from the Garching simulations can be made available upon request for download at `www.mpa-garching.mpg.de/ccsnarchive`.

3. – Perspectives for Future Supernova Neutrino Detection

Authors: K. Scholberg, A. Mirizzi, I. Tamborra

In this Section, we will consider the physics of neutrino detection in the regime relevant for SN neutrinos, and discuss the interaction channels for relevant detector types. We will survey main existing and planned detectors sensitive to SN neutrinos, and touch on some topics related to real-time SN neutrino astronomy and astrophysics.

3˙1. *Supernova neutrino detection.* – Few detectors are constructed with the primary aim of SN neutrino detection; most neutrino detectors are built for studies of neutrino oscillation with solar, atmospheric, reactor and beam neutrinos, or for high-energy astrophysical neutrino observation, or for nucleon decay searches. Happily, however, many large neutrino detectors — especially those sited underground — have excellent capabilities for the capture of a core-collapse SN neutrino burst.

Detectors suitable for SN neutrinos must in general be sensitive to the products of interactions of neutrinos in the few to few tens of MeV range. Typically the final-state particle energies are also in that energy range, although sometimes can be lower. Neutrinos interact with detector materials via both charged-current (CC) and neutral-current (NC) channels. For standard-model CC processes, the resulting lepton type depends on the incoming neutrino flavor, and the lepton charge is negative for a neutrino and positive for an antineutrino. Supernova neutrino spectra are, however, almost entirely below threshold for CC production of a muon or a tau particle (the thresholds are 110 MeV and 3.5 GeV respectively for quasi-elastic production). Therefore CC interactions are accessible only for ν_e and $\bar{\nu}_e$ from core collapse. The muon and tau components of the flux are accessible only via NC interactions.

The neutrino interaction products depend also on nature of the target; the observability of the interaction products depends on the nature of the detection technology. The following subsections describe the different channels, and relevant detector technologies, for the different components of the SN flux. Detection of SN neutrinos is reviewed in [178].

3˙1.1. *Neutrino interactions with matter*. The interaction products of SN neutrinos are detected using conventional means, typically via the energy loss of the primary particle out of the interaction, or via energy loss of secondary particles. Detectors have different capabilities for energy resolution, angular resolution, time resolution, and particle identification. They are limited usually by some combination of the intrinsic physics of the particle energy loss, the detection mechanism, and the parameters of the detector technology (i.e., by technical sophistication and cost).

Real detectors are plagued by backgrounds. For surface or near-surface detectors, cosmogenic backgrounds are a serious issue, typically inducing event rates at or above SN neutrino energies at rates far higher than the rate expected from a burst from all but the nearest SNe. Cosmogenics include direct cosmic rays (muons being the most penetrating) and secondaries, some of which can be long-lived and produce radioactive decays in the SN event energy range (e.g., [179-181]). Nevertheless, some surface detectors can expect to collect useful SN burst events when triggered by some external observation. With even modest overburden, cosmogenic rates can be reduced significantly, to the point where the expected background counts within a typical few-tens-of-second burst are negligible. Cosmogenic background rates depend on overburden, detector size and geometry, and penetrating particle veto capability. Intrinsic detector background from radioactivity

from detector components and nearby materials can also be a problem, especially at low energy. In the regime below about 5-10 MeV of energy deposition, radioactivity can be dominant. Radioactive background rates depend sharply on the composition of the nearby environment and the care taken with detector radio-cleanliness. Finally, instrumental backgrounds (electronic noise, calibration sources, etc.) can sometimes be a problem in practice. In general, underground detectors designed to measure low-energy neutrinos from steady-state sources such as the Sun, the atmosphere, or reactors, are able to achieve background levels low enough that a Galactic SN burst will have negligible background. Backgrounds become more of an issue for detection beyond the Milky Way, and for the DSNB (see Sec. **5**).

Different detector materials have different flavor sensitivities in part by virtue of the relative interaction rates of CC and NC channels in the material. The ability of a detector to determine flavor content by distinguishing different interactions on an event-by-event basis ("tagging capability") also affects the information content that will be possible to extract from a burst observation. We summarize here the main detection channels for different flavors.

- *Electron antineutrinos:* The detectors that were running during the SN 1987A neutrino burst, as well as most current detectors, are sensitive primarily to the $\bar{\nu}_e$ component of the neutrino flux. The reason is that the main detector materials for large underground detectors, water and liquid scintillator (C_nH_{2n}) are rich in free protons, which have a rather large, and well known, cross section for interaction with $\bar{\nu}_e$ via inverse beta decay (IBD) [182], $\bar{\nu}_e + p \to n + e^+$. This interaction has a threshold of $E_{\nu_{\rm thr}} = 1.8$ MeV. For typical expected SN neutrino spectra, IBD dominates in water and scintillator. The IBD interaction products are detected via the energy loss of the positron. In some cases, the neutron can be detected after moderation and capture (with well-defined delay on the tens or few hundred microsecond scale, depending on materials available for capture). For example, a neutron capture on a free proton, $n + p \to d + \gamma$, produces a 2.2-MeV gamma-ray, which can be detected via its Compton-scattering energy loss. Other nuclei (notably Gd) can also capture neutrons with high cross section, and the subsequent deexcitation gammas can be detected. If the time-delayed neutron can be detected via capture, it often provides an experimentally-useful tag of the IBD interaction. It is also possible to observe the energy loss of Compton-scattered 0.511-MeV gamma-rays resulting from annihilation of the positron.

  Charged-current $\bar{\nu}_e$ interactions on protons bound in nuclei of common detector materials (carbon, oxygen, argon, iron, lead) can also occur ($\nu_e + (N, Z) \to (N - 1, Z+1) + e^-$), and may result in ejected nucleons and nuclear deexcitation gamma-rays in addition to the positron (e.g., [183, 184]). However CC $\bar{\nu}_e$ interactions on nuclei are usually subdominant, as the production of a neutron in the final state is often Pauli-suppressed.

- *Electron neutrinos:* Electron neutrinos interact via CC channels on neutrons in nuclei (alas, no free-neutron neutrino target exists), according to $\bar{\nu}_e + (N, Z) \to (N + 1, Z - 1) + e^+$. This interaction will occur for oxygen in water, and on ^{12}C in liquid scintillator, and will represent an observable component of a large-statistics sample; however IBD will still be dominant for these detector materials, and it may be difficult to do an event-by-event tagging. As for CC $\bar{\nu}_e$ interactions, prompt and delayed final-state particles besides the electron may be produced, depending on

the nature of the target nucleus. One of the most promising targets for clean ν_e detection is liquid argon. This has a reasonably high-cross-section CC ν_e channel $\nu_e + {}^{40}\mathrm{Ar} \rightarrow e^- + {}^{40}\mathrm{K}^*$ [185, 186]. In a time projection chamber, the resulting electron track can be reconstructed. Furthermore, the resulting characteristic cascade of gamma rays, for which Compton scatters can be detected, can serve to tag the channel as ν_e. This channel should dominate in argon for the expected core-collapse spectrum.

Lead and iron also have a large cross sections (especially lead) for CC ν_e interaction [187-192], for which observable products are (in principle) the lepton, but also single or double emitted neutrons (for which there are different thresholds).

- *Muon and tau neutrinos:* As noted above, in order to access the ν_μ and ν_τ (and antineutrino) components of the signal, NC sensitivity is required. Because NC reactions are flavor-blind, all flavors will be entangled in the observed NC signal; nevertheless, since under many scenarios the mu/tau component is hotter (and furthermore represents two-thirds of the luminosity), the NC signal will have a significant ν_μ, ν_τ component. NC interaction channels occur in every detector type, although detectors differ in their ability to tag the channel. The NC interaction results in a scattered nuclear target, and is either elastic or inelastic. Inelastic NC scattering on nuclei produces excited final-state nuclei which can deexcite via gamma emission, or ejection of protons or neutrons. These deexcitation products are the experimental observables. While neutrino differential spectral information is lost, some integral spectral information may be available by counting observed events over threshold. In water, resulting protons and neutrons will always be below Cherenkov threshold; gammas may however produce Compton scatters that are observable. Neutrons may also be captured on protons or dopants such as Gd to produce above-Cherenkov-threshold light. In scintillator, all ejected products are in principle observable, and neutrons are generally visible via the gamma-rays emitted following their captures. A particularly attractive 15-MeV NC-induced deexcitation gamma (the cross section for which has been measured [193]) occurs for ^{12}C.

  In argon, some NC deexcitation channels may be observable [194]; however this is currently rather unexplored in the literature. Lead also has prominent neutron-ejection NC channels which can be exploited by detectors. (Note there is also a NC component to elastic scattering on electrons, which is discussed separately below.)

  Elastic NC scattering on protons or nuclei is also a possibility for detectors with low energy thresholds. Elastic scattering produces simple recoil spectra, the shapes of which retain source spectral information [195]. Elastic scattering on protons [196], which produces hundreds-of-keV recoils, is observable in scintillator, and coherent elastic neutrino-nucleus scattering (CEνNS) [197-199], will also yield events with recoils in the tens to hundreds of keV scale. This regime is out of reach for very large detectors, but is attainable by detectors designed to search for weakly-interacting dark matter.

- *Elastic scattering on electrons:* A final category of interaction, the simplest physically, is sensitive to all flavors of SN burst neutrinos; this is elastic scattering on electrons (ES). It proceeds via both CC and NC channels [200]. The detectable signature is the energy loss of scattered electron. The ES cross section is low compared to cross sections on nuclei, typically representing a few percent of a SN burst

signal. This interaction has directional sensitivity— the electron is scattered with respect to the incoming neutrino direction within an (energy-dependent) angle of about 30 degrees. Because all materials have electrons, this interaction will occur in all detector types, although detectors vary in the efficiency for observing the electron and in ability to track the scattered electron direction.

We note that although the cross sections for the simplest targets — elastic scattering on electrons and inverse beta decay of $\bar{\nu}_e$ on protons— are well understood, and have been employed as low-energy detection interactions for decades with e.g., solar and reactor neutrinos, the interactions of neutrinos on heavier nuclei are quite poorly understood. At present, the only other interactions studied experimentally with better than $\sim 10\%$ precision is ^{12}C [193, 201]. The targets of interest for SN neutrino detection have never been irradiated with a well-understood neutrino source to determine their cross sections and the properties of the interaction products (particle types, angular distributions, etc.). Furthermore, there are relatively few theoretical studies in the relevant energy regime. We note promising opportunities to study these cross sections using a pion decay-at-rest source, such as the Spallation Neutron Source at Oak Ridge National Laboratory in Tennessee, within the next decade [202].

3˙1.2. *Main detector types and considerations*. There are several kinds of relevant detector technologies, some currently running and others planned for the future. The most important and the main instances of these are described below.

- *Water Cherenkov (WC):* These employ water in liquid or ice form as the detector material. Optical-frequency Cherenkov radiation from particles moving faster than the speed of light in water is collected by photomultiplier tubes. The Super-Kamiokande detector, a 50-kton detector in Japan [18] is the main instance of this class. Among detectors running at the time of this review, Super-Kamiokande will collect the largest number of individually-reconstructed SN neutrino events. A possible enhancement to Super-Kamiokande currently under investigation is the potential loading with Gd to improve the neutron capture cross section for better tagging of $\bar{\nu}_e$ [203] (and ν_e [204]). The tagging efficiency for $\bar{\nu}_e$ via neutron capture on free protons is about 18%. A Gd tagging efficiency of at least 67% has been demonstrated [205], but it can likely be improved beyond that. We will discuss the impact of Gd tagging in the background reduction for DSNB in Sec. **5**. The next-generation anticipated large WC detector is Hyper-Kamiokande, with half a Mton of mass [206].

  An important special case of WC detector for SN detection is the "long-string" type. This type of detector comprises a very large volume of water or ice (part of a natural body), instrumented with strings of photomultiplier tubes. These kinds of detectors are nominally intended for ultra-high-energy neutrino detection (>GeV), and they are too sparsely instrumented to resolve individual SN neutrino interactions. However, they are still able to observe a SN neutrino burst as a diffuse glow of Cherenkov photons in the ice or water, via coincident increase in count rate of all the photomultiplier tubes within the time window of the burst [207,208]. Although event-by-event energy, angle and flavor information is not available, the photon statistics are high enough to provide good time resolution for the overall time structure of the burst [209]. Instances of this class are IceCube, which has a SN trigger; in its complete configuration, IceCube has 5160 optical modules [210]

and about 3 Mton effective detection mass, representing the largest current detector for SN neutrinos. Others, which are noisier [211], may still retain information. Increased photomultiplier tube density, such as that proposed for the PINGU infill [212], will improve SN sensitivity by enhancing the probability to for multiple photons per interaction to be recorded.

- *Liquid scintillator:* These detectors employ organic hydrocarbons in liquid form. Like water, the material has a large fraction of free protons. Scintillator detectors are therefore also primarily sensitive to IBD and hence to $\bar{\nu}_e$. Scintillators emit photons in response to energy loss of charged particles. Rather large light yields per energy loss ($\sim$50 times higher than light yields for Cherenkov radiation) can be obtained, resulting in good event-by-event energy resolution and potentially low energy thresholds. Typically neutrons can be detected via capture on free protons with high efficiency; gadolinium doping is often employed to enhance capture rate and deexcitation gamma energy release. In order to take advantage of low energy thresholds, scintillator detectors must tackle the difficulties of radioactive contamination which are typically fierce below a few MeV.

  The currently-running instances of large scintillator detectors are LVD [19,213,214], Borexino [215,216], and KamLAND [217]; the SNO+ [218] experiment should turn on in the near future. A future planned 20-kton detector is JUNO [219, 220]; another well-developed concept is the 50-kton LENA detector [221]. Surface reactor-neutrino scintillator detectors (all Gd-loaded), although relatively small (tens of ton scale) and unprotected by significant overburden, also represent a SN burst detection opportunity. Daya Bay in particular can defeat cosmogenic background by high IBD selection efficiency and by the requirement of coincidence between multiple, spatially-separated detectors [222]. Because scintillation light is emitted isotropically, the direction sensitivity of these detectors is limited (although see Sec. **3**˙3.2). Thanks to the low energy threshold, scintillator also has sensitivity to NC elastic scattering of neutrinos on protons. "Quenching" of scintillation light from heavy recoil products suppresses observability of this channel; nevertheless there should be some capability for existing and future detectors. Furthermore, information about the neutrino spectrum is available via the proton recoil spectrum [195].

- *Liquid argon (LAr):* An extremely interesting possibility for the future is liquid argon time projection chamber (LAr TPC) technology. These detectors drift ionization charge from energy loss of charged particles in an electric field, and collect this charge on a planar anode (via different mechanisms– either collection or induction wires, or multiplication at a liquid-gas interface). Two dimensions of the track can be reconstructed from collected-charge projection on the anode plane, and the third dimension is determined from drift at known constant velocity; therefore three-dimensional tracks can be reconstructed. Products of low-energy SN neutrino interactions can be in general reconstructed as short ($\sim$10-cm scale) lepton tracks. In principle energy loss from Compton scatters from deexcitation and bremsstrahlung gamma rays can also be recorded, and used to tag interaction channels. The primary interaction from a SN neutrino burst will be ν_e absorption which gives liquid argon excellent sensitivity to the electron flavor component of the flux [223]. The detector also has intrinsic directional capability for anisotropic interaction products. Liquid argon time projection chamber technology has been

demonstrated for the Icarus [224] detector, as well as smaller prototypes such as ArgoNEUT (although with little emphasis on low-energy events). MicroBooNE, a 200-ton fiducial surface detector at Fermilab [225], will be online soon. The prospects for a large detector, DUNE, underground in the United States are very good [226].

- *Lead:* Another possible method of SN neutrino detection is to employ a heavy material, such as lead or iron. These materials have a high cross section for neutrino interactions in the few tens of MeV range. In principle, detectors can observe energy loss of leptons, gammas, or other interaction products. However a potentially inexpensive mode of operation is to exploit the high probability for ejection of neutrons subsequent to a CC or NC neutrino interaction; counting single and double neutrons gives crude spectral information [227]. The ejected neutrons can be detected with dedicated neutron-detection technology. There is currently one operating instance of a lead-based SN neutrino detector, the HALO experiment at SNOLAB [228], which incorporates 76 ton of lead in conjunction with leftover ^{3}He neutron counters from the SNO experiment. The HALO-2 detector of kton scale is an envisioned future upgrade.

- *Dark matter detectors:* Another category of detector will have some sensitivity to SN neutrinos via CEνNS, the neutral-current interaction of a neutrino with an entire nucleus [199]. The cross section for this process is relatively high, producing a handful of events per ton of detector material for a 10-kpc core collapse. However recoil energies are very low (few tens to hundreds of keV), making this channel experimentally challenging. Dark matter direction detection detectors are optimized to observe these low energy recoils and hence will have sensitivity to the total SN flux [229]. Current-generation detectors of less than ton scale will observe small statistics, but with potential scale-ups to multi-ton scales, this category of detectors will provide useful information about a SN burst.

3˙2. *Detector summary and future prospects.* – The possible distribution of core-collapse SNe in the Galaxy must follow the regions of star formation, notably in the spiral arms. The expected distance distribution for a simple model is shown in Fig. 16. One realizes that the distribution is very broad and that 10 kpc is probably a reasonable benchmark value. However, every distance between 2 and 20 kpc has similar probability. Therefore, one would expect a factor of ∼100 for variations in the predicted neutrino event rate for a future Galactic SN explosion. For definiteness, Table I summarizes neutrino event rates for current and future detectors assuming a benchmark SN at $d = 10$ kpc. Despite the scaling of the event rates with $1/d^2$, most of the existing detectors would be massive enough to assure a sensitivity to a SN event in the whole Galaxy. Moreover, a 0.5 Mton water Cherenkov detector would collect ~ 10 events from an extragalactic SN in nearby galaxies at $d \sim 1$ Mpc, such as M31 and M33. The prospects for detecting mini-neutrino bursts from nearby galaxies is quite exciting, since about one SN per year is expected within distances up to 10 Mpc [231, 232]. In this regard, the patient accumulation of data on an event-by-event basis from SN in nearby galaxies (up to 10 Mpc) would be an additional possibility for study of the average supernova neutrino spectrum [231, 232].

Figure 17 shows some examples of expected event rates as a function of time for several models in proposed future large detectors for a 11 $M_\odot$ and a 27 $M_\odot$ SN progenitors with LS EoS (see Sec. **2˙4**), and Fig. 18 shows the time profile for the same models observable

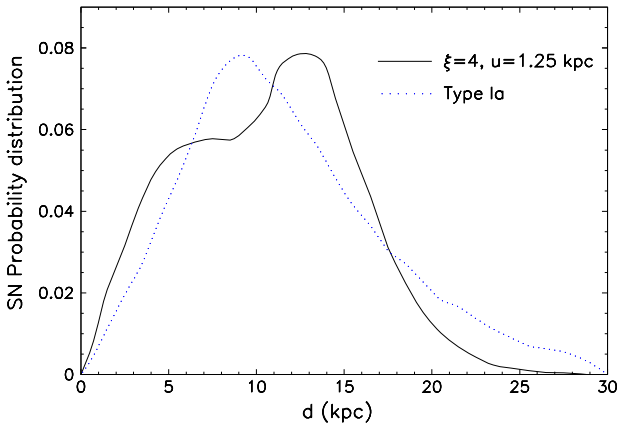

Fig. 16. – SN probability vs. distance from the Sun for a simple model of progenitor distribution (continuous curve). In comparison also the SN distribution for Type Ia SNe is shown (dotted curve). (Reprinted figure from [230]; copyright (2003) by the Institute Of Physics Publishing.)

by IceCube. Among the current detectors IceCube is the one having the largest volume for SN neutrinos. Moreover, before two decades have passed we will possibly have a 40-kton argon detector (DUNE), a 560-kton water detector (Hyper-K) and a 20-kton scintillator detector (JUNO). For water and scintillator, the event rates are dominated by $\bar{\nu}_e$, and for argon, the event rates are dominated by ν_e. This figure shows that all detectors can clearly distinguish the accretion phase, resulting in a "hump" in the neutrino signal, lasting $\simeq 0.5$ s and the following cooling on a timescale of ~ 10 s. In the ν_e signal collected by the argon detector one would also clearly see the neutronization peak, lasting $\simeq 50$ ms just after the core-bounce, unless suppressed by oscillations (see Sec. **4**). We note that for large detectors, provision must be made when designing electronics and data acquisition to prevent data loss for the very high event rates expected for core collapses at $\lesssim$ kpc distances.

3˙3. *Neutrino astronomy and astrophysics.* – The neutrino burst from a core collapse is also useful to astronomers and astrophysicists. In the following we present some of the applications discussed in literature.

3˙3.1. *Finding the supernova: Early alert.* Because neutrinos are released from the stellar collapse on a timescale of seconds, starting within milliseconds of infall, detection of a SN burst offers an opportunity to provide astronomers with an early alert of a SN occurrence. The relative delay between the neutrino wavefront reaching Earth and the first photons from shock breakout is expected to be on the timescale of hours ([6]). The SuperNova Early Warning System (SNEWS) [236, 237] is a world-wide network designed to alert astronomers, or any other interested scientists, of a burst. At the time of this review, the SNEWS network involves Super-Kamiokande, LVD, Borexino,

([6]) The delay of three hours between the $\bar{\nu}_e$ burst and the optical signal from SN 1987A implies that the velocity of electron antineutrinos is equal to that of light with an accuracy $\sim 2 \times 10^{-9}$ [233, 234]. This bound represents an accurate test of special relativity.

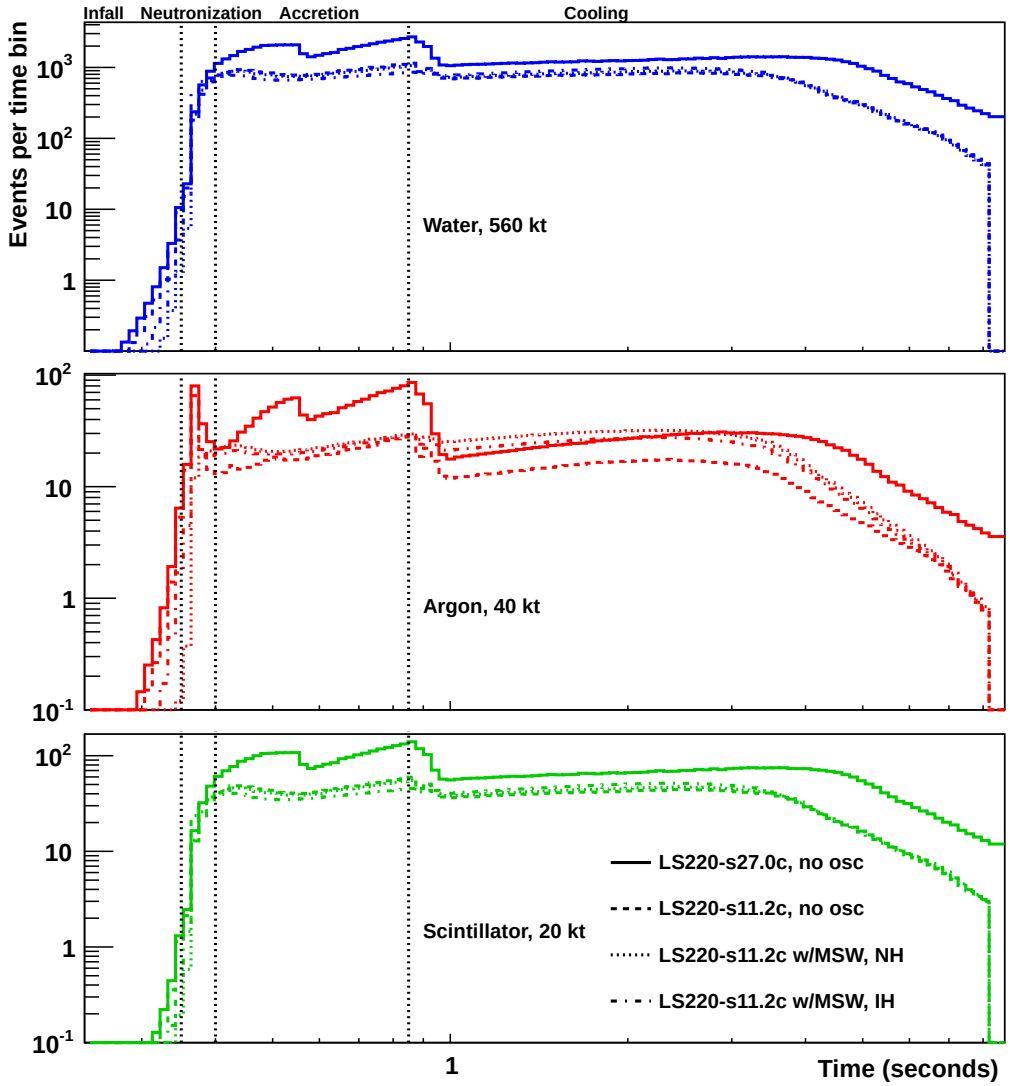

Fig. 17. – Examples of total event rates per time bin for 27 $M_\odot$ and 11 $M_\odot$ SN progenitors (see Sec. **2**˙4), for water, argon and scintillator detectors, respectively from the top to the bottom panel. Core bounce is at 0.35 seconds. The dotted (dashed dotted) lines are rates for a simplified MSW oscillation assumption for the normal (inverted) hierarchy case (see Sec. **4**˙11). Note that expected events in non-equal logarithmic time bins are plotted, not rates.

KamLAND, IceCube and Daya Bay; sensitivity is to core collapses within the Milky Way. A central computer at Brookhaven National Lab (with backup at Bologna) receives datagrams sent by individual experiments and sends an automated alert to a mailing list if a coincidence is found within ten seconds according to the burst UT time stamps. The SNEWS network has been operational for an automated alert since 2005, although no coincidences have been detected. It is worth noting that gravitational waves also

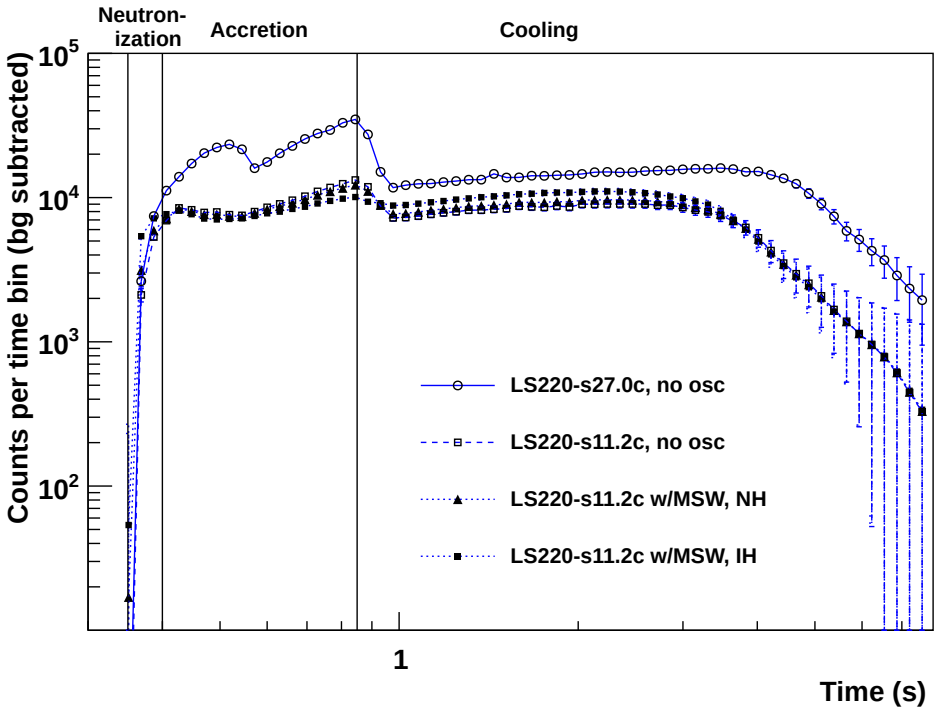

Fig. 18. – Expected background-subtracted counts per time bin for IceCube, for IBD events (following [235]), for the same models as in Fig. 17. Error bars are statistical. Again note non-equal logarithmic time bins.

potentially provide a prompt signal of core collapse, and correlation with neutrino burst can potentially enhance the early alert [209, 238]. Moreover, assuming that the angular location of the SN burst can be determined quickly, there is a very high probability for detection of the SN shock breakout in the infrared [239]. Such cross-correlations would be extremely useful against false triggers.

It has been estimated that the silicon-burning phase preceding a SN explosion can release an energy of about 5×10^{50} erg for a few days in neutrino-antineutrino pairs with average energy ~ 2 MeV [240,241]. IBD events from silicon burning have very low (below nominal detection threshold) positron energies, and the best prospects for detection are via neutron capture by adding Gd, provided that the events can be statistically distinguished from background fluctuations. For a very nearby SN at a distance $d = 1$ kpc, one would expect ~ 500 events per day in a 0.5-Mton WC detector [242]. The kton liquid scintillator detector KamLAND will be able to detect pre-SN neutrinos for progenitors at distances within $d = 660$ pc in the most optimistic scenario [243]. Detection prospects for detectors under construction or proposed, e.g., SNO+, JUNO, and LENA, look also excellent. Such detection would make it possible to foresee the death of a massive star a few days before the stellar core collapse; eventually this could allow discrimination of the progenitor type [244]. Possible pre-supernova candidates that could explode at unpredictable future times include Betelgeuse, 3 Ceti, Antares, Epsilon Pegasi, Pi Puppis,

TABLE I. – *Current and proposed SN neutrino detectors as of the time of this writing. Event rate estimates are approximate for 10 kpc; note there may be significant variation by SN model. The "Flavors" column indicates the dominant flavor sensitivity (note that other flavor components may be detectable, with varied tagging quality). Not included are smaller detectors (e.g., reactor neutrino scintillator experiments) and detectors sensitive primarily to coherent elastic neutrino-nucleus scattering (e.g., WIMP dark matter search detectors). An asterisk indicates a surface detector, which may not be self-triggering due to background. Numbers in parentheses indicate that individual events will not be reconstructed; see text.*

Detector	Type	Mass (kt)	Location	Events	Flavors	Status
Super-Kamiokande	H_2O	32	Japan	7,000	$\bar{\nu}_e$	Running
LVD	C_nH_{2n}	1	Italy	300	$\bar{\nu}_e$	Running
KamLAND	C_nH_{2n}	1	Japan	300	$\bar{\nu}_e$	Running
Borexino	C_nH_{2n}	0.3	Italy	100	$\bar{\nu}_e$	Running
IceCube	Long string	(600)	South Pole	(10^6)	$\bar{\nu}_e$	Running
Baksan	C_nH_{2n}	0.33	Russia	50	$\bar{\nu}_e$	Running
MiniBooNE*	C_nH_{2n}	0.7	USA	200	$\bar{\nu}_e$	(Running)
HALO	Pb	0.08	Canada	30	ν_e, ν_x	Running
Daya Bay	C_nH_{2n}	0.33	China	100	$\bar{\nu}_e$	Running
NOνA*	C_nH_{2n}	15	USA	4,000	$\bar{\nu}_e$	Turning on
SNO+	C_nH_{2n}	0.8	Canada	300	$\bar{\nu}_e$	Near future
MicroBooNE*	Ar	0.17	USA	17	ν_e	Near future
DUNE	Ar	34	USA	3,000	ν_e	Proposed
Hyper-Kamiokande	H_2O	560	Japan	110,000	$\bar{\nu}_e$	Proposed
JUNO	C_nH_{2n}	20	China	6000	$\bar{\nu}_e$	Proposed
RENO-50	C_nH_{2n}	18	Korea	5400	$\bar{\nu}_e$	Proposed
LENA	C_nH_{2n}	50	Europe	15,000	$\bar{\nu}_e$	Proposed
PINGU	Long string	(600)	South Pole	(10^6)	$\bar{\nu}_e$	Proposed

NS Puppis, and Sigma Canis Majoris.

3˙3.2. *Pointing to the supernova with neutrinos.* It is of clear value to know the position in the sky of the SN, for several reasons. First, obviously astronomers need to know where to look— given that the visible SN may not show up in electromagnetic wavelengths for some time, a direction will aid in observing the very early stages. Furthermore, it is not clear that the core collapse always results in a bright SN, and direction information will help to potentially locate a weak explosion, or even a vanished progenitor. Knowledge of distance to the progenitor is valuable for precise determination of neutrino luminosity. Knowledge of the direction will aid as well in interpretation of the signal itself, in that the specific matter effects undergone by the neutrino flux will depend on the pathlength through the Earth [230].

The ability of a detector to determine the direction of a signal depends both on the intrinsic anisotropy of the interaction, and on the capability of tracking the resulting products. CC and NC interactions with nuclei, including IBD, have some energy-dependent anisotropy (e.g., [245]), but this is generally relatively weak for the most important interactions. Elastic scattering of electrons is however fairly strongly peaked forward. The angular distribution of IBD and ES events for a simulated SN is shown in Fig. 19. Of the interactions relevant for current detectors, argon and oxygen interactions do have some potentially observable anisotropy (e.g., [246]).

Of the detector types currently available, Cherenkov and LAr tracking detectors are

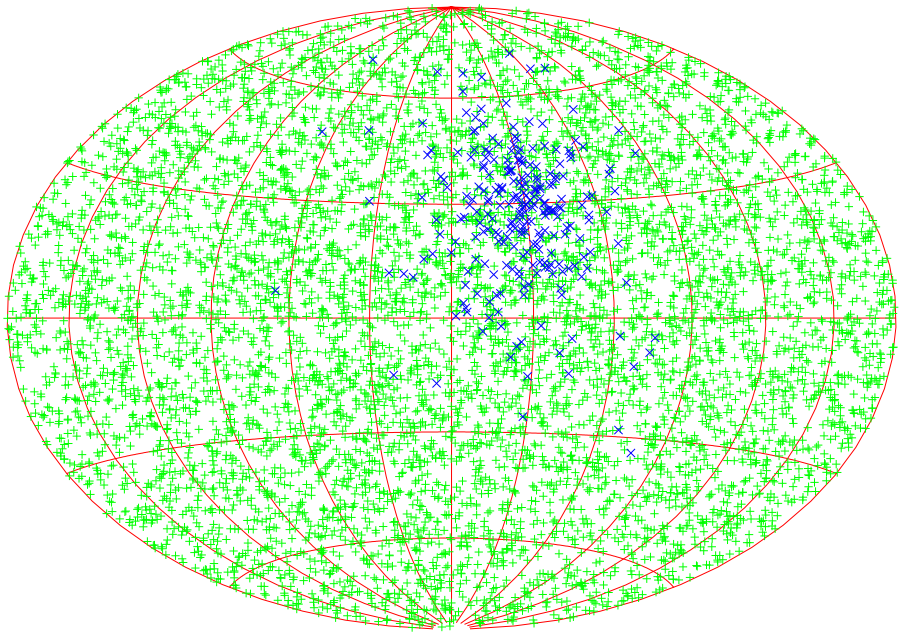

Fig. 19. – Angular distribution of IBD events (green) and ES events (blue) of one simulated SN. (Reprinted figure with permission from [248]; copyright (2003) by the American Physical Society.)

capable of determining the direction of charged particle tracks. Unfortunately scintillator produces mostly isotropic light with little chance of determining scattered particle direction (some information may be available from reconstructed relative positions of IBD-produced positron and neutron energy loss [247]). Of detectors currently running, Super-Kamiokande has the only plausible chance of determining the SN direction using ES events (which should constitute a few percent of the observed events). This ability should improve with addition of Gd by reducing the near-isotropic background of IBD events [248]. Hyper-Kamiokande's statistics would improve determination even further. LAr should also have decent pointing capabilities via lepton tracking.

Another potential method for source direction determination is via triangulation, using timing of several signals observed in different locations around the Earth [249, 250]. This is challenging, given that the spread over time of the burst is longer than the travel time through the Earth; therefore, detection statistics of the burst need to be such that a sharp feature of the signal, such as the risetime or other feature, can be determined. IceCube may be the best prospect for contributing to this kind of determination. With current detectors, triangulation in real time may be difficult, although with large future detectors prospects are more promising. Another possible pointing method is via the matter oscillation effect pattern, which might be possible to combine with timing information [251]. However this requires large statistics and good energy resolution, and is unlikely to do better than ES in a single directional detector.

3˙3.3. *Probing supernova hydrodynamical instabilities through neutrinos*. As discussed in Sec. **2**, the first hydrodynamical 3D SN simulations with sophisticated neutrino transport have recently become available. The more massive cases of the simulated SN progenitors (with 27 and 20 $M_\odot$ progenitor masses) show pronounced SASI phases interrupted by episodes of dominant convective overturn activity. The neutrino signal carries imprints of these hydrodynamical instabilities (see Fig. 5) and the detection of such modulations will therefore offer a unique chance to probe the core-collapse mechanism. It has been recently shown [87, 88] that measurements of neutrinos from a future Galactic SN with neutrino Cherenkov telescopes (i.e., IceCube and Hyper-Kamiokande, see Sec. **3˙2**) will indeed be able to discriminate the SASI neutrino modulation.

Figure 20 (top panel) shows the expected IceCube rate as a function of time for an observer located close to the SASI plane([7]) for a 3D SN simulation of a 27 $M_\odot$ star (see Sec. **2**). Large-amplitude sinusoidal modulations of the IceCube event rate signal appear in correspondence to the first SASI episode at 120–260 ms. After a phase where convective motions dominate, a second SASI episode begins at about 410 ms. Given our scarce knowledge of neutrino flavor oscillations in the presence of SASI, two extreme cases have been plotted: One in which flavor conversions have been neglected and therefore the signal is caused by the non-oscillated $\bar{\nu}_e$ (blue curve) and another one where complete flavor swap was assumed so that the signal is caused by $\bar{\nu}_x$ (red curve). Both cases exhibit large-amplitude signal modulations with clear periodicity.

The possibility to detect neutrino signal modulations depends on the viewing angle relative to the plane of the SASI sloshing or spiral motions. Observers located along the direction orthogonal to the plane of the first SASI episode will only detect very weak SASI modulations, as shown in the second panel of Fig. 20 (see also right panel of Fig. 5 for an estimation of the favorable locations of the observer with respect to the SASI plane); observers placed on opposite directions away from the source will detect almost the same signal modulations but with opposite phases.

The third panel of Fig. 20 shows the IceCube signal in 5 ms time bins, including a random shot noise realization, and the IceCube background fluctuations are plotted in black for comparison. For a SN up to 15 kpc, the SASI modulations in the neutrino signal will be clearly visible. The correspondent rate in a 560-kton water Cherenkov detector is plotted in the bottom panel of Fig. 20. A 560-kton water Cherenkov telescope will have no background in contrast to IceCube and it will be able to collect event-by-event energy information, but its expected rate should be about 1/5 of the IceCube one. Similar modulations of the neutrino signal due to SASI are also clearly detectable for the 20 $M_\odot$ SN progenitor [87, 88].

The Fourier power spectrum of the IceCube rate exhibits a prominent peak at about 80 Hz both for the 20 $M_\odot$ and the 27 $M_\odot$ SN progenitors. Such a frequency corresponds to the sloshing frequency of the shock front and is a function of the neutron star radius (similar for both progenitors as they were modeled with the same EoS) and of the shock radius (again comparable for both progenitors as their mass-infall history in the collapsing stellar core is fairly similar) [88].

In synthesis, the observation of SASI modulations by Cherenkov neutrino telescopes

([7]) Note that for all angular locations of the observer, the detected neutrino rate has been computed by integrating the neutrino emission emitted from the hemisphere facing the observer including projection effects associated with limb darkening. We refer the reader to Ref. [87] for details on the projection procedure.

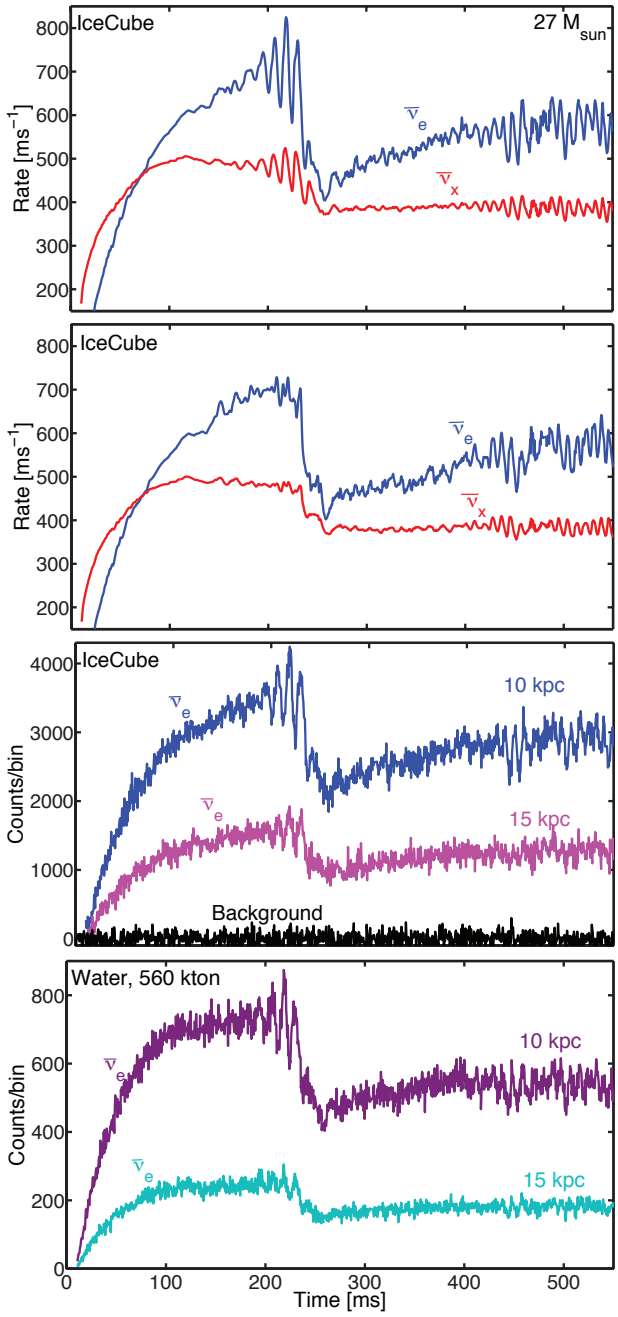

Fig. 20. – Detection rate in IceCube (three upper panels) and in a 560-kton WC detector (bottom panel) for a 27 $M_\odot$ SN progenitor at 10 kpc for $\bar{\nu}_e$ (no flavor conversions) and $\bar{\nu}_x$ (complete flavor swap). The observer direction is chosen close to the SASI plane during the first SASI episode (120–260 ms), where a strong modulation of the neutrino signal is expected, except for the second panel where a direction of minimal modulation of the neutrino signal is shown. The lower panels include a random shot-noise realisation in 5 ms bins; the IceCube background fluctuations in the absence of a SN are shown in black. (Figure adapted from [88].)

will provide a confirmation of our current theories of stellar core collapse. However, the possibility to discriminate SASI signatures will be dependent on the location of the observer relative to the plane where SASI sloshing or spiral motions develop.

3˙4. *Outlook*. – We are reasonably well prepared world-wide for the next SN burst, with a number of detectors online, of which Super-Kamiokande will give the largest event signal, and potentially provide pointing information. Additional scintillator detectors, some surface detectors, and a small lead detector, will enhance the yield, and IceCube will provide excellent burst time structure information. However, the current sensitivity is overwhelming for the $\bar{\nu}_e$ component of the flux. The planned next generation of very large detectors will provide even more abundant $\bar{\nu}_e$ statistics and, in addition, should also have broader flavor sensitivity via ν_e detection in argon, and high-statistics NC channels in water and scintillator. We look forward to recording the next burst with these enhanced capabilities.

A high-statistics detection of a Galactic SN ν burst would allow accurate studies of the signal in energy and time domains and in different interaction channels. In particular, we have shown how the observable SN ν light curve would carry interesting information concerning the explosion mechanism and the hydrodynamical instabilities occurring in the deepest SN regions. Moreover, by reconstructing the duration of the different phases of the ν burst one could have a direct empirical test for the predictions of the SN simulations. Furthermore, the duration of the neutrino signal is an important diagnostic parameter to constrain exotic energy-loss processes in a SN, associated with the emission of novel light weakly-interacting particles [13]. These would shorten the duration of the observable SN neutrino signal. Finally, the SN ν light curves and energy spectra would also carry intriguing signatures associated with the flavor conversions occurring in the deepest stellar regions, as we will discuss in the next Section.

4. – Supernova Neutrino Flavor Conversions

Authors: A. Mirizzi, N. Saviano, I. Tamborra, S. Chakraborty

In this Section, we will present an overview of the neutrino flavor transitions in core-collapse SNe. At first we introduce the equations of motion (EoMs) for SN neutrinos in the formalism of the density matrix, describing the vacuum, matter and ν-ν refractive terms entering the neutrino Hamiltonian. Then the phenomenology of self-induced flavor conversions, associated with the large ν-ν interaction potential, is illustrated through representative examples of its rich phenomenology. The Mikheyev-Smirnov-Wolfenstein (MSW) matter effects are also discussed as well as the impact of the SN shock-wave propagation and of matter turbulence on the neutrino conversion probabilities. Finally, observable signatures of the SN neutrino oscillations imprinted on the neutrino burst are characterized. Particular attention is devoted to the sensitivity of these observables to the unknown neutrino mass hierarchy.

4˙1. *Three-neutrino oscillation framework.* – There is compelling experimental evidence [252] that the three known active neutrino states with definite flavor ν_α ($\alpha = e, \mu, \tau$) are linear combinations of the mass eigenstates ν_i ($i = 1, 2, 3$), and that the Hamiltonian of neutrino propagation in vacuum [253-255] and matter [256] does not commute with flavor. The evidence for flavor non-conservation (i.e., "neutrino oscillations") comes from a series of experiments performed in about four decades of research with very different neutrino beams and detection techniques. Namely, the solar neutrino [257-259] experiments: Homestake [260], SAGE [261], GALLEX-GNO [262, 263], Kamiokande [264], Super-Kamiokande (SK) [265, 266], the Sudbury Neutrino Observatory (SNO) [267-269], and Borexino [270]; the long-baseline reactor-neutrino experiment KamLAND [271, 272]; the atmospheric neutrino experiments like Super-Kamiokande [273-275], MACRO [276], and Soudan-2 [277]; the long-baseline accelerator neutrino experiments: KEK-to-Kamioka (K2K) [278], MINOS [279], OPERA [280] and Tokai-to-Kamioka (T2K) [281, 282].

Except for yet controversial results from short-baseline neutrino experiments, that point towards the existence of extra sterile neutrino states [with $m \sim \mathcal{O}(1)$ eV] [283,284], all the data from the above experiments are consistent with the simplest extension of the standard electroweak model needed to accommodate nonzero neutrino masses and mixings. Namely, with a scenario where the three known flavor eigenstates $\nu_{e,\mu,\tau}$ are mixed with the three mass eigenstates $\nu_{1,2,3}$, through a unitary matrix U, which in terms of one-particle neutrino states $|\nu\rangle$, is defined as (see, e.g., [252])

$$|\nu_\alpha\rangle = \sum_{i=1}^{3} U^*_{\alpha i} |\nu_i\rangle \ . \tag{16}$$

A common parametrization for the matrix U is [285]:

$$U = \begin{pmatrix} 1 & 0 & 0 \\ 0 & c_{23} & s_{23} \\ 0 & -s_{23} & c_{23} \end{pmatrix} \begin{pmatrix} c_{13} & 0 & s_{13}e^{-i\delta} \\ 0 & 1 & 0 \\ -s_{13}e^{i\delta} & 0 & c_{13} \end{pmatrix} \begin{pmatrix} c_{12} & s_{12} & 0 \\ -s_{12} & c_{12} & 0 \\ 0 & 0 & 1 \end{pmatrix} \tag{17}$$

with $c_{ij} = \cos\theta_{ij}$ and $s_{ij} = \sin\theta_{ij}$, θ_{ij} being the mixing angles and $\delta \in [0, 2\pi]$ being the

CP-violating phase ([8]).

The current neutrino phenomenology implies that the three-neutrino mass spectrum $\{m_i\}_{i=1,2,3}$ is made by a "doublet" of relatively close states and by a third "lone" neutrino state, which may be either heavier than the doublet ("normal hierarchy," NH) or lighter ("inverted hierarchy," IH). Typically, the lightest (heaviest) neutrino in the doublet is called ν_1 (ν_2) and the corresponding mass squared difference is defined as

$$\delta m^2 = m_2^2 - m_1^2 > 0 \tag{18}$$

by convention. The δm^2 is traditionally named the *solar* mass squared difference. The lone state is then labeled as ν_3, and the physical sign of $m_3^2 - m_{1,2}^2$ distinguishes NH from IH. The second independent squared mass difference Δm^2, called also *atmospheric* mass squared difference, is

$$\Delta m^2 = \left| m_3^2 - \frac{m_1^2 + m_2^2}{2} \right| , \tag{19}$$

so that the two hierarchies (NH and IH) are simply related by the transformation $+\Delta m^2 \to -\Delta m^2$. Numerically, it results that $\delta m^2 \ll \Delta m^2$.

The latest solar, reactor and long-baseline neutrino oscillation analyses indicate the following $\pm 2\sigma$ ranges for each parameter (95% C.L.) taken from [286] (see also [287, 288] for other updated analyses)

$$\begin{aligned} \Delta m^2 &= (2.43^{+0.12}_{-0.13}) \times 10^{-3} \text{ eV}^2 , \\ \delta m^2 &= (7.54^{+0.46}_{-0.39}) \times 10^{-5} \text{ eV}^2 , \\ \sin^2\theta_{12} &= (3.08^{+0.17}_{-0.34}) \times 10^{-1}, \\ \sin^2\theta_{23} &= (4.37^{+1.15}_{-0.44}) \times 10^{-1} , \\ \sin^2\theta_{13} &= (2.34^{+0.40}_{-0.39}) \times 10^{-2} . \end{aligned} \tag{20}$$

Remarkably, the $1-3$ mixing angle θ_{13} has been the last one measured in 2012 by the Daya Bay [289] and RENO [290] reactor experiments. These recent measurements confirmed and greatly strengthened the significance of early hints suggested by the long-baseline ν_μ-ν_e experiments T2K [291] and MINOS [292] as well as by the Double Chooz reactor experiment [293], especially when analyzed in combination with other oscillation data [294, 295]. The measurement of a "large" value of θ_{13} has siginifcantly reduced the ambiguity in characterizing the oscillated SN neutrino oscillations. Notably, the latest global analysis hints towards a non-zero CP-violation around $\delta \sim 1.4\pi$ at $\gtrsim 1\sigma$ level [286], see also [287, 288] ([9]).

Within the three-neutrino scenario, the most important unsolved problems require probing the CP-violating phase δ, the mass hierarchy, and the absolute neutrino masses.

([8]) We neglect here extra-phases possible if neutrinos are Majorana particles, since they are not relevant in oscillations.

([9]) It has been shown that in the context of SN neutrino oscillations, CP-violation effects are negligible [296-298]. Therefore, we will not include them in the following discussion.

In this context, a high–statistics detection of Galactic SN neutrinos could give a unique help to solve some of these open issues.

4˙2. *Equations of motion for supernova neutrinos.* – The treatment of neutrino mixing is well understood in terms of the propagation of a beam of particles in vacuum or in a medium, and neutrino flavor transitions have been described by means of a Schrödinger-like equation [299]. Neutrinos free streaming beyond the neutrinosphere also interact among themselves (*neutrino self-interactions*). As pointed out in seminal papers [163,300-314], in the deepest regions of a SN (as well as in the Early Universe) the neutrino gas is so dense that neutrinos themselves form a background medium leading to intriguing non-linear effects in the flavor distribution. Neutrino-neutrino interactions could trigger large *self-induced* flavor conversions in the deepest SN regions [2, 3]. Under these circumstances, neutrinos emitted with different energies would be locked to oscillate in a collective fashion.

A natural treatment to properly characterize the flavor evolution in this situation requires the formalism of the neutrino density matrix [315]

$$\varrho_{\mathbf{p},\mathbf{x}} = \begin{pmatrix} \varrho_{ee} & \varrho_{e\mu} & \varrho_{e\tau} \\ \varrho_{\mu e} & \varrho_{\mu\mu} & \varrho_{\mu\tau} \\ \varrho_{\tau e} & \varrho_{\tau\mu} & \varrho_{\tau\tau} \end{pmatrix} \ . \tag{21}$$

The diagonal entries of this matrix are the usual occupation numbers, whereas the off-diagonal terms encode phase information related to the oscillations. An analogous expression holds for the antineutrino density matrix, $\overline{\varrho}_{\mathbf{p},\mathbf{x}}$. See also [316-320] for similar derivations and [321-324] for recent developments on the formalism.

In SNe one is concerned with the spatial evolution of the neutrino fluxes in a quasi-stationary situation. Therefore, the matrices $\varrho_{\mathbf{p},\mathbf{x}}$ do not explicitly depend on time, so that the EoMs reduce to the Liouville term involving only spatial derivatives [315, 322]

$$\begin{aligned} \mathbf{v}_{\mathbf{p}} \cdot \nabla_{\mathbf{x}} \varrho_{\mathbf{p},\mathbf{x}} &= -i[\Omega^{\rm vac}_{\mathbf{p}}, \varrho_{\mathbf{p},\mathbf{x}}] - i[\Omega^{\rm ref}_{\mathbf{p},\mathbf{x}}, \varrho_{\mathbf{p},\mathbf{x}}] \ , \\ \mathbf{v}_{\mathbf{p}} \cdot \nabla_{\mathbf{x}} \overline{\varrho}_{\mathbf{p},\mathbf{x}} &= +i[\Omega^{\rm vac}_{\mathbf{p}}, \overline{\varrho}_{\mathbf{p},\mathbf{x}}] - i[\Omega^{\rm ref}_{\mathbf{p},\mathbf{x}}, \overline{\varrho}_{\mathbf{p},\mathbf{x}}] \ . \end{aligned} \tag{22}$$

In the flavor basis the first term in the Hamiltonian at the right-hand-side (r.h.s.) of Eq. (22) for ultrarelativistic neutrinos represents the vacuum oscillation term,

$$\Omega^{\rm vac}_{\mathbf{p}} = U \frac{M^2}{2p} U^\dagger \ . \tag{23}$$

The U matrix describes the mixing [Eq. (17)] and M^2 is the squared mass matrix which, except for a common term proportional to the identity matrix and irrelevant for oscillations, is parametrized, in terms of the solar δm^2 [Eq. (18)] and atmospheric Δm^2 [Eq. (19)] mass-squared differences, as [285]

$$M^2 = {\rm diag}\left(m_1^2, m_2^2, m_3^2\right) = \left(-\frac{\delta m^2}{2}, +\frac{\delta m^2}{2}, \pm \Delta m^2\right) \ . \tag{24}$$

The sign $\pm$ in front of Δm^2 refers to NH (+) and IH (-), respectively. One can associate two vacuum oscillation frequencies to these mass-squared differences, i.e.,

$$\omega_L = \frac{\delta m^2}{2E} \ \text{and} \ \omega_H = \frac{\Delta m^2}{2E} \ . \tag{25}$$

The vacuum energy can be affected by a shift (similar to the photon index of refraction) when neutrinos propagate in a medium. This effect is induced by their forward scatterings with the medium constituents [299]. The refractive effect for SN neutrinos is described by the second term in the Hamiltonian at the r.h.s. of Eq. (22)

$$\Omega^{\rm ref}_{\mathbf{p},\mathbf{x}} = \lambda_{\mathbf{x}}\mathsf{L} + \sqrt{2}\,G_{\rm F}\int \frac{d^3\mathbf{q}}{(2\pi)^3}\left(\varrho_{\mathbf{q},\mathbf{x}} - \overline{\varrho}_{\mathbf{q},\mathbf{x}}\right)(1 - \mathbf{v}_{\mathbf{q}}\cdot\mathbf{v}_{\mathbf{p}})\,. \tag{26}$$

The first term at the r.h.s. in Eq. (26) represents the ordinary refractive matter effect. In particular, for typical energies of SN neutrinos [$E \sim \mathcal{O}(10)$ MeV] the only relevant process is due to charged-current interactions of electron neutrinos ν_e (or antineutrinos $\bar{\nu}_e$) with the background $e^{\pm}$ (the neutral current is flavor conserving and therefore equal for all neutrino flavors). This is the well-known MSW effect, first pointed out by Wolfenstein, and by Mikheyev and Smirnov [256]. This term is represented by $\lambda_{\mathbf{x}} = \sqrt{2}\,G_{\rm F}(n_{e^-} - n_{e^+})$ with $\mathsf{L} = \mathrm{diag}(1,0,0)$ in the weak interaction basis.

Neutrino-neutrino interactions, dominant in the deepest SN regions, make an additional contribution to the refractive energy shift, represented by the second term at the r.h.s. of the Eq. (26). This term is proportional to the neutrino density matrix $\varrho_{\mathbf{p},\mathbf{x}}$ that in the presence of mixing has also off-diagonal elements, giving rise to "off-diagonal refractive indices" as first pointed out by Pantaleone [300-302]. The main complication in the ν-ν refractive term for SN neutrinos is the angular factor $(1 - \mathbf{v}_{\mathbf{q}}\cdot\mathbf{v}_{\mathbf{p}}) = (1 - \cos\theta_{\mathbf{pq}})$ coming from the current-current nature of the weak interactions, where $\mathbf{v}_{\mathbf{p}} = \mathbf{p}/p$ is the neutrino velocity. This angular term averages to zero for an isotropic ν gas. However, for the non-isotropic neutrino emission from the SN core this velocity-dependent term would not average to zero, producing a net current that leads to a different refractive index for neutrinos that propagate on different trajectories. This is at the origin of the so-called "multi-angle effects" [3, 325-327]. Remarkably, while in an isotropic neutrino gas the self-induced effects would lead to a collective behavior in the flavor evolution [4], in an anisotropic case this is not guaranteed. Indeed the multi-angle term in some cases challenges the collective behavior of the flavor evolution, leading to *flavor decoherence* under certain conditions, with a resultant flux equilibration among electron and non-electron (anti)neutrino species [325-327].

The multi-angle flavor evolution described by the partial differential equations, Eq. (22), has not been solved in its full complexity until now. However, a few years ago the first large-scale multi-angle simulations were developed within the so-called *"bulb model"* [2, 5, 326], whose geometry is represented in Fig. 21. In this framework it is assumed that neutrinos are emitted uniformly and half-isotropically (i.e., with all the outward-going modes occupied, and all the backward going modes empty) from the surface of a spherical neutrinosphere, like in a blackbody. Moreover, it is assumed that there is azimuthal symmetry of the neutrino emission at the neutrinosphere and that all the physical conditions in the star only depend on the distance r from the center of the star.

Under the assumption of azimuthal symmetry, one can reduce the general partial differential equations [Eq. (22)] into ordinary differential equations, projecting the evolution along the radial direction. Then

$$\begin{aligned} \mathbf{v}_{\mathbf{p}}\cdot\nabla_{\mathbf{x}} &\to v_r\frac{d}{dr}\ , \\ \mathbf{p} &\to (E \simeq |\mathbf{p}|, u \equiv \sin^2\theta_R)\ , \\ \varrho_{\mathbf{p},\mathbf{x}} &\to \varrho_{p,u,r}\ , \end{aligned} \tag{27}$$

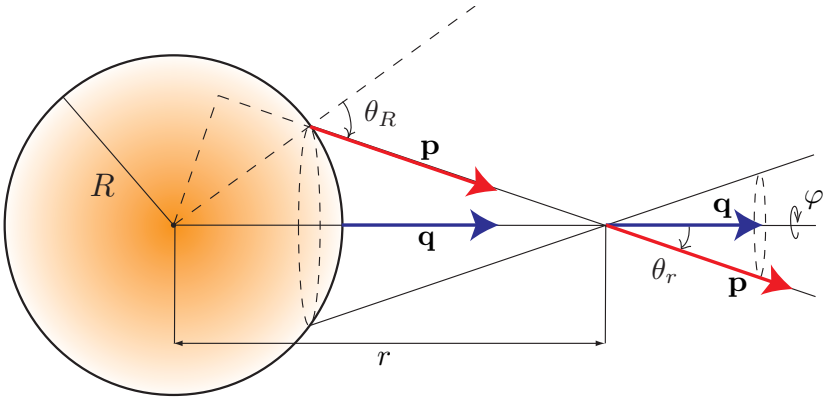

Fig. 21. – Geometrical picture of the neutrino bulb model. Courtesy of A. Marrone.

where θ_R is the emission angle relative to the radial direction at the neutrinosphere, $r = R$.

The distribution matrices $\varrho_{p,\theta,r}$ (or $\varrho_{p,u,r}$) are not especially useful to describe a spherically symmetric system because they vary with radius even in absence of oscillations. A quantity that is conserved in absence of oscillations is the total flux matrix [326]

$$\mathsf{J}_r = 4\pi r^2 \int \frac{d^3\mathbf{p}}{(2\pi)^3} \varrho_{p,\theta,r} v_r \ , \tag{28}$$

that in terms of $\varrho_{p,u,r}$ reads

$$\mathsf{J}_r = \int_0^\infty dp \int_0^1 du \ \mathsf{J}_{p,u,r} = \int_0^\infty dp \int_0^1 du \ \frac{\varrho_{p,u,r} p^2 R^2}{2\pi} \ . \tag{29}$$

This implies that the trace of $\mathsf{J}_{p,u,r}$ is r-independent. For the sake of brevity, we address the interested reader to [326] for the explicit form of the EoMs for the $\mathsf{J}_{p,u,r}$ matrices.

4˙3. *Polarization vectors and equations of motion for a* 2ν *system.* – Often SN neutrino flavor evolution can be characterized in a 2ν flavor scenario, associated with Δm^2 and θ_{13}, in which the electron state ν_e mixes with the non-electron one ν_x. We will comment later about possible three-flavor effects associated with δm^2 and θ_{12} [328, 329].

In the 2ν framework, one can expand the 2×2 matrices in the EoMs in terms of the unit matrix I and the Pauli matrices $\boldsymbol{\sigma}$. One can introduce polarization vectors $\mathbf{P}_{p,u,r}$ from the expansion of the flux matrices $\mathsf{J}_{p,u,r}$. One of the possible definitions suitable in the SN context is the following [326]

$$\mathsf{J}_{p,u,r} = \frac{F(\nu_e)_{p,u} + F(\nu_x)_{p,u}}{2} + \frac{F(\bar{\nu}_e) - F(\bar{\nu}_x)}{2} \mathbf{P}_{p,u,r} \cdot \boldsymbol{\sigma} \ ,$$

$$\overline{\mathsf{J}}_{p,u,r} = \frac{F(\bar{\nu}_e)_{p,u} + F(\bar{\nu}_x)_{p,u}}{2} + \frac{F(\bar{\nu}_e) - F(\bar{\nu}_x)}{2}\overline{\mathbf{P}}_{p,u,r}\cdot\boldsymbol{\sigma} \ , \tag{30}$$

where the quantities $F(\nu_\alpha)_{p,u}$ are the number flux of ν_α emitted from the neutrinosphere with energy $E = |\mathbf{p}|$ and emission angle $u = \sin^2\theta_R$. The total number flux of flavor α is a simple integral $F(\nu_\alpha) = \int dp \int du F(\nu_\alpha)_{p,u}$. Note that the normalization of the second term in Eq. (30) is the same for ν and $\bar{\nu}$ and it is the difference between the $\bar{\nu}_e$'s and $\bar{\nu}_x$'s fluxes. We factorize the flux of each flavor as $F(\nu_\alpha)_{p,u} = N_{\nu_\alpha} \times f_{\nu_\alpha}(p) \times \varphi_{\nu_\alpha}(u)$. The ν number $N_{\nu_\alpha} = L_{\nu_\alpha}/\langle E_{\nu_\alpha}\rangle$ is expressed in terms of the ν luminosity L_{ν_α} and of the ν average energy $\langle E_{\nu_\alpha}\rangle$ of the different species. The function $f_{\nu_\alpha}(p)$ is the normalized neutrino energy spectrum ($\int dp f_{\nu_\alpha}(p) = 1$). An example of a quasi-thermal energy spectrum, widely used in SN literature is given in Eq. (9). Finally, $\varphi_{\nu_\alpha}(u)$ represents the ν angular distribution that we assume flat in u and flavor and energy independent, i.e. $\varphi_{\nu_\alpha}(u) = 1$.

One can expand the other quantities in Eqs. (22)-(23)-(26) as

$$\begin{aligned} \Omega^{\rm vac}_{\mathbf{p}} &= \tfrac{1}{2}\left(\omega_0 \mathsf{I} + \omega_{\mathbf{p}}\,\mathbf{B}\cdot\boldsymbol{\sigma}\right), \\ \mathsf{L} &= \tfrac{1}{2}\left(\mathsf{I} + \mathbf{L}\cdot\boldsymbol{\sigma}\right), \end{aligned} \tag{31}$$

where $\omega_0 = m^2_{1,2} + m^2_3$, and the vacuum oscillations are determined by the mass difference Δm^2 and vacuum mixing angle θ_{13} [4]:

$$\begin{aligned} \omega_{\mathbf{p}} &= \Delta m^2/2p\,, \\ \mathbf{B} &= (\sin 2\theta_{13}, 0, \mp\cos 2\theta_{13}) \ , \end{aligned} \tag{32}$$

with the upper (lower) sign refers to normal (inverted) mass hierarchy. For small θ_{13}, $\mathbf{B} \simeq \mp\mathbf{z}$. Moreover, in an ordinary medium composed by electrons and positrons, $\mathbf{L} = \mathbf{e}_z$.

Using the definition of Eqs. (30)–(32) one can write the EoMs [Eq. (22)] for the polarization vectors [326]

$$\begin{aligned} \partial_r \mathbf{P}_{p,u,r} = &\left[\frac{1}{v_{r,u}}(\omega_p \mathbf{B} + \lambda_r \mathbf{L})\right. \\ &\left. + \mu_r \int dq \int du' (\mathbf{P}_{q,u',r} - \overline{\mathbf{P}}_{q,u',r})\left(\frac{1}{v_{r,u}v_{r,u'}} - 1\right)\right] \times \mathbf{P}_{p,u,r} \ , \\ \partial_r \overline{\mathbf{P}}_{p,u,r} = &\left[\frac{1}{v_{r,u}}(-\omega_p \mathbf{B} + \lambda_r \mathbf{L})\right. \\ &\left. + \mu_r \int dq \int du' (\mathbf{P}_{q,u',r} - \overline{\mathbf{P}}_{q,u',r})\left(\frac{1}{v_{r,u}v_{r,u'}} - 1\right)\right] \times \overline{\mathbf{P}}_{p,u,r} \ , \end{aligned} \tag{33}$$

where we introduced the self-interaction potential

$$\mu_r = \sqrt{2} G_F \frac{F(\bar{\nu}_e) - F(\bar{\nu}_x)}{4\pi r^2} \ , \tag{34}$$

and the radial neutrino velocity

$$v_{u,r} = \cos\theta_r = \sqrt{1 - u\left(\frac{R}{r}\right)^2} \ . \tag{35}$$

The initial conditions for the polarization vectors at the neutrinosphere are the following

$$P^z_{p,u}(R) = \frac{F(\nu_e)_{p,u} - F(\nu_x)_{p,u}}{F(\bar{\nu}_e) - F(\bar{\nu}_x)} \ ,$$
$$\overline{P}^z_{p,u}(R) = \frac{F(\bar{\nu}_e)_{p,u} - F(\bar{\nu}_x)_{p,u}}{F(\bar{\nu}_e) - F(\bar{\nu}_x)} \ . \quad (36)$$

The presence of the trajectory-dependent factor $v_{u,r}$ in the neutrino-neutrino interaction term in Eq. (33) leads to the multi-angle effects in the self-induced oscillations. In this regard, it has been understood [325] that the flavor asymmetry is crucial to assess the impact of multi-angle effects. In particular, in the presence of a sufficiently large flux hierarchy among different species, multi-angle decoherence would be suppressed.

4˙3.1. *Matter suppression of self-induced flavor conversions*. Remarkably also the matter term in Eq. (33) is affected by multi-angle effects due to the factor $v_{u,r}$. It has been shown in [330] that matter effects play a sub-dominant role in the development of self-induced flavor conversions when

$$n_{e^-} - n_{e^+} \ll n_{\bar{\nu}_e} - n_{\bar{\nu}_x} \ . \quad (37)$$

Conversely, if $n_{e^-} - n_{e^+} \gg n_{\bar{\nu}_e} - n_{\bar{\nu}_x}$, the multi-angle matter effects could produce a large spread in the oscillation frequencies for neutrinos travelling on different trajectories, blocking the self-induced flavor conversions. Finally, when $n_{e^-} - n_{e^+} \sim n_{\bar{\nu}_e} - n_{\bar{\nu}_x}$, matter-induced multi-angle decoherence in the neutrino ensemble may occur. According to realistic SN models, the matter density is expected to dominate over the neutrino one during the early accretion phase (see Sec. **4˙**4). In this situation, dedicated studies have been performed in [331-336] using inputs from recent hydrodynamic SN simulations. It has been found that the large matter term inhibits the development of collective oscillations at early times for iron-core SNe. Only in the case of low-mass O-Ne-Mg SNe, where the matter density is never larger than the neutrino one, the matter suppression is not complete and partial self-induced flavor conversions are possible at early times [331, 332, 336].

The matter suppression of self-induced effects for iron-core SNe makes relatively easy the prediction of the oscillation effects during the accretion phase, since the neutrino fluxes will be processed by the only MSW matter effects. As a consequence, as we will discuss in Sec. **4˙**11, the detection of the SN neutrino signal at early times is particularly relevant for the mass hierarchy discrimination. Nevertheless, for all types of SN progenitors self-induced effects still remain crucial during the later cooling phase, when the matter density decreases continuously (at post-bounce times $t_{\rm pb} \gtrsim 1$ s) and becomes sub-dominant with respect to the neutrino density.

As final caveat, we remark that the matter suppression of collective oscillations studied in [331-336] has been characterized referring to spherically symmetric one-dimensional SN models. However, as discussed in Sec. **2**, large deviations from a spherical neutrino emission can be generated by hydrodynamical instabilities such as SASI or LESA especially during the accretion phase. Before the explosion sets in, during the standing-accretion-shock phase, the recently discovered LESA instability [98] is responsible for a neutrino lepton number flux emerging primarily in one hemisphere (see Sec. **2**). The asymmetry between ν_e and $\bar{\nu}_e$ can be very small and even negative in some regions of the star, becoming potentially responsible for flavor instabilities [326]. LESA also influences

the electron density and therefore the matter background felt by neutrinos. Moreover, the neutrino flavor ratio can also be affected by SASI that seems to coexist with LESA in more massive SN progenitors (see Sec. **2**) and that is responsible for wild shock oscillations and a time-dependent directional bias of the neutrino emission. Exploratory work conducted within a simplified setup [337] confirmed the suppression of flavor conversions within the shock front radius in the presence of LESA. However, such results need to be tested within a more realistic scenario and in the presence of SASI. Besides the relevance for phenomenological purposes, the confirmation of the possible suppression of self-induced flavor conversions will also be crucial for the modeling of the neutrino propagation in the hydrodynamical SN simulations.

4˙4. *Supernova potential profiles.* – Before discussing the solution of the neutrino EoMs for the dense SN neutrino gas, we find it worthwhile to show snapshots of the interaction potentials appearing in the r.h.s. of Eq. (33) in Fig. 22. We use the data from a 27 $M_\odot$ SN simulation for different post-bounce times (see Sec. **2**). As from Eq. (34), the neutrino-neutrino potential is

$$\begin{aligned}\mu_r &= \sqrt{2}G_F\frac{F(\bar\nu_e)-F(\bar\nu_x)}{4\pi r^2} = \frac{1}{4\pi r^2}\left(\frac{L_{\bar\nu_e}}{\langle E_{\bar\nu_e}\rangle}-\frac{L_{\bar\nu_x}}{\langle E_{\bar\nu_x}\rangle}\right)\\ &= 7.0\times10^5\ \text{km}^{-1}\left(\frac{L_{\bar\nu_e}}{\langle E_{\bar\nu_e}\rangle}-\frac{L_{\bar\nu_x}}{\langle E_{\bar\nu_x}\rangle}\right)\frac{15\ \text{MeV}}{10^{52}\ \text{erg/s}}\left(\frac{10\ \text{km}}{r}\right)^2\ ,\end{aligned} \tag{38}$$

where the number fluxes of the different species ν_α are expressed in terms of the neutrino luminosities L_{ν_α} and of the average energies $\langle E_{\nu_\alpha}\rangle$. As shown in Fig. 22, the ν-ν potential decreases as the SN cools.

Matter effects on SN neutrinos [Eq. (33)] depend on the potential

$$\lambda_r = \sqrt{2}G_F n_e(r) = 1.9\times10^6\ \text{km}^{-1}\times\left(\frac{Y_e}{0.5}\right)\left(\frac{\rho}{10^{10}\ \text{g/cm}^3}\right)\ , \tag{39}$$

encoding the net electron density $n_e \equiv n_{e^-} - n_{e^+}$, where $Y_e = Y_{e^-} - Y_{e^+}$ is the net electron fraction and ρ is the matter density. The numerical values of μ_r and λ_r from the previous two expressions are quoted in km^{-1}.

Figure 22 shows that the SN electron density profile is non-monotonic, time-dependent, and presents an abrupt discontinuity, corresponding to the position of the *forward shock-front*. In fact, the shock-wave, while propagating outwards at supersonic speed, leaves behind a rarefaction zone, and creates a high-density front with a sharp density drop (down to the static value) at ([10])

$$r_{\text{fwd}} = \text{forward shock radius}\ . \tag{40}$$

We also note that additional features can appear such as the *reverse* shock propagation [338]. For example, after the explosion, a neutrino-driven baryonic wind can develop

([10]) Note that in hydrodynamical simulations, like the ones shown in Fig. 22, the forward shock-front is typically softened because of the limited numerical resolution. Therefore it has to be steepened by hand when adopted for studying the neutrino flavor evolution.

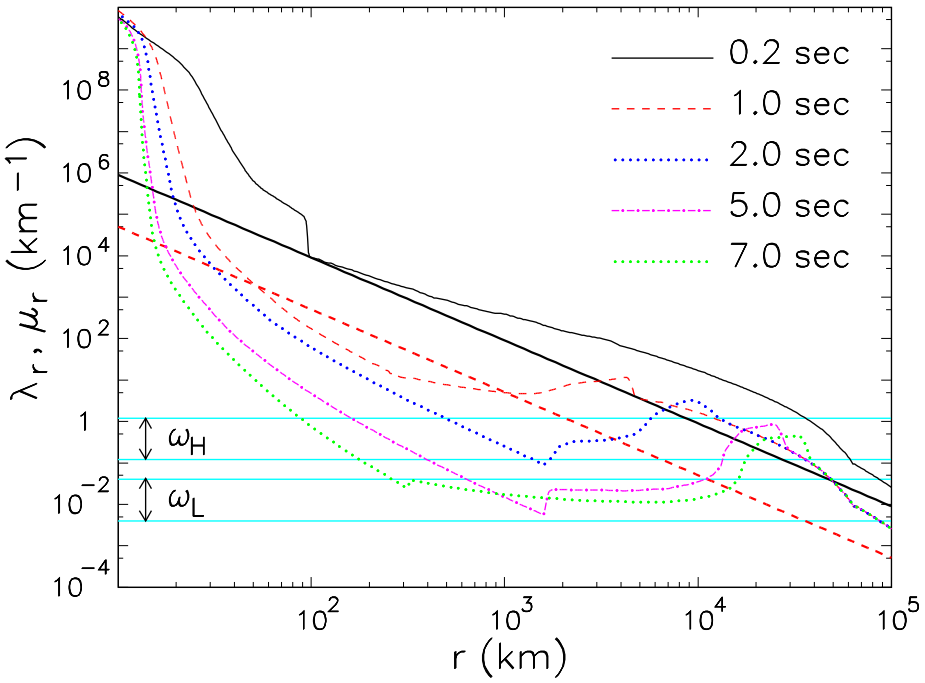

Fig. 22. – Snapshots of SN potentials for different post-bounce times (1.0 − 7.0 s) for a 27 $M_\odot$ SN progenitor (see Sec. **2**). The profile at 0.2 s is an illustrative case for a typical condition before shock revival. The matter potential λ_r is drawn with thin curves, while the neutrino potential μ_r with thick ones. The horizontal bands represent the vacuum oscillation frequencies relevant for the MSW resonant conversions associated with Δm^2 (ω_H) and δm^2 (ω_L), respectively (see the text for details).

and collide with the (slower) SN ejecta, thus triggering a second (reverse) shock at

$$r_{\rm rev} = \text{reverse shock radius} \ , \tag{41}$$

which propagates (at lower velocity) behind the forward one [338]. Neutrinos may thus encounter two subsequent density discontinuities, leading to significantly different spectral features with respect to the case of a single discontinuity.

One expects that the matter term would lead to *resonant* flavor conversions via the MSW effect [256] when the matter potential is of the order of the vacuum oscillation frequencies [Eq. (25)] $\omega_{H,L}$ [339], i.e.

$$\lambda_r \simeq \omega_{L,H} \ . \tag{42}$$

These oscillation frequencies are represented by the two horizontal strips in Fig. 22 for a neutrino energy range $E \in [5 - 50]$ MeV. Note that resonant flavor conversions should be expected for $r \in [10^3, 10^5]$ km.

Comparing the neutrino and matter density profiles, we realize that in the deepest SN regions $n_\nu \gg n_e$ ($r < 10^3$ km, see $t = 1.0$ s in Fig. 22), except during the accretion

phase ($t = 0.2$ s in Fig. 22). When the neutrino density dominates over the matter one (as during the cooling phase), self-induced flavor conversions would develop without any hindrance. This schematic investigation suggests that intriguing effects should be expected in the SN neutrino flavor evolution, with an interplay between self-induced and matter terms. Moreover, self-induced oscillations usually develop at lower r than the MSW flavor conversions, so that their effects effects could be studied separately for this progenitor.

4˙5. *Self-induced flavor conversions: Single-angle approximation.* – In order to simplify the numerical treatment of the EoMs [Eq. (33)] and to develop analytical interpretations of neutrino self-interactions, it has been often adopted in the literature the so-called *"single-angle"* approximation [2, 5, 326]. The main idea is to assume a single angular mode representative of all the neutrino ensemble. For a blackbody emission, in which all of the angular modes are equally occupied, it is natural to take neutrinos emitted at $\theta_R = \pi/4$ (i.e., $u_0 = 0.5$) as the representative ones ([11]). In this case, there is no integration over u and all the radial velocities appearing in the EoMs are set to

$$v_{r,u_0} = \sqrt{1 - \frac{R^2}{2r^2}} \ . \tag{43}$$

The EoMs in the single-angle approximation read

$$\begin{aligned} \partial_r \mathbf{P}_p &= [+\omega_p \mathbf{B} + \lambda_r \mathbf{L} + \mu_r^* \mathbf{D}] \times \mathbf{P}_p \ , \\ \partial_r \overline{\mathbf{P}}_p &= [-\omega_p \mathbf{B} + \lambda_r \mathbf{L} + \mu_r^* \mathbf{D}] \times \overline{\mathbf{P}}_p \ , \end{aligned} \tag{44}$$

where the self-interaction term only depends on the radial neutrino self-interaction strength

$$\mu_r^* = \sqrt{2} G_F \frac{F(\bar{\nu}_e) - F(\bar{\nu}_x)}{4\pi R^2} \frac{R^4}{2r^4} \frac{1}{1 - \frac{R^2}{2r^2}} = \mu_r \frac{R^2}{2r^2} \frac{1}{1 - \frac{R^2}{2r^2}} \ , \tag{45}$$

that at large distances from the core declines as $\mu_r^* \sim R^4/2r^4$, and on the difference of the total polarization vectors $\mathbf{D} = \mathbf{P} - \overline{\mathbf{P}}$, where $\mathbf{P} = \int dp \mathbf{P}_p$ (and analogously for $\overline{\mathbf{P}}$). In order to simplify the notation we remove the subscript r in the polarization vectors.

Assuming that self-induced effects are not suppressed by the multi-angle effects associated with a dominant matter term, it has been shown that in the single-angle approximation, when $\lambda_r \gg \omega_p$, the EoMs can be studied in a co-rotating frame with angular velocity $\lambda_r \mathbf{L}$ [4-6]. After this rotation, the only notable matter effect would be the suppression of the in-medium mixing angle with respect to the vacuum one.

The EoMs [Eq. (44)] for $\lambda_r = 0$ imply conservation of the scalar product

$$\mathbf{D} \cdot \mathbf{B} = \text{const} = \mathbf{D}^i \cdot \mathbf{B} \simeq \mp \mathbf{D}^i \cdot \mathbf{z} = \mp \frac{F_{\nu_e} - F_{\overline{\nu}_e}}{F_{\overline{\nu}_e} - F_{\overline{\nu}_x}} \equiv \mp \epsilon \ , \tag{46}$$

where ϵ indicates the flavor asymmetry. Equation (46) corresponds to the conservation of the lepton number [4], and implies *pair conversions* $\nu_e \overline{\nu}_e \to \nu_x \overline{\nu}_x$ [4]. In the co-rotating frame $\mathbf{D} \cdot \mathbf{L}$ is the corresponding conserved quantity.

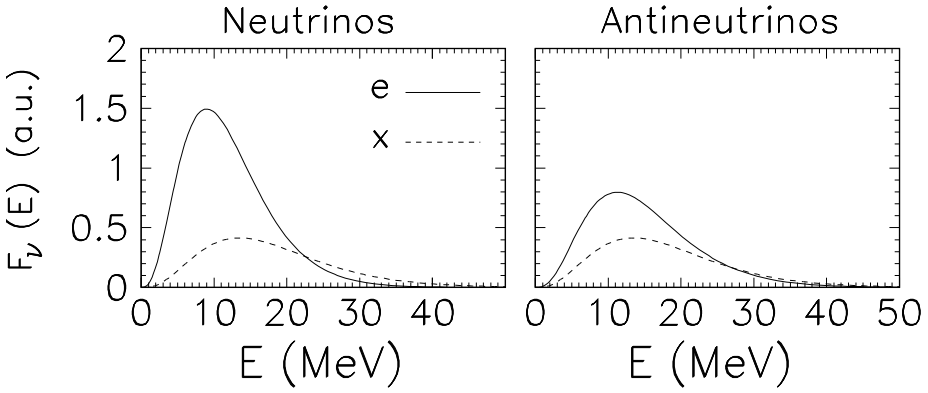

Fig. 23. – Initial SN neutrino and antineutrino fluxes with $F^0_{\nu_e} : F^0_{\bar{\nu}_e} : F^0_{\nu_x} = 2.40 : 1.60 : 1.0$. Neutrinos are plotted in the panel on the left, while antineutrinos are on the right panel. Electron species (e) are plotted with continuous curves, while non-electron species ($x = \mu, \tau$) with dashed curves.

4˙6. *Synchronized vs. bipolar oscillations and spectral splits*. – We will start to characterize the SN neutrino flavor conversion phenomenology, first discussing self-induced effects associated with the neutrino-neutrino interactions in the single-angle approximation [Eq. (44)]. Assuming to be in a co-rotating frame such that $\lambda_r = 0$ (see Sec. **4˙5**), the EoMs for the flavor evolution of the dense SN neutrino gas, even in the single-angle approximation, present a rich phenomenology since neutrino-neutrino interactions are strongly dependent on the ordering and hierarchy of the SN neutrino fluxes of the different species. Since the ordering of the SN fluxes changes significantly during the different post-bounce phases, one should expect a rich phenomenology as a function of the time after the bounce [2, 5, 329, 341-345].

In this Section, we take as illustrative example a "classical" case, where the flavor dynamics of the polarization vectors under the self-induced effects is analytically well-understood through an analogy with a *gyroscopic pendulum in flavor space* [4-6, 346]. This behavior is realized for cases presenting a large excess of electron neutrinos over non-electron species, i.e. $F^0_{\nu_e} \gg F^0_{\bar{\nu}_e} \gg F^0_{\nu_x}$ (as expected, e.g., during the accretion phase). In the pendulum analogy, the generic motion of the polarization vectors in flavor space is a combination of nutation and precession. The neutrino-antineutrino asymmetry ϵ [Eq. (46)] acts as a "spin" for the system with a large asymmetry inducing a precession-like motion around $\omega_p \mathbf{B}$, leaving only the nutation motion when the asymmetry is vanishing [4]. The role of the inertia moment in the pendulum analogy is played by the inverse strength of neutrino-neutrino interaction μ^*_r [Eq. (45)]. The neutrino mass hierarchy sets the behavior of the system. In NH, the pendulum starts in downward (stable) position and, assuming a small mixing angle, stays nearby, i.e. only manifests small flavor changes. Conversely, the pendulum starts in upward (unstable) position in IH—the misalignment being of $\mathcal{O}(\theta_{13})$—and it is subject to the maximal flavor reversal *pair-conversions* $\nu_e\overline{\nu}_e \to \nu_x\overline{\nu}_x$ [4], that conserve the lepton number [Eq. (46)].

([11]) A formal derivation of the single-angle approximation has been presented in [340].

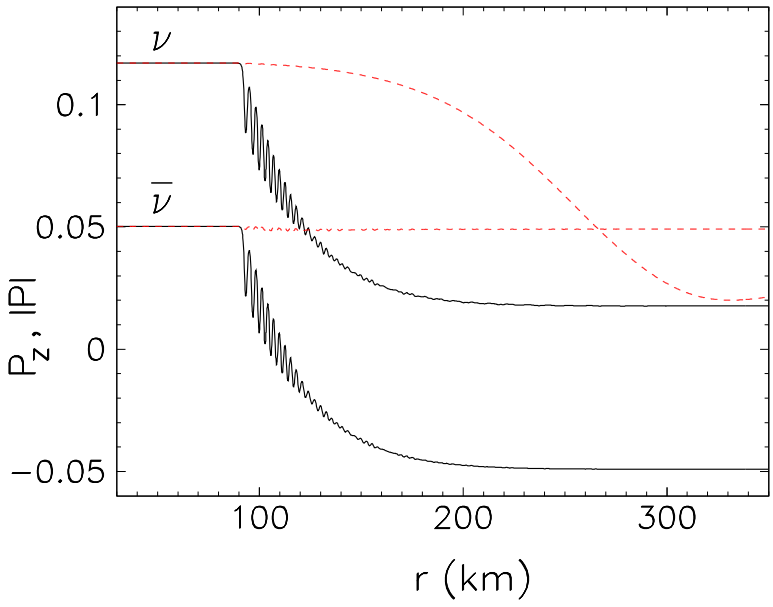

Fig. 24. – Single-angle simulation in inverted mass hierarchy for an initial flux ordering $F^0_{\nu_e} : F^0_{\overline{\nu}_e} : F^0_{\nu_x} = 2.40 : 1.60 : 1.0$. Modulus (dashed curves) and z-component of the global polarization vector (continuous curves) of neutrinos ($\mathbf{P}$) and antineutrinos ($\overline{\mathbf{P}}$), as a function of radius.

It has been shown that large flavor asymmetry could block possible multi-angle decoherence effects [326]. Therefore, the single-angle approximation is well justified in this case [5,347]. Figure 23 shows an example of this flux configuration, obtained considering representative neutrino fluxes with the following spectral ordering at the neutrinosphere: $F^0_{\nu_e} : F^0_{\overline{\nu}_e} : F^0_{\nu_x} = 2.40 : 1.60 : 1.0$.

In order to illustrate the self-induced flavor dynamics, Fig. 24 shows the radial evolution of the modulus $P = |\mathbf{P}|$ and z-component P_z of the global neutrino polarization vector $\mathbf{P}$ (and analogously for the antineutrino vector $\overline{\mathbf{P}}$) in the nontrivial case of IH for the fluxes shown in Fig. 23 (no significant effect occurs in NH). The radial evolution of the polarization vectors can be interpreted as follows. Up to ~ 90 km, it is $P = P_z$ and $\overline{P} = \overline{P}_z$: all polarization vectors are "glued" along the vertical axis. In the gyroscopic pendulum analogy, this corresponds to a precessing top with a huge spin and negligible displacement from the vertical z-axis. It just spins in the upward position without falling. This behavior is named *synchronized oscillation* regime [4,310]. At $r \sim 90$ km, the pendulum falls for the first time and nutations appear, marking the transition from synchronized to the so-called *bipolar oscillation* regime ([12]). The nutation amplitude gradually decreases as $\sim \mu_r^{*1/2}$ being driven down by the decreasing ν-ν potential strength. In the spinning top analogy, the relaxation of the pendulum to its downward rest position as kinetic energy is extracted by the reduction of the neutrino-neutrino interaction poten-

([12]) Notably, matter effects delay this transition by a few nutation periods with respect to what expected in the presence of ν-ν interactions only [4].

tial and thus the increase of the pendulum moment of inertia. This would lead to large self-induced flavor transitions, occurring in the form of *pair-conversions* $\nu_e\overline{\nu}_e \to \nu_x\overline{\nu}_x$ [4] that conserve the lepton number [Eq. (46)].

As a consequence of the self-induced flavor dynamics, antineutrinos tend to completely reverse the polarization vector ($\overline{\mathbf{P}} \to -\overline{\mathbf{P}}$), so that $\overline{P}_z \simeq -\overline{P}$ asymptotically. Neutrinos also try to invert their global polarization vector. Then, $|\mathbf{P}|$ decreases for $r \gtrsim 150$ km. However, the inversion cannot be complete, because of the lepton number conservation $D_z = P_z - \overline{P}_z$ at any r [see Eq. (46)]. We remark that the inversion of the polarization vectors corresponds to large flavor conversions occurring at low-radii ($r < 200$ km) where the system would not have exhibited any flavor change in the presence of matter effects only.

A generic outcome of the self-induced flavor conversions is the development of "spectral swaps" among the fluxes of different flavors, marked by "spectral splits" at the boundary features of each swap interval [342, 344, 348-354]. In order to elucidate these effects with the specific example we are discussing, we refer to the flavor evolution of the total polarization vectors $\mathbf{P}$ and $\overline{\mathbf{P}}$ shown in Fig. 24, for the initial fluxes of Fig. 23. One would not expect complete flavor conversions in both neutrino and antineutrino sectors, due to the partial inversion of $\mathbf{P}$. The initial spectra shown in Fig. 23 give a larger number of ν_e over $\bar{\nu}_e$ and ν_x. Therefore, if all antineutrinos are swapped, the conservation of the net lepton number [5]

$$\int_{E_{\rm split}}^{\infty} dE(F_{\nu_e} - F_{\nu_x}) = \int_{0}^{\infty} dE(F_{\bar{\nu}_e} - F_{\bar{\nu}_x}) \ , \tag{47}$$

prevents the same thing happening to the neutrino channel. This explains the appearance of the spectral neutrino splits in the oscillated fluxes. The previous equation allows us to determine the "spectral split" energy $E_{\rm split}$ separating the swapped part of the spectrum from the unswapped one. This is shown in Fig. 25, where we plot the initial energy spectra for ν_e (black dashed curves) and ν_x (light dashed curves) and after collective oscillations for ν_e (black continuous curves) and ν_x (light continuous curves) at $r = 350$ km. Neutrino oscillated spectra (left panel) clearly show the split effect and also the corresponding sudden swap of ν_e and ν_x fluxes above $E_{\rm split} \simeq 10$ MeV. The antineutrino spectra (right panel) are almost completely swapped with respect to the initial ones. However, they also present a spectral split at low-energy $E_{\rm split} \simeq 3$ MeV. This feature is not explained by the conservation law expressed by Eq. (47) and its nature is associated with non-adiabatic features of the flavor evolution, as discussed in [347]. We address the interested reader to [349-351] for a detailed theoretical explanation of the spectral splits through the adiabatic solution of the EoMs.

4˙7. *Self-induced spectral splits and multi-angle effects.* – For a long time the results shown in Fig. 25—an almost complete flavor exchange in the antineutrino sector and a spectral split in the neutrino channel in IH, no conversion in NH, and sub-leading multi-angle effects—have been considered the paradigm of the self-induced effects in SN neutrino flavor conversions. However, later it has been realized that this is not the most general situation [341]. Indeed, when ν's have a moderate flavor hierarchy of fluxes and spectral energies are not large, as expected during the cooling phase, more complicated conversion patterns could be associated with the self-induced effects [345]. *Multiple* spectral splits are possible in both NH and IH [341, 345] for neutrinos and antineutrinos. Under such conditions, also multi-angle and three-flavor effects may play a crucial role.

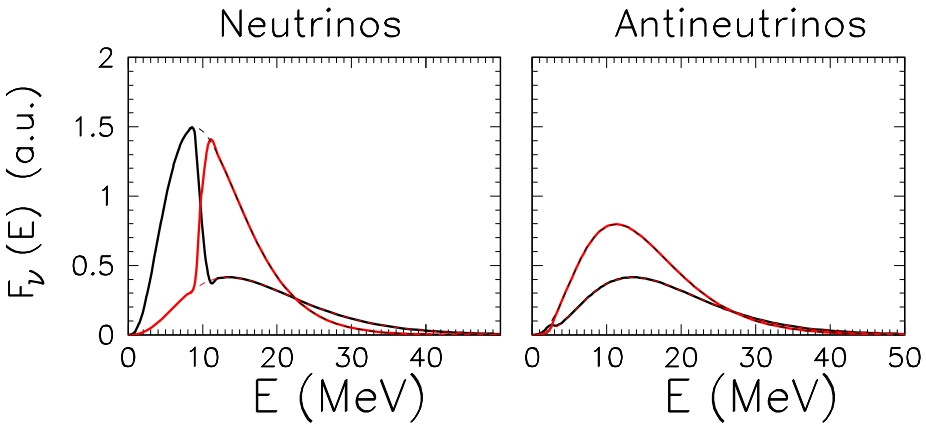

Fig. 25. – Two-flavor single-angle simulation in inverted hierarchy for an initial flux ordering $F^0_{\nu_e} : F^0_{\bar{\nu}_e} : F^0_{\nu_x} = 2.40 : 1.60 : 1.0$. Initial energy spectra for ν_e (black dashed curves) and ν_x (light dashed curves) and after collective oscillations for ν_e (black continuous curves) and ν_x (light continuous curves) at $r = 350$ km.

The first large-scale multi-angle simulations have been performed in 2006 in Ref. [2], adopting the neutrino bulb model. After that, different groups developed independent multi-angle simulations (see, e.g. [5,326,347,355-357]) that extended the seminal findings of [2] and explored the dependence of the flavor evolution on the initial SN neutrino fluxes. Surprises and unexpected results were found with a strong dependence on many details (e.g. neutrino flavor asymmetries [326,345], angular distributions [358,359], three-flavor effects [328, 329, 343, 344, 356]). Despite the numerous studies on the subject, at the moment a complete picture of the self-induced flavor conversions under multi-angle effects in SNe is still missing. Here we show a few examples of the possible behavior due to self-induced flavor conversions in a 3ν scenario in the presence of multi-angle effects during different post-bounce phases:

- $F^0_{\nu_e} \gg F^0_{\nu_x} \gg F^0_{\bar{\nu}_e}$. This is the typical flux ordering expected during the neutronization phase (see Fig. 9), where the ν_e flux is strongly enhanced with respect to ν_x, while the $\bar{\nu}_e$ flux is strongly suppressed. In this case, bipolar flavor conversions, proceeding through pair productions of $\nu_e\bar{\nu}_e \to \nu_x\bar{\nu}_x$, are not possible [4]. Therefore, only synchronized oscillations occur, with no relevant effect of flavor conversion, since the in-medium mixing angle is small. Multi-angle effects are also negligible ([13]).

- $F^0_{\nu_e} \gg F^0_{\bar{\nu}_e} \gg F^0_{\nu_x}$. This flux hierarchy is typically expected during the accretion phase (see Fig. 9), where the first part of the hierarchy is caused by the deleptonization of the collapsed core, and the second is caused by the absence of charged-current interactions for neutrino species other than ν_e and $\bar{\nu}_e$. Figures 26

([13]) A different scenario could be encountered in the case of low-mass SNe with an oxygen-neon-magnesium core. For these SN progenitors, the matter density profile can be very steep. The usual MSW matter effect occurs within the region of high neutrino densities close to the neutrino sphere. Therefore, self-induced flavor conversions will be possible at low-radii [352, 360].

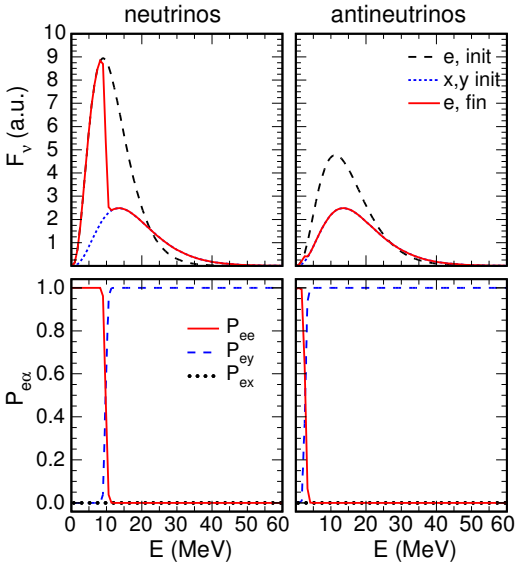

Fig. 26. – Case with $F^0_{\nu_e} : F^0_{\bar{\nu}_e} : F^0_{\nu_x} = 2.40 : 1.60 : 1.0$. Three-flavor evolution in the single-angle case and in inverted mass hierarchy for neutrinos (left panels) and antineutrinos (right panels). Upper panels: Initial energy spectra for ν_e (long-dashed curve) and $\nu_{x,y}$ (short-dashed curve) and for ν_e after collective oscillations (solid curve). Lower panels: Probabilities P_{ee} (solid red curve), P_{ey} (dashed blue curve), P_{ex} (dotted black curve). (Reprinted figure from [356]; copyright (2011) by the American Physical Society.)

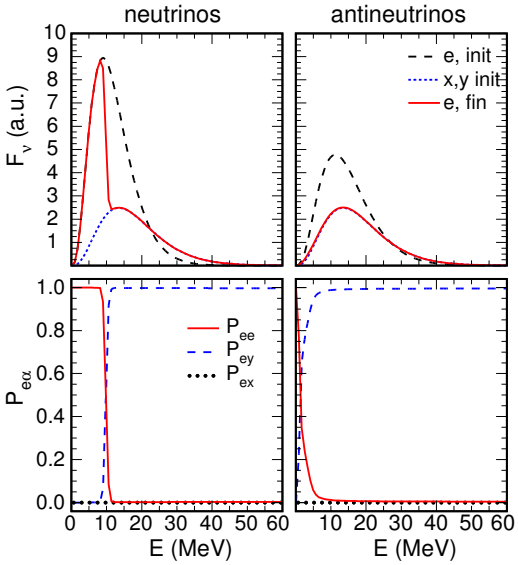

Fig. 27. – The same as Fig. 26 but in the multi-angle case. (Reprinted figure from [356]; copyright (2011) by the American Physical Society.)

and 27, as examples of this configuration, show the three-flavor multi-angle flavor evolution in IH for a flux ordering $F^0_{\nu_e} : F^0_{\bar{\nu}_e} : F^0_{\nu_x} = 2.40 : 1.60 : 1.0$ (already used in Figs. 23 and 25). In particular, Fig. 26 refers to the single-angle evolution, while Fig. 27 is for the multi-angle case. The initial ν_e fluxes (dashed curves) and the final ones for ν_e and $\nu_{x,y}$ are represented in the upper panels. Note that $\nu_{x,y}$ are linear combinations of the $\nu_{\mu,\tau}$ fluxes, defined as $\nu_{x,y} = \cos\theta_{23}\nu_\mu \mp \sin\theta_{23}\nu_\tau$ [339], with $\theta_{23} \simeq \pi/4$ [see Eq. (20)]. The conversion probabilities P_{ee}, P_{ey}, P_{ex} are shown in the lower panels. As already discussed, one can see that the final $\bar{\nu}_e$ flux is almost completely *swapped* with respect to the initial one, while the final ν_e flux presents a peculiar spectral *split* at $E_{\rm split} \simeq 10$ MeV, being swapped to ν_y at higher energies. Flavor conversions occur in the 2ν $(e-y)$ sub-system associated with Δm^2 and θ_{13} (as shown in Fig. 25). From the comparison with the multi-angle case, we see that these effects play a sub-leading role, being suppressed by the large flavor hierarchy of the accretion phase [326]. No self-induced flavor conversion occurs in NH, as expected.

The results presented in Figs. 26 and 27 have been obtained adopting an effective small mixing angle to simulate the matter effects; other multi-angle studies [331-337], conducted under a simplified setup, but including the matter background have shown as during the accretion phase the dense matter would dominate over the neutrino density, generally suppressing the self-induced flavor conversions (see Sec. **4**˙3). Therefore, it is not clear wether this type of flavor evolution is realized in SNe, since probably the flux hierarchy is not large during the cooling phase.

- $F^0_{\nu_x} \gtrsim F^0_{\nu_e} \gtrsim F^0_{\bar{\nu}_e}$. This spectral ordering with a less pronounced flavor hierarchy among the different species is possible during the cooling phase (see Fig. 9). For definitiveness we take $F^0_{\nu_e} : F^0_{\bar{\nu}_e} : F^0_{\nu_x} = 0.85 : 0.75 : 1.0$. Figures 28–29 are in the same format adopted in Fig. 26 and 27 for the accretion phase. In particular, Fig. 28 refers to the single-angle case, while Fig. 29 is for the multi-angle evolution. Differently from the accretion phase, *multiple spectral splits* are present in both neutrino and antineutrino channels. Three-flavor effects are observable in the single-angle scheme, while get suppressed in the multi-angle case. Moreover, the spectral swaps and splits are less pronounced, due to some amount of multi-angle decoherence in the flavor conversions. In this regard, complete decoherence could occur further reducing the flavor asymmetry [356]. Finally, we mention that for the flux ordering of the cooling phase spectral splits and swaps would occur also in NH.

In Table I we summarize the results on the role of multi-angle effects, 3ν effects (associated with δm^2) and spectral splits for different SN neutrino fluxes. Matter suppression effects (see Sec. **4**˙3.1) should be mainly relevant during the accretion phase, see two dedicated cases.

4˙8. *Multi-azimuthal-angle instability.* – As discussed until now, numerical studies of self-induced flavor conversions have been performed within the bulb model. However, it has been recently questioned if removing some of the symmetries assumed in this model, this would trigger new instabilities in the flavor evolution. A crucial assumption of the bulb model is the spherical neutrino emission from the neutrinosphere, that reduces to a cylindrical symmetry along a given neutrino trajectory (see Fig. 21). Recently, by means of a stability analysis of the linearized neutrino EoMs [361], it has been pointed

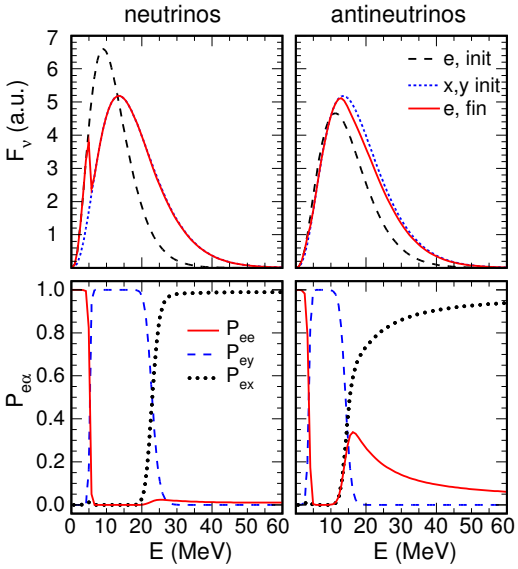

Fig. 28. – Case with $F^0_{\nu_e} : F^0_{\bar{\nu}_e} : F^0_{\nu_x} = 0.85 : 0.75 : 1.0$. Three-flavor evolution in the single-angle case and in inverted mass hierarchy for neutrinos (left panels) and antineutrinos (right panels). Upper panels: Initial energy spectra for ν_e (long-dashed curve) and $\nu_{x,y}$ (short-dashed curve) and for ν_e after collective oscillations (solid curve). Lower panels: Probabilities P_{ee} (solid red curve), P_{ey} (dashed blue curve), P_{ex} (dotted black curve). (Reprinted figure from [356]; copyright (2011) by the American Physical Society.)

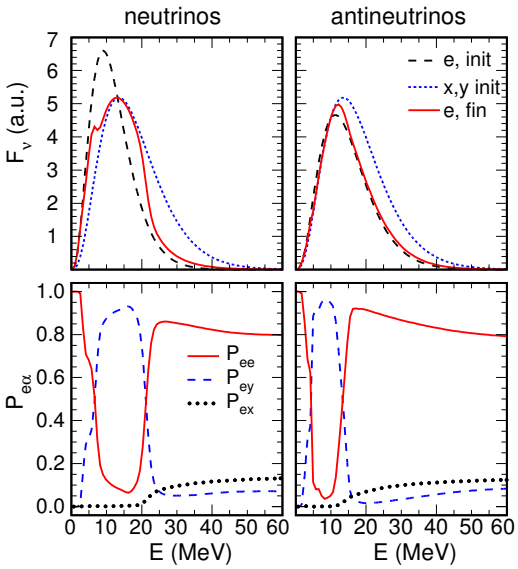

Fig. 29. – The same as Fig. 28 but in the multi-angle case. (Reprinted figure from [356]; copyright (2011) by the American Physical Society.)

TABLE II. – *Summary of multi-angle effects, 3ν effects and spectral splts for different SN neutrino fluxes, assuming sub-leading matter effects. The cases "accretion, $\lambda_r \ll \mu_r$" ("accretion, $\lambda_r \gg \mu_r$") stand for absence (presence) of multi-angle matter suppression effects.*

Initial spectral pattern	Multi-angle effects	δm^2-effects	Spectral splits
$F^0_{\nu_e} \gg F^0_{\nu_x} \gg F^0_{\bar{\nu}_e}$ (neutronization)	no	no	no
$F^0_{\nu_e} \gg F^0_{\bar{\nu}_e} \gg F^0_{\nu_x}$ (accretion, $\lambda_r \ll \mu_r$)	marginal	absent	robust
$F^0_{\nu_e} \gg F^0_{\bar{\nu}_e} \gg F^0_{\nu_x}$ (accretion, $\lambda_r \gg \mu_r$)	relevant	absent	no
$F^0_{\nu_x} \gtrsim F^0_{\nu_e} \gtrsim F^0_{\bar{\nu}_e}$ (cooling)	relevant	present/absent	smeared
$F^0_{\nu_e} \simeq F^0_{\nu_x} \simeq F^0_{\bar{\nu}_e}$ (cooling)	strong	present	washed-out

out that removing the assumption of axial symmetry in the ν propagation, a new multi-azimuthal-angle (MAA) instability could emerge in the flavor evolution of the dense SN neutrino gas. The occurrence of this instability has been then clarified with simple toy models [362, 363]. The presence of MAA effects unavoidably implies the breaking of the spherical symmetry in the flavor evolution after the onset of the flavor conversions. This would lead to a challenging multi-dimensional problem involving partial differential equations. However, assuming that the variations of the global solution in the direction transverse to the radial one are small, one can still study the local solution along a given line of sight, without worrying about its global behavior. This approach, even if not completely self-consistent, allowed to obtain the first numerical solutions of the non-linear neutrino propagation equations in SNe, introducing the azimuthal angle as angular variable in addition to the usual zenith angle in the multi-angle kernel [see Eq. (26)].

Adopting this generalized bulb model, it has been shown [364,365] that the pattern of the spectral crossings (energies where $F_{\nu_e} = F_{\nu_x}$, and $F_{\bar{\nu}_e} = F_{\bar{\nu}_x}$) is crucial in determining the impact of MAA effects on the flavor evolution. For neutrino spectra with a strong excess of ν_e over $\bar{\nu}_e$, as expected during the accretion phase, new flavor conversions occur in NH. This is represented in Fig. 30, where we have considered initial fluxes as the ones of Fig. 25. In particular the initial (dashed curves) and final fluxes (continuous curves) are shown for e (black curves) and x (light curves) flavors, for neutrinos (left panels) and antineutrinos (right panels). Upper panels show the NH case while lower panels refer to the IH one. One realizes that MAA effects produce flavor conversions in NH, otherwise absent in the azimuthal symmetric model. However, the dominance of matter terms during the accretion phase would typically suppress also the MAA effects [336,337]. For spectra with a moderate flavor hierarchy, as the ones expected during the cooling phase, the growth of the MAA instability should be inhibited. As a result, the oscillated spectra are rather close to the ones seen in the azimuthal symmetric case; see Fig. 29 for comparison (see also [365]).

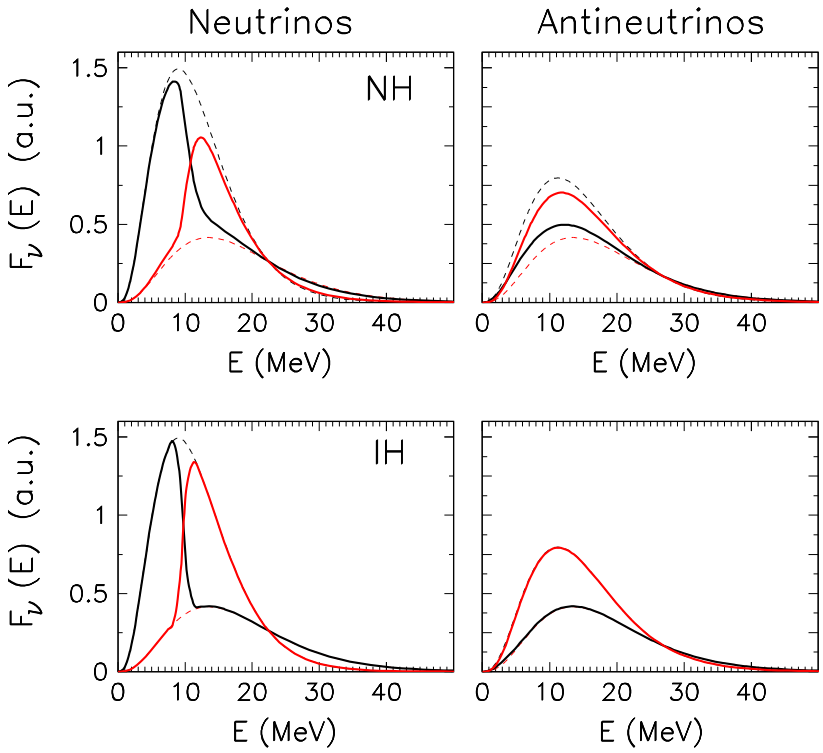

Fig. 30. – Multi-azimuthal-angle flavor evolution for ν's (left panel) and $\bar{\nu}$'s (right panel) in NH (upper panels) and IH (lower panels) for fluxes with an initial ordering $F^0_{\nu_e} : F^0_{\bar{\nu}_e} : F^0_{\nu_x} = 2.40 : 1.60 : 1.0$. Energy spectra for ν_e (black dashed curves) and ν_x (light dashed curves) in absence of flavor oscillations and for ν_e (black continuous curves) and ν_x (light continuous curves) after collective oscillations. (Reprinted figure from [365]; copyright (2014) by the American Physical Society.)

4˙9. *Spontanueous breaking of space-time symmetries.* – The MAA instability has shown as self-interacting neutrinos can *spontaneously break* the symmetries of the initial conditions. Such insight stimulated further investigations about the validity of the solution of the SN neutrino EoMs worked out within the bulb model (see Sec. **4˙2**).

The assumptions of azimuthal symmetry in neutrino propagation and quasi-stationary neutrino emission reduce the general partial differential equations [see Eq. (22)] into ordinary differential equations describing the stationary spatial evolution of the dense neutrino gas along the radial direction. These assumptions, although adopted since the earliest papers on the subject, are unjustified. Indeed, it was tacitly assumed that small deviations from them do not significantly perturb the flavor evolution. However, it has been recently realized that instabilities may grow once initial symmetries are relaxed, since self-interacting neutrinos can spontaneously break the translation symmetries in time [366] and space [367-371]. This implies that the characterization of the self-induced effects obtained within the spherically symmetric bulb model should be taken *cum grano salis*.

A self-consistent solution of the flavor evolution would eventually lead to solve the

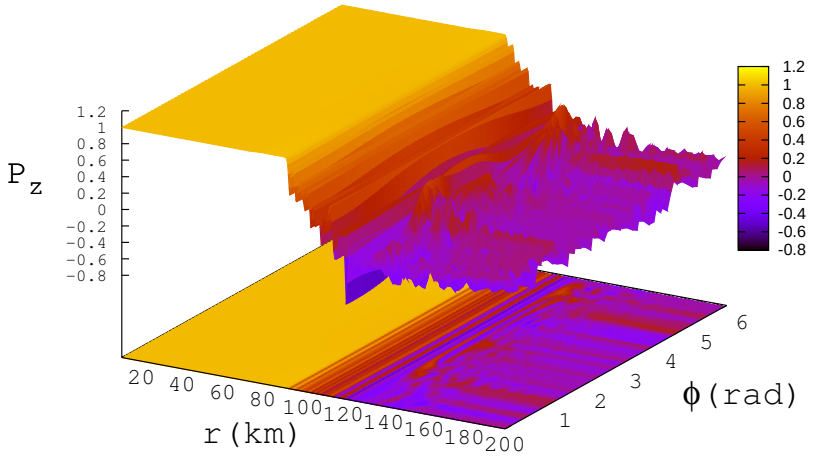

Fig. 31. – Two-dimensional evolution of the z component P_z of the $\bar{\nu}$ polarization vector in the r-ϕ plane, and its map on the bottom plane breaking the azimuthal invariance and the spherical symmetry in NH. (Figure adapted from [369].)

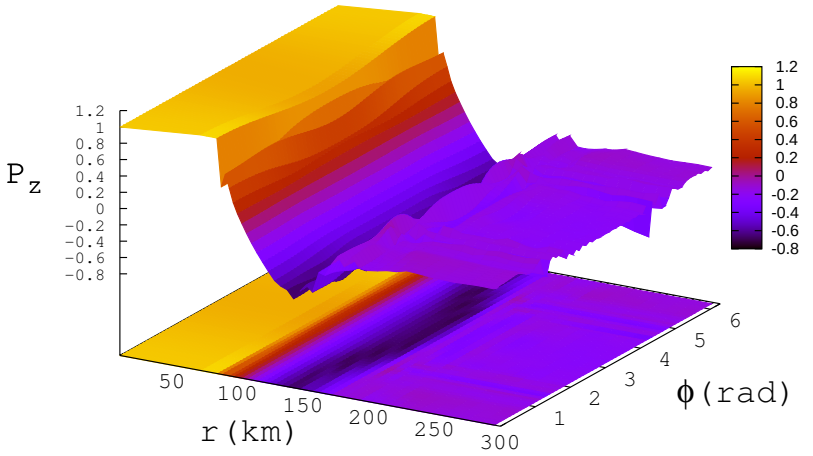

Fig. 32. – The same as Fig. 31 but in IH case. (Figure adapted from [369].)

complete space-time-dependent problem described by the following partial differential equations [315]

$$\left(\frac{\partial}{\partial t} + \mathbf{v}_{\mathbf{p}} \cdot \nabla_{\mathbf{x}}\right) \varrho_{t,\mathbf{p},\mathbf{x}} = -i[\Omega_{\mathbf{p},\mathbf{x}}, \varrho_{t,\mathbf{p},\mathbf{x}}] \ , \tag{48}$$

where $\Omega_{\mathbf{p},\mathbf{x}} = \Omega^{\rm vac}_{\mathbf{p}} + \Omega^{\rm ref}_{\mathbf{p},\mathbf{x}}$, and an analogous equation exists for antineutrinos [see Eq. (22)]. This represents a formidable seven-dimensional problem. First attempts of solution have been recently presented in [366,368,369] by Fourier transforming Eq. (48).

For example, performing a spatial Fourier transform one finds

$$\left(\frac{\partial}{\partial t} + \mathbf{v_p}\cdot\mathbf{k}\right)\varrho_{t,\mathbf{p},\mathbf{k}} = -i\int d^3\mathbf{x}\ e^{-i\mathbf{k}\cdot\mathbf{x}}[\Omega_{\mathbf{p},\mathbf{x}},\varrho_{t,\mathbf{p},\mathbf{x}}]\ , \tag{49}$$

which represents a tower of ordinary differential equations in t for the different Fourier modes $\varrho_{t,\mathbf{p},\mathbf{k}}$ with wavenumber $\mathbf{k}$, which are coupled through the interaction term.

This technique sheds the basis to study this challenging problem in the SN case. For example, Figs. 31-32 show the behavior of the z component of the $\bar{\nu}$ polarization vector ($\bar{P}_z$) obtained solving the flavor EoMs in a two-dimensional plane spanned by the radial coordinate r and the angular one ϕ, without enforcing neither the axial nor the spherical symmetry [369]. Both in NH (Fig. 31) and IH (Fig. 32), flavor conversions start as in the spherically symmetric case, i.e. the planes of common oscillation phase are flat in the ϕ direction. However, this behavior is not stable. In both the mass hierarchies the $\bar{P}_z$ component is no longer flat in ϕ, while it starts to acquire significant variations at different angles.

The above described very recent results add new challenges in the characterization of the self-induced SN neutrino flavor conversions. Remarkably, the final goal would be a realistic treatment of the self-induced flavor conversions within the SN environment, where large deviations from a spherical neutrino emission can be generated by hydrodynamical instabilities such as SASI or LESA, especially during the accretion phase, as discussed in Sec. **2**.

Another assumption that has recently been questioned is that neutrinos are free-streaming after the neutrinosphere [372], as even a fraction of neutrinos that occasionally scatter outside of the neutrinosphere should produce a small "neutrino halo" [372, 373]. On the basis of a stability analysis, it has been concluded that the neutrino halo should not drastically affect flavor oscillations during the accretion phase [374]; however a self-consistent numerical simulation is not available at the moment. The inclusion of the halo effect in the numerical simulations would change the nature of the flavor evolution, turning it into a boundary value problem instead of a non-stationary initial value one. All these open issues require further dedicated work to fully clarify the role of flavor instabilities in the interacting neutrino field.

4˙10. *Mikheyev-Smirnov-Wolfenstein matter effect in the wake of the shock-wave.* – Self-induced effects in SN neutrino oscillations, occurring in the deepest stellar regions would eventually die out at $r \gtrsim \mathcal{O}(10^3)$ km. However, as neutrinos stream through the outer layers of the stellar envelope, they would feel ordinary matter effects. There is a wide literature on (SN) neutrino oscillations in matter to which we refer the interested reader (see, e.g., [299, 339, 375-378]). As the SN matter potential $\lambda_r = \sqrt{2}G_F n_e(r)$ declines, neutrinos would eventually encounter Mikheyev-Smirnov-Wolfenstein (MSW) *resonances* when [299, 339]

$$\lambda_r = \omega_{H,L}\ , \tag{50}$$

corresponding to the atmospheric Δm^2 (H-resonance) and the solar δm^2 (L-resonance) mass-squared differences, respectively.

Typical regions where we expect H and L resonances have been shown in Fig. 22. We realize that the two resonant regions are rather separated due to the hierarchy $\delta m^2 \ll \Delta m^2$, so that one can typically factorize the dynamics studying the resonant effects in 2ν

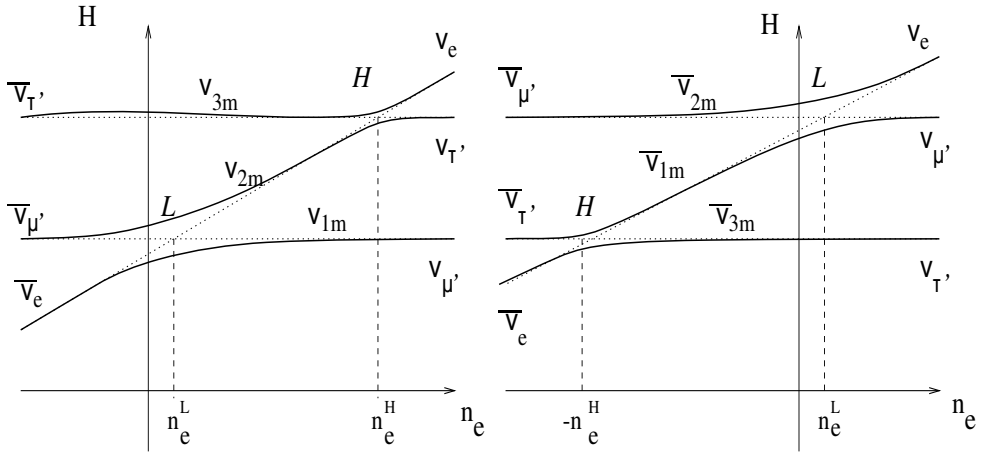

Fig. 33. – Three-flavor level diagram for neutrino propagation eigenmodes, relevant for neutrinos streaming from a SN core [339] for normal hierarchy (left) and inverted hierarchy (right). (Figure taken from [16] with permission.)

sub-sectors. When one of the conditions in Eq. (50) is fulfilled a resonant amplification of the flavor conversions is expected. From the Hamiltonian (in absence of self-interactions), one can build the *level crossing* diagrams for the two mass hierarchies (see Fig. 33) showing the neutrino propagation eigenstates from the regions at high-density to the vacuum, where $\lambda_r = 0$ [339]. These diagrams allow us to determine in which mass eigenstate will emerge a neutrino produced in a given interaction eigenstate. In the case of antineutrinos, the effective potential for $\bar{\nu}_e$ is $\lambda_r = -\sqrt{2}G_F n_e(r)$. Antineutrinos can be represented on the same level crossing diagram, as neutrinos traveling through matter with "effectively" negative $n_e(r)$. Given the resonance conditions in Eq. (50), the sign of the matter potential λ_r and of the mass-squared splittings, we realize that the H-resonance can be satisfied by neutrinos in NH ($\lambda_r, \Delta m^2 > 0$) or by antineutrinos in IH ($\lambda_r, \Delta m^2 < 0$). Therefore, in principle, the neutrino burst is sensitive to the neutrino mass hierarchy thanks to the matter effects, associated with the H-resonance. Conversely, the L-resonance can be satisfied only by neutrinos in both the mass hierarchies (since $\delta m^2 > 0$).

For typical SN simulations, the matter density profile declines so slowly that the neutrino propagation is *adiabatic*, i.e., each mass eigenstate in Fig. 33 remains the same. However, this condition is violated at the (forward and reverse) shock-fronts where, due to the abrupt density change (see Fig. 22), strong non-adiabatic conversions occur. Neglecting self-induced flavor conversions, the neutrino flux arriving at Earth can be expressed in terms of energy-dependent ν_e survival probabilities $P_{ee}(E)$ at the shock-front [339]:

$$F_{\nu_e} = P_{ee}(E)F^0_{\nu_e}(E) + [1 - P_{ee}(E)]F^0_{\nu_x}(E) \ . \tag{51}$$

An analogous expression exists for $\bar{\nu}_e$ with survival probabilities $\bar{P}_{ee}(E)$. In particular, considering for simplicity a static SN matter profile and a complete adiabatic propagation we have $(P_{ee}, \bar{P}_{ee}) = (0, \cos^2\theta_{12})$ in normal mass hierarchy, and $(P_{ee}, \bar{P}_{ee}) = (\sin^2\theta_{12}, 0)$

in inverted mass hierarchy [339].

Corrections to a pure adiabatic neutrino propagation are expressed in terms of *level crossing* probabilities among the instantaneous eigenstates in matter at the resonance point [299]. As shown in Fig. 22, the real SN density profile is non-monotonic and time-dependent, so that multiple resonances would occur along it. For θ_{13} as large as recently measured, the H-resonance is adiabatic, except at the shock-fronts, where the crossing probability $P_H = P_H(\Delta m^2, \theta_{13})$ between the eigenmodes $\nu_{3,m}$ and $\nu_{2,m}$ (see Fig. 33) would be extremely non-adiabatic, giving $P_H \simeq 1$. Then, as ν's propagate at larger radii, they would eventually encounter the L-resonance between the $\nu_{2,m}$ and $\nu_{1,m}$ states, associated with the $(\delta m^2, \theta_{12})$ sub-sector. The L-resonance intercepts the shock-front only at relatively late times ($t_{\rm pb} \gtrsim 10$ s) and it is never strongly non-adiabatic. Therefore, sub-leading effects related a level crossing probability $P_L \neq 0$ are typically neglected.

The survival probability P_{ee} of SN neutrinos at Earth (neglecting Earth matter crossing) is related to the crossing probability P_H at the shock-front [379]:

$$P_{ee} \simeq \begin{cases} \sin^2\theta_{12}\, P_H & (\nu,\ \text{NH}), \\ \cos^2\theta_{12} & (\overline{\nu},\ \text{NH}), \\ \sin^2\theta_{12} & (\nu,\ \text{IH}), \\ \cos^2\theta_{12}\, P_H & (\overline{\nu},\ \text{IH}). \end{cases} \tag{52}$$

It is clear as P_H can modulate the (otherwise constant) survival probability of ν_e in NH and of $\bar{\nu}_e$ in IH, thus providing an important handle to solve the current hierarchy ambiguity.

In order to compute P_H, one has to numerically integrate the flavor evolution equations [Eq. (44)] in the basis of the instantaneous matter eigenstates. Analytical prescriptions have been presented in [379, 380]. In Fig. 34, we show the crossing probability P_H as a function of energy E for the SN matter density profile of Fig. 22 at post-bounce time $t_{\rm pb} = 5$ s. We closely follow the approach of Ref. [379] to compute P_H (the interested reader is referred to this reference for further details). The crossing probability has a typical top-hat structure, jumping from $P_H \sim 0$ (adiabatic regime) to $P_H \sim 1$ (extremely non-adiabatic regime) when the resonance condition is satisfied across the forward shock-front. A more complicated pattern would emerge when resonances occur on both the forward and the reverse shock fronts [242, 338]. It is expected that the transient violation of the adiabaticity condition, when neutrinos cross the shock-fronts, would emerge as an observable modulation of the neutrino signal. This signature could be particularly useful to follow in "real-time" the shock-wave propagation, as well as to probe the neutrino mass hierarchy. This opportunity has been widely discussed in literature [242, 338, 379, 381-384].

A realistic characterization of matter effects, during neutrino propagation across the SN shock-wave, must also take into account stochastic density fluctuations, inhomogeneities of various magnitudes as well as correlation lengths in the ejecta layer in the wake of the shock front. These fluctuations are a result of hydrodynamic instabilities between the proto-neutron star and the SN shock during the very early stages of the SN explosion. They lead to large-scale explosion asymmetries and turbulence in a dense shell of shock-accelerated ejecta, which subsequently also seed secondary instabilities in the outer shells of the exploding star (e.g., Refs. [131, 385-390]).

Neutrino flavor conversions in a stochastic matter background have been subject of intense investigations both in a general context [391-397] and specifically in relation to SN

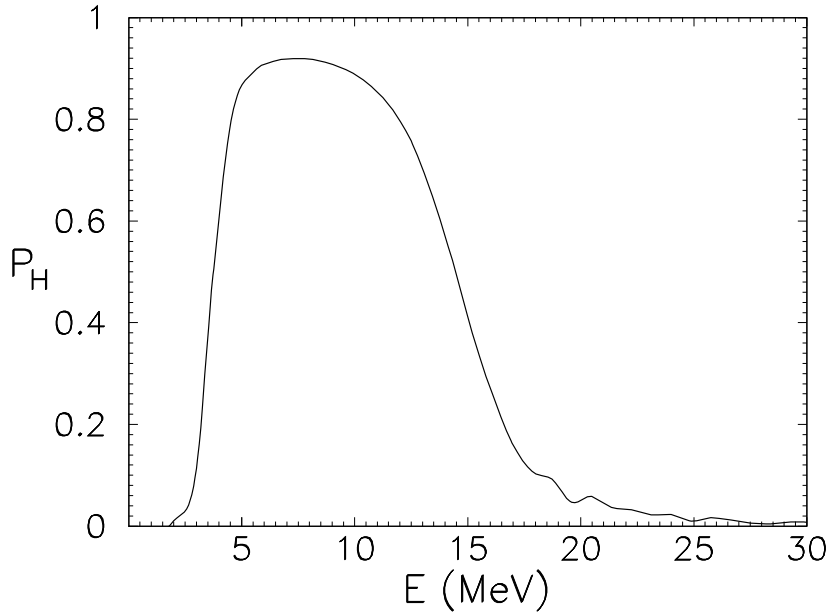

Fig. 34. – Neutrino crossing probability P_H as function of the neutrino energy E for the SN matter potential of Fig. 22 at post-bounce time $t_{\rm pb} = 5$ s.

neutrinos [398-405]. It is expected that stochastic matter fluctuations of sufficiently large amplitude may suppress flavor conversions and lead to $P_H \simeq 1/2$ when the suppression is strong [398]. Therefore, the spectral properties of the fluctuations are very important for understanding the neutrino signal emerging from a core-collapse SN. At the moment there is no unanimous consensus about the impact of matter fluctuations on the SN neutrino flavor conversions. A recent study based on two-dimensional SN simulations has shown a modest damping of the neutrino crossing probabilities [406]. However, further analysis would be mandatory when high-resolution three-dimensional simulations will become available.

4˙11. *Observable signatures of supernova neutrino flavor conversions*. – After discussing in detail how self-induced and matter effects would process the SN neutrino fluxes, we present some of the possible observable signatures of flavor conversions in SNe and their sensitivity to the neutrino mass hierarchy. For definitiveness, we will refer to a Galactic SN at a distance $d = 10$ kpc from the Earth. We address the interested reader to Sec. **3** for a detailed discussion on SN neutrino detection techniques.

(a) Self-induced spectral splits. As discussed in this Section, in recent years the picture of SN neutrino oscillations, based only on the MSW matter effects, has undergone a change of paradigm by the insight that the refractive effects of neutrinos on themselves are crucial. Observationally, the most important consequence of the self-induced flavor conversions is a swap of the ν_e and $\bar{\nu}_e$ spectrum with the non-electron species ν_x and $\bar{\nu}_x$ in certain energy intervals, and the resultant spectral splits at the edges of these swap intervals. Some of the spectral splits could occur sufficiently close to the peak energies to produce significant distortions in the SN neutrino signal, observable in the

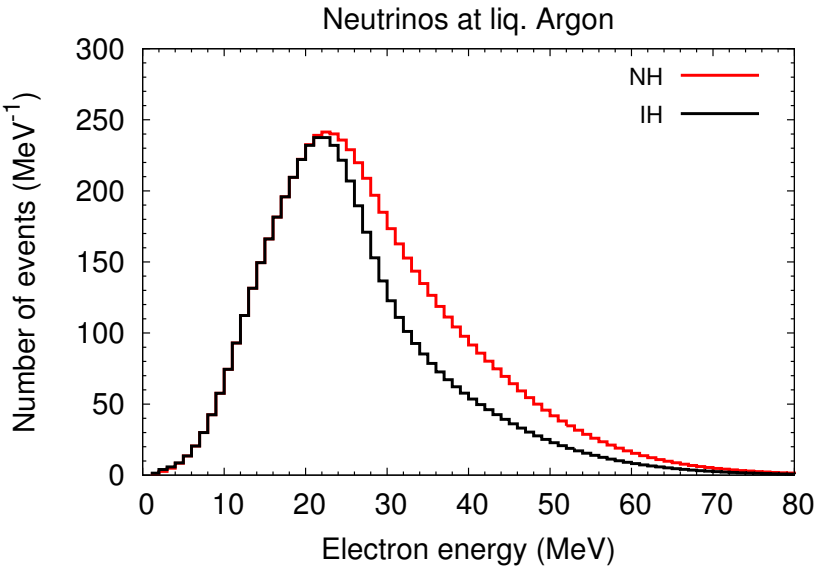

Fig. 35. – Observable SN ν_e spectra in a 40-kton LAr TPC for benchmark fluxes as in Fig. 28 in both the mass hierarchies. (Figure adapted from [354]; courtesy of B. Dasgupta.)

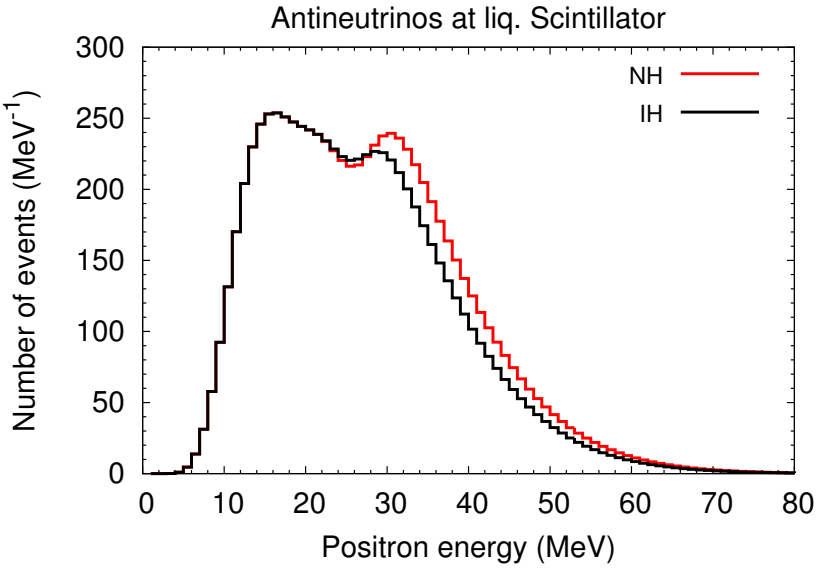

Fig. 36. – Observable SN $\bar{\nu}_e$ spectra in a 20-kton liquid scintillator detector for benchmark fluxes of Fig. 28 in both the mass hierarchies. (Figure adapted from [354]; courtesy of B. Dasgupta.)

large underground dectectors. As an example, we show in Fig. 35 the observable ν_e signal in a 40-kton LAr TPC, while Fig. 36 refers to the $\bar{\nu}_e$ signal in a 20-kton liquid scintillator

detector. Both the mass hierarchy cases are shown. The initial fluxes in these figures are the same as in Fig. 28 (during the cooling phase) where self-induced conversions are not matter-suppressed. The self-induced flavor evolution has been characterized in a single-angle and three-flavors scenario (as in Fig. 28). The MSW effect is calculated according to Eq. (51) and (52), where it is assumed complete adiabatic propagation ($P_H = 1$) neglecting possible shock-wave effects (see [354] for details).

Concerning the electron spectrum produced by ν_e in a LAr TPC (Fig. 35), the observable flux is mostly due to the initial $F^0_{\nu_x}$ and then it does not present any special spectral feature in both the mass hierarchies. Conversely, for the $\bar{\nu}_e$ signal in a scintillator detector (Fig. 36), the observable positron spectrum would be mostly due to $F^0_{\bar{\nu}_e}$ for $E < E_{\rm split}$ and $F^0_{\nu_x}$ at higher energies (see also Fig. 28). This would produce a bimodal positron spectrum, with two peaks produced by the two initial antineutrino distributions. The result is similar in both the mass hierarchies. This example shows that spectral splits are potentially identifiable during the cooling phase, if the average energies and luminosities of non-electron fluxes are sufficiently large.

(b) Neutrinos from the SN neutronization burst. The ν_e neutronization burst is a particularly interesting probe of flavor conversions, since it can be considered almost as a "standard candle" being independent of the mass progenitor and nuclear EoS [136]. As discussed in Sec. **4**˙**7**, self-induced effects are not operative on the SN ν_e neutronization burst because of the large excess of ν_e due to the core deleptonization. Therefore, the ν_e flux would be only affected by MSW effects. At the very early post-bounce times relevant for the prompt burst, MSW flavor conversions would occur along the static progenitor matter density profile. We expect that the observable ν_e flux at Earth would be [Eq. (51)]

$$F_{\nu_e} = F^0_{\nu_x} \qquad \text{(NH)} \ , \tag{53}$$

$$F_{\nu_e} = \sin^2\theta_{12} F^0_{\nu_e} + \cos^2\theta_{12} F^0_{\nu_x} \qquad \text{(IH)} \ . \tag{54}$$

The observation of the neutronization peak would indicate the inverted mass hierarchy, while we do not expect its detection in NH.

Concerning the possibility to detect the ν_e neutronization burst, while Mton class WC detectors measure predominantly the $\bar{\nu}_e$ flux using inverse beta decay, they are also sensitive to the subdominant ν_e channel via elastic scatterings on e^- (see Sec. **3**). On the other hand, a large LAr TPC will make the cleanest identification of the prompt ν_e burst through its unique feature of measuring ν_e charged-current interactions, enabling to probe oscillation physics during the early stage of the SN explosion. We show the observable ν_e neutronization burst from 11 $M_\odot$ and a 27 $M_\odot$ SN progenitors with LS EoS (see Sec. **2**˙**4**) in a 560-kton WC detector (Fig. 37) and in a 40-kton LAr TPC (Fig. 38); the neutronization burst peak is clearly visible in IH in both detectors. Moreover, from these two figures one realizes that the variation in the progenitor mass has a sub-leading impact in the features of the signal.

The detection of the SN neutronization burst has also been proposed to constrain nonstandard scenarios, like Lorentz invariance violation [407], neutrino decay [408], oscillations into light sterile neutrinos [409], neutrino-antineutrino oscillations mediated by a neutrino magnetic moment [410]. All these scenarios would lead to a suppression of the neutronization burst.

(c) Rise time of the neutrino signal. The rise time of a Galactic iron-core SN $\overline{\nu}_e$ light curve, observable in large underground detectors, can provide a diagnostic tool for the neutrino mass hierarchy. Due to the combination of matter suppression of collective

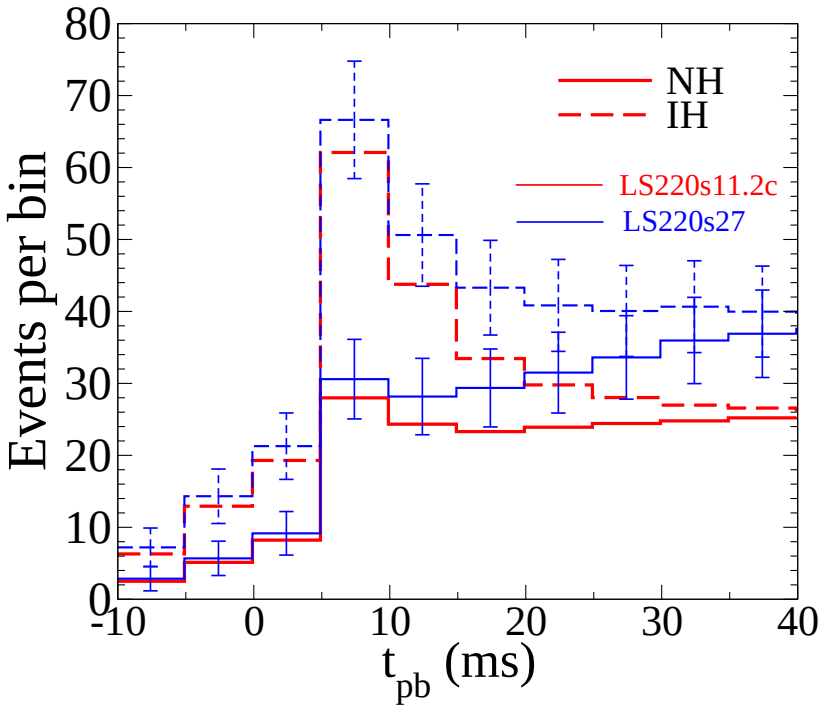

Fig. 37. – Neutronization events rate per time bin in a 560-kton WC detector for 27 $M_\odot$ and 11 $M_\odot$ SN progenitors (see Sec. **2**·4) at $d = 10$ kpc for both NH (continuous curve) and IH (dashed curve).

effects at early post-bounce times (see Sec. **4**·3) and the presence of the ordinary MSW effect in the outer layers of the SN, one expects that the observable $\bar{\nu}_e$ flux at Earth would be given by

$$F_{\bar{\nu}_e} = \cos^2\theta_{12} F^0_{\bar{\nu}_e} + \sin^2\theta_{12} F^0_{\bar{\nu}_x} \quad \text{(NH)} \ , \tag{55}$$

$$F_{\bar{\nu}_e} = F^0_{\bar{\nu}_x} \quad \text{(IH)} \ . \tag{56}$$

It is clear that the $F_{\bar{\nu}_e}$ flux at the Earth would basically reflect the original $F^0_{\bar{\nu}_x}$ flux if IH occurs, or closely match the $F^0_{\bar{\nu}_e}$ flux in NH. As from state-of-the-art simulations [411,412], temporal profiles of the original $\overline{\nu}_x$ and $\overline{\nu}_e$ fluxes appear quite different in the accretion phase, and relatively model-independent. In particular, the $\overline{\nu}_x$ signal rises faster than the $\overline{\nu}_e$ one. Figure 39 shows the early post-bounce evolution of luminosities (left panels), and mean energies (right panels) for a set of eleven 1D simulations with progenitor of different masses obtained by the Garching group. Due to this feature, it would be possible to distinguish the two mass hierarchies from the rise time on $\mathcal{O}(100)$ ms scale.

Figure 40 shows the expected *overall* signal rate $R(t)$ in the IceCube detector for a Galactic SN (see Sec. **3** for details about the SN neutrino detection technique in IceCube). We refer to the case of a 15 $M_\odot$ SN progenitor also adopted for illustration in Fig. 39. The NH cases are shown with continuous curves, while the IH cases with the dashed ones. The right panel overlies the error size using 2 ms bins with typical error estimates from

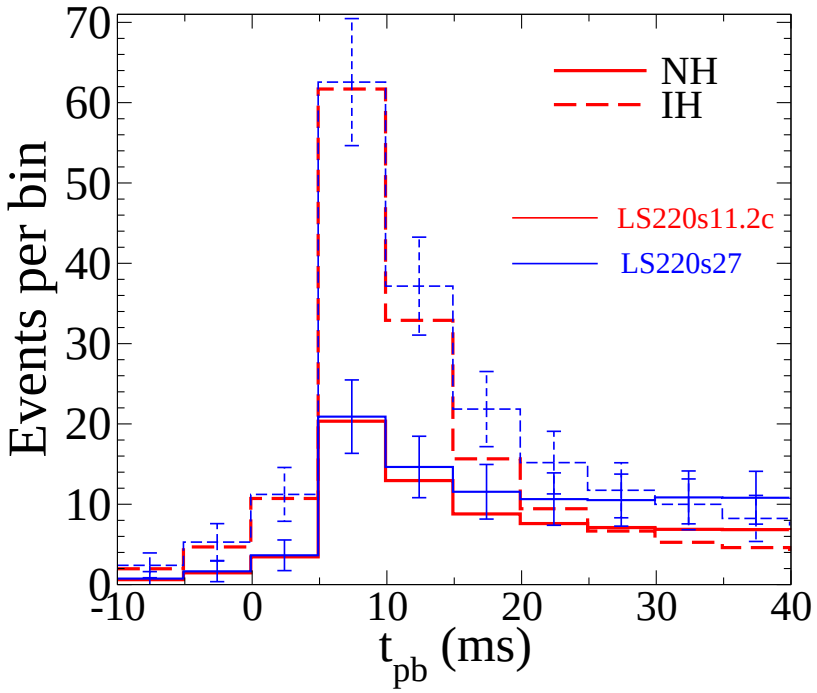

Fig. 38. – Neutronization events rate per time bin in a 40-kton LAr TPC for 27 $M_\odot$ and 11 $M_\odot$ SN progenitors (see Sec. **2**˙4) at $d = 10$ kpc for both NH (continuous curve) and IH (dashed curve).

the photomultiplier background noise. The difference between the observed neutrino light curve in the NH and IH is evident. For the NH case, a relatively longer hump in the signal, associated with the accretion, is clearly visible. While in IH, the light curve has a sudden rise.

An important issue is the dependence of this signature is from theoretical uncertainties, most notably the progenitor structure, EoS, and numerical schemes. The models tested in [235] provide quite a satisfactory test that the uncertainties associated with progenitor structure do not spoil the viability of the method. Concerning numerical schemes, the same signature has been found also within the hydrodynamical simulations of the Basel/Darmstadt group [30] and independently with the simulations of the Tapir group [412]. On the other hand, a firm conclusion on the other uncertainties requires further studies. Therefore, given the potential importance of the rise time signature in shedding light on the unknown neutrino mass hierarchy, it would be mandatory to further explore the robustness of this feature with more accurate simulations.

(d) Earth matter effect. It is widely known that if SN neutrinos should reach the detector from "below" [230], the Earth crossing would induce an energy-dependent modulation in the neutrino survival probability [339,413]. The appearance of the Earth effect depends on the neutrino fluxes and on the mixing scenario. The accretion phase is particularly promising to detect Earth crossing signatures because the absolute SN ν flux is large and the flavor-dependent flux differences are also large. Due to the matter suppres-

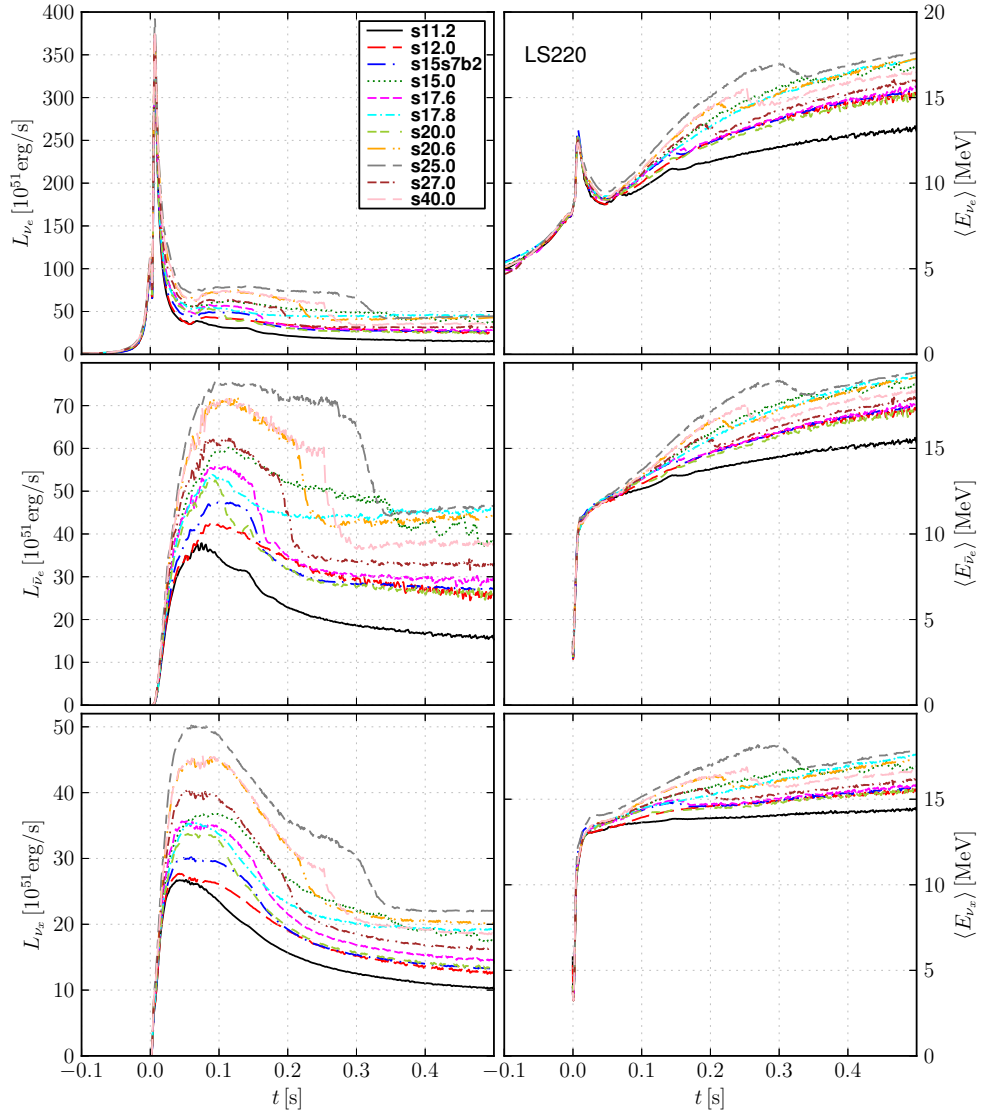

Fig. 39. – Early postbounce evolution of luminosities (left panels), and mean energies (right panels) for a set of eleven 1D simulations with progenitors of different masses as obtained by the Garching group. Quantities for ν_e, $\bar{\nu}_e$, and ν_x are shown in the top, middle and bottom panel, respectively. The vertical line indicates the early timescale (100 ms). (Figure taken from [64, 411].)

sion of the collective oscillations during the accretion phase, SN neutrino initial fluxes will be processed by the only MSW effect. In this situation the oscillated SN ν fluxes at Earth (before Earth crossing) are given by Eq. (51) in terms of the energy-dependent ν_e survival probabilities $P_{ee}(E)$ (or $\bar{P}_{ee}(E)$ for $\bar{\nu}_e$). The Earth effect can be taken into account by just mapping the non-vanishing $P_{ee} \to 1 - P_{2e}$ and $\bar{P}_{ee} \to 1 - \bar{P}_{2e}$, where P_{2e} is the $\nu_2 \to \nu_e$ transition probability for neutrinos propagating through the Earth, and

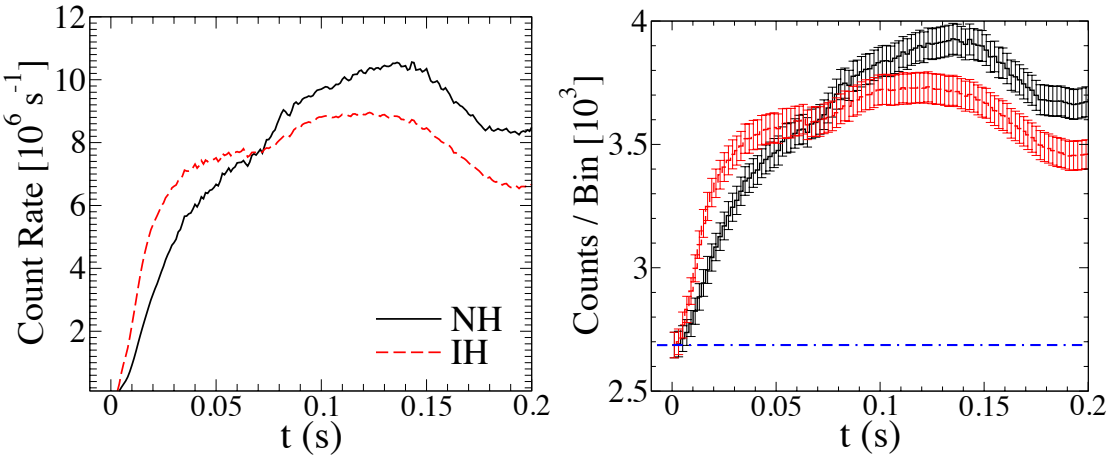

Fig. 40. – Supernova signal in IceCube assuming a distance of 10 kpc, based on a simulation for a 15 $M_\odot$ SN progenitor from the Garching group. In the right panel it is illustrated the error size using 2 ms bins with typical error estimates from the photomultiplier background noise. (Figure adapted from [235].)

analogously for $\bar{P}_{2e}$ [413]. For large θ_{13}, the neutrino fluxes at Earth for NH are [339]:

$$F^{\oplus}_{\bar{\nu}_e} = (1-\bar{P}_{2e})F^0_{\bar{\nu}_e} + \bar{P}_{2e}F^0_{\bar{\nu}_x} \qquad \text{and} \qquad F^{\oplus}_{\nu_e} = F^0_{\nu_x} \ , \tag{57}$$

while for IH

$$F^{\oplus}_{\bar{\nu}_e} = F^0_{\bar{\nu}_x} \qquad \text{and} \qquad F^{\oplus}_{\nu_e} = (1-P_{2e})F^0_{\nu_e} + P_{2e}F^0_{\nu_x} \ , \tag{58}$$

where $F^{\oplus}_{\nu}$ indicates the neutrino fluxes after Earth crossing.

The analytical expressions for P_{2e} and $\bar{P}_{2e}$ can be calculated for the approximate two-density model of the Earth [414]. When neutrinos traverse a distance L through the mantle of the Earth, these quantities assume a very simple form [339, 413]

$$P_{2e} = \sin^2\theta_{12} + \sin 2\theta^m_{12}\,\sin(2\theta^m_{12} - 2\theta_{12})\sin^2\left(\frac{\delta m^2 \sin 2\theta_{12}}{4E\,\sin 2\theta^m_{12}}\,L\right) , \tag{59}$$

$$\bar{P}_{2e} = \sin^2\theta_{12} + \sin 2\bar{\theta}^m_{12}\,\sin(2\bar{\theta}^m_{12} - 2\theta_{12})\sin^2\left(\frac{\delta m^2 \sin 2\theta_{12}}{4E\,\sin 2\bar{\theta}^m_{12}}\,L\right) , \tag{60}$$

where θ^m_{12} and $\bar{\theta}^m_{12}$ are the effective values of θ_{12} in the Earth matter for neutrinos and antineutrinos respectively [378]. The Earth crossing induces a peculiar oscillatory signature in the neutrino energy spectrum. From Eqs. (57)–(58), it results that the Earth matter effect should be present for antineutrinos in NH and for neutrinos in IH, providing a potential tool to distinguish between these two cases.

Since the typical event rate associated with an inverse beta decay process is $\propto E^2 F^{\oplus}_{\bar{\nu}_e}(E)$—the detection cross section being $\sigma \propto E^2$—we show in Fig. 41 the $E^2 F^{\oplus}_{\bar{\nu}_e}$ as representative of the observable Earth-modulated signal, where we have taken as initial ν fluxes the ones in Fig. 28. Earth matter effects could be measured in a single detector, if it has enough energy resolution and statistics to track the wiggles in the

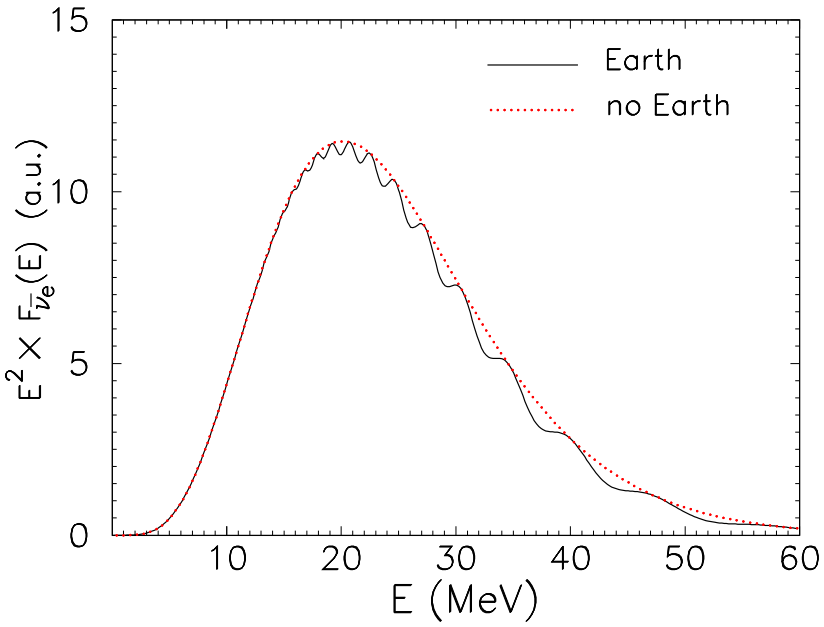

Fig. 41. – Observable signal $E^2 F_{\bar{\nu}_e}$ with (continuous curve) and without (dotted curve) Earth crossing.

observed energy spectrum, induced by the neutrino oscillations in the Earth. In this context, a Fourier analysis of the SN neutrino signal has been proposed as a powerful tool to diagnose this modulation, identifying the peak associated with the Earth crossing in the power spectrum [415].

The observability of the Earth matter effect largely depends on the neutrino average energies and on the flavor-dependent differences between the primary spectra. In this regard, recent SN simulations indicate lower average energies than previously expected [30, 411] and a tendency towards the equalization of the neutrino fluxes of different flavors during the cooling phase (at $t_{\rm pb} \gtrsim 1$ s). Motivated by these new inputs, an updated study on the observability of this effect at large next-generation underground detectors (i.e., 0.4-Mton WC, 50-kton scintillation and 100-kton LAr detectors) was performed in Ref. [416]. It has been found that the detection of the SN neutrino Earth matter effect could be more challenging than expected from previous studies. Remarkably, it was argued that none of the proposed detectors shall be able to detect the Earth modulation for the neutrino signal of a typical Galactic SN at 10 kpc. This should be observable in a 100-kton LAr detector for a SN at few kpc, while all three detectors would clearly see the Earth signature for very close-by stars only ($d \sim 0.2$ kpc).

The Earth effect could also produce a modification in the SN $\bar{\nu}_e$ light curve measured by the IceCube neutrino telescope. Therefore, IceCube could detect the Earth effect by the relative difference in the temporal signals with a high-statistics Mton WC detector, if only one of the two detectors is shadowed [417]. However, using the neutrino fluxes as from recent SN simulations also IceCube, used as co-detector together with a Mton-class WC detector, seems not to be able to detect any sizable variation in the SN neutrino

event rate for any Galactic SN.

Synopsis of signatures of flavor conversions. To summarize, we present a synopsis of the discussed signatures of flavor conversions in SN neutrinos and their sensitivity to the neutrino mass hierarchy in Table III. We focus on early time neutrino signal (neutronization or accretion phase) where we assume that the self-induced effects are matter suppressed. Moreover, we take the MSW matter effects along a progenitor static matter density profile.

TABLE III. – *Different detectable signatures of SN neutrino oscillations at early times and sensitivity to the mass hierarchy.*

Mass Hierarchy	P_{ee}	$\bar{P}_{ee}$	ν_e burst	$\bar{\nu}_e$ rise time	Earth effects
NH	0	$\cos^2\theta_{12}$	absent	long	$\bar{\nu}_e$
IH	$\sin^2\theta_{12}$	0	present	short	ν_e

4˙12. *Outlook.* – The dense SN core represents a unique laboratory to probe neutrino flavor mixing in high-density conditions. Indeed, within a radius of a few hundred kilometers, the neutrino gas is so dense to become a "background to itself." In these conditions, we have shown how the neutrino flavor evolution equations become highly non-linear, leading to surprising and counterintuitive phenomena, like neutrinos and antineutrinos of different energies collectively oscillating to some other flavor. Another surprising result is the partial or complete energy-dependent flavor exchange, namely spectral swapping or spectral splits, as neutrinos travel out from a dense central region to the low neutrino density of the outer layers. During the past few years, our understanding of non-linear neutrino oscillations has seen substantial progress. Analytical and numerical works by several groups have shed light on the basic picture of non-linear neutrinos oscillations, although still many open issues remain to be clarified. In particular, it has been appreciated that self-induced flavor conversions are related to instabilities in the flavor space. While the self-induced flavor evolution is a non-linear phenomenon, the onset of these conversions can be examined through a standard *stability analysis* of the linearized EoMs [418] (see also [327]). Moreover, interesting conceptual studies have been also carried on to clarify some of the aspects related to the collective flavor dynamics in SNe [419-423].

The recent insight that interacting neutrino fields can *spontaneously break* symmetries inherent to the initial conditions in the flavor evolution together with hints of asymmetric neutrino emission from the the most recent SN simulations in 3D will require a critical reinvestigation of the previous results obtained within the bulb model. Seminal studies in this directions have just started. Furthermore, it has been speculated that in the transition region between the neutrino scattering-dominated regime (at high-densities) and the oscillation-dominated one (at lower densities) spin-flavor oscillations could take place, allowing for coherent transformations between neutrinos and antineutrinos [324, 424, 425]. A possible role of anomalous neutrino-antineutrino correlations in the development of the self-induced oscillations has also been discussed [426-428]. Remarkably, new physics scenarios could have a strong impact on the self-induced flavor conversions. In this

regard, strong effects on collective oscillations have been found due to spin-flip transitions [429, 430], triggered by a ν magnetic moment 100 times larger than the Standard Model one, assuming typical magnetic fields in the SN envelope ($B \sim 10^{10} - 10^{12}$ G). Moreover, the presence of non-standard flavor changing interactions among SN neutrinos and the background fermions [431] or among neutrinos themselves [432] would dramatically affect the self-induced flavor changes. The putative existence of extra light sterile neutrino families is also expected to modify the active neutrino fluxes and the above described picture of neutrino self-interactions [164, 166, 167].

An appropriate characterization of these effects would motivate additional work to investigate their impact on the observable neutrino signal [88, 165, 433], on the r-process nucleosynthesis in SNe [167, 434], and on the neutrino energy transfer to the stalled shock wave [87, 88, 98].

Matter effects on SN neutrino oscillations can imprint peculiar signatures on the observable neutrino signal with a strong sensitivity to the mass hierarchy. Neutrino flavor conversions on the wake of the shock-wave propagation represent an intriguing possibility to follow the SN dynamics in real time through the neutrino signal. An accurate prediction of the observable oscillation signatures imprinted on the SN neutrino signal is extremely timely now, in relation to the intense experimental activity for the realization of large-volume detectors for low energy neutrino astronomy.

5. – Diffuse Supernova Neutrino Background

Author: I. Tamborra

While the occurrence rate of a Galactic SN is only ≤ 3 per century [435, 436] and the probability of detecting neutrinos from the next Galactic explosion will be challenged by the location of the SN with respect to the detectors on Earth, on average one SN is exploding every second somewhere in the Universe. The Diffuse Supernova Neutrino Background (DSNB) is the total flux of neutrinos and antineutrinos with MeV energy emitted by all SNe in our Universe. It is expected to be isotropic and stationary and it will provide us with a unique portrait of the SN population. Although not yet detected, the DSNB discovery prospects are excellent. The DSNB detection will be crucial to test our current understanding of the SN dynamics and SN redshift distribution. In this section, we report on the present status of the DSNB searches and its theoretical uncertainties.

5˙1. *Main ingredients and DSNB upper limits.* – The DSNB flux depends on the SN distribution according to their progenitor mass M and redshift z and on the neutrino energy spectra. For each neutrino flavor ν_α ($\alpha = e, \bar{e}, \mu$ or τ) with observed energy E, the DSNB is defined as [437]:

$$\Phi_{\nu_\alpha}(E) = \frac{c}{H_0} \int_{M_0}^{M_{\rm max}} dM \int_0^{z_{\rm max}} dz \, \frac{\dot{\rho}_{SN}(z, M) F_{\nu_\alpha}(E(1+z), M)}{\sqrt{\Omega_M (1+z)^3 + \Omega_\Lambda}} \, , \tag{61}$$

where c is the speed of light, $H_0 = 70$ km s^{-1} Mpc^{-1} the Hubble constant, $\Omega_M = 0.3$ and $\Omega_\Lambda = 0.7$ are the matter and dark energy fractions of the cosmic energy density. $F_{\nu_\alpha}(E, M)$ is the oscillated ν_α energy flux for a SN progenitor with mass M introduced in Sec. **4˙3**. The comoving SN rate (SNR) is labelled as $\dot{\rho}_{SN}$ and it is expected to be larger between $z = 0$ and $z_{\rm max} \simeq 5$ (see Sec. **5˙1.1**). The redshift correction of the energy in Eq. (61) is due to the fact that each neutrino emitted from a SN at redshift z will have energy $E' = E(1+z)$ being E the neutrino energy observed on Earth. As a consequence, neutrinos coming from high-z are pushed towards lower energies; therefore the DSNB flux is dominated by the $z \leq 1$ contribution [437]. As it will be discussed in the next section, the SN mass distribution is such that the least massive stars (with $M \sim M_0 \simeq 8\ M_\odot$, being M_0 the minimum progenitor mass necessary to have a core-collapse SN) give the larger contribution to the DSNB. The DSNB is then weakly dependent on $M_{\rm max} \simeq 125\ M_\odot$ (tentative upper limit for the occurrence of core-collapse SNe [437]) and $z_{\rm max}$.

Since first studies on the DSNB and on its possible detection [438-442], our knowledge on the topic has increased considerably (see, e.g., Refs.[443, 444] for dedicated review papers). From the experimental standpoint, a milestone was reached when Super-Kamiokande placed an upper limit on the $\bar{\nu}_e$ component of the flux [445] ($\phi_{\bar{\nu}_e} \sim$ 0.1–1. cm^{-2}s^{-1} above 19.3 MeV threshold), excluding some theoretical models [21]; while the upper limits on the other neutrino flavors above 19.3 MeV are less strong: $\phi_{\nu_e} <$ 73.30–154 cm^{-2}s^{-1}, $\phi_{\nu_\mu + \nu_\tau} <$ (1.–1.4) $\times 10^3$ cm^{-2}s^{-1} and $\phi_{\bar{\nu}_\mu + \bar{\nu}_\tau} <$ (1.3–1.8)$\times 10^3$ cm^{-2}s^{-1} [446]. The current most stringent upper limits have been placed by the Super-Kamiokande experiment on the $\bar{\nu}_e$ component of the flux above 17.3 MeV threshold, $\phi_{\bar{\nu}_e} \leq$ 2.8–3.0 cm^{-2}s^{-1} at 90% C.L. [18, 447, 448]. More recently, Super-Kamiokande released a new upper limit by performing an analysis with a neutron-tagging technique:

$\Phi_{\bar{\nu}_e} < 5$–$30.\ \mathrm{cm}^{-2}\mathrm{s}^{-1}\mathrm{MeV}^{-1}$ for neutrino energies between 13.3 MeV and 17.3 MeV [449]. As we will discuss later, the most promising energy window relevant for the DSNB detection against background is 11 MeV $\leq E \leq$ 40 MeV [24, 447, 450, 451].

5˙1.1. *Cosmic supernova rate*. One of the key ingredients to compute the DSNB flux is the distribution of core-collapse SNe (i.e., Type II SNe and the subdominant Type Ib/c SNe) with the redshift z and progenitor mass M. The SNR, $\dot{\rho}_{SN}(z, M)$, is proportional to the Star Formation Rate (SFR), $\dot{\rho}_{SF}(z)$, through the initial mass function (IMF), $\psi(M)$:

$$\dot{\rho}_{SN}(z, M) = \frac{\psi(M)}{\int_{0.5M_\odot}^{M_{\rm max}} dM\ M\psi(M)} \dot{\rho}_{SF}(z)\ ; \tag{62}$$

therefore normalization uncertainties on the IMF do not affect $\dot{\rho}_{SN}(z, M)$. The distribution of stellar masses is assumed to follow a universal IMF, as the conventional Salpeter scaling law: $\psi(M) \propto M^{-2.35}$ for stellar masses M between 0.1 $M_\odot$ and 100 $M_\odot$ [452], although even other IMF scaling laws have been suggested, such as an intermediate one [453] or a shallow one [454].

Recent studies [455, 456] suggest that the SFR can be fitted by a piecewise function of the redshift, for example [457]:

$$\dot{\rho}_{SF}(z) \propto \begin{cases} (1+z)^\delta & z < 1 \\ (1+z)^\alpha & 1 < z < 4.5\ , \\ (1+z)^\gamma & 4.5 < z \end{cases} \tag{63}$$

with $\delta = 3.28$, $\alpha = -0.26$, $\gamma = -7.8$, normalized such that $\int_{M_0}^{M_{\rm max}} dM\ \dot{\rho}_{SN}(0, M) = 1.5 \times 10^{-4}\ \mathrm{Mpc}^{-3}\mathrm{yr}^{-1}$. Note that the DSNB dependence on $\dot{\rho}_{SF}(z > 1)$ is weak as the DSNB is mainly determined by the contribution coming from $z \leq 1$. The SNR defined as in Eq. (63) is a growing function of the redshift implying that SNe were most frequent in the past (see also Fig. 42). Given the definition of the SNR (via the IMF), the DSNB is dominated by the low-mass threshold M_0, although this quantity is difficult to predict accurately from theory since stellar properties change rapidly between 6–10 $M_\odot$. On the other hand, the upper limit mass $M_{\rm max}$ is less important because of the fast decline of the IMF with M.

In order to estimate the DSNB, one could rely on direct measurements of the SNR, instead of using Eq. (62). However, while the shape of the SNR is basically well known, its measurements are governed by normalization errors [52, 455]. Reference [52] pointed out that the normalization from direct SN observations was lower than that from SFR data by a factor ~ 2, this discrepancy is known as the "supernova-rate problem." The reasons for such a mismatch may be manifold. It might be that a large number of SNe are actually dim (either due to dust obscuration or being intrinsically weak), or that systematic changes are needed in our understanding of stars and SN formation.

Measurements of the SNR have greatly improved in the last few years [458-462]. Figure 42 shows the SNR from the most recent cosmic measurements in comparison with the one predicted from the SFR assuming that all SNe with $M \geq 8\ M_\odot$ yield optical SNe [52, 455, 463]. It is clear as the SNR problem has been cured at low z where we now have a better understanding of the dust extinction in the host galaxies and of the SN luminosity function, but the SNR is still affected by large uncertainties at high z. It

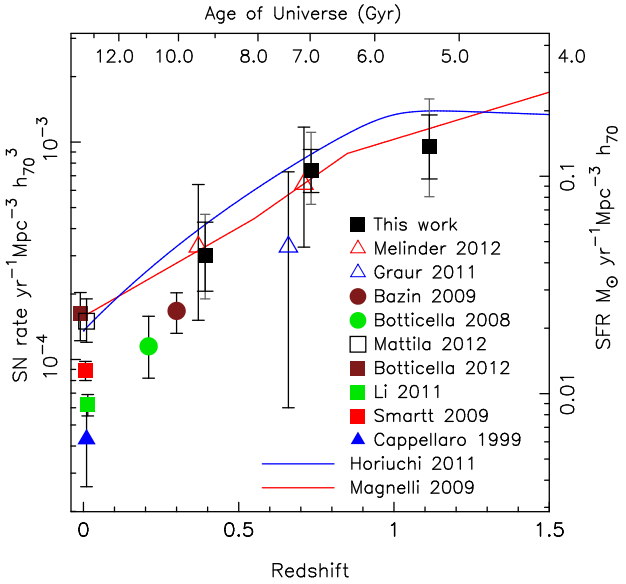

Fig. 42. – Cosmic supernova rate as a function of the redshift. The SFRs from [52, 463] are shown as continue lines after extrapolating the SNR from the SFR as from Eq. (62), assuming that progenitors with mass 8 $M_\odot \leq M \leq 50\ M_\odot$ produce optical SNe. Measured SNRs from recent work are also shown. (Reprinted figure with permission from [461]; copyright (2012) by the American Astronomical Society.)

might also be that the fraction of "invisible" SNe (i.e., not optically visible SNe) increases with the redshift [460, 464].

The SNR estimation will hopefully further improve within the next few years. In fact SNR measurements will come from synoptic surveys which will scan the full sky and probe the SN population with high sensitivity (see, e.g., discussion in Ref. [465] and references therein). Such surveys are expected to pin down the error on the normalization of the SNR and, as a consequence, on the DSNB normalization. On the other hand, note that the forthcoming detection of the DSNB could provide independent constraints on the SFR [466].

5˙1.2. *Time and progenitor dependence of the neutrino energy fluxes*. The dependence of the DSNB on neutrino oscillation physics and SN progenitors has been discussed in Ref. [468]. As shown in Sec. **2** and Fig. 39, the neutrino luminosities and spectra depend on the compactness of the progenitor star [467]. Moreover, the luminosities of the different flavors are almost equal during the cooling phase, while $L_{\nu_e}, L_{\bar{\nu}_e} > L_{\nu_{\mu,\tau}}$ during the accretion phase. The mean energies are $\langle E_{\bar{\nu}_e,\nu_{\mu,\tau}} \rangle > \langle E_{\nu_e} \rangle$ during the cooling phase (see Fig. 9 and Sec. **2**˙4).

Concerning the neutrino oscillation scenario (see Sec. **4**), while the MSW effect is well understood analytically and it occurs far away from the neutrinosphere, neutrino self-interactions crucially depend on the initial hierarchy among neutrinos of different flavors, number of energy crossings and on the neutrino mass hierarchy. During the accretion phase ($t_{\rm pb} \leq 1$ s), complete or partial multi-angle matter suppression of neutrino self-interactions occurs because of the high matter potential [331,332,334,335]. While during

the cooling phase, multiple spectral splits might appear according to the neutrino mass hierarchy and the number of crossings in the non-oscillated spectra. However, the shape of the spectral splits is smeared and their size reduced due to the similarity of the non-oscillated flavor energy spectra and to ν–ν multi-angle effects, partial neutrino flavor conversions occur and the flavor transition become gentler as time increases [468].

As discussed in Sec. **4**, it is possible to factorize the effects of ν–ν interactions and the MSW resonances for sake of simplicity, as they occur in well separated spatial regions. Denoting with $F^c_{\nu_\alpha}$ the fluxes after the collective oscillations, the unchanged $F^0_{\nu_\alpha}$ will undergo the traditional MSW conversions after ν–ν interactions. The fluxes (F_{ν_e} and $F_{\bar{\nu}_e}$) reaching the Earth after both the collective and MSW oscillations for NH and IH are [328, 469, 470]:

$$F^{\rm NH}_{\nu_e} = \sin^2\theta_{12}[1 - P_c(F^c_{\nu_e}, F^c_{\bar{\nu}_e}, E)](F^0_{\nu_e} - F^0_{\nu_y}) + F^0_{\nu_y} \ , \tag{64}$$

$$F^{\rm NH}_{\bar{\nu}_e} = \cos^2\theta_{12}\bar{P}_c(F^c_{\nu_e}, F^c_{\bar{\nu}_e}, E)(F^0_{\bar{\nu}_e} - F^0_{\nu_y}) + F^0_{\nu_y} \ , \tag{65}$$

$$F^{\rm IH}_{\nu_e} = \sin^2\theta_{12}P_c(F^c_{\nu_e}, F^c_{\bar{\nu}_e}, E)(F^0_{\nu_e} - F^0_{\nu_y}) + F^0_{\nu_y} \ , \tag{66}$$

$$F^{\rm IH}_{\bar{\nu}_e} = \cos^2\theta_{12}[1 - \bar{P}_c(F^c_{\nu_e}, F^c_{\bar{\nu}_e}, E)](F^0_{\bar{\nu}_e} - F^0_{\nu_y}) + F^0_{\nu_y} \ . \tag{67}$$

In Eqs. (64)–(67) we have considered multi-angle ν–ν interactions driven by Δm^2 and θ_{13} between ν_e and ν_y, while the other flavor (ν_x) does not evolve, the effects on self-induced flavor conversions induced by the third flavor being a negligible correction for our purpose [7, 342-344].

5˙2. *Dependence of the DSNB from flavor oscillations and SN progenitor properties.* – Adopting the SNR as from the SFR [Eq. (62)] and time-(and progenitor-) dependent oscillation physics described as in Sec.**5˙**1.2, the dependence of the DSNB on the neutrino oscillation physics and on the SN progenitors has been studied in Ref. [468], adopting long-term SN simulations for three progenitors with masses $M = 18, 10.8, 8.8\ M_\odot$ [30] (with Shen EoS [146]). The features of the neutrino signal of these three progenitors have been extended to the whole estimated SN mass range ($[M_0, M_{\rm max}] = [8\ M_\odot, 125\ M_\odot]$) and time-dependent oscillated neutrino spectra have been included in the DSNB computation implementing MSW and multi-angle ν–ν interactions as a function of the post-bounce time. Notice that, as we will discuss later, the upper limit of the SN mass progenitor as well as the neutrino fluxes might change including failed SNe [471].

Figure 43 shows the DSNB, $E^2 \times \Phi_{\nu_\alpha}$ [with Φ_{ν_α} as in Eq. (61)], as a function of the energy for ν_e ($\bar{\nu}_e$) on the top (bottom). In the plots on the right, the region of interest for Super-Kamiokande detection ($E > 17.3$ MeV) is zoomed. A variation of 10–20% due to the neutrino mass hierarchy is visible at $E \simeq 20$ MeV. In order to investigate the DSNB dependence from the SN cooling and progenitor mass, a case using $t_{\rm pb} = 0.5$ s as representative of all post-bounce times and the 10.8 $M_\odot$ SN progenitor as representative of the whole SN population is shown (thin lines) in comparison to the one computed including all SN mass models (thick lines).

No signature due to ν–ν interactions is visible in Fig. 43, since neutrino self-interactions are suppressed during the accretion phase and they occur at different energies for each post-bounce time during the cooling [468]. Note that Ref. [30] does not include nucleon recoil effects responsible for reducing the differences among the mean energies of different flavors during the cooling phase [29, 60, 472]. Therefore, the adopted SN inputs are useful to estimate the largest oscillation effects that could realistically affect the DSNB.

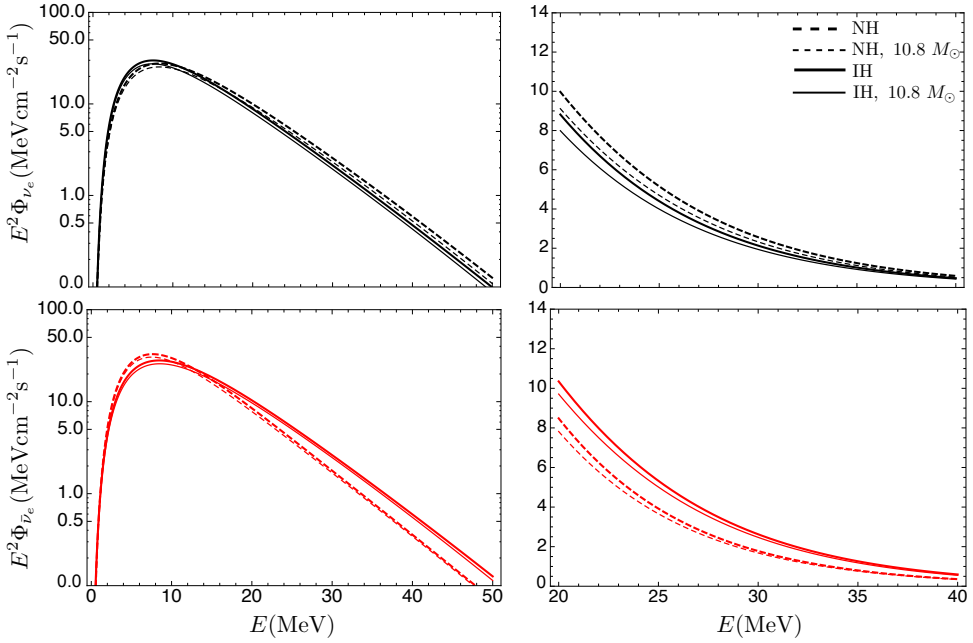

Fig. 43. – Left panels: DSNB as a function of the neutrino energy. Right panels: Zoom of the DSNB flux in the region of Super-Kamiokande detection ($E > 17.3$ MeV). The ν_e ($\bar{\nu}_e$) flux is plotted in black (red). The solid (dashed) line represents the DSNB in IH (NH). The thick lines represent the DSNB including the three SN progenitors and the thin line shows the DSNB obtained considering the 10.8 $M_\odot$ SN progenitor as representative of the whole stellar population. (Reprinted figure from [468]; copyright (2012) by the Institute Of Physics Publishing.)

Note that any flavor conversion occurring during the accretion phase will have a larger impact on the total DSNB, the luminosities during the accretion phase being larger than the cooling ones. While, during the cooling phase, the fluxes are similar and any flavor conversion scarcely affect the DSNB.

Summarizing the impact of the different ingredients on the DSNB: MSW effects are the largest source of variation of the DSNB with respect to the case without oscillations (50–60%), the mass hierarchy induces variations of $\sim 20\%$; neutrino-neutrino interactions, time-dependence of the neutrino energy spectra over ~ 10 s and stellar population are responsible for a smaller variations ($\sim$ 5–10%) [468]. Astrophysical uncertainties in the determination of the DSNB are instead larger: Besides the SN rate problem discussed above, the SNR is affected by a normalization error of $\sim 25\%$, although such error is expected to be dramatically reduced within the next decade. Another potentially small source of error on the DSNB is the nuclear EoS [473]. Moreover, Refs. [474, 475] pointed out as SN models with longer shock revival time produce a resultant higher DSNB event rate, since the larger the gravitational energy of the accreted matter, the larger is the resultant emitted neutrino energy. In principle, the shock revival time might be progenitor dependent and therefore introduce a non-negligible variation of the high-energy tail of the DSNB.

Although theoretical studies have pointed out that the DSNB is sensitive to the SN

progenitor mass, EoS, variations of the shock revival time, neutrino mass hierarchy, and oscillation physics, we stress that the DSNB carries integrated population information. In view of our current knowledge of the flavor oscillation physics and stellar dynamics, it will therefore be extremely difficult to extract information on each of the mentioned aspects from a forthcoming DSNB detection. In this sense, the high statistics of neutrino events potentially provided by the next galactic explosion will be more useful to constrain the SN engine and to learn about its dynamics. As we will discuss in the next section, the DSNB might also be affected by the presence of invisible SNe (probably also responsible for the mismatch between the measured SNR and the one extracted from the SFR) and the DSNB detection will be an extremely powerful instrument to learn about the whole SN population.

5˙3. *Contribution from invisible supernovae.* – Besides stellar core-collapse events that trigger SN explosions, a significant fraction (some 10–30%, possibly even more; e.g., [52-55,176,177,476-478]) could lead to black holes (BH) "directly," i.e., after a relatively short (fractions of a second to seconds) accretion phase of a transiently existing hot neutron star. Such "failed SNe" are expected to produce only faint electromagnetic emission by stripping their loosely bound hydrogen envelopes [55, 479, 480]. The dim emission and red color make them hard to detect at extragalactic distances. Their neutrino emission, however, could account for an important contribution to the DSNB. In Sec. **2˙5** neutrino signals of such events were presented as predicted by recent hydrodynamic simulations. The Super-Kamiokande Collaboration [22, 23] has provided constraints on the neutrino flux from failed SNe, setting a limit about a factor of four higher than predicted in Ref. [471].

Black hole formation may also occur with considerably longer delay, if the SN mechanism does not release enough energy to unbind the whole star. In this case a fair fraction of the stellar matter can fall back to the neutron star (on time scales of minutes to hours) and can push the neutron star beyond the mass limit for the black-hole formation. Such "fallback SNe" would radiate SN-like, though possibly sub-luminous, electromagnetic displays [481]. Their neutrino signals, however, are initially indistinguishable from those of forming neutron stars in ordinary core-collapse SNe. Whether the potentially massive fallback of matter to the neutron star produces observable neutrino emission is presently not clear because of the lack of detailed studies, which are difficult due to the long time scales involved and the likely importance of asymmetries and angular momentum (but see Ref. [482]). Since the rate of fallback SNe in the present-day Universe is predicted to be low [177], we will not consider them in our discussion of the DSNB.

Taking into account the current uncertainties, we will focus on the contributions from core-collapse and failed SNe to the DSNB in the following. We will see that the neutrino emission of failed SNe may indeed not be negligible but instead could make the more luminous component of the observable DSNB.

Neglecting the progenitor mass dependence of the neutrino fluxes as well as of the SN rate, Eq. (61) can be generalized as

$$\Phi_{\nu_\alpha}(E) = \Phi^{\rm BH}_{\nu_\alpha}(E) + \Phi^{\rm NS}_{\nu_\alpha}(E) = \\ = \frac{c}{H_0}\int_0^{z_{\rm max}} dz\, \frac{\dot\rho_{\rm SN}(z)[f_{\rm BH}F^{\rm BH}_{\nu_\alpha}(E(1+z)) + f_{\rm NS}F^{\rm NS}_{\nu_\alpha}(E(1+z))]}{\sqrt{\Omega_M(1+z)^3+\Omega_\Lambda}}\,, \tag{68}$$

with $f_{\rm NS}$ ($f_{\rm BH}$) the fraction of core-collapse (failed) SN, such that $f_{\rm NS} + f_{\rm BH} = 1$, where we have subdivided the whole SN family in two major categories, neglecting the fallback

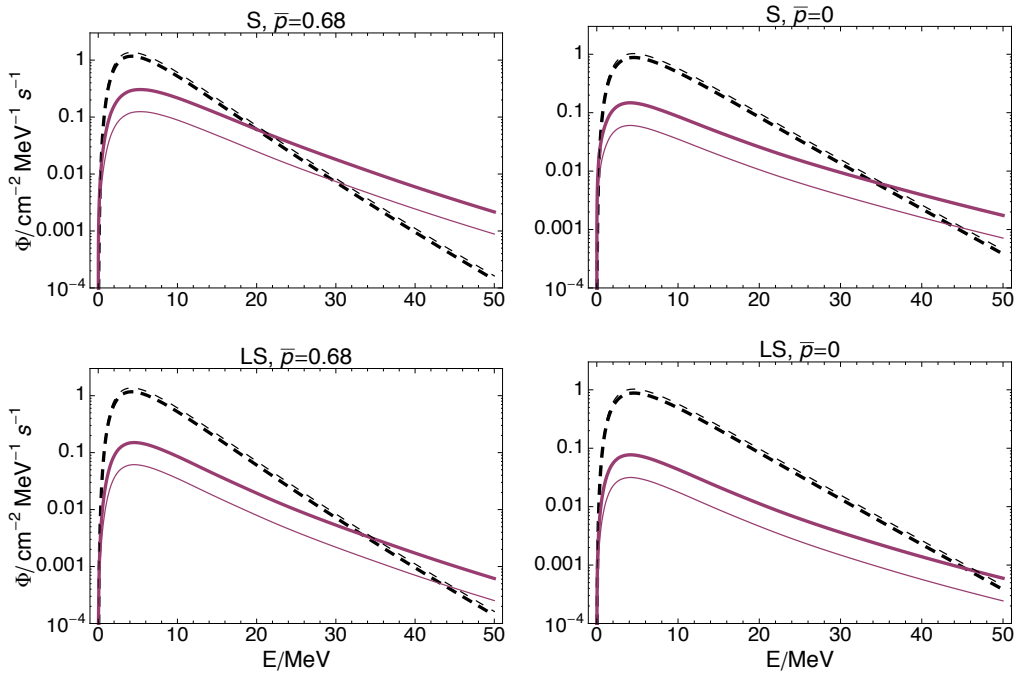

Fig. 44. – Diffuse flux of $\bar{\nu}_e$ from core-collapse SNe (failed SNe) as a function of the energy plotted with dashed (solid) curves for S and LS EoS and survival probability $\bar{P} = 0.68$ (including MSW effects, left panels) and $\bar{P}_{ee} = 0$ (no oscillations, right panels). The fraction of failed SN is $f_{\rm BH} = 22\%$ (thick curves) and $f_{\rm BH} = 9\%$ (thin curves). (Reprinted figure with permission from [471]; copyright (2009) by the American Physical Society.)

SN class (that could easily fall in one or the other case according to the progenitor mass) and assumed that both these families follow the SFR redshift dependence.

The expected diffuse flux has been discussed in Ref. [471], assuming typical neutrino spectral parameters for the NS case as in Ref. [27] (i.e., $L_{\bar{\nu}_e} = L_{\bar{\nu}_x} = 5 \times 10^{52}$ erg/s, $\langle E_{\bar{\nu}_e} \rangle = 15$ MeV, $\langle E_{\bar{\nu}_x} \rangle = 18$ MeV, $\alpha_{\bar{\nu}_e} = 3.5$, $\alpha_{\bar{\nu}_e} = 2.5$) and modeling the BH case as in Ref. [172] for a typical failed SN progenitor of 40 $M_\odot$ with stiffer Shen (S) EoS [146] (i.e., $L_{\bar{\nu}_e} = 12.8 \times 10^{52}$ ergs, $L_{\bar{\nu}_x} = 4.9 \times 10^{52}$ erg/s, $\langle E_{\bar{\nu}_e} \rangle = 23.6$ MeV, $\langle E_{\bar{\nu}_x} \rangle = 24.1$ MeV) and softer Lattimer-Swesty (LS) EoS [86] (i.e., $L_{\bar{\nu}_e} = 4.5 \times 10^{52}$ ergs, $L_{\bar{\nu}_x} = 2.2 \times 10^{52}$ erg/s, $\langle E_{\bar{\nu}_e} \rangle = 20.4$ MeV, $\langle E_{\bar{\nu}_x} \rangle = 22.2$ MeV).

The uncertainty of the fraction of failed SNe has been parametrized with $f_{\rm NS} \in [0.78 - 0.91]$, corresponding to an upper limit for neutron-star-forming collapses varying in the interval 24–50 $M_\odot$. Moreover, since the role of neutrino oscillations (especially of neutrino self-induced flavor conversions) has not been explored in this context, only MSW effects have been included: $F_{\bar{\nu}_e}(E) = \bar{P}_{ee} F^0_{\bar{\nu}_e}(E) + (1 - \bar{P}_{ee}) F^0_{\bar{\nu}_x}(E)$, with $\bar{P}_{ee} = 0, 0.68$ (see Tab. III, with $\bar{P}_{ee} = 0.68$ coming from the dependence of the survival probability from θ_{12}). The corresponding DSNB is shown in Fig. 44.

Assuming flavor conversions play a non-negligible role (i.e., $\bar{P}_{ee} = 0.68$), the largest contribution from failed SNe comes from the stiffer EoS (S EoS case). In the latter case, the $\Phi_{\rm BH}$ enhances the DSNB for $E \geq 20$ MeV, improving the DSNB detection chances (compare dashed with continue lines in Fig. 44) [471]. More recently, similar conclusions

have been reached by adopting the progenitor dependence as from hydrodynamical simulations of a range of SN progenitors and redshift dependence of the BH-formation rate based on the metallicity evolution of galaxies [475].

Although the largest contribution to the DSNB comes from $z \leq 1$, the flux from failed SNe from higher redshifts might still be substantial [460, 464, 483]. In this sense, the DSNB detection could directly allow to investigate the black-hole forming collapse, constrain its energetics and cosmological rate even beyond $z \simeq 1$.

If the neutrino emission is larger for failed SNe than for ordinary SNe as expected, then the signal increase in the detectors will be significantly larger in the high-energy tail of the DSNB spectrum [24, 170-172, 471, 475, 484]. This is promising in terms of neutrino detection chances and it would be a unique opportunity to study such SN progenitors, being otherwise optically invisible [485, 486].

As discussed in Ref. [465], we can already constrain the visible and invisible SN rate at $z = 0$ on the basis of current data under the assumption that the shape of the SNR is known. It emerges that the allowed region for invisible SNe is indeed non-zero, but it cannot be arbitrarily large. Future observations will be extremely helpful on restricting the allowed region for visible SNe.

Assuming that in the next few years, upcoming SN surveys will be able to pin down to 5% the uncertainty on the SNR, the variation of the one-year detection rate in Super-Kamiokande for different fractions of $f_{\rm BH}$ is discussed in Ref. [465] by approximating the neutrino energy spectrum with a Fermi-Dirac distribution with zero chemical potential and total energy emitted for each flavor to $L_{\nu_\alpha} = 0.5 \times 10^{53}$ erg, $\langle E_\alpha \rangle = 12.6$ MeV for the failed SNe, while $L_{\nu_\alpha} = 0.9 \times 10^{53}$ erg, $\langle E_{\nu_\alpha} \rangle = 23.6$ MeV for core-collapse SNe. Figure 45 shows the expected one-year detection rate in Super-Kamiokande for $f_{\rm BH} = f_{\rm invis} = 0, 10, 40\%$. It is evident as, increasing the fraction of invisible SNe, a higher detection rate is expected especially in the high energy tail of the energy spectrum. Note as, any indirect experimental constraint of this kind on the the NS/BH formation ratio will be also useful to constrain the still disputed mechanism(s) by which stars explode as SNe.

We assumed that "failed" SNe are a fraction of the total SNR through this Section. However, a first attempt to model the rate of failed SNe as a function of the redshift has been done in Ref. [464], based on gamma-ray burst observations which could originate from core collapses yielding rapidly rotating BHs. Reference [464] seems indeed to find a much higher fraction of failed SNe at $z \geq 1$ than locally. See also Refs. [177, 475] for dedicated discussions.

5˙4. *Detection perspectives.* – The DSNB detection is one of the main goals of neutrino astrophysics. However, the DSNB detection is strongly affected by backgrounds, which reduce the detectable energy window to 11 MeV $\leq E \leq$ 40 MeV [24, 447]. Figure 46 shows the expected DSNB, in the presence of standard core-collapse (blue line) and failed (brown line) SNe and their sum (black line), as discussed in Sec. **5˙3**. The expected atmospheric, reactor and solar neutrino backgrounds are also plotted.

Water Cherenkov detectors, such as Super-Kamiokande, being mostly sensitive to $\bar{\nu}_e$, have atmospheric and reactor neutrinos as major backgrounds. The atmospheric neutrinos fall within the same DSNB energy range and have an isotropic distribution in space, therefore it is very difficult to discriminate the DSNB signal from the background. However, the DSNB is larger than the atmospheric background around 30–40 MeV (see Fig. 46), thus restricting the experimental detection window to this range [242]. Reactor neutrino events could instead be distinguishable from their direction [487], but no

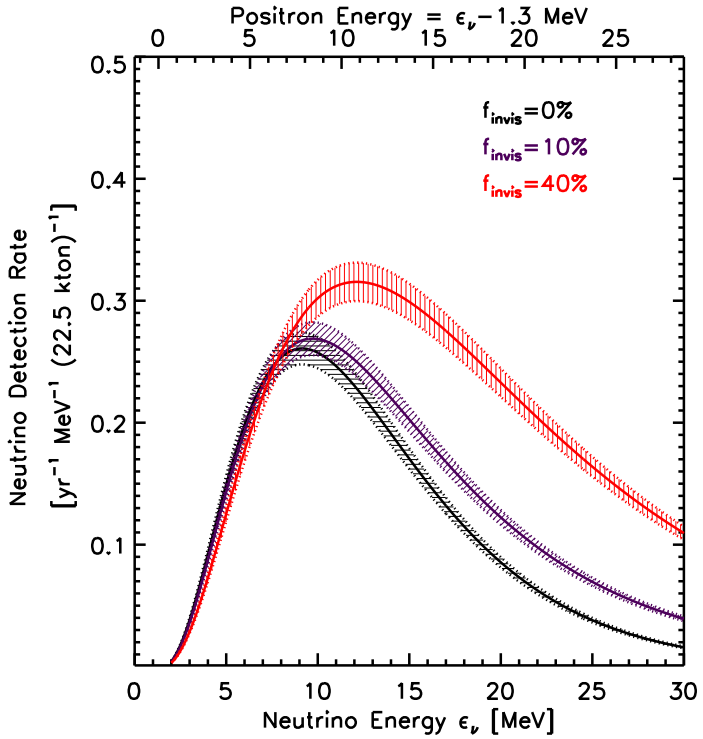

Fig. 45. – One-year neutrino detection rate in Super-Kamiokande as a function of the observed neutrino energy for three different fractions of invisible SNe ($f_{\rm BH} = f_{\rm invis} = 0, 10, 40\%$). The band thickness of the curves is given by 5% of the uncertainty on the SNR as expected from upcoming SN surveys. (Reprinted figure with permission from [465]; copyright (2010) by the American Physical Society.)

dedicated study concerning the DSNB exists yet. Liquid argon detectors are mostly sensitive to ν_e, and therefore solar and atmospheric neutrino fluxes are the main backgrounds [488]. Solar neutrinos prevent studying the DSNB below 18 MeV for all the above-mentioned detectors (see Fig. 46); however they can be subtracted very effectively since their direction and flux can be well determined([14]). Clearly the detection-energy windows would be larger for an enhanced DSNB (i.e., including the contribution from failed SNe), and therefore a larger $f_{\rm BH}$ would be advantageous for signal to background discrimination.

An enhanced signal discrimination over the background for the DSNB detection in Super-Kamiokande will be reached by dissolving gadolinium in water [203] (see Sec. **3**); this option is currently being tested through the Evaluating Gadolinium's Action on Detector Systems (EGADS) facility [489] and the Super-Kamiokande Collaboration has

([14]) Note that solar neutrinos might constitute a non-minor impediment to the DSNB detection in LAr detectors possibly due to uncertainties in the cross section and poor pointing.

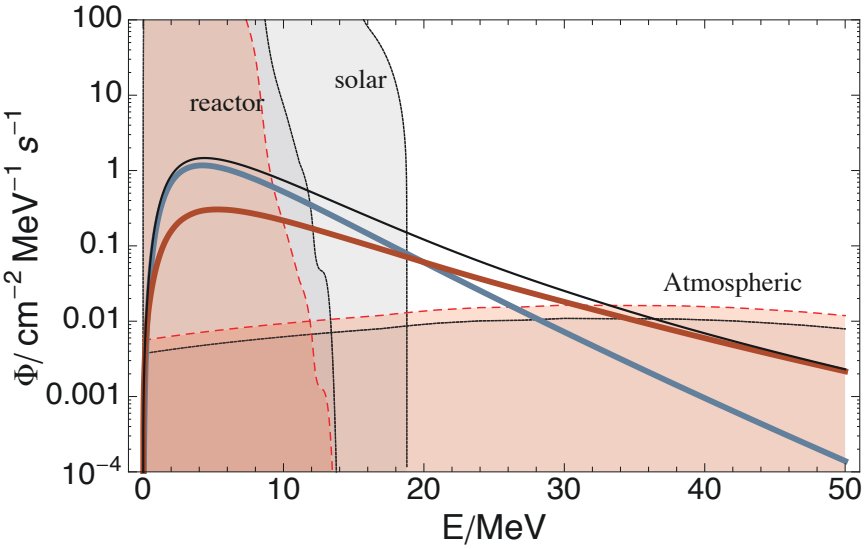

Fig. 46. – Expected diffuse flux of $\bar{\nu}_e$ from core-collapse SNe in blue and failed SNe (S EoS, $\bar{P}_{ee} = 0.68$ and $f_{\rm NS} = 0.78$) in brown. Their sum is in black (see Sec. **5**˙3). The atmospheric and reactor fluxes are shown for the Kamioka (solid, gray) and Homestake (dashed, red) sites. Since the ν_e and $\bar{\nu}_e$ atmospheric fluxes are very similar, only one is plotted. (Reprinted figure with permission from [483]; copyright (2012) by the American Physical Society.)

just approved the future enrichment of Super-Kamiokande with Gd, the so-called SuperK-Gd project [490]. This would result in a reduction of the background by a factor of ~ 5 for invisible muons and by at least an order of magnitude for spallation [180,181,203,242]. The planned liquid scintillator detector, JUNO, should also be able to separate DSNB neutrino events from the background very efficiently, offering a great opportunity to detect the DSNB [219, 220, 491].

In order to give an idea of the expected number of events for the detectors described above (see also Sec. **3**), Fig. 47 shows the smeared event rates as a function of the detected energy for a 560-kton WC detector (blue curve), a 20-kton liquid scintillator (green curve) and a 40-kton LAr detector (red curve). The rates have been computed including the dominant reaction channels (i.e., IBD in water and scintillator detectors, and ν_e CC interactions on ^{40}Ar for the LAr detector) and assuming the 27 $M_\odot$ SN progenitor introduced in Sec. **2**˙4 as representative of the whole SN population; for simplicity, ν–ν interactions have been neglected. Note as the presented rates may be optimistic because of the high NS mass of the adopted 27 $M_\odot$ SN progenitor.

5˙5. *Outlook*. – The study of the DSNB is still affected by several theoretical uncertainties, preventing us from a precise forecasting of the expected signal. Assuming that synoptic surveys will be able to pin down the uncertainty on the SNR up to 5% and that the neutrino mass hierarchy will be known within the next decade, what could we learn from the DSNB detection?

- Constraints on the stellar population. The DSNB receives contributions from all families of SN progenitors and it will be an independent test of the global SN rate.
- Constraints on the fraction of core-collapse and failed SNe. The DSNB will be

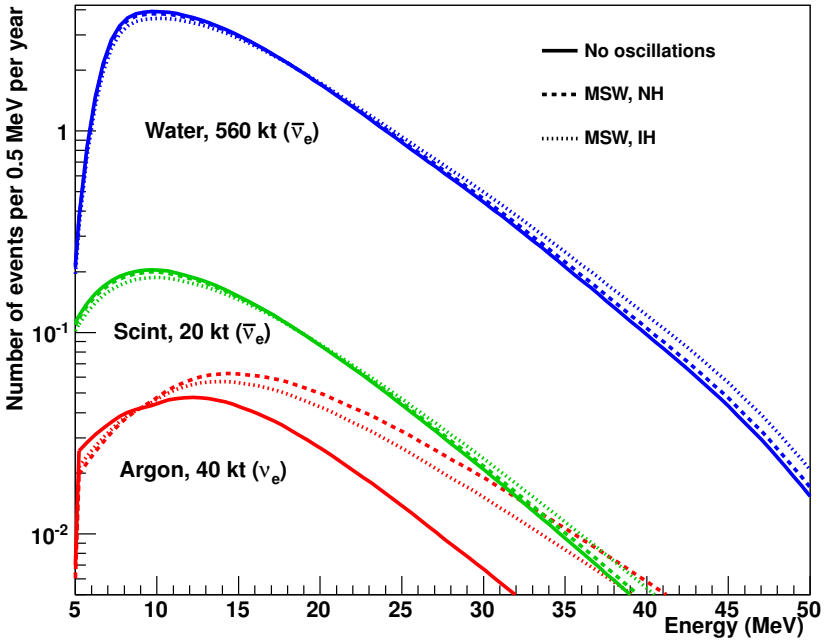

Fig. 47. – Smeared event rates as a function of detected energy based on an optimistic estimation of the DSNB obtained assuming a 27 $M_\odot$ SN progenitor (see Sec. **2**˙4) as representative of the SN population and MSW effects only. The rates are shown for a 560-kton WC detector (top, blue curves), a 20-kton liquid scintillator (center, green curves) and a 40-kton LAr detector (bottom, red curves). MSW oscillations under NH and IH assumptions are included.

a precious instrument to test our current knowledge of the core-collapse physics, especially for the failed SN class only detectable through its neutrinos. Constraints on the NS/BH formation ratio may also indirectly help to decipher the still disputed mechanism(s) by which stars explode as supernovae.

- Constraints on the neutrino emission properties. As discussed in Ref. [492], with the existing current upper limits on the $\bar{\nu}_e$ diffuse background from Super-Kamiokande and the few events from the SN 1987A, it is possible to exclude some regions of the $L_{\bar{\nu}_e}$–$\langle E_{\bar{\nu}_e} \rangle$ parameter space. Such bounds will surely be improved by real data.

- A precise estimation of the DSNB is also relevant for the background modeling in direct dark matter searches [493, 494].

- The DSNB detection could be useful to constrain neutrino decay models [495, 496], neutrino electric or magnetic transition moments [497] and the existence of light scalar bosons [498].

6. – Conclusions and Perspectives

Neutrinos play a crucial role during all stages of stellar collapse and explosion. The emission of electron neutrinos produced by electron captures accelerates the implosion of the unstable, degenerate stellar core and mediates the neutronization of its matter. The absorption of electron neutrinos and antineutrinos above the neutrinospheric layers initiates and powers the blast wave of the explosion and determines the trans-iron nucleosynthesis by setting the neutron-to-proton ratio in the innermost, neutrino-heated ejecta. The emission of neutrinos and antineutrinos of all flavors drives the cooling evolution of the newly formed neutron star that is left behind at the center of the supernova explosion. In order to summarize the expected neutrino emission characteristics, we show in Fig. 48 the source luminosities L_ν (upper panels), average energies $\langle E_\nu \rangle$ (middle panels), and spectral shape parameters α (lower panels) of ν_e, $\bar{\nu}_e$ and ν_x for the shock-breakout, accretion and cooling phases of a 27 $M_\odot$ supernova progenitor simulated by the Garching group.

The detection of two dozen electron antineutrinos from SN 1987A in three underground experiments splendidly confirmed our basic theoretical picture of stellar collapse and the birth of neutron stars. However, the signal statistics were too poor to yield detailed information of the explosion mechanism, which is still one of the most nagging problems in stellar astrophysics. The solution of this riddle is of fundamental importance for a better understanding of the origin of neutron stars and black holes and for the definition of the role of supernovae in the cosmic cycle of element formation. In this context only neutrinos (and gravitational waves) can serve as direct probes of the physics taking place at the center of the explosion. A well resolved time and energy dependent neutrino signal from a future Galactic event will therefore provide a benchmark of unprecedented value for supernova physics.

Hydrodynamical supernova simulations have now reached the multi-dimensional front including a full and sophisticated treatment of the neutrino reactions that play a role in the stellar core. The first three-dimensional supernova models of that sort have shown that neutrinos carry imprints of hydrodynamic processes occurring around the newly formed neutron star during the accretion phase. In particular, quasi-periodic modulations of the neutrino emission reflect dynamical mass motions that precede and enable the onset of the explosion. Rapid declines of the neutrino luminosity and non-monotonicities in the evolution of the spectral parameters may reveal the composition-shell structure of the progenitor and can indicate the end of the accretion phase (see Fig. 48). The spectral evolution of the neutrino signal is determined by the neutrinospheric conditions and thus carries radius and mass information of the contracting proto-neutron star. The late-time evolution of the neutrinos radiated during the cooling phase has a great potential to yield important insights into the still incompletely understood properties of matter at supranuclear densities in the interior of the nascent neutron star.

While multi-dimensional supernova modeling seems to be on a good track to confirm the viability of the neutrino-driven explosion mechanism within the present uncertainties of input physics and initial conditions, an empirical validation of the theoretical concept is still missing. A Super-Kamiokande-size detector for electron neutrinos like DUNE, in combination with existing (Super-Kamiokande, IceCube, etc.) and proposed (Hyper-Kamiokande, JUNO) water and liquid scintillator detectors for electron antineutrinos, would provide excellent time and/or spectral resolution for a Galactic supernova. Therefore, they would offer a fundamentally new quality for supernova research through neutrino measurements. Resolving the prompt shock-breakout burst of electron neutri-

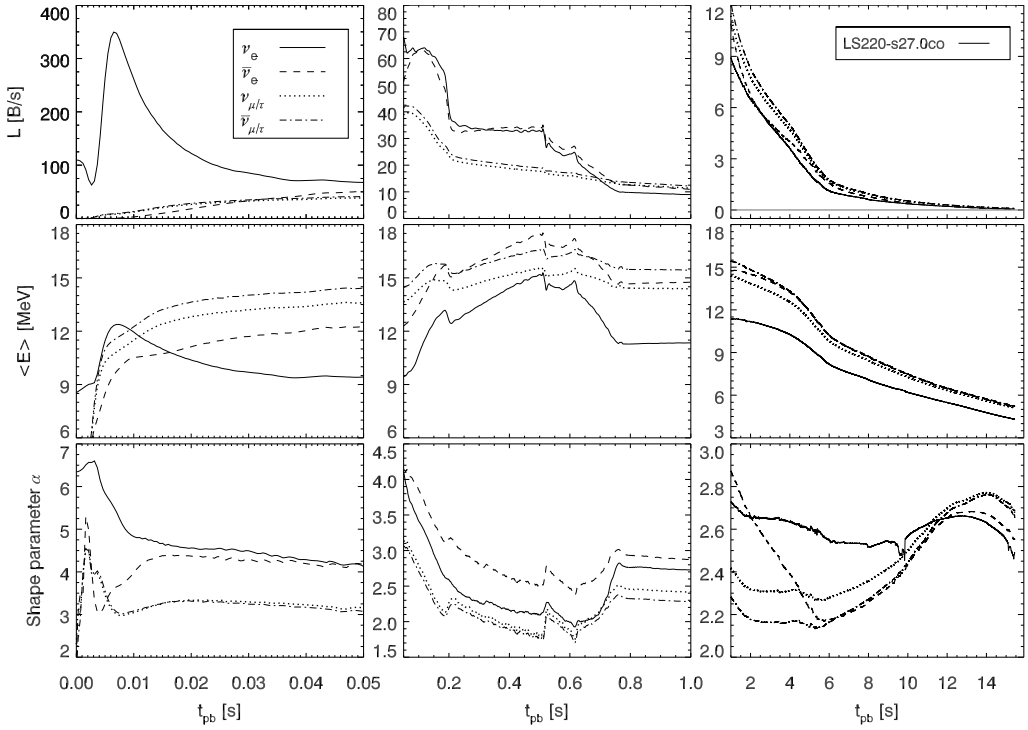

Fig. 48. – Post-bounce evolution of the neutrino signal from a neutron star with baryonic (final gravitational) mass of ∼1.776 (∼1.592) $M_\odot$ formed in the explosion of a 27 $M_\odot$ progenitor. The panels show the luminosities (*top*, in units of $\mathrm{B\,s^{-1}} = 10^{51}\,\mathrm{erg\,s^{-1}}$), mean energies (ratios of energy fluxes to number fluxes; *middle*), and spectral shape parameters (*bottom*) for ν_e (solid lines), $\bar{\nu}_e$ (dashed), $\nu_{\mu,\tau}$ (dotted) and $\bar{\nu}_{\mu,\tau}$ (dash-dotted) during the shock-breakout burst of ν_e (*left column*), accretion phase (*middle column*), and proto-neutron star cooling phase (*right column*). The 1D simulation was performed with the nuclear EoS of Lattimer & Swesty [86]; using the incompressibility modulus of $K = 220\,\mathrm{MeV}$) and took into account self-energy shifts in the β-interactions of free nucleons and a mixing-length treatment of proto-neutron star convection. The steep decline of the ν_e and $\bar{\nu}_e$ luminosities at ∼0.2 s is associated with the decrease of the mass-accretion rate when the edge of the stellar silicon layer falls through the stalled shock. The explosion was artificially initiated at 0.5 s and accretion finally ends at ∼0.8 s after bounce.

nos would allow to determine the distance to the supernova even without electromagnetic detection and would define a precise reference point for the instant of core bounce. The simultaneous information in both electron neutrino and antineutrino sectors could set constraints on the equation of state (e.g., the baryonic symmetry energy) at neutrinospheric conditions and, in particular, it would help to answer the long-standing question whether supernovae are sources of r-process elements or of certain proton-rich isotopes produced by the neutrino-proton process. The direct comparison of electron neutrino and antineutrino measurements could also serve to clarify the existence of a dipolar lepton-emission asymmetry (LESA) that is a recent, unexpected (though yet unconfirmed) discovery by the first three-dimensional supernova models with important implications for supernova nucleosynthesis and pulsar kicks. Moreover, a multitude of complex and not yet fully understood flavor transformation effects can modify the neutrino signal on the way from

the source at the supernova center to the detectors on Earth. Supernova neutrino data would provide extremely valuable information to decipher the evolution of the neutrino flavor field, which is indispensable for disentangling the source properties from effects imprinted on the signal by flavor transformations.

The role of astrophysical messengers played by supernova neutrinos is largely associated with the signatures imprinted on the observable neutrino burst by the supernova core dynamics and by the flavor conversions occurring deep inside the star. Within a radius of a few hundred kilometers from the neutrinosphere, the neutrino field is so dense to become a "background to itself," making the neutrino flavor evolution highly non-linear and leading to surprising and counterintuitive collective phenomena, when the entire neutrino system oscillates coherently as a single collective mode. The rich phenomenology associated with these non-linear flavor dynamics is still in its infancy and many unexpected results have been found in the past years. It is therefore mandatory to further investigate the role of flavor instabilities in the interacting neutrino field. Directions of further studies include: The characterization of the self-induced oscillations in models with reduced symmetries compared to what is usually assumed in the neutrino light-bulb model; investigations of the role of flavor conversions in the light of multi-dimensional hydrodynamic supernova simulations and their impact on the explosion dynamics and nucleosynthesis; or the role of residual scatterings and the possibility of self-induced spin-flavor transitions.

Matter effects on supernova neutrino oscillations could imprint peculiar signatures on the observable neutrino signal with a strong sensitivity to the still-unknown neutrino mass hierarchy. Neutrino flavor conversions in the wake of the shock-wave propagation could also represent an intriguing possibility to follow the supernova dynamics in real time through measurements of the neutrino signal. The impact of the matter turbulence on the shock-wave signature would require further investigations. Studies in these directions will be mandatory once future, high-resolution supernova simulations will become available.

Current and planned large underground neutrino detectors offer unprecedented opportunities to study supernova and neutrino properties through high-statistics signals from different interaction channels. However, the exciting possibilities associated with the next Galactic explosion are in tension with the low Galactic supernova rate. The supernova rate in our Galaxy and within the Magellanic Cloud is estimated to be between one and several per century, but even with a high assumed rate we might have to wait a long time for the next Galactic supernova. In contrast, the DSNB, i.e., the flux of neutrinos and antineutrinos coming from all past core-collapse supernovae in our Universe, is a guaranteed signal to study supernovae by their neutrinos in the forseeable future. The perspectives for a detection of the DSNB within the next decade are promising, especially with the just approved SuperK-Gd project (i.e., gadolinium-enhanced Super-Kamiokande detector) and with JUNO as a planned liquid scintillator experiment. Such a measurement would push the frontier of neutrino astronomy literally towards the edges of our Universe.

In conclusion, the detection of supernova neutrinos represents the next frontier of low-energy neutrino astrophysics. Supernovae are celestial laboratories where neutrinos, after escaping from the highly opaque core, play a crucial role in the mechanism of the stellar explosion and where they might allow us to gain new insights into fundamental neutrino properties. In spite of remarkable progress, a satisfactory understanding of the formation of the neutrino emission as well as of the flavor conversions in this exotic environment is still lacking. Further theoretical and experimental work is therefore needed in order to get prepared for exploiting the wealth of information that the next Galactic supernova

explosion is going to provide.

* * *

A.M. thanks A. Bettini and G.L. Fogli for proposing this review project during the ISAPP School 2013 in Carfranc (Spain). We thank Basudeb Dasgupta and Antonio Marrone for providing adapted versions of some of the plots shown in this review. The supernova modeling at Garching acknowledges input by Alexander Lohs, Andreas Marek, and Bernhard Müller. It received financial support by the Deutsche Forschungsgemeinschaft through the Cluster of Excellence EXC 153 "Origin and Structure of the Universe" (http://www.universe-cluster.de) and by the European Research Council through ERC-AdG No. 341157-COCO2CASA. The numerical simulations became possible by high performance computing resources (Tier-0) provided by PRACE on SuperMUC (GCS@LRZ, Germany), CURIE TN (GENCI@CEA, France), and MareNostrum (BSC, Spain), and by the Gauss Centre for Supercomputing on SuperMUC (LRZ, Germany). We also thank the Max Planck Computing and Data Facility (MPCDF) for computing time on the IBM iDataPlex system *hydra*. The work of A.M. is supported by the Italian Ministero dell'Istruzione, Università e Ricerca (MIUR) and Istituto Nazionale di Fisica Nucleare (INFN) through the "Theoretical Astroparticle Physics" projects. I.T. acknowledges support from the Netherlands Organization for Scientific Research (NWO). N.S. thanks the European Union FP7 ITN INVISIBLES (Marie Curie Actions, PITN- GA-2011- 289442). The research of K.S. has been supported by the US Department of Energy and the National Science Foundation. S.C. acknowledges the European Union through a Marie Curie Fellowship, Grant No. PIIF-GA-2011-299861 and through the ITN Invisibles, Grant No. PITN-GA-2011-289442.

Acronyms

TABLE IV. – *List of the most used acronyms.*

1D	One-dimensional
2D	Two-dimensional
3D	Three-dimensional
BH	Black Hole
CC	Charged Current
CEνNS	Coherent Elastic Neutrino-Nucleus Scattering
DSNB	Diffuse Supernova Neutrino Background
EoM	Equations of Motion
EoS	Equation of State
ES	Elastic scattering
IBD	Inverse Beta Decay
IMB	Irvine-Michigan-Brookhaven
IMF	Initial Mass Function
IH	Inverted Hierarchy
LAr TPC	Liquid Argon Time Projection Chamber
LESA	Lepton Emission Self-sustained Asymmetry
l.h.s.	left-hand-side
LSD	Large Scintillator Detector
LVD	Large Volume Detector
LS EoS	Lattimer-Swesty Equation of State
MAA	Multi-azimuthal-angle
MSW	Mikheyev-Smirnov-Wolfenstein
NC	Neutral Current
NH	Normal Hierarchy
NS	Neutron Star
r.h.s.	right-hand-side
S EoS	Shen et al. Equation of State
SASI	Standing Accretion Shock Instability
SFR	Star Formation Rate
SN	Supernova
SNe	Supernovae
SNEWS	SuperNova Early Warning System
SNR	Supernova Rate
WC	Water Cherenkov

REFERENCES

[1] H. Duan, G. M. Fuller and Y. -Z. Qian, Phys. Rev. D **74**, 123004 (2006) [astro-ph/0511275].
[2] H. Duan, G. M. Fuller, J. Carlson and Y. -Z. Qian, Phys. Rev. D **74**, 105014 (2006) [astro-ph/0606616].
[3] H. Duan, G. M. Fuller, J. Carlson and Y. Z. Qian, Phys. Rev. Lett. **97**, 241101 (2006) [astro-ph/0608050].
[4] S. Hannestad, G. G. Raffelt, G. Sigl and Y. Y. Y. Wong, Phys. Rev. D **74**, 105010 (2006) [Erratum-ibid. D **76**, 029901 (2007)] [astro-ph/0608695].
[5] G. L. Fogli, E. Lisi, A. Marrone and A. Mirizzi, JCAP **0712**, 010 (2007) [arXiv:0707.1998 [hep-ph]].

[6] H. Duan, G. M. Fuller, J. Carlson and Y. Z. Qian, Phys. Rev. D **75**, 125005 (2007) [astro-ph/0703776].
[7] H. Duan, G. M. Fuller and Y. -Z. Qian, Ann. Rev. Nucl. Part. Sci. **60**, 569 (2010) [arXiv:1001.2799 [hep-ph]].
[8] K. Hirata *et al.* [Kamiokande-II Collaboration], Phys. Rev. Lett. **58**, 1490 (1987).
[9] R. M. Bionta *et al.*, Phys. Rev. Lett. **58**, 1494 (1987).
[10] A. Mirizzi and G. G. Raffelt, Phys. Rev. D **72**, 063001 (2005) [astro-ph/0508612].
[11] E. N. Alekseev, L. N. Alekseeva, V. I. Volchenko and I. V. Krivosheina, JETP Lett. **45**, 589 (1987) [Pisma Zh. Eksp. Teor. Fiz. **45**, 461 (1987)].
[12] M. Aglietta *et al.*, Europhys. Lett. **3**, 1315 (1987).
[13] G. G. Raffelt, Mod. Phys. Lett. A **5**, 2581 (1990).
[14] B. Jegerlehner, F. Neubig and G. Raffelt, Phys. Rev. D **54**, 1194 (1996) [astro-ph/9601111].
[15] F. Vissani, J. Phys. G **42**, 013001 (2015) [arXiv:1409.4710 [astro-ph.HE]].
[16] G. G. Raffelt, Proc. Int. Sch. Phys. Fermi **182**, 61 (2012) [arXiv:1201.1637 [astro-ph.SR]].
[17] E. N. Alekseev and L. N. Alekseeva, J. Exp. Theor. Phys. **95**, 5 (2002) [Zh. Eksp. Teor. Fiz. **95**, 10 (2002)] [astro-ph/0212499].
[18] M. Ikeda *et al.* [Super-Kamiokande Collaboration], Astrophys. J. **669**, 519 (2007) [arXiv:0706.2283 [astro-ph]].
[19] N. Y. Agafonova *et al.* [LVD Collaboration], Astrophys. J. **802**, no. 1, 47 (2015) [arXiv:1411.1709 [astro-ph.HE]].
[20] L. M. Krauss, S. L. Glashow and D. N. Schramm, Nature **310**, 191 (1984).
[21] H. Yuksel and J. F. Beacom, Phys. Rev. D **76**, 083007 (2007) [astro-ph/0702613 [ASTRO-PH]].
[22] T. Iida,PhD Thesis, U. of Tokyo (2009)
[23] K. R. Bays, PhD Thesis, U. of California Irvine (2012)
[24] S. Horiuchi, J. F. Beacom and E. Dwek, Phys. Rev. D **79**, 083013 (2009) [arXiv:0812.3157 [astro-ph]].
[25] G. Martínez-Pinedo, T. Fischer and L. Huther, J. Phys. G: Nucl. Part. Phys. **41**, 044008 (2014) [arXiv:1309.5477 [astro-ph.HE]].
[26] A. Burrows and J. Lattimer, Astrophys. J. **307**, 178 (1986).
[27] M. T. Keil, G. G. Raffelt and H. T. Janka, Astrophys. J. **590**, 971 (2003) [astro-ph/0208035].
[28] R. Buras, H.-Th. Janka, M. Rampp and K. Kifonidis, Astron. Astrophys. **457**, 281 (2006) [astro-ph/0512189].
[29] L. Hüdepohl, B. Müller, H.-Th. Janka, A. Marek and G. G. Raffelt, Phys. Rev. Lett. **104**, 251101 (2010) [Erratum-ibid. **105**, 249901 (2010)] [arXiv:0912.0260 [astro-ph.SR]].
[30] T. Fischer, S. C. Whitehouse, A. Mezzacappa, F.-K. Thielemann and M. Liebendorfer, Astron. Astrophys. **517**, A80 (2010) [arXiv:0908.1871 [astro-ph.HE]].
[31] S. Hannestad and G. Raffelt, Astrophys. J. **507**, 339 (1998) [astro-ph/9711132].
[32] T. A. Thompson, A. Burrows and J. E. Horvath, Phys. Rev. C **62**, 035802 (2000) [astro-ph/0003054].
[33] H. Suzuki, PhD Thesis, University of Tokyo (1989).
[34] G. G. Raffelt, Astrophys. J. **561**, 890 (2001) [astro-ph/0105250].
[35] F. Vissani and G. Pagliaroli, Astronomy Letters **35**, 1 (2009) [arXiv:0810.0456 [astro-ph]].
[36] T. J. Loredo and D. Q. Lamb, Phys. Rev. D **65**, 063002 (2002) [astro-ph/0107260].
[37] G. Pagliaroli, F. Vissani, M. L. Costantini and A. Ianni, Astropart. Phys. **31**, 163 (2009) [arXiv:0810.0466 [astro-ph]].
[38] D. N. Schramm and L. E. Brown, in: Jerusalem Winter School for Theoretical Physics. Supernovae. Volume 6. Eds. J. C. Wheeler, T. Piran, and S. Weinberg (World Scientific, Singapore, 1990), p. 261.
[39] V. S. Imshennik, Physics Uspekhi **53**, 1081 (2011).
[40] V. S. Imshennik and O. G. Ryazhskaya, Astronomy Letters **30**, 14 (2004) [astro-ph/0401613].
[41] M. Rampp, M. Ruffert and E. Müller, Astron. Astrophys. **332**, 969 (1998) [astro-ph/9711122].

[42] P. B. Demorest, T. Pennucci, S. M. Ransom, M. S. E. Roberts, and J. W. T. Hessels, Nature **467**, 1081 (2010) [arXiv:1010.5788 [astro-ph.HE]].
[43] J. Antoniadis, *et al.*, Science **340**, 448 (2013) [arXiv:1304.6875 [astro-ph.HE]].
[44] W. D. Arnett, J. N. Bahcall, R. P. Kirshner and S. E. Woosley, Annual Review of Astronomy and Astrophysics **27**, 629 (1989).
[45] J. Larsson, *et al.*, Nature **474**, 484 (2011) [arXiv:1106.2300 [astro-ph.SR]].
[46] I. Seitenzahl, F. X. Timmes and G. Magkotsios, Astrophys. J. **792**, 10 (2014) [arXiv:1408.5986 [astro-ph.SR]].
[47] W. C. G. Ho and C. O. Heinke, Nature **462**, 71 (2009) [arXiv:0911.0672 [astro-ph.HE]].
[48] D. Page, U. Geppert and F. Weber, Nuclear Physics A **777**, 497 (2006) [astro-ph/0508056].
[49] P. S. Shternin, D. G. Yakovlev, C. O. Heinke, W. C. G. Ho and D. J. Patnaude, Mon. Not. R. Astron. Soc. Letters **412**, L108 (2011) [arXiv:1012.0045 [astro-ph.SR]].
[50] G. Zanardo, *et al.*, Astrophys. J. **796**, 82 (2014) [arXiv:1409.7811 [astro-ph.HE]].
[51] G. G. Raffelt, Nuclear Physics B Proc. Suppl. **221**, 218 (2011).
[52] S. Horiuchi, J. F. Beacom, C. S. Kochanek, J. L. Prieto, K. Z. Stanek and T. A. Thompson, Astrophys. J. **738**, 154 (2011) [arXiv:1102.1977 [astro-ph.CO]].
[53] M. Ugliano, H. T. Janka, A. Marek and A. Arcones, Astrophys. J. **757**, 69 (2012) [arXiv:1205.3657 [astro-ph.SR]].
[54] S. Horiuchi, K. Nakamura, T. Takiwaki, K. Kotake and M. Tanaka, MNRASL 445, L99-L103 (2014) [arXiv:1409.0006 [astro-ph.HE]].
[55] C. S. Kochanek, Astrophys. J. **785**, 28 (2014) [arXiv:1308.0013 [astro-ph.HE]].
[56] M. Rampp and H.-Th. Janka, Astron. Astrophys. **396**, 361 (2002) [arXiv:astro-ph/0203101].
[57] R. Buras, M. Rampp, H.-Th. Janka and K. Kifonidis, Astron. Astrophys. **447**, 1049 (2006) [astro-ph/0512189].
[58] A. Marek, H. Dimmelmeier, H.-Th. Janka, E. Müller and R. Buras, an improved effective gravitational potential for supernova simulations," Astron. Astrophys. **445**, 273 (2006) [arXiv:astro-ph/0502161].
[59] H.-Th. Janka, Annual Review of Nuclear and Particle Science **62**, 407 (2012) [arXiv:1206.2503 [astro-ph.SR]].
[60] B. Müller, H.-Th. Janka and A. Marek, Astrophys. J. **756**, 84 (2012) [arXiv:1202.0815 [astro-ph.SR]].
[61] R. Bollig, Diploma Thesis, Technische Universität München (2013).
[62] J. von Groote, PhD Thesis, Technische Universität München (2014).
[63] T. Fischer, S. C. Whitehouse, A. Mezzacappa, F. -K. Thielemann and M. Liebendorfer, Astron. Astrophys. **499**, 1 (2009) [arXiv:0809.5129 [astro-ph]].
[64] L. Hüdepohl, PhD Thesis, Technische Universität München (2013).
[65] H. A. Bethe and J. R. Wilson, Astrophys. J. **295**, 14 (1985).
[66] F. Hanke, B. Müller, A. Wongwathanarat, A. Marek and H.-Th. Janka, Astrophys. J. **770**, 66 (2013) [arXiv:1303.6269 [astro-ph.SR]].
[67] A. Heger, S. E. Woosley and H. C. Spruit, Astrophys. J. **626**, 350 (2005) [arXiv:astro-ph/0409422].
[68] A. Burrows and J. Goshy, Astrophys. J. Lett. **416**, L75 (1993).
[69] H.-Th. Janka and E. Müller, Astron. Astrophys. **306**, 167 (1996).
[70] J. W. Murphy and A. Burrows, Astrophys. J. **688**, 1159 (2008) [arXiv:0805.3345 [astro-ph]].
[71] J. Nordhaus, A. Burrows, A. Almgren and J. Bell, Astrophys. J. **720**, 694 (2010) [arXiv:1006.3792 [astro-ph.SR]].
[72] R. Fernández, Astrophys. J. **749**, 142 (2012) [arXiv:1111.0665 [astro-ph.HE]].
[73] F. Hanke, A. Marek, B. Müller and H.-Th. Janka, Astrophys. J. **755**, 138 (2012) [arXiv:1108.4355 [astro-ph.SR]].
[74] T. Yamasaki and S. Yamada, Astrophys. J. **650**, 291 (2006) [astro-ph/0606504].
[75] O. Pejcha and T. A. Thompson, Astrophys. J. **746**, 106 (2012) [arXiv:1103.4864 [astro-ph.HE]].

[76] B. Müller and H.-Th. Janka, Mon. Not. R. Astron. Soc. **448**, 2141 (2015) [arXiv:1409.4783 [astro-ph.SR]].
[77] F. S. Kitaura, H.-Th. Janka and W. Hillebrandt, Astron. Astrophys. **450**, 345 (2006) [astro-ph/0512065].
[78] L. Dessart, A. Burrows, C. D. Ott, E. Livne, S.-C. Yoon and N. Langer, Astrophys. J. **644**, 1063 (2006) [astro-ph/0601603].
[79] T. Melson, H.-Th. Janka and A. Marek, Astrophys. J. Lett. **801**, L24 (2015) [arXiv:1501.01961 [astro-ph.SR]].
[80] S. Wanajo, H.-Th. Janka and B. Müller, Astrophys. J. Lett. **726**, L15 (2011) [arXiv:1009.1000 [astro-ph.SR]].
[81] M. Herant, W. Benz, W. R. Hix, C. L. Fryer and S. A. Colgate, Astrophys. J. **435**, 339 (1994) [arXiv:astro-ph/9404024].
[82] A. Burrows, J. Hayes and B. Fryxell, Astrophys. J. **450**, 830 (1995) [arXiv:astro-ph/9506061].
[83] A. Marek and H.-Th. Janka, Astrophys. J. **694**, 664 (2009) [arXiv:0708.3372 [astro-ph]].
[84] J. W. Murphy, J. C. Dolence and A. Burrows, Astrophys. J. **771**, 52 (2013) [arXiv:1205.3491 [astro-ph.SR]].
[85] S. M. Couch and C. D. Ott, Astrophys. J. **799**, 5 (2015) [arXiv:1408.1399 [astro-ph.HE]].
[86] J. M. Lattimer and F. D. Swesty, Nucl. Phys. A **535**, 331 (1991).
[87] I. Tamborra, G. Raffelt, F. Hanke, H.-Th. Janka and B. Müller, Phys. Rev. D **90**, 045032 (2014) [arXiv:1406.0006 [astro-ph.SR]].
[88] I. Tamborra, F. Hanke, B. Müller, H.-Th. Janka and G. Raffelt, Phys. Rev. Lett. **111**, 121104 (2013) [arXiv:1307.7936 [astro-ph.SR]].
[89] H. A. Bethe, Rev. Mod. Physics **62**, 801 (1990).
[90] H. A. Bethe, G. E. Brown and J. Cooperstein, Astrophys. J. **322**, 201 (1987).
[91] A. Burrows and B. A. Fryxell, Science **258**, 430 (1992)
[92] A. Burrows and B. A. Fryxell, Astrophys. J. Lett. **418**, L33 (1993)
[93] E. Müller and H.-Th. Janka, Astron. Astrophys. **317**, p.140 (1997).
[94] R. I. Epstein, Mon. Not. R. Astron. Soc. **188**, 305 (1979).
[95] A. Burrows and J. M. Lattimer, Physics Reports **163**, 51 (1988)
[96] W. Keil, H.-Th. Janka and E. Müller, Astrophys. J. Lett. **473**, L111 (1996) [astro-ph/9610203].
[97] H.-Th. Janka, K. Kifonidis and M. Rampp, Lect. Notes Phys. **578**, 333 (2001).
[98] I. Tamborra, F. Hanke, H.-Th. Janka, B. Müller, G. G. Raffelt and A. Marek, Astrophys. J. **792**, 96 (2014) [arXiv:1402.5418 [astro-ph.SR]].
[99] J.M. Blondin, A. Mezzacappa and C. DeMarino, Astrophys. J. **584**, 971 (2003) [astro-ph/0210634].
[100] J.M. Blondin and A. Mezzacappa, Astrophys. J. **642**, 401 (2006) [astro-ph/0507181].
[101] T. Foglizzo, L. Scheck and H.-Th. Janka, Astrophys. J. **652**, 1436 (2006) [astro-ph/0507636].
[102] T. Foglizzo, P. Galletti, L. Scheck and H.-Th. Janka, Astrophys. J. **654**, 1006 (2007) [astro-ph/0606640].
[103] J.M. Blondin and A. Mezzacappa, Astrophys. J. **445**, 58 (2007) [astro-ph/0611680].
[104] T. Foglizzo, Astron. Astrophys. **392**, 353 (2002) [astro-ph/0206274].
[105] L. Scheck, H.-Th. Janka, T. Foglizzo and K. Kifonidis, Astron. Astrophys. **477**, 931 (2008) [arXiv:0704.3001 [astro-ph]].
[106] J. Guilet and T. Foglizzo, Mon. Not. R. Astron. Soc. **421**, 546 (2012) [arXiv:1112.1427 [astro-ph.HE]].
[107] T. Foglizzo, F. Masset, J. Guilet and G. Durand, Phys. Rev. Lett. **108**, 051103 (2012) [arXiv:1112.3448 [astro-ph.HE]].
[108] T. Foglizzo, *et al.*, Publ. Astron. Soc. Australia **32**, 9 (2015) [arXiv:1501.01334 [astro-ph.HE]].
[109] Y. Suwa, K. Kotake, T. Takiwaki, S. C. Whitehouse, M. Liebendörfer and K. Sato, Publ. Astron. Soc. Japan **62**, L49 (2010) [arXiv:0912.1157 [astro-ph.HE]].

[110] Y. Suwa, T. Takiwaki, K. Kotake, T. Fischer, M. Liebendörfer and K. Sato, Astrophys. J. **764**, 99 (2013) [arXiv:1206.6101 [astro-ph.HE]].
[111] B. Müller, H.-Th. Janka and A. Marek, Astrophys. J. **766**, 43 (2013) [arXiv:1210.6984 [astro-ph.SR]].
[112] B. Müller and H.-Th. Janka, Astrophys. J. **788**, 82 (2014) [arXiv:1402.3415 [astro-ph.SR]].
[113] H.-Th. Janka, F. Hanke, L. Hüdepohl, A. Marek, B. Müller and M. Obergaulinger, Prog. Theoret. Exp. Phys. **2012**, 01A309 (2012) [arXiv:1211.1378 [astro-ph.SR]].
[114] S. W. Bruenn *et al.*, Astrophys. J. Lett. **767**, L6 (2013) [arXiv:1212.1747 [astro-ph.SR]].
[115] K.-C. Pan, M. Liebendörfer, M. Hempel and F.-K. Thielemann, [arXiv:1505.02513 [astro-ph.HE]].
[116] J. C. Dolence, A. Burrows and W. Zhang, Multi-dimensional Transport," Astrophys. J. **800**, 10 (2015) [arXiv:1403.6115 [astro-ph.SR]].
[117] C. L. Fryer and M. S. Warren, Astrophys. J. Lett. **574**, L65 (2002) [astro-ph/0206017].
[118] C. L. Fryer and M. S. Warren, Astrophys. J. **601**, 391 (2004) [astro-ph/0309539].
[119] T. Takiwaki, K. Kotake and Y. Suwa, Astrophys. J. **749**, 98 (2012) [arXiv:1108.3989 [astro-ph.HE]].
[120] T. Takiwaki, K. Kotake and Y. Suwa, Astrophys. J. **786**, 83 (2014) [arXiv:1308.5755 [astro-ph.SR]].
[121] T. Melson, H.-Th. Janka, R. Bollig, F. Hanke, A. Marek and B. Müller, [arXiv:1504.07631 [astro-ph.SR]].
[122] E. J. Lentz, S. W. Bruenn, W. R. Hix, A. Mezzacappa, O. E. B. Messer, E. Endeve, J. M. Blondin, J. A. Harris, P. Marronetti and K. N. Yakunin, [arXiv:1505.05110 [astro-ph.SR]].
[123] R. Fernández, [arXiv:1504.07996 [astro-ph.HE]].
[124] B. Müller, [arXiv:1506.05139 [astro-ph.SR]].
[125] E. Radice, S. M. Couch and C. D. Ott, [arXiv:1501.03169 [astro-ph.HE]].
[126] S. M. Couch and E. P. O'Connor, Astrophys. J. **785**, 123 (2014) [arXiv:1310.5728 [astro-ph.HE]].
[127] E. Abdikamalov *et al.*, [arXiv:1409.7078 [astro-ph.HE]].
[128] S. M. Couch and C. D. Ott, Triggered by Precollapse Asphericity in the Progenitor Star," Astrophys. J. Lett. **778**, L7 (2013) [arXiv:1309.2632 [astro-ph.HE]].
[129] S. M. Couch, E. Chatzopoulos, A. W. Arnett and F. X. Timmes, [arXiv:1503.02199 [astro-ph.HE]].
[130] A. Wongwathanarat, H.-Th. Janka and E. Müller, Astrophys. J. Lett. **725**, L106 (2010) [arXiv:1010.0167 [astro-ph.HE]].
[131] A. Wongwathanarat, H.-Th. Janka and E. Müller, Astron. Astrophys. **552**, A126 (2013) [arXiv:1210.8148 [astro-ph.HE]].
[132] A. Wongwathanarat, E. Müller, and H.-Th. Janka, Astron. Astrophys. **577**, A48 (2015) [arXiv:1409.5431 [astro-ph.HE]].
[133] T. Lund, A. Marek, C. Lunardini, H.-Th. Janka and G. Raffelt, Phys. Rev. D **82**, 063007 (2010) [arXiv:1006.1889 [astro-ph.HE]].
[134] T. Lund, A. Wongwathanarat, H.-Th. Janka, E. Müller and G. Raffelt, Phys. Rev. D **86**, 105031 (2012) [arXiv:1208.0043 [astro-ph.HE]].
[135] A. Weiss, W. Hillebrandt, H.-C. Thomas and H. Ritter, Cox and Giuli's Principles of Stellar Structure (Cambridge Scientific Publishers, Cambridge, 2004).
[136] M. Kachelriess, R. Tomàs, R. Buras, H.-Th. Janka, A. Marek and M. Rampp, Phys. Rev. D **71**, 063003 (2005) [astro-ph/0412082].
[137] A. Marek, H.-Th. Janka and E. Müller, Astron. Astrophys. **496**, 475 (2009) [arXiv:0808.4136 [astro-ph]].
[138] H.-Th. Janka and W. Hillebrandt, Astron. Astrophys. **224**, 49 (1989).
[139] I. Tamborra, B. Müller, L. Hüdepohl, H.-Th. Janka and G. G. Raffelt, Phys. Rev. D **86**, 125031 (2012) [arXiv:1211.3920 [astro-ph.SR]].
[140] G. Martínez-Pinedo, T. Fischer, A. Lohs and L. Huther, Phys. Rev. Lett. **109**, 251104 (2012) [arXiv:1205.2793 [astro-ph.HE]].
[141] L. F. Roberts, Astrophys. J. **755**, 26, (2012) [arXiv:1205.3228 [astro-ph.HE]].

[142] C. J. Horowitz, G. Shen, E. O'Connor and C. D. Ott, Phys. Rev. C **86**, 065806 (2012) [arXiv:1209.3173 [astro-ph.HE]].
[143] T. Fischer, M. Hempel, I. Sagert, Y. Suwa and J. Schaffner-Bielich, Europ. Phys. J. A **50**, 46 (2014) [arXiv:1307.6190 [astro-ph.HE]].
[144] M. Hempel, Phys. Rev. C **91**, 055807 (2015) [arXiv:1410.6337 [nucl-th]].
[145] T. Fischer, G. Martínez-Pinedo, M. Hempel and M. Liebendörfer, Phys. Rev. D **85**, 083003 (2012) [arXiv:1112.3842 [astro-ph.HE]].
[146] H. Shen, H. Toki, K. Oyamatsu and K. Sumiyoshi, Nucl. Phys. A **637**, 435 (1998) [nucl-th/9805035].
[147] A. W. Steiner, M. Hempel and T. Fischer, Astrophys. J. **774**, 17 (2013) [arXiv:1207.2184 [astro-ph.SR]].
[148] C. J. Horowitz, Phys. Rev. D **65**, 043001 (2002) [astro-ph/0109209].
[149] S. E. Woosley and T. A. Weaver, Astrophys. J. Suppl. **101**, 181 (1995).
[150] S. E. Woosley, A. Heger and T. A. Weaver, Rev. Mod. Phys. **74**, 1015 (2002).
[151] Y.-Z. Qian and S. E. Woosley, Astrophys. J. **471**, 331 (1996).
[152] T. A. Thompson, A. Burrows and B.S. Meyer, Astrophys. J. **562**, 887 (2001) [astro-ph/0105004].
[153] M. Arnould, S. Goriely and K. Takahashi, Physics Reports **450**, 97 (2007) [arXiv:0705.4512 [astro-ph]].
[154] A. Arcones and F.-K. Thielemann, J. Phys. G: Nucl. Part. Phys. **40**, 013201 (2013) [arXiv:1207.2527 [astro-ph.SR]].
[155] S. E. Woosley, J. R. Wilson, G. J. Mathews, R. D. Hoffman and B. S. Meyer, Astrophys. J. **433**, 229 (1994).
[156] K. Takahashi, J. Witti and H.-Th. Janka, Astron. Astrophys. **286**, 857 (1994).
[157] R. D. Hoffman, S. E. Woosley and Y.-Z. Qian, Astrophys. J. **482**, 951 (1997) [astro-ph/9611097].
[158] C. Fröhlich, G. Martínez-Pinedo, M. Liebendörfer, F.-K. Thielemann, E. Bravo, W. R. Hix, K. Langanke and N. T. Zinner," Phys. Rev. Lett. **96**, 142502 (2006) [astro-ph/0511376].
[159] J. Pruet, R. D. Hoffman, S. E. Woosley, H.-Th. Janka and R. Buras, Astrophys. J. **644**, 1028 (2006) [astro-ph/0511194].
[160] Y.-Z. Qian, G. M. Fuller, G. J. Mathews, R. W. Mayle, J. R. Wilson and S. E. Woosley, Phys. Rev. Lett. **71**, 1965 (1993).
[161] G. C. McLaughlin, J. M. Fetter, A. B. Balantekin and G. M. Fuller, Phys. Rev. C **59**, 2873 (1999) [astro-ph/9902106].
[162] J. Fetter, G. C. McLaughlin, A. B. Balantekin and G. M. Fuller, Astropart. Phys. **18**, 433 (2003) [hep-ph/0205029].
[163] A. B. Balantekin and H. Yuksel, New J. Phys. **7**, 51 (2005) [astro-ph/0411159].
[164] M. R. Wu, T. Fischer, L. Huther, G. Martínez-Pinedo and Y. Z. Qian, Phys. Rev. D **89**, no. 6, 061303 (2014) [arXiv:1305.2382 [astro-ph.HE]].
[165] M. R. Wu, Y. Z. Qian, G. Martinez-Pinedo, T. Fischer and L. Huther, Phys. Rev. D **91**, no. 6, 065016 (2015) [arXiv:1412.8587 [astro-ph.HE]].
[166] I. Tamborra, G. G. Raffelt, L. Hüdepohl and H.-Th. Janka, JCAP **1201**, 013 (2012) [arXiv:1110.2104 [astro-ph.SR]].
[167] E. Pllumbi, I. Tamborra, S. Wanajo, H.-Th. Janka and L. Hüedepohl, Astrophys. J. (2015, in press), arXiv:1406.2596 [astro-ph.SR].
[168] L. F. Roberts, G. Shen, V. Cirigliano, J. A. Pons, S. Reddy and S. E. Woosley, Phys. Rev. Lett. **108**, 061103 (2012) [arXiv:1112.0335 [astro-ph.HE]].
[169] K. Sumiyoshi, S. Yamada, H. Suzuki and S. Chiba, Phys. Rev. Lett. **97**, 091101 (2006) [astro-ph/0608509].
[170] K. Sumiyoshi, S. Yamada and H. Suzuki, Astrophys. J. **688**, 1176 (2008) [arXiv:0808.0384 [astro-ph]].
[171] K. Sumiyoshi, S. Yamada and H. Suzuki, Astrophys. J. **667**, 382 (2007) [arXiv:0706.3762 [astro-ph]].

[172] K. Nakazato, K. Sumiyoshi, H. Suzuki and S. Yamada, Phys. Rev. D **78**, 083014 (2008) [Erratum-ibid. D **79**, 069901 (2009)] [arXiv:0810.3734 [astro-ph]].
[173] K. Nakazato, S. Furusawa, K. Sumiyoshi, A. Ohnishi, S. Yamada and H. Suzuki, Astrophys. J. **745**, 197 (2012) [arXiv:1111.2900 [astro-ph.HE]].
[174] R. Buras, H.-Th. Janka, M. Th. Keil, G. G. Raffelt and M. Rampp, Astrophys. J. **587**, 320 (2003) [astro-ph/0205006].
[175] O. Pejcha and T. A. Thompson, Astrophys. J. **801**, 90 (2015) [arXiv:1409.0540 [astro-ph.HE]].
[176] E. O'Connor and C. D. Ott, Astrophys. J. **730**, 70 (2011) [arXiv:1010.5550 [astro-ph.HE]].
[177] T. Ertl, H.-Th. Janka, S. E. Woosley, T. Sukhbold and M. Ugliano, arXiv:1503.07522 [astro-ph.SR].
[178] K. Scholberg, Ann. Rev. Nucl. Part. Sci. **62**, 81 (2012) [arXiv:1205.6003 [astro-ph.IM]].
[179] S. Abe *et al.* [KamLAND Collaboration], Phys. Rev. C **81**, 025807 (2010) [arXiv:0907.0066 [hep-ex]].
[180] S. W. Li and J. F. Beacom, Phys. Rev. C **89**, 045801 (2014) [arXiv:1402.4687 [hep-ph]].
[181] S. W. Li and J. F. Beacom, Phys. Rev. D **91**, no. 10, 105005 (2015) [arXiv:1503.04823 [hep-ph]].
[182] A. Strumia and F. Vissani, Phys. Lett. B **564**, 42 (2003) [astro-ph/0302055].
[183] E. Kolbe, K. Langanke, G. Martínez-Pinedo and P. Vogel, J. Phys. G **29**, 2569 (2003) [nucl-th/0311022].
[184] C. Volpe, N. Auerbach, G. Colo, T. Suzuki and N. Van Giai, Phys. Rev. C **62**, 015501 (2000) [nucl-th/0001050].
[185] R. S. Raghavan, Phys. Rev. D **34**, 2088 (1986).
[186] M. Bhattacharya *et al.*, Phys. Rev. C **58**, 3677 (1998).
[187] G. M. Fuller, W. C. Haxton and G. C. McLaughlin, Phys. Rev. D **59**, 085005 (1999) [astro-ph/9809164].
[188] C. Volpe, N. Auerbach, G. Colo and N. Van Giai, Phys. Rev. C **65**, 044603 (2002) [nucl-th/0103039].
[189] E. Kolbe and K. Langanke, Phys. Rev. C **63**, 025802 (2001) [nucl-th/0003060].
[190] E. Kolbe, K. Langanke and P. Vogel, Phys. Rev. D **66**, 013007 (2002).
[191] J. Toivanen, E. Kolbe, K. Langanke, G. Martinez-Pinedo and P. Vogel, Nucl. Phys. A **694**, 395 (2001).
[192] K. Langanke, P. Vogel and E. Kolbe, Phys. Rev. Lett. **76**, 2629 (1996) [nucl-th/9511032].
[193] B. Armbruster *et al.* [KARMEN Collaboration], Phys. Lett. B **423**, 15 (1998).
[194] A. Hayes, Private communication.
[195] B. Dasgupta and J. F. Beacom, Phys. Rev. D **83**, 113006 (2011) [arXiv:1103.2768 [hep-ph]].
[196] J. F. Beacom, W. M. Farr and P. Vogel, Phys. Rev. D **66**, 033001 (2002) [hep-ph/0205220].
[197] D. Z. Freedman, D. N. Schramm and D. L. Tubbs, Ann. Rev. Nucl. Part. Sci. **27**, 167 (1977).
[198] A. Drukier and L. Stodolsky, Phys. Rev. D **30**, 2295 (1984).
[199] C. J. Horowitz, K. J. Coakley and D. N. McKinsey, Phys. Rev. D **68**, 023005 (2003) [astro-ph/0302071].
[200] W. J. Marciano and Z. Parsa, J. Phys. G **29**, 2629 (2003) [hep-ph/0403168].
[201] L. B. Auerbach *et al.* [LSND Collaboration], Phys. Rev. C **66**, 015501 (2002) [nucl-ex/0203011].
[202] A. Bolozdynya *et al.*, arXiv:1211.5199 [hep-ex].
[203] J. F. Beacom and M. R. Vagins, Phys. Rev. Lett. **93**, 171101 (2004) [hep-ph/0309300].
[204] R. Laha and J. F. Beacom, Phys. Rev. D **89**, 063007 (2014) [arXiv:1311.6407 [astro-ph.HE]].
[205] H. Watanabe *et al.* [Super-Kamiokande Collaboration], Astropart. Phys. **31**, 320 (2009) [arXiv:0811.0735 [hep-ex]].
[206] K. Abe *et al.*, arXiv:1109.3262 [hep-ex].
[207] F. Halzen, J. E. Jacobsen and E. Zas, Phys. Rev. D **49**, 1758 (1994).
[208] F. Halzen, J. E. Jacobsen and E. Zas, Phys. Rev. D **53**, 7359 (1996) [astro-ph/9512080].

[209] F. Halzen and G. G. Raffelt, Phys. Rev. D **80**, 087301 (2009) [arXiv:0908.2317 [astro-ph.HE]].
[210] R. Abbasi *et al.* [IceCube Collaboration], Astron. Astrophys. **535**, A109 (2011) [Astron. Astrophys. **563**, C1 (2014)] [arXiv:1108.0171 [astro-ph.HE]].
[211] M. Ageron *et al.* [ANTARES Collaboration], Nucl. Instrum. Meth. A **656** (2011) 11 [arXiv:1104.1607 [astro-ph.IM]].
[212] M. G. Aartsen *et al.* [IceCube PINGU Collaboration], arXiv:1401.2046 [physics.ins-det].
[213] M. Aglietta *et al.*, Nuovo Cim. A **105**, 1793 (1992).
[214] N. Y. Agafonova *et al.*, Astropart. Phys. **28**, 516 (2008) [arXiv:0710.0259 [astro-ph]].
[215] L. Cadonati, F. P. Calaprice and M. C. Chen, Astropart. Phys. **16**, 361 (2002) [hep-ph/0012082].
[216] M. E. Monzani, Nuovo Cim. C **29**, 269 (2006).
[217] K. Eguchi *et al.* [KamLAND Collaboration], Phys. Rev. Lett. **90**, 021802 (2003) [hep-ex/0212021].
[218] C. Kraus *et al.* [SNO+ Collaboration], Prog. Part. Nucl. Phys. **64**, 273 (2010).
[219] Y. F. Li, Int. J. Mod. Phys. Conf. Ser. **31**, 1460300 (2014) [arXiv:1402.6143 [physics.ins-det]].
[220] F. An *et al.* [JUNO Collaboration], arXiv:1507.05613 [physics.ins-det].
[221] M. Wurm *et al.* [LENA Collaboration], Astropart. Phys. **35**, 685 (2012) [arXiv:1104.5620 [astro-ph.IM]].
[222] H. Wei [Daya Bay Collaboration], arXiv:1310.5783 [physics.ins-det].
[223] I. Gil Botella and A. Rubbia, JCAP **0408**, 001 (2004) [hep-ph/0404151].
[224] S. Amoruso *et al.* [ICARUS Collaboration], Eur. Phys. J. C **33**, 233 (2004) [hep-ex/0311040].
[225] M. Soderberg [MicroBooNE Collaboration], AIP Conf. Proc. **1189**, 83 (2009) [arXiv:0910.3497 [physics.ins-det]].
[226] C. Adams *et al.* [LBNE Collaboration], arXiv:1307.7335 [hep-ex].
[227] D. Väänänen and C. Volpe, JCAP **1110**, 019 (2011) [arXiv:1105.6225 [astro-ph.SR]].
[228] C. A. Duba *et al.*, J. Phys. Conf. Ser. **136**, 042077 (2008).
[229] S. Chakraborty, P. Bhattacharjee and K. Kar, Phys. Rev. D **89**, no. 1, 013011 (2014) [arXiv:1309.4492 [astro-ph.HE]].
[230] A. Mirizzi, G. G. Raffelt and P. D. Serpico, JCAP **0605**, 012 (2006) [astro-ph/0604300].
[231] S. Ando, J. F. Beacom and H. Yuksel, Phys. Rev. Lett. **95**, 171101 (2005) [astro-ph/0503321].
[232] M. D. Kistler, H. Yuksel, S. Ando, J. F. Beacom and Y. Suzuki, Phys. Rev. D **83**, 123008 (2011) [arXiv:0810.1959 [astro-ph]].
[233] L. Stodolsky, Phys. Lett. B **201**, 353 (1988).
[234] M. J. Longo, Phys. Rev. D **36**, 3276 (1987).
[235] P. D. Serpico, S. Chakraborty, T. Fischer, L. Hüdepohl, H. T. Janka and A. Mirizzi, Phys. Rev. D **85**, 085031 (2012) [arXiv:1111.4483 [astro-ph.SR]].
[236] P. Antonioli *et al.*, New J. Phys. **6**, 114 (2004) [astro-ph/0406214].
[237] K. Scholberg, Astron. Nachr. **329**, 337 (2008) [arXiv:0803.0531 [astro-ph]].
[238] G. Pagliaroli, F. Vissani, E. Coccia and W. Fulgione, Phys. Rev. Lett. **103**, 031102 (2009) [arXiv:0903.1191 [hep-ph]].
[239] S. M. Adams, C. S. Kochanek, J. F. Beacom, M. R. Vagins and K. Z. Stanek, Astrophys. J. **778**, 164 (2013) [arXiv:1306.0559 [astro-ph.HE]].
[240] A. Odrzywolek, M. Misiaszek and M. Kutschera, Astropart. Phys. **21**, 303 (2004) [astro-ph/0311012].
[241] M. Misiaszek, A. Odrzywolek and M. Kutschera, Phys. Rev. D **74**, 043006 (2006) [astro-ph/0511555].
[242] G. L. Fogli, E. Lisi, A. Mirizzi and D. Montanino, JCAP **0504**, 002 (2005) [hep-ph/0412046].
[243] K. Asakura *et al.*, arXiv:1506.01175 [astro-ph.HE].
[244] C. Kato, M. D. Azari, S. Yamada, K. Takahashi, H. Umeda, T. Yoshida and K. Ishidoshiro, arXiv:1506.02358 [astro-ph.HE].

[245] P. Vogel and J. F. Beacom, Phys. Rev. D **60**, 053003 (1999) [hep-ph/9903554].
[246] W. Haxton and C. Johnson, Phys. Rev. Lett. **65**, 1325 (1990).
[247] V. Fischer *et al.*, arXiv:1504.05466 [astro-ph.IM].
[248] R. Tomàs, D. Semikoz, G. G. Raffelt, M. Kachelriess and A. S. Dighe, Phys. Rev. D **68**, 093013 (2003) [hep-ph/0307050].
[249] J. F. Beacom and P. Vogel, Phys. Rev. D **60**, 033007 (1999) [astro-ph/9811350].
[250] T. Mühlbeier, H. Nunokawa and R. Zukanovich Funchal, Phys. Rev. D **88**, 085010 (2013) [arXiv:1304.5006 [astro-ph.HE]].
[251] K. Scholberg, A. Burgmeier and R. Wendell, Phys. Rev. D **81**, 043007 (2010) [arXiv:0910.3174 [astro-ph.IM]].
[252] K. A. Olive *et al.* [Particle Data Group Collaboration], Chin. Phys. C **38** (2014) 090001.
[253] B. Pontecorvo, Sov. Phys. JETP **7**, 172 (1958) [Zh. Eksp. Teor. Fiz. **34**, 247 (1957)].
[254] B. Pontecorvo, Sov. Phys. JETP **26**, 984 (1968) [Zh. Eksp. Teor. Fiz. **53**, 1717 (1967)].
[255] Z. Maki, M. Nakagawa and S. Sakata, Prog. Theor. Phys. **28**, 870 (1962).
[256] L. Wolfenstein, Phys. Rev. D **17**, 2369 (1978); S.P. Mikheev and A.Yu. Smirnov, Yad. Fiz. **42**, 1441 (1985) [Sov. J. Nucl. Phys. **42**, 913 (1985)].
[257] R.J. Davis, D. S. Harmer and K. C. Hoffman, Phys. Rev. Lett. **20**, 1205 (1968).
[258] J.N. Bahcall, *Neutrino Astrophysics* (Cambridge U. Press, Cambridge, England, 1989).
[259] J.N. Bahcall, M.H. Pinsonneault, and S. Basu, Astrophys. J. **555**, 990 (2001) [astro-ph/0010346].
[260] B.T. Cleveland *et al.* [Homestake Collaboration], Astrophys. J. **496**, 505 (1998).
[261] J.N. Abdurashitov *et al.* [SAGE Collaboration], J. Exp. Theor. Phys. **95**, 181 (2002) [Zh. Eksp. Teor. Fiz. **95**, 211 (2002)], [astro-ph/0204245].
[262] W. Hampel *et al.* [GALLEX Collaboration], Phys. Lett. B **447**, 127 (1999).
[263] M. Altmann *et al.* [Gallium Neutrino Observatory (GNO) Collaboration], Phys. Lett. B **616**, 174 (2005) [hep-ex/0504037].
[264] Y. Fukuda *et al.* [Kamiokande Collaboration], Phys. Rev. Lett. **77**, 1683 (1996).
[265] S. Fukuda *et al.* [Super-Kamiokande Collaboration], Phys. Rev. Lett. **86**, 5651 (2001) [hep-ex/0103032]; Phys. Rev. Lett. **86**, 5656 (2001) [hep-ex/0103033]; Phys. Lett. B **539**, 179 (2002) [hep-ex/0205075].
[266] M.B. Smy *et al.* [Super-Kamiokande Collaboration], Phys. Rev. D **69**, 011104 (2004) [hep-ex/0309011].
[267] Q. R. Ahmad *et al.* [SNO Collaboration], Phys. Rev. Lett. **87**, 071301 (2001) [nucl-ex/0106015]; Phys. Rev. Lett. **89**, 011301 (2002) [nucl-ex/0204008]; Phys. Rev. Lett. **89**, 011302 (2002) [nucl-ex/0204009].
[268] S.N. Ahmed *et al.* [SNO Collaboration], Phys. Rev. Lett. **92**, 181301 (2004) [nucl-ex/0309004].
[269] B. Aharmim *et al.* [SNO Collaboration], Phys. Rev. C **72**, 055502 (2005) [nucl-ex/0502021].
[270] C. Arpesella *et al.* [Borexino Collaboration], Phys. Lett. B **658**, 101 (2008) [arXiv:0708.2251 [astro-ph]].
[271] K. Eguchi *et al.* [KamLAND Collaboration], Phys. Rev. Lett. **90**, 021802 (2003) [hep-ex/0212021].
[272] T. Araki *et al.* [KamLAND Collaboration], Phys. Rev. Lett. **94**, 081801 (2005) [hep-ex/0406035].
[273] Y. Fukuda *et al.* [Super-Kamiokande Collaboration], Phys. Rev. Lett. **81**, 1562 (1998) [hep-ex/9807003].
[274] Y. Ashie *et al.* [Super-Kamiokande Collaboration], Phys. Rev. Lett. **93**, 101801 (2004) [hep-ex/0404034].
[275] Y. Ashie *et al.* [Super-Kamiokande Collaboration], Phys. Rev. D **71**, 112005 (2005) [hep-ex/0501064].
[276] M. Ambrosio *et al.* [MACRO Collaboration], Phys. Lett. B **566**, 35 (2003) [hep-ex/0304037]; Eur. Phys. J. C **36**, 323 (2004).
[277] M. Sanchez *et al.* [Soudan 2 Collaboration], Phys. Rev. D **68**, 113004 (2003) [hep-ex/0307069].

[278] M.H. Ahn *et al.* [K2K Collaboration], Phys. Rev. Lett. **90**, 041801 (2003) [hep-ex/0212007].
[279] P. Adamson *et al.* [MINOS Collaboration], Phys. Rev. Lett. **110**, no. 25, 251801 (2013) [arXiv:1304.6335 [hep-ex]].
[280] N. Agafonova *et al.* [OPERA Collaboration], Phys. Rev. D **89**, 051102 (2014) [arXiv:1401.2079 [hep-ex]].
[281] K. Abe *et al.* [T2K Collaboration], Phys. Rev. Lett. **111**, no. 21, 211803 (2013) [arXiv:1308.0465 [hep-ex]].
[282] K. Abe *et al.* [T2K Collaboration], Phys. Rev. Lett. **112**, 181801 (2014) [arXiv:1403.1532 [hep-ex]].
[283] K. N. Abazajian *et al.*, arXiv:1204.5379 [hep-ph].
[284] S. Gariazzo, C. Giunti, M. Laveder, Y. F. Li and E. M. Zavanin, arXiv:1507.08204 [hep-ph].
[285] G. L. Fogli, E. Lisi, A. Marrone and A. Palazzo, Prog. Part. Nucl. Phys. **57**, 742 (2006) [hep-ph/0506083].
[286] F. Capozzi, G. L. Fogli, E. Lisi, A. Marrone, D. Montanino and A. Palazzo, Phys. Rev. D **89**, 093018 (2014) [arXiv:1312.2878 [hep-ph]].
[287] D. V. Forero, M. Tortola and J. W. F. Valle, arXiv:1405.7540 [hep-ph].
[288] M. C. Gonzalez-Garcia, M. Maltoni and T. Schwetz, JHEP **1411**, 052 (2014) [arXiv:1409.5439 [hep-ph]].
[289] F. P. An *et al.* [DAYA-BAY Collaboration], Phys. Rev. Lett. **108**, 171803 (2012) [arXiv:1203.1669 [hep-ex]].
[290] J. K. Ahn *et al.* [RENO Collaboration], Phys. Rev. Lett. **108**, 191802 (2012) [arXiv:1204.0626 [hep-ex]].
[291] K. Abe *et al.* [T2K Collaboration], Phys. Rev. Lett. **107**, 041801 (2011) [arXiv:1106.2822 [hep-ex]].
[292] P. Adamson *et al.* [MINOS Collaboration], Phys. Rev. Lett. **107**, 181802 (2011) [arXiv:1108.0015 [hep-ex]].
[293] Y. Abe *et al.* [DOUBLE-CHOOZ Collaboration], Phys. Rev. Lett. **108**, 131801 (2012) [arXiv:1112.6353 [hep-ex]].
[294] G. L. Fogli, E. Lisi, A. Marrone, A. Palazzo and A. M. Rotunno, Phys. Rev. Lett. **101**, 141801 (2008) [arXiv:0806.2649 [hep-ph]].
[295] G. L. Fogli, E. Lisi, A. Marrone, A. Palazzo and A. M. Rotunno, Phys. Rev. D **84**, 053007 (2011) [arXiv:1106.6028 [hep-ph]].
[296] E. K. Akhmedov, C. Lunardini and A. Yu. Smirnov, Nucl. Phys. B **643**, 339 (2002) [hep-ph/0204091].
[297] A. B. Balantekin, J. Gava and C. Volpe, Phys. Lett. B **662**, 396 (2008) [arXiv:0710.3112 [astro-ph]].
[298] J. Gava and C. Volpe, Phys. Rev. D **78**, 083007 (2008) [arXiv:0807.3418 [astro-ph]].
[299] T. -K. Kuo and J. T. Pantaleone, Rev. Mod. Phys. **61**, 937 (1989).
[300] J. T. Pantaleone, Phys. Rev. D **46**, 510 (1992).
[301] J. T. Pantaleone, Phys. Lett. B **342**, 250 (1995) [astro-ph/9405008].
[302] J. T. Pantaleone, Phys. Lett. B **287**, 128 (1992).
[303] V. A. Kostelecky, J. T. Pantaleone and S. Samuel, Phys. Lett. B **315**, 46 (1993).
[304] J. T. Pantaleone, Phys. Rev. D **58**, 073002 (1998).
[305] S. Samuel, Phys. Rev. D **48**, 1462 (1993).
[306] V. A. Kostelecky and S. Samuel, Phys. Rev. D **49**, 1740 (1994).
[307] V. A. Kostelecky and S. Samuel, Phys. Rev. D **52**, 621 (1995) [hep-ph/9506262].
[308] S. Samuel, Phys. Rev. D **53**, 5382 (1996) [hep-ph/9604341].
[309] V. A. Kostelecky and S. Samuel, Phys. Lett. B **385**, 159 (1996) [hep-ph/9610399].
[310] S. Pastor, G. G. Raffelt and D. V. Semikoz, Phys. Rev. D **65**, 053011 (2002) [hep-ph/0109035].
[311] A. D. Dolgov, S. H. Hansen, S. Pastor, S. T. Petcov, G. G. Raffelt and D. V. Semikoz, Nucl. Phys. B **632**, 363 (2002) [hep-ph/0201287].
[312] S. Pastor and G. G. Raffelt, Phys. Rev. Lett. **89**, 191101 (2002) [astro-ph/0207281].

[313] Y. Y. Y. Wong, Phys. Rev. D **66**, 025015 (2002) [hep-ph/0203180].
[314] R. F. Sawyer, Phys. Rev. D **72**, 045003 (2005) [hep-ph/0503013].
[315] G. Sigl and G. G. Raffelt, Nucl. Phys. B **406**, 423 (1993).
[316] G. G. Raffelt, G. Sigl and L. Stodolsky, Phys. Rev. D **45**, 1782 (1992).
[317] G. G. Raffelt, G. Sigl and L. Stodolsky, Phys. Rev. Lett. **70**, 2363 (1993) [Erratum-ibid. **98**, 069902 (2007)] [hep-ph/9209276].
[318] B. H. J. McKellar and M. J. Thomson, Phys. Rev. D **49**, 2710 (1994).
[319] A. D. Dolgov, Sov. J. Nucl. Phys. **33**, 700 (1981) [Yad. Fiz. **33**, 1309 (1981)].
[320] R. Barbieri and A. Dolgov, Nucl. Phys. B **349**, 743 (1991).
[321] A. B. Balantekin and Y. Pehlivan, J. Phys. G **34**, 47 (2007) [astro-ph/0607527].
[322] C. Y. Cardall, Phys. Rev. D **78**, 085017 (2008) [arXiv:0712.1188 [astro-ph]].
[323] C. Volpe, Väänänen and C. Espinoza, Phys. Rev. D **87**, no. 11, 113010 (2013) [arXiv:1302.2374 [hep-ph]].
[324] A. Vlasenko, G. M. Fuller and V. Cirigliano, Phys. Rev. D **89**, no. 10, 105004 (2014) [arXiv:1309.2628 [hep-ph]].
[325] G. G. Raffelt and G. Sigl, Phys. Rev. D **75**, 083002 (2007) [hep-ph/0701182].
[326] A. Esteban-Pretel, S. Pastor, R. Tomàs, G. G. Raffelt and G. Sigl, Phys. Rev. D **76**, 125018 (2007) [arXiv:0706.2498 [astro-ph]].
[327] R. F. Sawyer, Phys. Rev. D **79**, 105003 (2009) [arXiv:0803.4319 [astro-ph]].
[328] B. Dasgupta and A. Dighe, Phys. Rev. D **77**, 113002 (2008) [arXiv:0712.3798 [hep-ph]].
[329] G. Fogli, E. Lisi, A. Marrone and I. Tamborra, JCAP **0904**, 030 (2009) [arXiv:0812.3031 [hep-ph]].
[330] A. Esteban-Pretel, A. Mirizzi, S. Pastor, R. Tomàs, G. G. Raffelt, P. D. Serpico and G. Sigl, Phys. Rev. D **78**, 085012 (2008) [arXiv:0807.0659 [astro-ph]].
[331] S. Chakraborty, T. Fischer, A. Mirizzi, N. Saviano and R. Tomàs, Phys. Rev. Lett. **107**, 151101 (2011) [arXiv:1104.4031 [hep-ph]].
[332] S. Chakraborty, T. Fischer, A. Mirizzi, N. Saviano and R. Tomàs, Phys. Rev. D **84**, 025002 (2011) [arXiv:1105.1130 [hep-ph]].
[333] B. Dasgupta, E. P. O'Connor and C. D. Ott, Phys. Rev. D **85**, 065008 (2012) [arXiv:1106.1167 [astro-ph.SR]].
[334] S. Sarikas, G. G. Raffelt, L. Hüdepohl and H.-Th. Janka, Phys. Rev. Lett. **108**, 061101 (2012) [arXiv:1109.3601 [astro-ph.SR]].
[335] N. Saviano, S. Chakraborty, T. Fischer and A. Mirizzi, Phys. Rev. D **85**, 113002 (2012) [arXiv:1203.1484 [hep-ph]].
[336] S. Chakraborty, A. Mirizzi, N. Saviano and D. d. S. Seixas, Phys. Rev. D **89**, no. 9, 093001 (2014) [arXiv:1402.1767 [hep-ph]].
[337] S. Chakraborty, G. Raffelt, H.-Th. Janka and B. Müeller, arXiv:1412.0670 [hep-ph].
[338] R. Tomàs, M. Kachelriess, G.G. Raffelt, A. Dighe, H.-Th. Janka and L. Scheck, JCAP **0409**, 015 (2004) [astro-ph/0407132].
[339] A.S. Dighe and A.Yu. Smirnov, Phys. Rev. D **62**, 033007 (2000).
[340] B. Dasgupta, A. Dighe, A. Mirizzi and G. G. Raffelt, Phys. Rev. D **78**, 033014 (2008) [arXiv:0805.3300 [hep-ph]].
[341] B. Dasgupta, A. Dighe, G. G. Raffelt and A. Y. Smirnov, Phys. Rev. Lett. **103**, 051105 (2009) [arXiv:0904.3542 [hep-ph]].
[342] A. Friedland, Phys. Rev. Lett. **104**, 191102 (2010) [arXiv:1001.0996 [hep-ph]].
[343] B. Dasgupta, G. G. Raffelt and I. Tamborra, Phys. Rev. D **81**, 073004 (2010) [arXiv:1001.5396 [hep-ph]].
[344] B. Dasgupta, A. Mirizzi, I. Tamborra and R. Tomàs, Phys. Rev. D **81**, 093008 (2010) [arXiv:1002.2943 [hep-ph]].
[345] G. L. Fogli, E. Lisi, A. Marrone and I. Tamborra, JCAP **0910**, 002 (2009) [arXiv:0907.5115 [hep-ph]].
[346] H. Duan, G. M. Fuller and Y. Z. Qian, Phys. Rev. D **76**, 085013 (2007) [arXiv:0706.4293 [astro-ph]].
[347] G. L. Fogli, E. Lisi, A. Marrone, A. Mirizzi and I. Tamborra, Phys. Rev. D **78**, 097301 (2008) [arXiv:0808.0807 [hep-ph]].

[348] H. Duan, G. M. Fuller, J. Carlson and Y. Z. Qian, Phys. Rev. Lett. **99**, 241802 (2007) [arXiv:0707.0290 [astro-ph]].
[349] G. G. Raffelt and A. Yu. Smirnov, Phys. Rev. D **76**, 081301 (2007) [Erratum-ibid. D **77**, 029903 (2008)] [arXiv:0705.1830 [hep-ph]].
[350] G. G. Raffelt and A. Yu. Smirnov, Phys. Rev. D **76**, 125008 (2007) [arXiv:0709.4641 [hep-ph]].
[351] H. Duan, G. M. Fuller and Y. Z. Qian, Phys. Rev. D **77**, 085016 (2008) [arXiv:0801.1363 [hep-ph]].
[352] B. Dasgupta, A. Dighe, A. Mirizzi and G. G. Raffelt, Phys. Rev. D **77**, 113007 (2008) [arXiv:0801.1660 [hep-ph]].
[353] S. Galais and C. Volpe, Phys. Rev. D **84**, 085005 (2011) [arXiv:1103.5302 [astro-ph.SR]].
[354] S. Choubey, B. Dasgupta, A. Dighe and A. Mirizzi, arXiv:1008.0308 [hep-ph].
[355] H. Duan and A. Friedland, Phys. Rev. Lett. **106**, 091101 (2011) [arXiv:1006.2359 [hep-ph]].
[356] A. Mirizzi and R. Tomàs, Phys. Rev. D **84**, 033013 (2011) [arXiv:1012.1339 [hep-ph]].
[357] J. F. Cherry, G. M. Fuller, J. Carlson, H. Duan and Y. Z. Qian, Phys. Rev. D **82**, 085025 (2010) [arXiv:1006.2175 [astro-ph.HE]].
[358] A. Mirizzi and P. D. Serpico, Phys. Rev. Lett. **108**, 231102 (2012) [arXiv:1110.0022 [hep-ph]].
[359] A. Mirizzi and P. D. Serpico, Phys. Rev. D **86**, 085010 (2012) [arXiv:1208.0157 [hep-ph]]. [360]
[360] H. Duan, G. M. Fuller, J. Carlson and Y. Z. Qian, Phys. Rev. Lett. **100**, 021101 (2008) [arXiv:0710.1271 [astro-ph]].
[361] G. G. Raffelt, S. Sarikas and D. de Sousa Seixas, Phys. Rev. Lett. **111**, no. 9, 091101 (2013) [Erratum-ibid. **113**, no. 23, 239903 (2014)] [arXiv:1305.7140 [hep-ph]].
[362] G. G. Raffelt and D. d. S. Seixas, Phys. Rev. D **88**, 045031 (2013) [arXiv:1307.7625 [hep-ph]].
[363] H. Duan, Phys. Rev. D **88**, 125008 (2013) [arXiv:1309.7377 [hep-ph]].
[364] A. Mirizzi, Phys. Rev. D **88**, no. 7, 073004 (2013) [arXiv:1308.1402 [hep-ph]].
[365] S. Chakraborty and A. Mirizzi, Phys. Rev. D **90**, no. 3, 033004 (2014) [arXiv:1308.5255 [hep-ph]].
[366] G. Mangano, A. Mirizzi and N. Saviano, Phys. Rev. D **89**, no. 7, 073017 (2014) [arXiv:1403.1892 [hep-ph]].
[367] H. Duan and S. Shalgar, Phys. Lett. B **747**, 139 (2015) [arXiv:1412.7097 [hep-ph]].
[368] A. Mirizzi, G. Mangano and N. Saviano, Phys. Rev. D **92**, no. 2, 021702 (2015) [arXiv:1503.03485 [hep-ph]].
[369] A. Mirizzi, arXiv:1506.06805 [hep-ph].
[370] H. Duan, arXiv:1506.08629 [hep-ph].
[371] S. Chakraborty, R. S. Hansen, I. Izaguirre and G. Raffelt, arXiv:1507.07569 [hep-ph].
[372] J. F. Cherry, J. Carlson, A. Friedland, G. M. Fuller and A. Vlasenko, Phys. Rev. Lett. **108**, 261104 (2012) [arXiv:1203.1607 [hep-ph]].
[373] J. F. Cherry, J. Carlson, A. Friedland, G. M. Fuller and A. Vlasenko, Phys. Rev. D **87**, 085037 (2013) [arXiv:1302.1159 [astro-ph.HE]].
[374] S. Sarikas, I. Tamborra, G. Raffelt, L. Hüdepohl and H.-Th. Janka, Phys. Rev. D **85**, 113007 (2012) [arXiv:1204.0971 [hep-ph]].
[375] L. Wolfenstein, Phys. Rev. D **20**, 2634 (1979).
[376] P. Reinartz and L. Stodolsky, Z. Phys. C **27**, 507 (1985).
[377] S.P. Mikheev and A.Yu. Smirnov, Sov. Phys. JETP **64**, 4 (1986) [Zh. Eksp. Teor. Fiz. **91**, 7 (1986)]. [arXiv:0706.0454 [hep-ph]].
[378] G.L. Fogli, E. Lisi, D. Montanino and A. Palazzo, Phys. Rev. D **65**, 073008 (2002) [Erratum-ibid. D **66**, 039901 (2002)].
[379] G. L. Fogli, E. Lisi, D. Montanino and A. Mirizzi, Phys. Rev. D **68**, 033005 (2003) [hep-ph/0304056].
[380] J. P. Kneller and G. C. McLaughlin, Phys. Rev. D **73**, 056003 (2006) [hep-ph/0509356].
[381] R.C. Schirato and G.M. Fuller, astro-ph/0205390 (unpublished).

[382] B. Dasgupta and A. Dighe, Phys. Rev. D **75**, 093002 (2007) [hep-ph/0510219].
[383] S. Choubey, N. P. Harries and G. G. Ross, Phys. Rev. D **74**, 053010 (2006) [hep-ph/0605255].
[384] J. P. Kneller, G. C. McLaughlin and J. Brockman, Phys. Rev. D **77**, 045023 (2008) [arXiv:0705.3835 [astro-ph]].
[385] K. Kifonidis, T. Plewa, H.-Th. Janka and E. Müller, Astron. Astrophys. **408**, 621 (2003) [astro-ph/0302239].
[386] K. Kifonidis, T. Plewa, L. Scheck, H.-Th. Janka and E. Müller, Astron. Astrophys. **453**, 661 (2006) [astro-ph/0511369].
[387] L. Scheck, K. Kifonidis, H.-Th. Janka and E. Müller, Astron. Astrophys. **457**, 963 (2006) [astro-ph/0601302].
[388] N. Hammer, H.-Th. Janka, and E. Müller, Astrophys. J. **714**, 1371 (2010) [astro-ph/0908.3474].
[389] A. Arcones and H.-Th. Janka, Astron. Astrophys. **526**, 160 (2011) [astro-ph/1008.0882].
[390] E. Müller, H.-Th. Janka and A. Wongwathanarat, Astron. Astrophys. **537**, 63 (2012) [astro-ph/1106.6301].
[391] A. Schaefer and S. E. Koonin, Phys. Lett. B **185**, 417 (1987).
[392] R. F. Sawyer, Phys. Rev. D **42**, 3908 (1990).
[393] F. N. Loreti and A. B. Balantekin, Phys. Rev. D **50**, 4762 (1994) [nucl-th/9406003].
[394] H. Nunokawa, A. Rossi, V. B. Semikoz and J. W. F. Valle, Nucl. Phys. B **472**, 495 (1996) [hep-ph/9602307].
[395] A. B. Balantekin, J. M. Fetter and F. N. Loreti, Phys. Rev. D **54**, 3941 (1996) [astro-ph/9604061].
[396] C. P. Burgess and D. Michaud, Annals Phys. **256**, 1 (1997) [hep-ph/9606295].
[397] E. Torrente-Lujan, Phys. Rev. D **59**, 073001 (1999) [hep-ph/9807361].
[398] G. L. Fogli, E. Lisi, A. Mirizzi and D. Montanino, JCAP **0606**, 012 (2006) [hep-ph/0603033].
[399] A. Friedland and A. Gruzinov, astro-ph/0607244.
[400] J. P. Kneller and C. Volpe, Phys. Rev. D **82**, 123004 (2010) [arXiv:1006.0913 [hep-ph]].
[401] T. Lund and J. P. Kneller, Phys. Rev. D **88**, no. 2, 023008 (2013) [arXiv:1304.6372 [astro-ph.HE]].
[402] F. N. Loreti, Y. Z. Qian, G. M. Fuller and A. B. Balantekin, Phys. Rev. D **52**, 6664 (1995) [astro-ph/9508106].
[403] S. Choubey, N. P. Harries and G. G. Ross, Phys. Rev. D **76**, 073013 (2007) [hep-ph/0703092 [HEP-PH]].
[404] F. Benatti and R. Floreanini, Phys. Rev. D **71**, 013003 (2005) [hep-ph/0412311].
[405] J. P. Kneller and A. W. Mauney, Phys. Rev. D **88**, no. 2, 025004 (2013) [arXiv:1302.3825 [hep-ph]].
[406] E. Borriello, S. Chakraborty, H.-Th. Janka, E. Lisi and A. Mirizzi, JCAP **1411** (2014) 11, 030 [arXiv:1310.7488 [astro-ph.SR]].
[407] S. Chakraborty, A. Mirizzi and G. Sigl, Phys. Rev. D **87**, no. 1, 017302 (2013) [arXiv:1211.7069 [hep-ph]].
[408] S. Ando, Phys. Rev. D **70**, 033004 (2004) [hep-ph/0405200].
[409] A. Esmaili, O. L. G. Peres and P. D. Serpico, Phys. Rev. D **90**, no. 3, 033013 (2014) [arXiv:1402.1453 [hep-ph]].
[410] E. K. Akhmedov and T. Fukuyama, JCAP **0312**, 007 (2003) [hep-ph/0310119].
[411] Janka H.-Th., Hanke F., Hüdepohl L., Marek A., Müller B., Obergaulinger M.: *Progress of Theoretical and Experimental Physics (PTEP)* **2012**, 01A309 [arXiv:1211.1378].
[412] C. D. Ott, E. P. O'Connor, S. Gossan, E. Abdikamalov, U. C. T. Gamma and S. Drasco, Nucl. Phys. Proc. Suppl. **235-236**, 381 (2013) [arXiv:1212.4250 [astro-ph.HE]].
[413] C. Lunardini and A. Yu. Smirnov, Nucl. Phys. B **616**, 307 (2001) [hep-ph/0106149].
[414] A. S. Dighe, M. Kachelriess, G. G. Raffelt and R. Tomàs, JCAP **0401**, 004 (2004) [hep-ph/0311172].
[415] A. S. Dighe, M. T. Keil and G. G. Raffelt, JCAP **0306**, 006 (2003) [hep-ph/0304150].

[416] E. Borriello, S. Chakraborty, A. Mirizzi, P. D. Serpico and I. Tamborra, Phys. Rev. D **86**, 083004 (2012) [arXiv:1207.5049 [hep-ph]].
[417] A. S. Dighe, M. T. Keil and G. G. Raffelt, JCAP **0306**, 005 (2003) [hep-ph/0303210].
[418] A. Banerjee, A. Dighe and G. G. Raffelt, Phys. Rev. D **84**, 053013 (2011) [arXiv:1107.2308 [hep-ph]].
[419] G. G. Raffelt and I. Tamborra, Phys. Rev. D **82**, 125004 (2010) [arXiv:1006.0002 [hep-ph]].
[420] G. G. Raffelt, Phys. Rev. D **83**, 105022 (2011) [arXiv:1103.2891 [hep-ph]].
[421] S. Sarikas, D. d. S. Seixas and G. G. Raffelt, Phys. Rev. D **86**, 125020 (2012) [arXiv:1210.4557 [hep-ph]].
[422] Y. Pehlivan, A. B. Balantekin, T. Kajino and T. Yoshida, Phys. Rev. D **84**, 065008 (2011) [arXiv:1105.1182 [astro-ph.CO]].
[423] R. S. Hansen and S. Hannestad, Phys. Rev. D **90**, no. 2, 025009 (2014) [arXiv:1404.3833 [hep-ph]].
[424] V. Cirigliano, G. M. Fuller and A. Vlasenko, arXiv:1406.5558 [hep-ph].
[425] A. Vlasenko, G. M. Fuller and V. Cirigliano, arXiv:1406.6724 [astro-ph.HE].
[426] D. Väänänen and C. Volpe, Phys. Rev. D **88**, 065003 (2013) [arXiv:1306.6372 [hep-ph]].
[427] J. Serreau and C. Volpe, Phys. Rev. D **90**, no. 12, 125040 (2014) [arXiv:1409.3591 [hep-ph]].
[428] A. Kartavtsev, G. Raffelt and H. Vogel, Phys. Rev. D **91**, no. 12, 125020 (2015) [arXiv:1504.03230 [hep-ph]].
[429] A. de Gouvea and S. Shalgar, JCAP **1210**, 027 (2012) [arXiv:1207.0516 [astro-ph.HE]].
[430] A. de Gouvea and S. Shalgar, JCAP **1304**, 018 (2013) [arXiv:1301.5637 [astro-ph.HE]].
[431] A. Esteban-Pretel, R. Tomàs and J. W. F. Valle, Phys. Rev. D **81**, 063003 (2010) [arXiv:0909.2196 [hep-ph]].
[432] M. Blennow, A. Mirizzi and P. D. Serpico, Phys. Rev. D **78** (2008) 113004 [arXiv:0810.2297 [hep-ph]].
[433] J. Gava, J. Kneller, C. Volpe and G. C. McLaughlin, Phys. Rev. Lett. **103**, 071101 (2009) [arXiv:0902.0317 [hep-ph]].
[434] H. Duan, A. Friedland, G. C. McLaughlin and R. Surman, J. Phys. G **38**, 035201 (2011) [arXiv:1012.0532 [astro-ph.SR]].
[435] S. Van Den Bergh, Phys. Rept. **204**, 385 (1991).
[436] R. Diehl *et al.*, Nature **439**, 45 (2006) [astro-ph/0601015].
[437] S. Ando and K. Sato, New J. Phys. **6**, 170 (2004) [astro-ph/0410061].
[438] Y. B. Zeldovich, O. K. Guseinov, Sov. Phys. Dok. **10**, 524 (1965).
[439] O. K. Guseinov, Sov. Astron. **10**, 613 (1967).
[440] M. A. Ruderman, Rept. Prog. Phys. **28**, 411 (1965).
[441] G. S. Bisnovatyi-Kogan, and Z. F. Seidov, Sov. Astron. **26**, 132 (1982).
[442] L. M. Krauss, S. L. Glashow, D. M. Schramm, Nature 310, 191 (1984).
[443] J. F. Beacom, Ann. Rev. Nucl. Part. Sci. **60**, 439 (2010) [arXiv:1004.3311 [astro-ph.HE]].
[444] C. Lunardini, arXiv:1007.3252 [astro-ph.CO].
[445] M. Malek *et al.* [Super-Kamiokande Collaboration], Phys. Rev. Lett. **90**, 061101 (2003) [hep-ex/0209028]
[446] C. Lunardini and O. L. G. Peres, JCAP **0808**, 033 (2008) [arXiv:0805.4225 [astro-ph]].
[447] K. Bays *et al.* [Super-Kamiokande Collaboration], Phys. Rev. D **85**, 052007 (2012) [arXiv:1111.5031 [hep-ex]].
[448] H. Zhang *et al.* [Super-Kamiokande Collaboration], Astropart. Phys. **60**, 41 (2014) [arXiv:1311.3738 [hep-ex]].
[449] Y. Zhang [Super-Kamiokande Collaboration], Phys. Procedia **61** 384 (2015).
[450] S. Ando, K. Sato and T. Totani, Astropart. Phys. **18**, 307 (2003) [astro-ph/0202450].
[451] S. Ando and K. Sato, Phys. Lett. B **559**, 113 (2003) [astro-ph/0210502].
[452] E. E. Salpeter, Astrophys. J. **121**, 161 (1955).
[453] P. Kroupa, Mon. Not. Roy. Astron. Soc. **322** (2001) 231 [astro-ph/0009005].
[454] I. K. Baldry and K. Glazebrook, Astrophys. J. **593**, 258 (2003) [astro-ph/0304423].
[455] A. M. Hopkins and J. F. Beacom, Astrophys. J. **651**, 142 (2006) [astro-ph/0601463].

[456] H. Yuksel, M. D. Kistler, J. F. Beacom and A. M. Hopkins, Astrophys. J. **683**, L5 (2008) [arXiv:0804.4008 [astro-ph]].
[457] A. M. Hopkins, ASP Conf. Ser. **380**, 423 (2007) [astro-ph/0611283].
[458] W. Li, R. Chornock, J. Leaman, A. V. Filippenko, D. Poznanski, X. Wang, M. Ganeshalingam and F. Mannucci, Mon. Not. Roy. Astron. Soc. **412**, 1473 (2011) [arXiv:1006.4613 [astro-ph.SR]].
[459] M. T. Botticella, S. J. Smartt, R. C. Kennicutt, Jr., E. Cappellaro, M. Sereno and J. C. Lee, Astron. Astrophys. **537**, A132 (2012) [arXiv:1111.1692 [astro-ph.CO]].
[460] S. Mattila *et al.*, Astrophys. J. **756**, 111 (2012) [arXiv:1206.1314 [astro-ph.CO]].
[461] T. Dahlen, L.-G. Strolger, A. G. Riess, S. Mattila, E. Kankare and B. Mobasher, Astrophys. J. **757**, 70 (2012) [arXiv:1208.0342 [astro-ph.CO]].
[462] J. Melinder *et al.*, Astron. Astrophys. **545**, A96 (2012) [arXiv:1206.6897 [astro-ph.CO]].
[463] B. Magnelli *et al.*, Astron. Astrophys. **496**, 57 (2009) [arXiv:0901.1543 [astro-ph.CO]].
[464] H. Yuksel and M. D. Kistler, arXiv:1212.4844 [astro-ph.HE].
[465] A. Lien, B. D. Fields and J. F. Beacom, Phys. Rev. D **81**, 083001 (2010) [arXiv:1001.3678 [astro-ph.CO]].
[466] S. Ando, Astrophys. J. **607**, 20 (2004) [astro-ph/0401531].
[467] E. O'Connor and C. D. Ott, Astrophys. J. **762**, 126 (2013) [arXiv:1207.1100 [astro-ph.HE]].
[468] C. Lunardini and I. Tamborra, JCAP **1207**, 012 (2012) [arXiv:1205.6292 [astro-ph.SR]].
[469] S. Chakraborty, S. Choubey and K. Kar, Phys. Lett. B **702**, 209 (2011) [arXiv:1006.3756 [hep-ph]].
[470] A. S. Dighe and A. Yu. Smirnov, Phys. Rev. D **62**, 033007 (2000) [hep-ph/9907423].
[471] C. Lunardini, Phys. Rev. Lett. **102**, 231101 (2009) [arXiv:0901.0568 [astro-ph.SR]].
[472] B. Müeller, A. Marek, H.-Th. Janka and H. Dimmelmeier, ASP Conf. Ser. **459**, 137 (2012) [arXiv:1112.1920 [astro-ph.SR]].
[473] G. J. Mathews, J. Hidaka, T. Kajino and J. Suzuki, Astrophys. J. **790**, 115 (2014) [arXiv:1405.0458 [astro-ph.CO]].
[474] K. Nakazato, Phys. Rev. D **88** no. 8, 083012 (2013) [arXiv:1306.4526 [astro-ph.HE]]. [475]
[475] K. Nakazato, E. Mochida, Y. Niino and H. Suzuki, Astrophys. J. **804** no. 1, 75 (2015) [arXiv:1503.01236 [astro-ph.HE]].
[476] C. L. Fryer, Astrophys. J. **522**, 413 (1999) [astro-ph/9902315].
[477] A. Heger, C. L. Fryer, S. E. Woosley, N. Langer and D. H. Hartmann, Astrophys. J. **591**, 288 (2003) [astro-ph/0212469].
[478] S. J. Smartt, J. J. Eldridge, R. M. Crockett and J. R. Maund, Mon. Not. Roy. Astron. Soc. **395**, 1409 (2009) [arXiv:0809.0403 [astro-ph]].
[479] E. Lovegrove and S. E. Woosley, Astrophys. J. **769**, 109 (2013) [arXiv:1303.5055 [astro-ph.HE]].
[480] D. K. Nadezhin, Ap&SS **69**, 115 (1980).
[481] W.-Q. Zhang, S. E. Woosley and A. Heger, Astrophys. J. **679**, 639 (2008) [astro-ph/0701083].
[482] N. Fraija and C. G. Bernal, arXiv:1505.01062 [astro-ph.HE].
[483] J. G. Keehn and C. Lunardini, Phys. Rev. D **85**, 043011 (2012) [arXiv:1012.1274 [astro-ph.CO]].
[484] C. Lunardini, Phys. Rev. D **75**, 073022 (2007) [astro-ph/0612701].
[485] C. S. Kochanek, J. F. Beacom, M. D. Kistler, J. L. Prieto, K. Z. Stanek, T. A. Thompson and H. Yuksel, Astrophys. J. **684**, 1336 (2008) [arXiv:0802.0456 [astro-ph]].
[486] J. R. Gerke, C. S. Kochanek and K. Z. Stanek, arXiv:1411.1761 [astro-ph.SR].
[487] K. A. Hochmuth, F. V. Feilitzsch, B. D. Fields, T. Marrodan Undagoitia, L. Oberauer, W. Potzel, G. G. Raffelt and M. Wurm, Astropart. Phys. **27**, 21 (2007) [hep-ph/0509136].
[488] A. G. Cocco, A. Ereditato, G. Fiorillo, G. Mangano and V. Pettorino, JCAP **0412**, 002 (2004) [hep-ph/0408031].

[489] M. R. Vagins, Proceedings of the HAνSE 2011 workshop (Hamburg, Germany, 2011), ed. by A. Mirizzi, P. D. Serpico, G. Sigl, Verlag Deutsches Elektronen-Synchroton, pp. 147-158.
M. R. Vagins, talk given at Multi-Messenger Kakenhi 3$^{\rm rd}$ Annual Symposium, Hiroshima University, Febr. 21, 2015.
[490] L. M. Magro, talk given at Particle Physics and Cosmology Workshop 2015, Center for Theoretical Underground Physics and Related Areas, Deadwood, June 30, 2015.
[491] R. Mllenberg, F. von Feilitzsch, D. Hellgartner, L. Oberauer, M. Tippmann, V. Zimmer, J. Winter and M. Wurm, Phys. Rev. D **91**, no. 3, 032005 (2015) [arXiv:1409.2240 [astro-ph.IM]].
[492] H. Yuksel, S. Ando and J. F. Beacom, Phys. Rev. C **74**, 015803 (2006) [astro-ph/0509297].
[493] J. Billard, L. Strigari and E. Figueroa-Feliciano, Phys. Rev. D **89**, no. 2, 023524 (2014) [arXiv:1307.5458 [hep-ph]].
[494] P. Grothaus, M. Fairbairn and J. Monroe, Phys. Rev. D **90**, no. 5, 055018 (2014) [arXiv:1406.5047 [hep-ph]].
[495] S. Ando, Phys. Lett. B **570**, 11 (2003) [hep-ph/0307169].
[496] G. L. Fogli, E. Lisi, A. Mirizzi and D. Montanino, Phys. Rev. D **70**, 013001 (2004) [hep-ph/0401227].
[497] G. G. Raffelt and T. Rashba, Phys. Atom. Nucl. **73**, 609 (2010) [arXiv:0902.4832 [astro-ph.HE]].
[498] H. Goldberg, G. Perez and I. Sarcevic, JHEP **0611**, 023 (2006) [hep-ph/0505221].